VIENNA, 2019

ATOMIC AND PLASMA–MATERIAL INTERACTION DATA FOR FUSION

VOLUME 18

IAEA
International Atomic Energy Agency

ATOMIC AND PLASMA–MATERIAL INTERACTION DATA FOR FUSION

The following States are Members of the International Atomic Energy Agency:

AFGHANISTAN
ALBANIA
ALGERIA
ANGOLA
ANTIGUA AND BARBUDA
ARGENTINA
ARMENIA
AUSTRALIA
AUSTRIA
AZERBAIJAN
BAHAMAS
BAHRAIN
BANGLADESH
BARBADOS
BELARUS
BELGIUM
BELIZE
BENIN
BOLIVIA, PLURINATIONAL STATE OF
BOSNIA AND HERZEGOVINA
BOTSWANA
BRAZIL
BRUNEI DARUSSALAM
BULGARIA
BURKINA FASO
BURUNDI
CAMBODIA
CAMEROON
CANADA
CENTRAL AFRICAN REPUBLIC
CHAD
CHILE
CHINA
COLOMBIA
CONGO
COSTA RICA
CÔTE D'IVOIRE
CROATIA
CUBA
CYPRUS
CZECH REPUBLIC
DEMOCRATIC REPUBLIC OF THE CONGO
DENMARK
DJIBOUTI
DOMINICA
DOMINICAN REPUBLIC
ECUADOR
EGYPT
EL SALVADOR
ERITREA
ESTONIA
ESWATINI
ETHIOPIA
FIJI
FINLAND
FRANCE
GABON
GEORGIA
GERMANY
GHANA
GREECE
GRENADA
GUATEMALA
GUYANA
HAITI
HOLY SEE
HONDURAS
HUNGARY
ICELAND
INDIA
INDONESIA
IRAN, ISLAMIC REPUBLIC OF
IRAQ
IRELAND
ISRAEL
ITALY
JAMAICA
JAPAN
JORDAN
KAZAKHSTAN
KENYA
KOREA, REPUBLIC OF
KUWAIT
KYRGYZSTAN
LAO PEOPLE'S DEMOCRATIC REPUBLIC
LATVIA
LEBANON
LESOTHO
LIBERIA
LIBYA
LIECHTENSTEIN
LITHUANIA
LUXEMBOURG
MADAGASCAR
MALAWI
MALAYSIA
MALI
MALTA
MARSHALL ISLANDS
MAURITANIA
MAURITIUS
MEXICO
MONACO
MONGOLIA
MONTENEGRO
MOROCCO
MOZAMBIQUE
MYANMAR
NAMIBIA
NEPAL
NETHERLANDS
NEW ZEALAND
NICARAGUA
NIGER
NIGERIA
NORTH MACEDONIA
NORWAY
OMAN
PAKISTAN
PALAU
PANAMA
PAPUA NEW GUINEA
PARAGUAY
PERU
PHILIPPINES
POLAND
PORTUGAL
QATAR
REPUBLIC OF MOLDOVA
ROMANIA
RUSSIAN FEDERATION
RWANDA
SAINT LUCIA
SAINT VINCENT AND THE GRENADINES
SAN MARINO
SAUDI ARABIA
SENEGAL
SERBIA
SEYCHELLES
SIERRA LEONE
SINGAPORE
SLOVAKIA
SLOVENIA
SOUTH AFRICA
SPAIN
SRI LANKA
SUDAN
SWEDEN
SWITZERLAND
SYRIAN ARAB REPUBLIC
TAJIKISTAN
THAILAND
TOGO
TRINIDAD AND TOBAGO
TUNISIA
TURKEY
TURKMENISTAN
UGANDA
UKRAINE
UNITED ARAB EMIRATES
UNITED KINGDOM OF GREAT BRITAIN AND NORTHERN IRELAND
UNITED REPUBLIC OF TANZANIA
UNITED STATES OF AMERICA
URUGUAY
UZBEKISTAN
VANUATU
VENEZUELA, BOLIVARIAN REPUBLIC OF
VIET NAM
YEMEN
ZAMBIA
ZIMBABWE

The Agency's Statute was approved on 23 October 1956 by the Conference on the Statute of the IAEA held at United Nations Headquarters, New York; it entered into force on 29 July 1957. The Headquarters of the Agency are situated in Vienna. Its principal objective is "to accelerate and enlarge the contribution of atomic energy to peace, health and prosperity throughout the world".

ATOMIC AND PLASMA–MATERIAL INTERACTION DATA FOR FUSION

VOLUME 18

INTERNATIONAL ATOMIC ENERGY AGENCY
VIENNA, 2019

COPYRIGHT NOTICE

For further information on this publication, please contact:

Nuclear Data Section
International Atomic Energy Agency
Vienna International Centre
PO Box 100
1400 Vienna, Austria
Email: Official.Mail@iaea.org

ATOMIC AND PLASMA–MATERIAL INTERACTION DATA FOR FUSION, VOLUME 18
IAEA, VIENNA, 2019
STI/PUB/023/APID/18
ISBN 978–92–0–109119–2
ISSN 1018–5577

Printed by the IAEA in Austria
August 2019

FOREWORD

Any design concept for a fusion reactor will have to manage the damage to the reaction vessel caused by highly energetic neutrons released during the fusion process. In the case of the reaction most likely to be utilized in the first generation of such reactors, that between the two isotopes of hydrogen, deuterium and tritium, the neutrons are produced directly in the fusion of those two nuclei. Those neutrons that are not captured in the reactor's 'blanket' (where they give up their energy to ultimately drive the electricity-generating turbines) may cause significant damage when they impinge on structural and other components of the reactor.

The articles collected in this volume address the effect that such damage to one proposed material, tungsten, has on its relevant properties — in particular, its resistance to erosion in proximity to a fusion plasma and its propensity to absorb and retain the tritium fuel. It is crucial for the commercial viability of a fusion reaction based on the deuterium–tritium process that any material that is exposed to the plasma does not remove significant quantities of this isotope from the fuel mix. This is because tritium does not exist naturally and must be 'bred' from the interaction of neutrons with lithium in the reactor blanket in a process working at a nearly 100% conversion efficiency for sustainable, long term operation of the reactor.

The mission of the IAEA's Nuclear Data Section in the area of atomic and molecular data is to provide internationally recommended atomic, molecular, plasma–material interaction and material properties databases. One mechanism by which the IAEA pursues this mission is the coordinated research project. This edition of APID contains contributions from participants in the coordinated research project entitled Plasma-Wall Interaction with Irradiated Tungsten and Tungsten Alloys in Fusion Devices (2013–2018). Nineteen research groups from ten different Member States participated and attended three research coordination meetings over the five years of the project.

The IAEA thanks the participants in the coordinated research project for their contributions, in particular B.J. Braams. The IAEA officer responsible for this volume was C. Hill of the Division of Physical and Chemical Sciences.

EDITORIAL NOTE

This publication has been prepared from the original material as submitted by the contributors and has not been edited by the editorial staff of the IAEA. The views expressed remain the responsibility of the contributors and do not necessarily represent the views of the IAEA or its Member States.

Neither the IAEA nor its Member States assume any responsibility for consequences which may arise from the use of this publication. This publication does not address questions of responsibility, legal or otherwise, for acts or omissions on the part of any person.

The use of particular designations of countries or territories does not imply any judgement by the publisher, the IAEA, as to the legal status of such countries or territories, of their authorities and institutions or of the delimitation of their boundaries.

The mention of names of specific companies or products (whether or not indicated as registered) does not imply any intention to infringe proprietary rights, nor should it be construed as an endorsement or recommendation on the part of the IAEA.

The authors are responsible for having obtained the necessary permission for the IAEA to reproduce, translate or use material from sources already protected by copyrights.

The IAEA has no responsibility for the persistence or accuracy of URLs for external or third party Internet web sites referred to in this publication and does not guarantee that any content on such web sites is, or will remain, accurate or appropriate.

Contents

Introduction and Summary

The Coordinated Research Project (CRP) 'Plasma-Wall Interaction with Irradiated Tungsten and Tungsten Alloys in Fusion Devices' ran from 2013 to 2018 and involved 19 research groups from ten Member States of the IAEA. The CRP was concerned with the provision of data for the prediction and modelling of the behaviour of tungsten after its exposure to the highly energetic neutrons produced in a nuclear fusion reaction. Because of the difficulty in producing neutrons of relevant energies, either a theoretical approach is taken (computational modelling using molecular dynamics or density functional theory) or, in experimental studies, 'surrogate radiation' in the form of charged particle beams is used.

This edition of *Atomic and Plasma-Material Interaction Data for Fusion (APID)* collects together ten articles describing the coordinated research that took place as part of the CRP and reflects the advances made in the analysis, prediction and modelling of tungsten as a plasma-facing material, particularly in relation to its propensity to absorb and retain tritium when damaged and the effect of radiation damage on its resistance to erosion.

The CRP also brought about a round-robin comparison exercise in which samples of damaged tungsten were implanted with deuterium and analysed by 17 different labs using thermal desorption spectroscopy (TDS); a wide variation in the amount of implanted deuterium reported by the labs was found and the reasons for the discrepancies and a set of best-practice guidelines for TDS is the subject of a separate publication [1].

The paper by Deshpande, Raole and colleagues describes experiments involving ion-irradiation of tungsten samples as a surrogate for neutron damage, and the subsequent analysis identified distinct types of damage structure for the different ions and energies considered. Damaged tungsten samples were exposed to 100 keV deuterium ions, and in an analysis complemented by atomistic simulations, the greater propensity of damaged tungsten to trap deuterium was confirmed.

The strong influence of radiation damage on deuterium and helium retention was also confirmed by the experimental study reported in the paper of Gasparyan *et al.* A novel TDS procedure enabled detrapping energies for D in single vacancies and in vacancy clusters to be derived. A large amount of deuterium retention in irradiated tungsten was reported, suggesting that such defect sites can be associated with high binding energies.

The paper by Hatano *et al.* reports a study of the trapping and transport of hydrogen in tungsten samples damaged by neutrons from a fission reactor. As well as the kinetics of hydrogen penetration, the authors also report the effect of rhenium (which is produced from transmutation of tungsten by interaction with neutrons) on the accumulation of defects and the retention of hydrogen and the influence of crystal orientation on displacement damage in tungsten.

Khripunov *et al.* report on their experiments of radiation damage in tungsten using surrogate heavy ions at MeV energies; subsequent exposure to a deuterium plasma led to enhanced erosion and retention of deuterium due to defect formation, a finding confirmed by computational simulation.

The paper by *Li et al.* describes computational simulations of 'self-healing' of damage in nano-(poly)crystalline tungsten. The vacancies and self-interstitial atoms (SIAs) are found to diffuse to the grain boundaries which serves as a sink for these defect structures. The kinetics of this process are analysed and the prospects for nanocrystalline tungsten as a plasma-facing material in a fusion reactor are discussed.

Luo *et al.* report on their study of deuterium retention and permeation in tungsten that has been pre-irradiated by heavy ions (used as a surrogate for the neutrons of a fusion reaction). They were able to produce a 'quasi-homogeneous' distribution of defects in tungsten samples within a depth of 50 μm using a novel energy degrader which varied the energy of the implanted ions from a 122 MeV beam of Ne^{7+} ions.

Deuterium retention and transport in damaged tungsten is the subject of a paper by Markelj *et al.* The nature and energetics of hydrogen traps are reported and the results of a benchmark experiment studying deuterium retention as a function of loading temperature is described: exposure temperature has a large influence on deuterium uptake and it is found that uptake of neutral atoms can be effectively ignored at temperatures below 450 K. For the first time, simultaneous self-damage (W-ion irradiation) and D atom loading was carried out, and synergistic effects identified.

Oda *et al.* report their study of the key processes and properties that are important in the evaluation of the trapping and migration of hydrogen in irradiated tungsten. Several key quantities, such as the bulk diffusion coefficient, effective diffusion coefficient along grain boundaries (GBs), and effective trapping energy in GBs are reported.

The paper by Sakamoto *et al.* describes their research on hydrogen isotope retention in tungsten damaged by heavy ions (2.4 MeV Cu^{2+}) as a surrogate for fusion neutrons. Deuterium retention, as measured by thermal desorption spectroscopy, is found to increase with the damage dose but saturates at a lower level (0.4 dpa) in the case of a high dose rate (5×10^{15} Cu^{2+} m^{-2} s^{-1}) than with a low dose rate (1×10^{15} Cu^{2+} m^{-2} s^{-1}; up to 2 dpa).

The final paper in this collection, by H.-B. Zhou and G.-H. Lu, reports on theoretical studies of the behaviour of helium (He), osmium (Os) and rhenium (Re) in irradiated tungsten. Helium is expected to be introduced at the surface of the plasma-facing material from the fusion plasma and forms bubbles which impair its structural integrity; Os and Rh are expected to reach concentrations of a few percent in the material through transmutation of tungsten atoms. They preferentially form clusters and precipitates which lead to hardening and embrittlement of the material, potentially severely limiting its useful lifetime.

[1] LEE, H.-T., SCHWARZ-SELINGER, T., ET AL., Hydrogen retention in tungsten films: an international round robin experiment on temperature programmed desorption, Manuscript in preparation, 2019.

SIMULATION OF RADIATION DAMAGE AND ION-IRRADIATION EXPERIMENTS WITH TUNGSTEN

S.P. DESHPANDE[1], P.M. RAOLE[1], P.N. MAYA[2], P. SHARMA[2], A. ATTRI[2], A. K. TYAGI[2], R. KUMAR[1], S. S. VALA[1], A. SATYAPRASAD[1], S. MUKHERJEE[3], P.K. PUJARI[3], P. KULRIYA[4], P.K BAJPAI[5], S.P. PATEL[5], T. TRIVEDI[5], M. WARRIER[6], P.V. SUBHASH[2], P. RAYJADA[1], P. KIKANI[1], C. DAVID[7], A. LAKHANI[8], V. KARKI[3], M. SINGH[3], M. ABHANGI[1], K. DEVRANI DEVI[4], KEDARMAL[4], K. SARAVANAN[3], S. KANNAN[3], S. MISHRA[3], K.B. KHAN[3], P. NANDI[2], C. BALASUBRAMANIAN[1], S. A. KHAN[4], M. H. MEHTA[1], S. KANPARA[1], C. JARIWALA[1], C. DUBE[2], S. KHIRWADKAR[1]

1. Institute for Plasma Research, Bhat, Gandhinagar, India- 382428

2. ITER-India, Institute for Plasma Research, Gandhinagar, India - 382428

3. Bhabha Atomic Research Centre, Trombay, Mumbai, India- 400085

4. Inter-University Accelerator Centre, New Delhi, India – 110067

5. Guru Ghasidas Vishwavidyalaya, Koni, Bilaspur CG, India - 495009

6. BARC, Vishakhapatnam, AP, India – 530012

7. Indira Gandhi Centre for Atomic Research, Kalpakkam, TN, India - 603102

8. UGC-DAE Consortium for Scientific Research, Indore, MP, India -452017

Abstract

Computer modelling and surrogate ion-irradiation experiments have been carried out to examine the radiation damage and deuterium trapping in tungsten. We have considered 80 MeV gold and 10 MeV boron ions for irradiation to create different types of defects and the samples were subsequently exposed to 100 keV deuterium. While the gold ions create a large number of vacancy clusters and the dislocation lines, boron irradiation produced dislocation loops predominantly. Atomistic simulations reveal fragmentation of cascades for PKA energies greater than 160 keV. This may help in understanding the experimental result of formation of large vacancy-clusters by heavy ion irradiation. A comparison of deuterium depth profile reveals that there is an increase of D trapping in the samples pre-irradiated samples.

1. INTRODUCTION

The aim of the project is to develop an understanding of the issues related to the defect creation and trapping of hydrogen isotopes in the polycrystalline tungsten and is motivated by emergence of tungsten as a candidate plasma-facing material for the divertor in fusion devices. In the absence of 14 MeV neutron source with sufficient flux, surrogate ion-irradiation experiments are being carried out by a number of researchers. Though surrogate ion-irradiation alone cannot substitute a fusion neutron source, a combination of modelling, experiments and intuitive understanding can give a reasonable picture of radiation induced effects. This report covers the work carried out by CRP participants at the Institute for Plasma Research, Gandhinagar and collaborating members from other institutions in India.

In this project we have carried out computer simulations and experiments of ion irradiation in tungsten. Simulations address the initial stages of point-defect creation due to fusion-like neutron spectrum, details of collision cascades, in-cascade clustering of defects and dislocation nucleation for different ion energies. This has been achieved by a combination of Molecular Dynamics (MD) simulations, Monte Carlo simulations and neutron transport calculations.

Experiments primarily addresses the defect creation due a variety of ions over a wide range of energy. This can be grouped into three categories, (a) low mass, low energy gaseous ions: 100 keV D^+ and 250 keV He^+; (b) medium mass, high energy ions: 10 MeV B^{3+}; and (c) high mass, high energy ions: 80 MeV Au $^{7+}$. Two types of tungsten samples were used for the experiments: 2 mm thick bulk samples annealed at 1173 K and 100 μm thick recrystallized at 1838 K. The samples were characterized for micro-structure, defects and surface morphology using X-ray diffraction, TEM, positron annihilation spectroscopy, resistivity by four-probe, SEM and AFM. The deuterium depth profiles in the samples were measured using both Elastic Recoil Detection Analysis (ERDA) and Secondary Ion Mass Spectroscopy (SIMS).

Rest of the report is organized as follows: Section 2 is devoted to simulations, Section 3 covers the experiments and results, discussion of the results is in Section 7 and the conclusions are given in Section 8.

2. COMPUTER SIMULATION OF RADIATION DAMAGE:

The ultimate aim of irradiation experiments is to assess the suitability of plasma-facing materials for future fusion reactors. In a fusion reactor, 14 MeV neutrons are expected to create radiation damage which may ultimately cause fuel atoms to trap within and accumulate. This is apart from the changes in properties of the material, which anyway may occur. The H-isotope trapping may depend on the defect structure and hence it is necessary to understand the defects produced by the radiation damage.

In a future fusion power reactor, the operation time (pulse length) would be much larger than in current fusion devices and in addition, the flux of neutrons per unit area would also be quite significant. The nearest device to a real fusion power plant today is ITER (where pulse length of the plasma would be about 400 s and the neutron wall-load will be about 0.5 $\mathrm{MW/m^2}$).

An energy resolved neutron spectrum was calculated by solving neutron transport equations using ATTILA code for 'ITER like' divertor geometry [1, 2]. The divertor geometry used for calculations is shown in FIG. 2 (a). The Primary Knock-on Atom (PKA) spectrum generated by the neutron distribution was estimated by using the neutron interaction cross-section with tungsten by using SPECTER code [3]. The energy resolved neutron flux at tungsten divertor and the corresponding PKA energy distribution obtained is shown below.

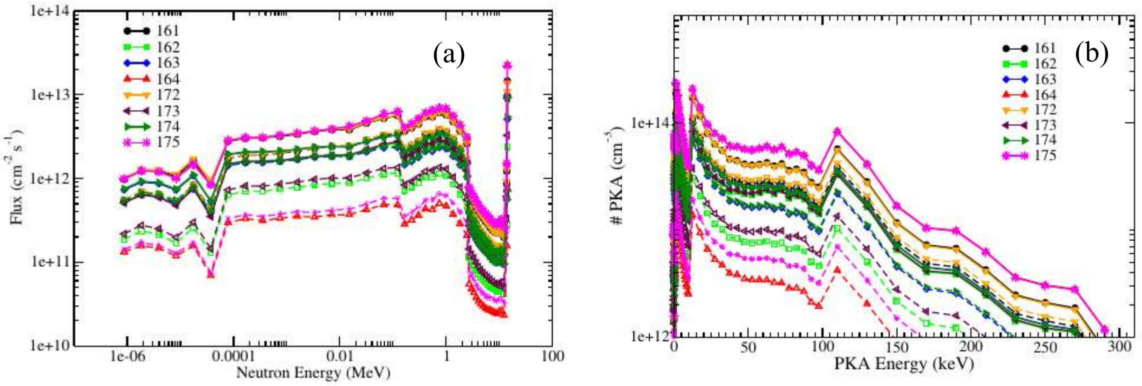

FIG. 1. (a) Energy resolved neutron flux and (b) the corresponding PKA energies for an ITER-like tungsten divertor. The colours/numbers represent a particular location on or within the divertor region as shown in FIG. 2 (a). The points ranging from 161 to 175 indicate different divertor regions used for computations. The neutrons fluence corresponds to 400 s exposure.

For the above PKA energy spectrum, the displacement per atom (dpa) in tungsten is calculated by using Norgett-Robinson-Torrens (NRT) model for a displacement energy of 90 eV. The dpa values are calculated at different mesh points in the divertor and the maximum dpa obtained was about 0.22 (cf. FIG. 1 (b)) for a lifetime neutron fluence (0.4 FPY at 0.5 MWa/m^2).

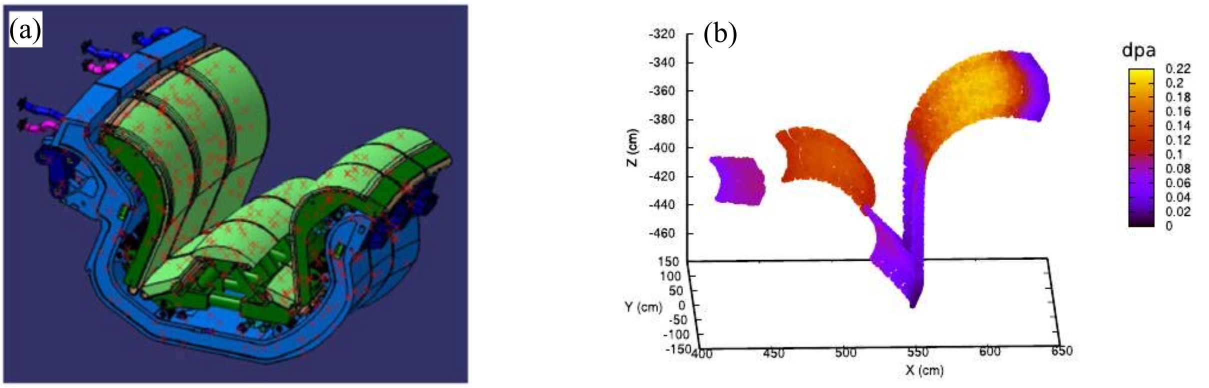

FIG. 2. (a) Location of points where energy resolved neutron flux and PKA energies for an ITER-like tungsten divertor were estimated for and (b) dpa values estimated at different grid points on the divertor.

We note that the maximum PKA energy is about 300 keV, with most of the PKAs below 150 keV. Correspondingly, we have carried out Molecular dynamics simulations for the PKA energy ranging from 500 eV to 150 keV.

To begin with, we have compared different inter-atomic potentials (cf FIG. 3 (a) and

TABLE 1) for tungsten to find out a reasonable potential for defect simulation. It has been observed that the number of vacancy-interstitial pairs (Frenkel pairs) obtained in different potentials were similar (FIG. 3 (b)). However, the defect structures showed considerable differences as shown FIG. 4 for (a) Zhou and (b) DNMD+ZBL1 potential (differences were seen for Juslin potential as well but not shown here).

TABLE 1. EQUILIBRIUM AND NON-EQUILIBRIUM PROPERTIES USING MOLECULAR STATICS (E_c: cohesive energy; *a* (3.1652Å): lattice parameter; C_{ij}: elastic constants; E_v: vacancy formation energy; E_i: interstitial formation energy).

	E_C (eV)	a (Å)	Elastic constants C_{ij} (Gpa)			E_V (eV)	E_I (eV)			
			C_{11}	C_{12}	C_{44}		E^d_{100}	E^d_{110}	E^d_{111}	E_{octa}
Expt.	8.90 [a]	3.1652 [b]	522.4 [b]	204.4 [b]	160.6 [b]	3.7			9.06	
DFT		3.18					11.513	9.84	9.55	11.7
EAM										
FS	-8.90	3.1652	522.44	204.41	160.61		8.652		7.805	8.524
AT	-8.90	3.1652	522.43	204.41	160.61		9.783		8.883	9.968
JW	-8.90	3.1652	522.47	204.45	160.64	3.554	10.277	10.157	9.50	10.393
DNMD	-8.90	3.1652	523.10	204.67	160.81	3.557	11.334	9.768	9.472	11.7
DNMD +ZBL1	-8.90	3.1652	523.10	204.67	160.81	3.557	11.332	9.766	9.472	
DNMD +ZBL2	-8.90	3.1652	523.10	204.67	160.81	3.557	11.333	9.768	9.472	
Zhou	-8.757	3.1652				3.567				
Tersoff										
Li	-8.86	3.1652	515	203	162	3.52	12.01	9.53	9.33	12.05
Juslin	-7.41	3.165	542	191	162	1.77	8.93	8.77	9.62	9.92

E_d (eV)	Expt [c]	AT	AT+ZBL	DNMD	DNMD+ZBL1	DNMD+ZBL2
Minimum	~ 40-50	64	48	55± 3	55	41± 1
Average	~ 80	166	128	88.3±0.7		84.5 ± 0.9

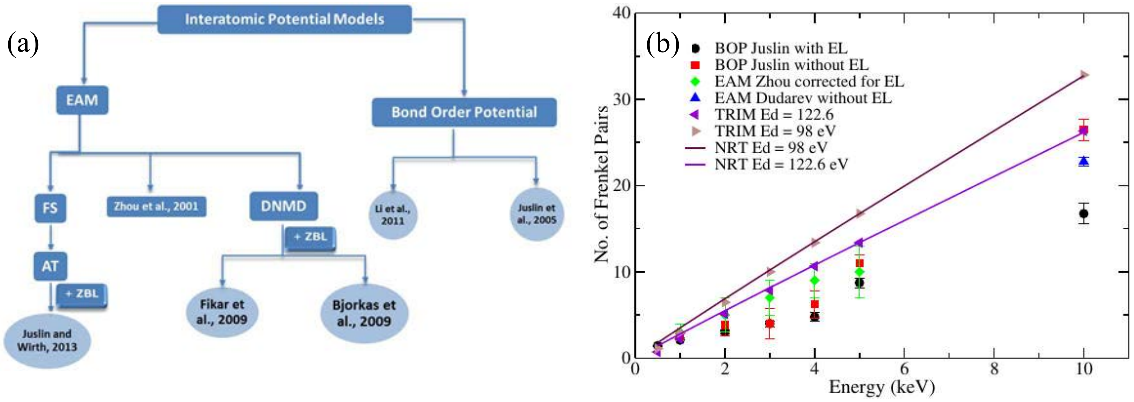

FIG. 3.(a)Types of Inter-Atomic potential, (b)Number of FP obtained in different potentials

Based on the defect structures in comparison with the published DFT and experimental data we have chosen DNMD+ZBL1 potential for final calculations. The simulations were carried out on single crystal tungsten lattice with X-Y plane oriented along (110) with periodic boundary conditions. The PKA energy varied between 500 eV to 200 keV and 50 non-cumulative bombardments were carried out for each energy using ParCAS code [4]. The number of atoms in the simulations was varied between 0.5 to 30 million, depending on the impact energy. These simulations were carried out in a 35 TF, 756 core HPC machines at IPR. From these simulations we have observed that the cascade structure as well as the defect structure varies with the energy of the PKA. The cluster size increased with the increase in PKA energy. For cascades below 40 keV PKA energy, we have observed the clusters of vacancies and interstitials. For energies above 50 keV, the clusters were found to form dislocations with distinct Burgers vector.

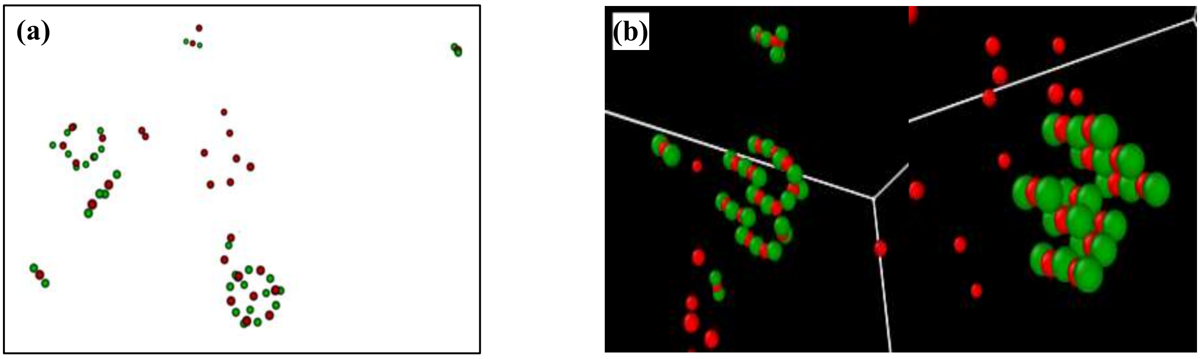

FIG. 4. Defect structures in different potentials Zhou, DNMD+ZBL1 potential

The maximum thermal spike formed due to collision cascades along with the surviving FP at the end of the cascade for 50 keV and 100 keV PKA energies is in Fig. 5. It can be seen that cluster of vacancies are formed at the core of cascade while, interstitial clustering is observed at the cascade periphery. The mean energy of atoms in the thermal spike was found about 0.2 eV and the maximum energy was about 10 eV for 100 keV.

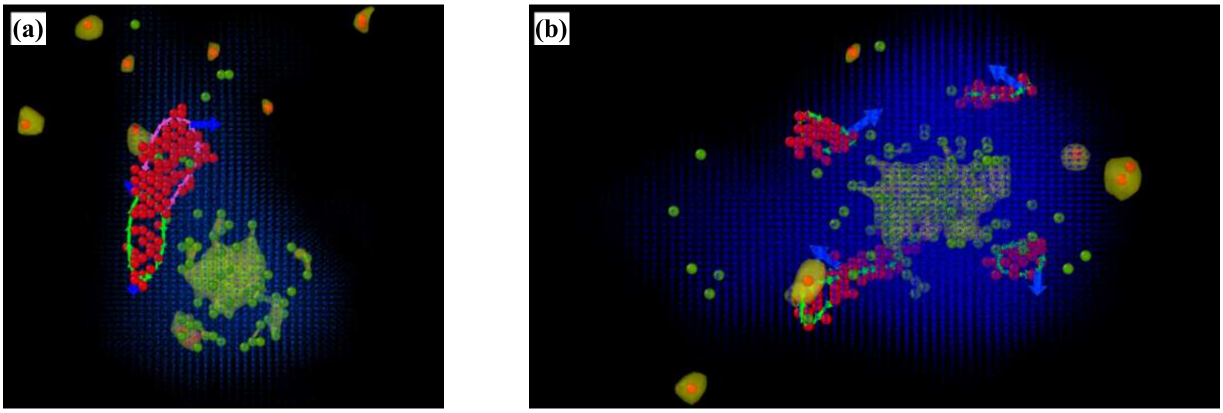

FIG. 5. Dislocations formed at 50 keV (left) and 100 keV (right) cascades along with thermal spike (blue dots) and vacancy clusters

The scaling of the cascade volume as a function of PKA energy is shown in FIG. 6. It can be seen that the cascade volume scales linearly with the PKA energy for energies below 200 keV.

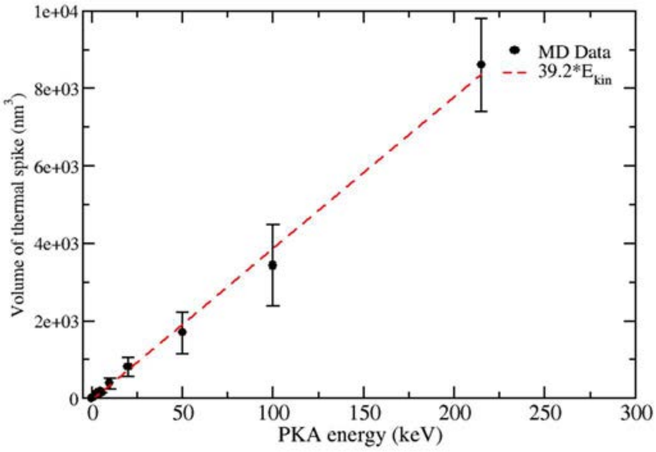

FIG. 6. Thermal spike volume as a function of PKA energy

However, splitting of cascades was observed at energies above 160 keV which is shown in

FIG. 7, where, from a single PKA, two separate thermal spikes are formed for 215 keV (

FIG. 7 (b)) and three thermal spikes were observed at 375 keV. It can be seen that each of the sub-cascades cools down to independent clustering of defects within the simulation time.

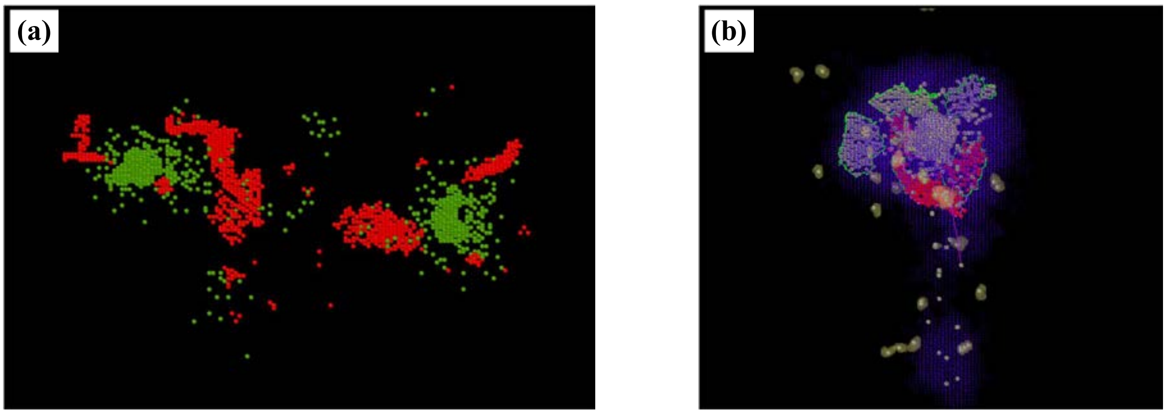

FIG. 7. Fragmentation of cascades at high energies (a) 375 keV and (b) 215 keV.

The interstitial and vacancy cluster size distribution for 100 keV PKA is shown in Fig. 8. The cluster analysis was done by the OVITO [5] tool with a cut-off of 5A. As the energy increases, clustering of defects also increases leading to larger size defect structures. For example, fifty eight percent of the total interstitials and 79 % of the total vacancies were of single type for 100 keV which is 8-10 % lesser than 50 keV. For 100 keV PKA, the interstitial and vacancy cluster size was up to 250 atoms, whereas it was up to 100 atoms for a 50 keV PKA.

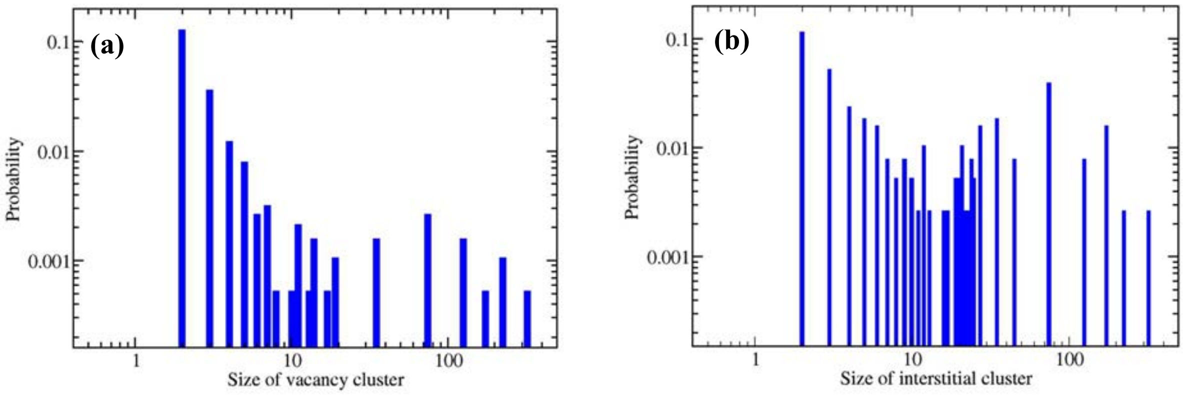

FIG. 8. Vacancy and Interstitial cluster frequency distribution for 100 keV cascade (x-axis indicates the number of vacancies/interstitials that form the cluster)

At energies above 50 keV, the interstitial clusters converted to perfect dislocations of either ½ <111> type of <100> type, which is shown in FIG. 5 for both 50 keV and 100 keV PKA energies.

The detailed study of dislocation nucleation was carried out and it has been observed that the dislocations nucleate at the periphery of the cascade. The initial stages of evolution of dislocation nucleation analysed using OVITO for 100 keV PKA energy is shown in FIG. 9 (a). We have not shown the atoms for clarity. The final structure formed at the end of the simulations is shown in FIG. 9 (b). We have found two major type of perfect dislocations with Burgers vector either along ½ <111> or <100>. We have also observed the annihilation of certain dislocations, splitting and merging of unstable dislocations to stable ones. The formation of <100> dislocations often took place by the annihilation of ½ <111> dislocation reactions of the type: [100] = ½ [1 -1 1] + ½ [1 1 1]. Formation of dislocation junctions of three or more line segments has also been observed. The length of the dislocations was found to increase with the PKA energy. The size of the interstitial clustering was found to increase up to a maximum of ~900 atoms, beyond which the sub-cascade seem to dominate the interstitial clustering. The loop size remained either unchanged or smaller. However, detailed statistical analysis is needed to quantify the maximum size of the defect cluster.

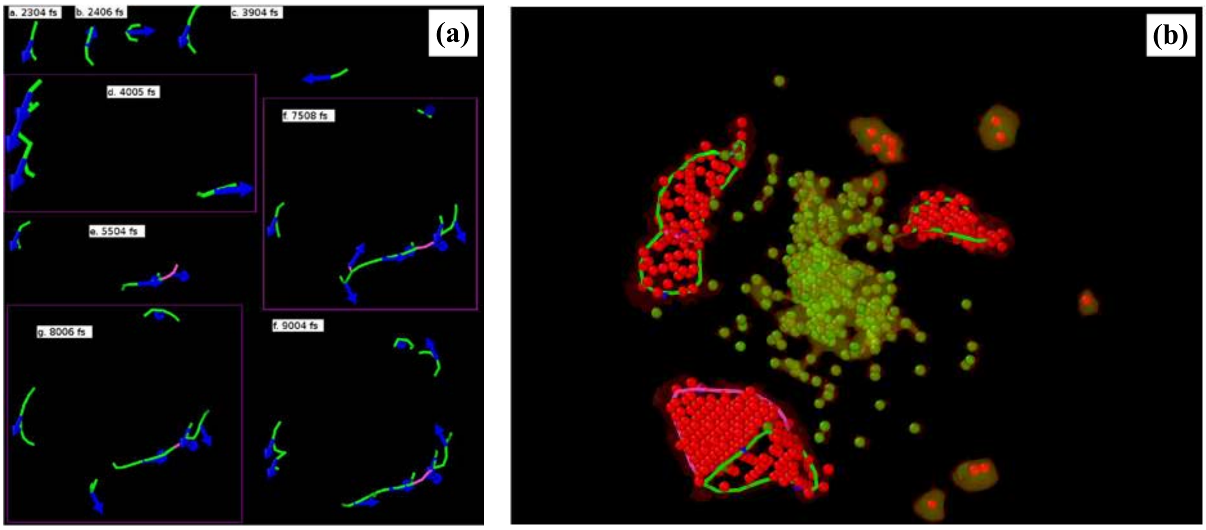

FIG. 9. (a) Initial stages of dislocation nucleation along with their Burger's vector and (b) Stable <100> (magenta) and ½ <111> (green) dislocations formed at the end of simulations for 100 keV PKA energy.

2.1 Simulation of experiments:

A part of modelling studies is dedicated to the simulation of experimental conditions and data. In irradiation experiments, in order to study the effect of ion mass in the damage profile, we have simulated a number of ion masses and it seems that compared to heavy ions, 10 MeV boron can generate a PKA spectrum closer to that of 14 MeV neutrons in tungsten (*cf.* FIG. 1 (b)).

One of the major differences between ions and neutrons (apart from the penetration depth) in radiation damage is the nature of inelastic energy loss. While neutrons lose their energy primarily with the target nuclei, ions lose a considerable energy with the electrons. This can change the nature of defects produced in the lattice. A quantitative estimate has been derived for the electronic loss of ion energy using the existing models. Another aspect of modelling studies is the interpretation of experimental data, especially for defect and trapping analysis. In order to understand the point defects obtained in experiments, both MD and positron-annihilation simulations were also carried out along with the analysis of existing experimental data from other experiments.

The recoil energy distribution of W atoms from 10 MeV boron and 80 MeV Au ions calculated from SRIM [6] is shown in FIG. 10. One thousand boron and gold projectiles were launched along random directions. At 10 MeV energy, boron produces PKA energies similar to 14 MeV neutrons in tungsten whereas, 80 MeV Au produces recoil energies up to 28 MeV. The range of both Au and B are roughly of the same order i.e., ~4.5 μm. This indicates denser cascading and defect production throughout the ion range in the case of 80 MeV Au, in contrast to 10 MeV B. It is also to be noted that at higher PKA energies, splitting of cascades leading to closely spaced sub-cascading in the case of 80 MeV Au.

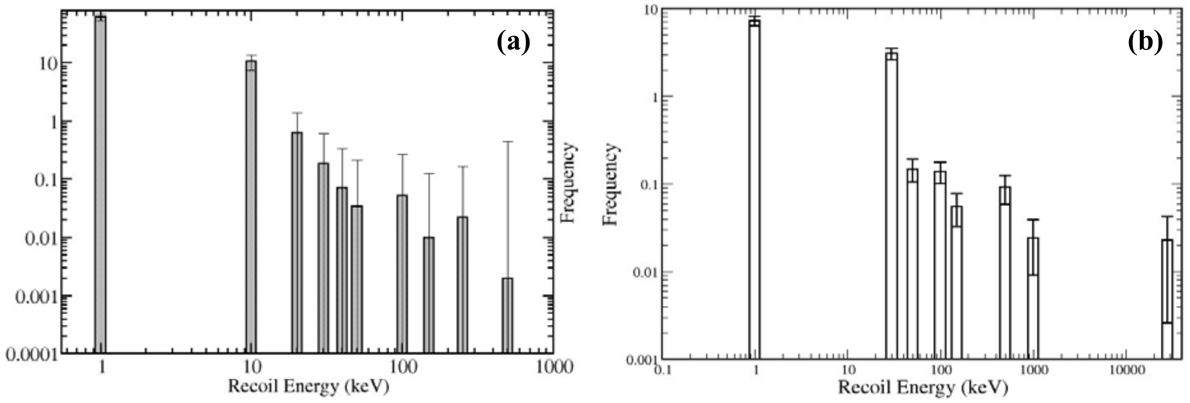

FIG. 10.Frequency distribution of PKA by a single ion (a) 10 MeV boron and (b) 80 MeV Au

3. EXPERIMENTS: ION-IRRADIATION IN TUNGSTEN

In this section, we present a summary of various experiments carried out under the CRP project.

3.1 Irradiation & characterization facilities

3.1.1 Irradiation Facilities

Following facilities have been used for irradiation of tungsten with various ions of different energies (FIG. 11).

- 15 MV van de Graff generator (Pelletron), at IUAC Delhi [7]
- 1.7 MV tandem accelerator at IGCAR Kalpakkam
- 3 MV tandem accelerator at Guru Ghasidas University at Bilaspur [8]
- Low Energy Ion Beam Facility (LEIBF) at IUAC Delhi
- Linear ion accelerator based 14 MeV neutron generator at IPR
- 150 keV tandem accelerator at IGCAR

The high energy W and Au (80 MeV) ions were irradiated in bulk tungsten samples (of 8 x 8 x 2 mm^3 size) and tungsten foil samples (of 8 x 8 x 0.1 mm^3 size), respectively in 15 MV van de Graff generator (Pelletron), at IUAC Delhi [7]. The beam current was varied between 7 nA to 21 nA which corresponds to 1 to 3 pnA (particle nano ampere = current in nA/charge state). The beam was rastered uniformly over the sample surface for a fluence of 1×10^{14} cm^{-2}.

Another set of bulk tungsten samples were irradiated with 7.5 MeV tungsten (W^{3+}) ions using a 1.7 MV tandem accelerator at IGCAR Kalpakkam.

The tungsten foils were irradiated by 10 MeV boron ions (B^{3+}) by using a high current 3 MV tandem accelerator at Guru Ghasidas University at Bilaspur [8]. The irradiation chamber was evacuated to a base-pressure of 1×10^{-6}mbar and the foils were exposed to a beam current of 200 pnA for two different fluences of 1.3×10^{14} ions-cm^{-2}and 1×10^{15} ions-cm^{-2}.

Helium-ions of 250 keV were implanted in samples which had been already irradiated by either gold or boron ions. For comparison, helium was also implanted in un-damaged tungsten foils. He-implantation was done using Low Energy Ion Beam Facility (LEIBF) at IUAC Delhi, for a fluence of 5×10^{15} ions-cm^{-2}.

The samples which had been irradiated by gold, boron and helium were further exposed to deuterium-ions of 100 keV, using a current of 20-100 μA from the 14 MeV neutron generator at IPR (Au+D, Au+He+D, B+D, He+D, D alone). The samples were exposed to a fluence of 5×10^{17} ions-cm^{-2}.

In a separate experiment, the H-ions of 50 keV were implanted using an accelerator at IGCAR Kalpakkam (7.5 MeV W ions).

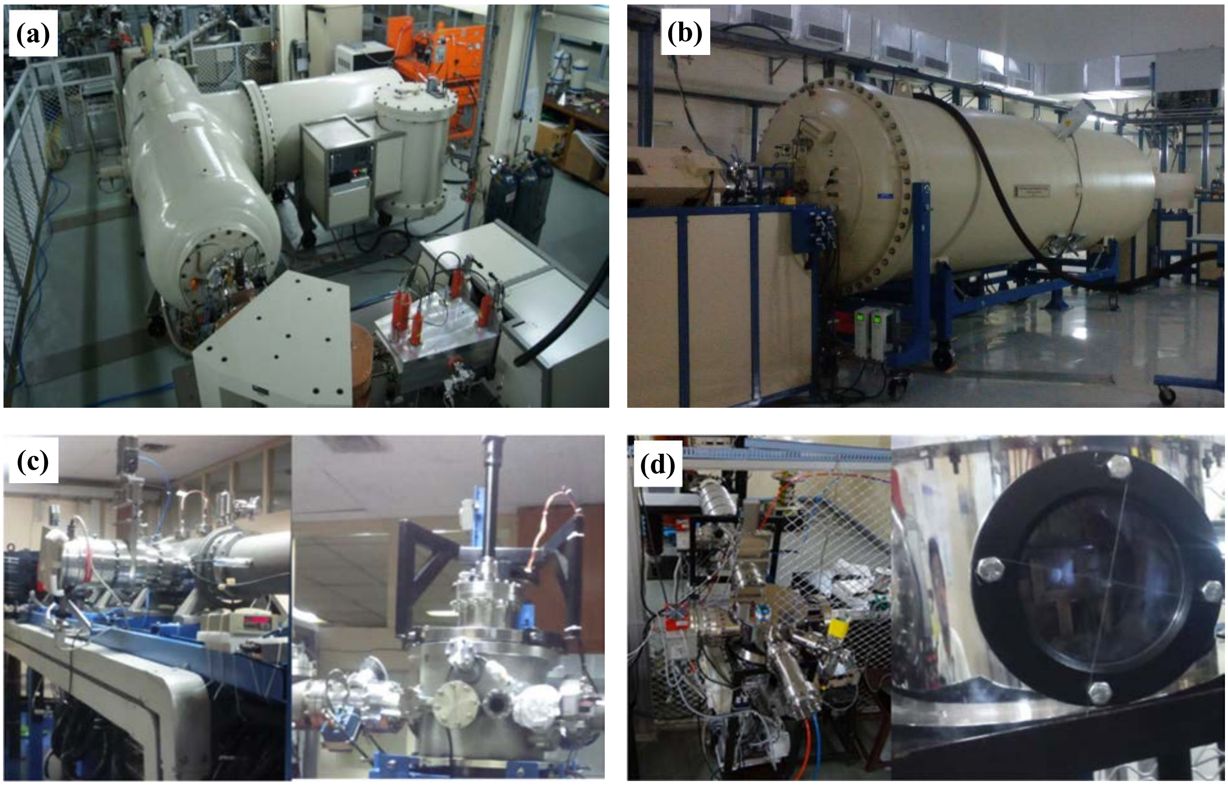

FIG. 11. Images showing accelerator facility used for ions irradiation (a) 1.7 MV tandetron at IGCAR (7.5 MeV W^{4+}), (b) 3 MV pelletron at GGU Bilaspur (10 MeV B^{3+}), (c) Low energy metal ion implanter at IUAC, Delhi (100 keV Au^{+}), and (d) 14 MeV neutron generator, IPR (100 keV D^{+})

3.1.2 Characterization techniques

Surface, near surface, micro-structural and structural properties of the samples were characterized using different techniques before and after irradiation. The deuterium and helium irradiated samples were also characterized for the depth profiles of the respective species.

Following techniques have been used for characterization.

- X-ray Diffraction (XRD)
- Scanning Electron Microscopy (SEM) & Atomic Force Microscopy (AFM)
- Transmission Electron Microscopy (TEM)
- Electron Back-scattered Diffraction (EBSD)
- Positron Annihilation Spectroscopy (PAS)
- Secondary Ion Mass Spectrometry (SIMS)
- Electron Recoil Detection Analysis (ERDA)
- Four Probe Resistivity measurements

Descriptions of some of these techniques are given below:

PAS: Positron lifetime spectroscopy and Doppler broadening techniques were used to characterize the point defects in the samples before and after irradiation. Positron lifetime spectroscopy is used to find type of defects and quantify those defects by measuring the lifetime of positrons and their intensities.

The ^{22}Na positron source is sandwiched between two identical tungsten samples. The positrons emitted from the source is attenuated and have a peak around 270 keV. The positrons get thermalized in the lattice and the thermal positrons are annihilated within the W sample, which results in two 511 keV gamma rays. The lifetime of positron is a measure of the point defects in the lattice which is estimated by measuring the time delay between the gamma ray emission at the birth of positron (1.27 MeV) and its annihilation in the lattice. The range of 270 keV positron in tungsten is ~16 μm. A schematic of the lifetime measurement set-up is shown in FIG. 12. The resolution of individual channels ~12.5 ps.

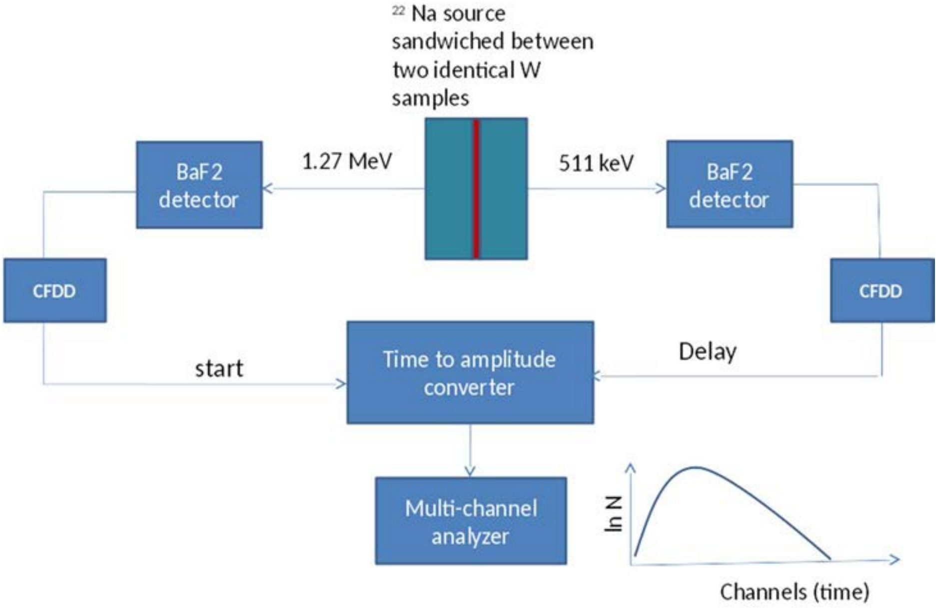

FIG. 12. Schematic of positron-annihilation life-time measurement setup

The lifetime data obtained is fitted with three lifetime components τ_1, τ_2 and τ_3, using PALSFIT software [9].

Doppler-broadening of annihilation-radiation was carried out using a variable-energy slow positron-beam. The positrons are generated by the ^{22}Na source. The emitted positrons are thermalized using a 1 μm thick tungsten foil placed close to the source. The thermalized positrons are emitted at an energy equal to the sum of the negative work function of tungsten (~3eV) and the positive bias on the moderator. For our experiments, the potentials are such that a 200 eV slow positron beam is produced. The slow positrons are guided to the sample using a bent solenoid with a B field of 100 G. The un-moderated positrons are filtered out by the rapidly changing direction of the B field. A 10 mm collimator placed at the exit of the solenoid further filters out the remaining fast positrons. A pair of Helmholtz coils guide the positrons from the solenoid exit to the sample. The incident positron energy is varied by negative biasing the sample. Thus the beam-energy can be varied from ~200 eV to 25 keV. The upper energy-bound corresponds to a mean implantation-depth of ~125 nm. The incident positron flux is roughly 10^3 e^+/sec. The incident positrons thermalize and annihilate with electrons in the sample, producing a pair of 511 keV gamma rays. These annihilation gamma rays are monitored by an HPGe detector (resolution of 1.3 keV at 511 keV) placed close to the sample. S-parameter, defined as the ratio of area of the central region (511 ± 1 keV) of the annihilation peak to the total peak area (511±3 keV), were evaluated as a function of incident-beam energy. Similarly, W-parameter, defined as the ratio of the counts in the wing region of the profile to the total peak area, is also evaluated as a function of the beam-energy. Due to their low degree of localization, the valance electrons contribute to the S-parameter and core electrons contribute to the W-parameter which is also known as high angular momentum component.

The implantation depth profile *P(z,E)* of positron beams of different energy calculated using Makhov profile [10] is shown in FIG. *13*, where *z* is the penetration depth, ρ is the density of the sample, *r*, *m* and *A* are free parameters and Γ is the gamma function [10].

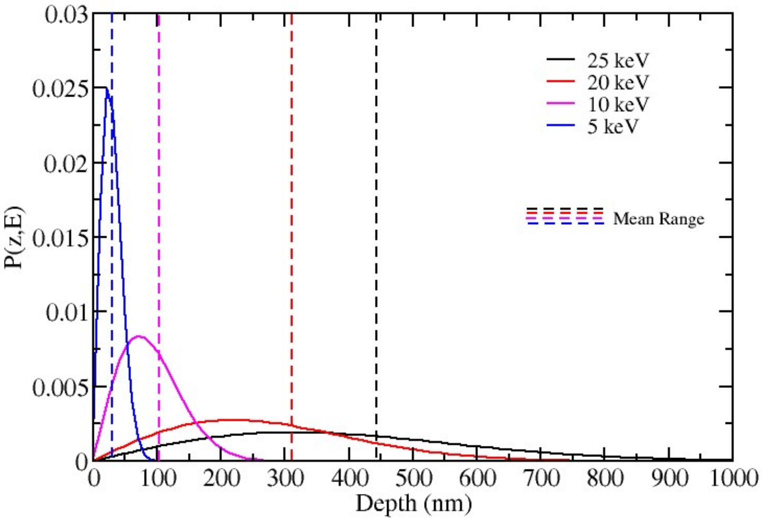

FIG. 13. Positron implantation profile for different energies. Mean range of depth position is indicated using dashed vertical lines.

$$P(z,E) = \frac{mz^{(m1)}}{z_0^m} exp\left[\frac{-z^m}{z_0}\right] \wedge z_0 = \frac{AE^r}{\rho\Gamma\left(1+\frac{1}{m}\right)} \qquad (1)$$

The typical values of A = 4.0 µg cm^{-2} (keV)$^{-r}$, m = 2 and r = 1.6 [11]. The mean penetration depth is $Z = \frac{AE^r}{\rho}$. Diffusion of positrons, after the penetration depth will broaden the profile further.

The deuterium depth profiles were measured using ERDA and SIMS techniques.

ERDA: A carbon beam (C^{4+}) of 7.6 MeV energy was used with a beam current of ~30 nA. A Si surface, barrier type detector having area 0.2 cm^2 was used and the recoiled D atoms were detected at an angle of 35°. The detector window was covered with 6 µm Al foil to stop forward-scattered carbon atoms. The distance between the detector and the target was about 6 cm. The obtained D-spectra were fitted using SIMNRA programme (Mayer, M. 1999) to obtain D depth profiles.

SIMS: The depth analyses of all the elements in all the specimens were carried out using magnetic sector based Cameca IMS-7f instrument equipped with both oxygen ($O^{2+}$and O^-) and caesium (Cs^+) primary ion beams. The depth distribution analyses were carried out using Caesium (Cs^+) primary ion beam at an impact energy of 15 KeV with negative secondary ion detection mode. Primary beam with beam current of 75±1 nA falls on the sample surface at an incidence angle of 23° w.r.t. surface normal. Primary ion beam was rastered over an area of 250 µm × 250 µm and secondary ions were collected from an analysis region of 63 µm in diameter at the centre of raster area, by selecting the field aperture of 750 µm in order to remove the crater edge effects. Mass resolution (m/dm) of 400 was selected in all the analysis. The pressure in the analysis chamber was maintained $\sim 7\times10^{-9}$ mbar.

Four probe resistivity measurements: DC resistivity measurement were done on tungsten samples. Copper wire of thickness 44 gauge was used for making the connections. Measurements are done along and perpendicular to the rolling direction of the foils, because of this reason contacts were made two times on the same sample. The measurements were taken at the step size of 5 K/min from 300 K to 10 K.

3.2 Sample Preparation

The summary of the samples is give in TABLE 2.

TABLE 2. SUMMARY OF THE SAMPLE SPECIFICATIONS

Sample Type	Sample source	Composition	Rolling Direction	Average Grain size (µm)
Tungsten Plate	PLANSEE AUSTRIA	99.95%	along the plate surface equiaxed grains	5-10 / equiaxed
Foil (~100 µm)	Princeton Scientific Corp. United States	99.96%	along the foil surface	1-3 / elongated
Tungsten Alloy ($W-La_2O_3$) Plate	PLANSEE AUSTRIA	99.98%	along the plate surface	-

Tungsten foil samples of 8×8 mm^2 dimension were cut with electrical discharge machining (EDM wire cutting). The samples were cold-mounted using casting method. The specimens were mechanically polished with different grade of emery papers.

The roughness measured by contact profilometer was ~0.5 µm and 0.35 µm for pristine tungsten foil and fine polished tungsten foil, respectively.

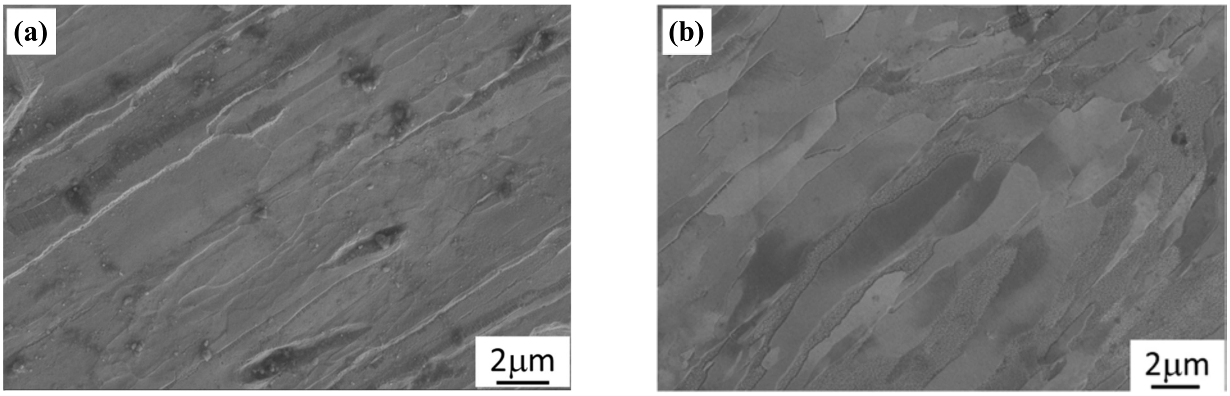

FIG. 14. Scanning electron micrograph of pristine tungsten foil (a) before polishing, (b) after polishing

The tungsten foils were annealed in vacuum at 10^{-3} mbar with 100 mbar Ar+8% H_2 gas at 1838 K for 50 min to obtain recrystallized foil. The microstructure of heavily cold-rolled tungsten foil consists of elongated grains with 1 µm to 3 µm grain sizes for pristine tungsten foil as shown in FIG. 14 (a). FIG. 15 (b) shows the scanning electron micrograph of tungsten foil after annealing at 1838 K. It may be noted that microstructure consists of significantly larger grains in tungsten foil after annealing at 1838 K temperature, which is much higher than the recrystallization temperature (~1473 K, 0.4 Tm) of tungsten. The maximum grain size obtained was ~ 50 µm.

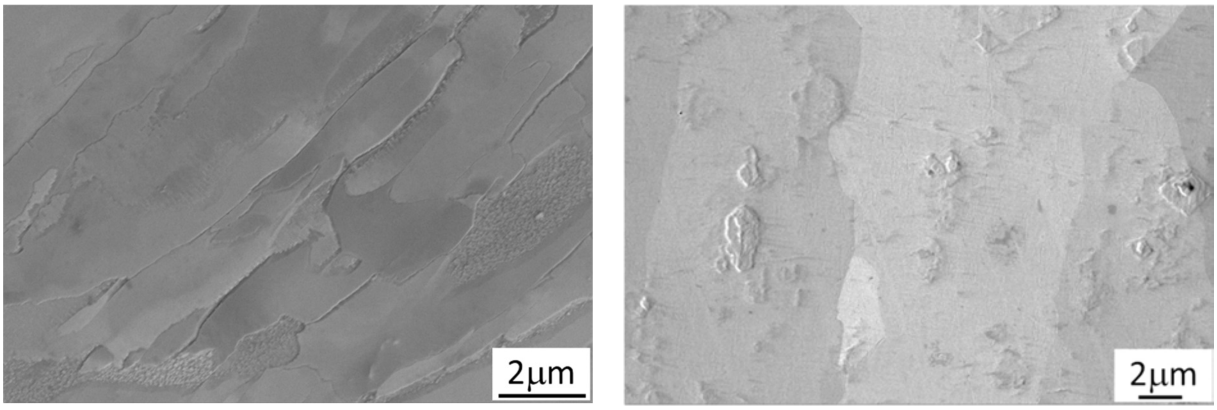

FIG. 15. Scanning electron micrograph of (a) pristine tungsten foil, (b) tungsten foil after annealing at 1838 K temperature.

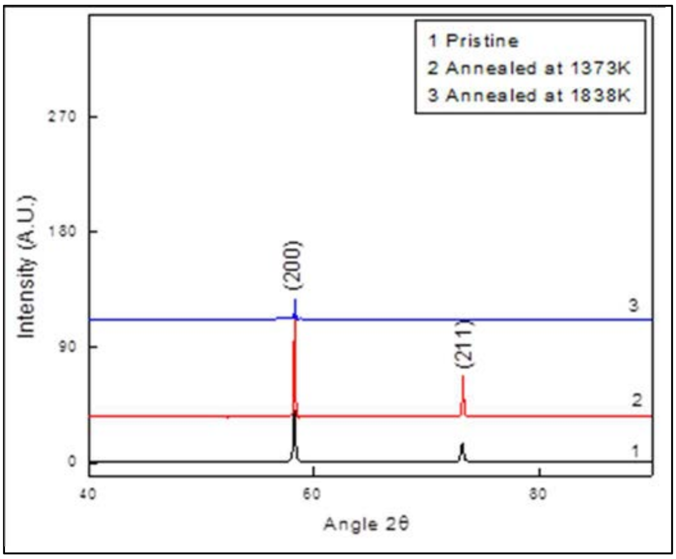

FIG. 16. X-ray diffraction patterns of (plot 1) pristine tungsten foil, (plot 2) annealed (1373K) tungsten foil (plot 3) annealed (1838K) tungsten foil

FIG. 16 shows two diffraction peaks due to (200) and (211) crystal planes in pristine tungsten (plot labelled '1' at the bottom) and a single (200) peak after annealing at 1838 K (plot labelled '3'). The XRD graph indicates re-crystallization and the crystallite-size was found to increase from 64 nm to >700 nm. The calculated average percentage lattice strain using Scherrer formula is reduced from 0.15 to 0.03.

FIG. 17 (a) shows the transmission electron micrograph of 'as received' tungsten foil revealing elongated grains with high dislocation-density along the grain boundaries and within the grains. The grain boundaries are shown by arrows in the micrograph. FIG. 17 (b) shows reduced dislocation density in comparison to pristine foil. It is observed that at higher magnification (FIG. 17 (c)) the dislocations are dispersed uniformly within the foil. The recrystallized foil contained a few dislocations with 200 nm to 900 nm line length with a density 3.6×10^{8}cm^{-2}.

Bulk positron lifetime measurements of the recrystallized tungsten foil show two lifetime components: (1) 107.3 ± 1.7 ps with 70% intensity and (2) 237.3 ± 5.3 ps with 30% intensity. For a perfect W crystal, the reported lifetime is 105 ± 3 ps with 100% intensity. This may indicate that 70% of the sample is defect free. The second lifetime component can be attributed to the presence of cluster of 3-4 vacancies [12].

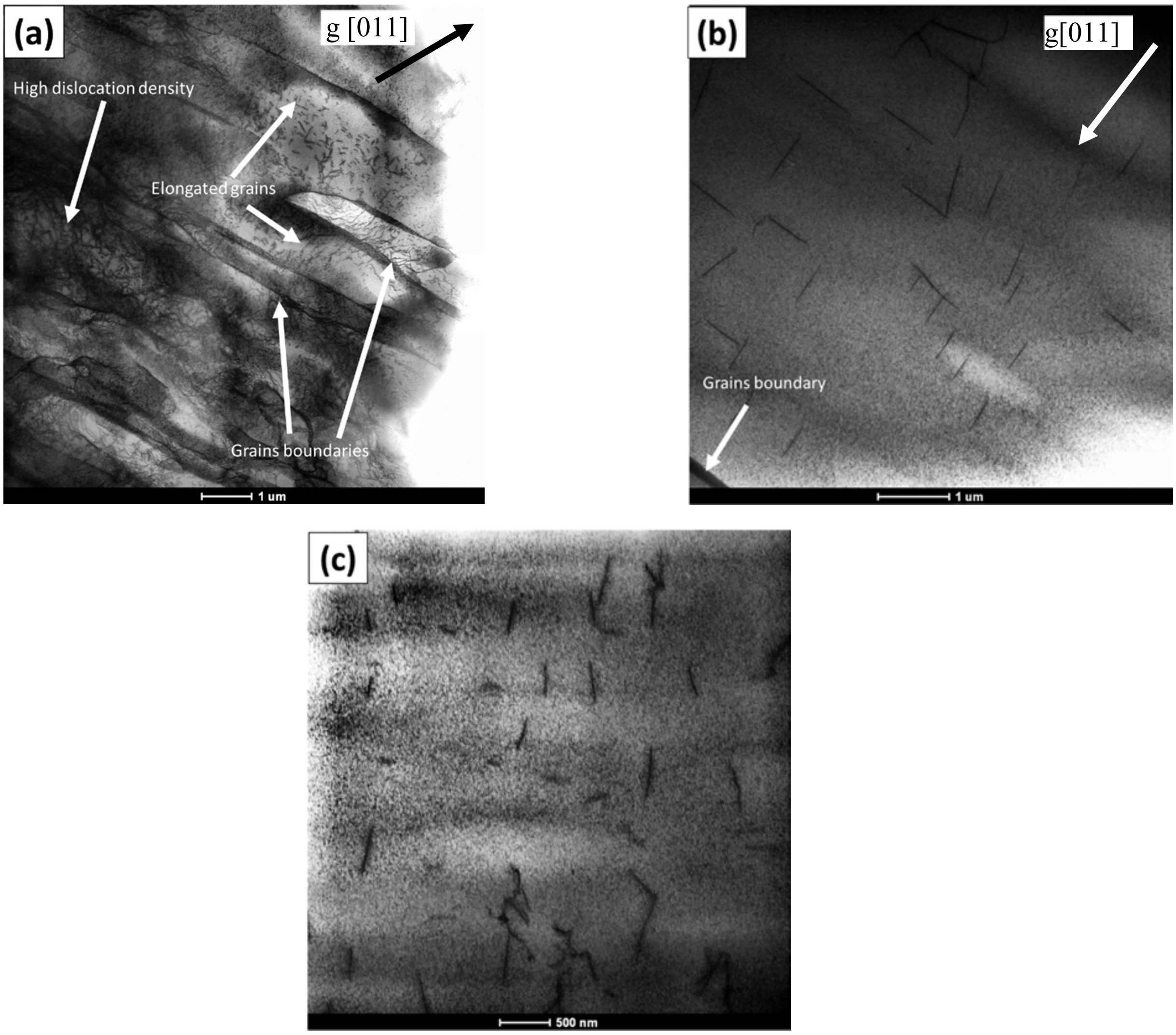

FIG. 17. Transmission electron micrographs of (a) pristine, (b) annealed and (c) annealed tungsten foil at high magnification

4. IRRADIATION EXPERIMENTS, OBSERVATIONS AND ANALYSIS

This section gives details of various ion irradiation experiments that have been carried out along with the results.

4.1.1 Irradiation with high-mass (Au and W) ions in bulk tungsten

Tungsten (W) and gold (Au) ion irradiation in 15 UD pelletron at IUAC, New Delhi has been carried out in bulk tungsten samples with dimensions 8 mm × 8 mm × 2 mm and 10 mm × 10 mm × 2 mm. The details of ion-irradiation parameters are given in TABLE 3.

Positron lifetime spectroscopy measurements were carried out in the bulk tungsten samples before and after annealing. The experimental setup was similar to what was described in FIG. 18. The positron lifetime spectra were fitted into two components (τ_1 and τ_2 with corresponding intensities I_1 and I_2 respectively). FIG. 18 (a) shows the first lifetime components of pristine and annealed samples. FIG. 18 (b) shows the second lifetime components for the same. The τ_1 for pristine is ~117 ps, whereas for annealed samples it is ~138 ps. For pristine samples, the τ_1 seems to be higher than its perfect crystal value (~105 ps) probably due to stress in the lattice, whereas the value in case of annealed samples may correspond to a convolution of its characteristic life-time (105 ps) and dislocation/vacancy life-time, in the case of annealed samples may be a convolution of defects along with its characteristic life-time of 105~ps.

TABLE 3. PARAMETERS FOR TUNGSTEN AND GOLD ION IRRADIATION IN BULK TUNGSTEN SAMPLES

S. No.	Ions	Atomic Mass	Sample Treatment before Irradiation	Fluence ($\times 10^{14}$ ions-cm^{-2})	Current (nA)
1.	W^{6+}	184	Annealed (1173 K)	1	7.0
2.	Au^{7+}	197	Annealed (1173 K)	6.26	11.5
3.	Au^{7+}	197	Annealed (1173 K)	1	7.0
4.	Au^{7+}	197	Pristine	6.26	11.5

The second lifetime component i.e. τ_2 which corresponds to the defects in both pristine as well as for annealed samples. We believe that the temperature may not be enough to anneal the initial defects at this temperature. The vacancy clusters present in the pristine sample (see τ_2 and I_2 of pristine) may be broken mostly into the increase in τ_2 indicate the formation of vacancy clusters during annealing. The reduction in the intensity indicates the partial annealing of vacancies took place during annealing.

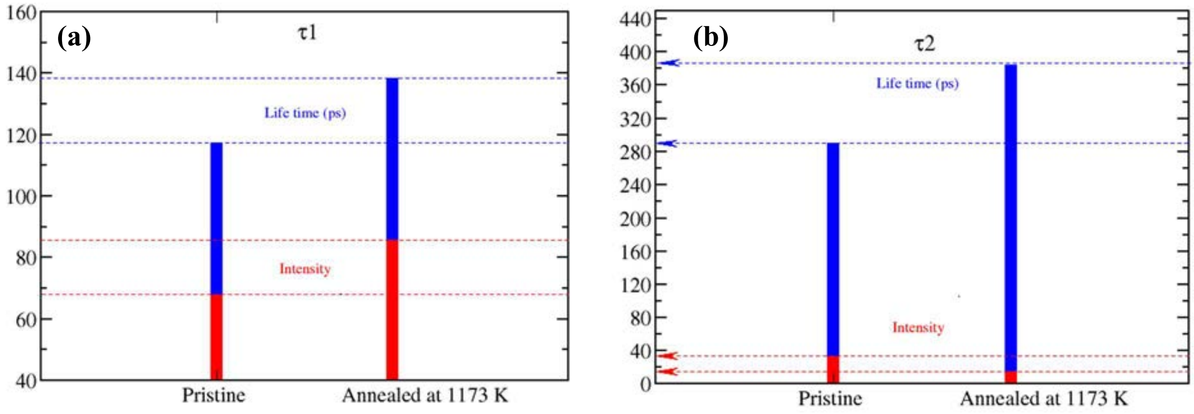

FIG. 18. *(a) First and (b) second lifetime for pristine and annealed samples*

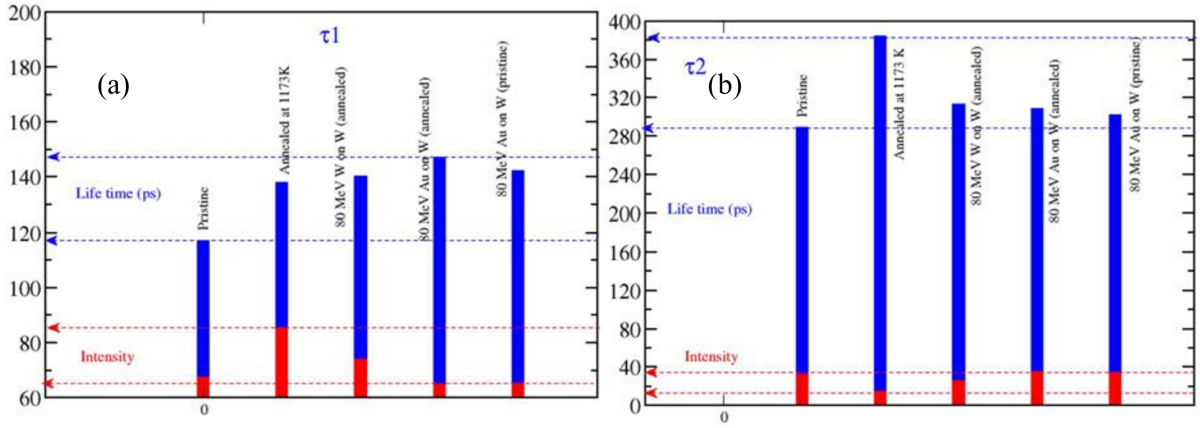

FIG. 19. *(a) First and (b) second lifetime for irradiated samples*

FIG. 19 shows the positron bulk lifetime data from un-irradiated as well as irradiated samples. It is to be noted that the lifetime increases in both annealed and irradiated samples. The range of 80 MeV Au in tungsten is about ~4.5 μm and the range of 270 keV positron is about 16 μm. Hence, in the case of the irradiated samples, it is possible to assume that a fraction of positrons also annihilates from the undamaged region and the resulting data is a mixture of information from damaged and undamaged regions. From FIG. 19 (a) it can be seen that 80 MeV tungsten irradiation increases the first lifetime however reduces its intensity in comparison with the annealed sample. A similar effect can be observed due to 80 MeV Au irradiation as well, although the relative intensity changes of Au irradiated samples is comparatively higher than that of 80 MeV tungsten irradiated samples. The irradiation reduces the second lifetime component, however increasing the corresponding intensity (FIG. 19 (b)). Irradiation on pristine samples also indicate the similar trend. This may indicate two things, (1) breaking down of large vacancy-clusters into smaller ones due to irradiation and subsequent annealing, (2) formation of dislocation loops which has a reported lifetime ~150 ps [13]. The resulting data could be a convolution of both dislocation and vacancy clusters (the TEM analysis has not been performed for this sample as yet).

4.2 Ion irradiation in tungsten foil and characterization

Gold (Au), boron (B), helium (He), and deuterium (D) ion irradiation and sequential irradiation with Au+D, Au+He+D and He+D ions have been carried out at different irradiation facilities as listed in TABLE 4.

TABLE 4. PARAMETERS FOR GOLD, BORON, HELIUM AND DEUTERIUM ION IRRADIATION IN 100 μm THICK TUNGSTEN FOILS

S. No	Ion type	Energy	Fluence (ions-cm^{-2})	Places
1	Gold (Au)	80 MeV	1.3×10^{14}	IUAC Delhi
2	Boron (B)	10 MeV	1.3×10^{14}	GGU Bilaspur
		10 MeV	1×10^{15}	GGU Bilaspur
3	Helium (He)	250 keV	5×10^{15}	IUAC Delhi
4	Deuterium (D)	100 keV	5×10^{17}	IPR Gandhinagar

The structural and microstructural characterizations of the irradiated foil are discussed below:

4.2.1 Structural changes after ion irradiation in tungsten foil

FIG. 20 shows XRD patterns of pristine (plot 1), annealed (plot 2), 80 MeV Au irradiated on annealed foils (plot 3). Plot 1 from FIG. 20 shows two different peaks at 58.4° and 72.8° (2θ) positions arising from planes (200) and (211) respectively. On the other hand, for annealed samples only one peak is observed at 58.4° (2θ) position. The annealing is indicative of recrystallization showing preferred orientation along (200).

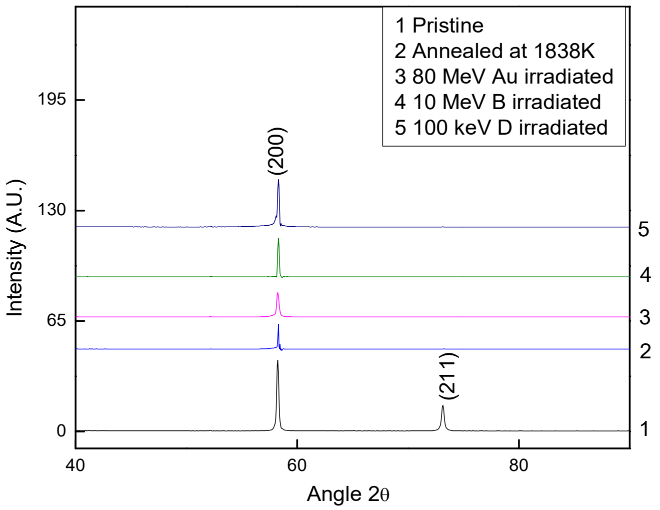

FIG. 20. XRD patterns of (plot 1) pristine tungsten foil, (plot 2) annealed, (plot 3) 80 MeV Au irradiated annealed, and (plot 4) 10MeV B irradiated annealed and (plot 5) 100keV D irradiated annealed

After 80 MeV Au irradiation the average crystallite size seems to have reduced as can be inferred by broadening of the peak as shown in FIG. 20 (plot 3). The lattice strain calculated by Scherrer's formula is found to have increased from 0.03% to 0.16% after irradiation. The peak broadening may be due to decrease in crystallite size and introduction of irradiation induced defects which results in increase in strain. For the case of deuterium irradiation, average lattice strain increased from 0.03% to 0.13% after D irradiation. Irradiation experiments with other ions did not show any significant change in crystallite size.

4.2.2 TEM analysis of 80 MeV gold irradiation in tungsten foil

High energy gold irradiation was carried out in recrystallized tungsten foil samples. Defects created were characterized and quantified in terms of dislocation line length and their densities using transmission electron microscopy (described in the section 7).

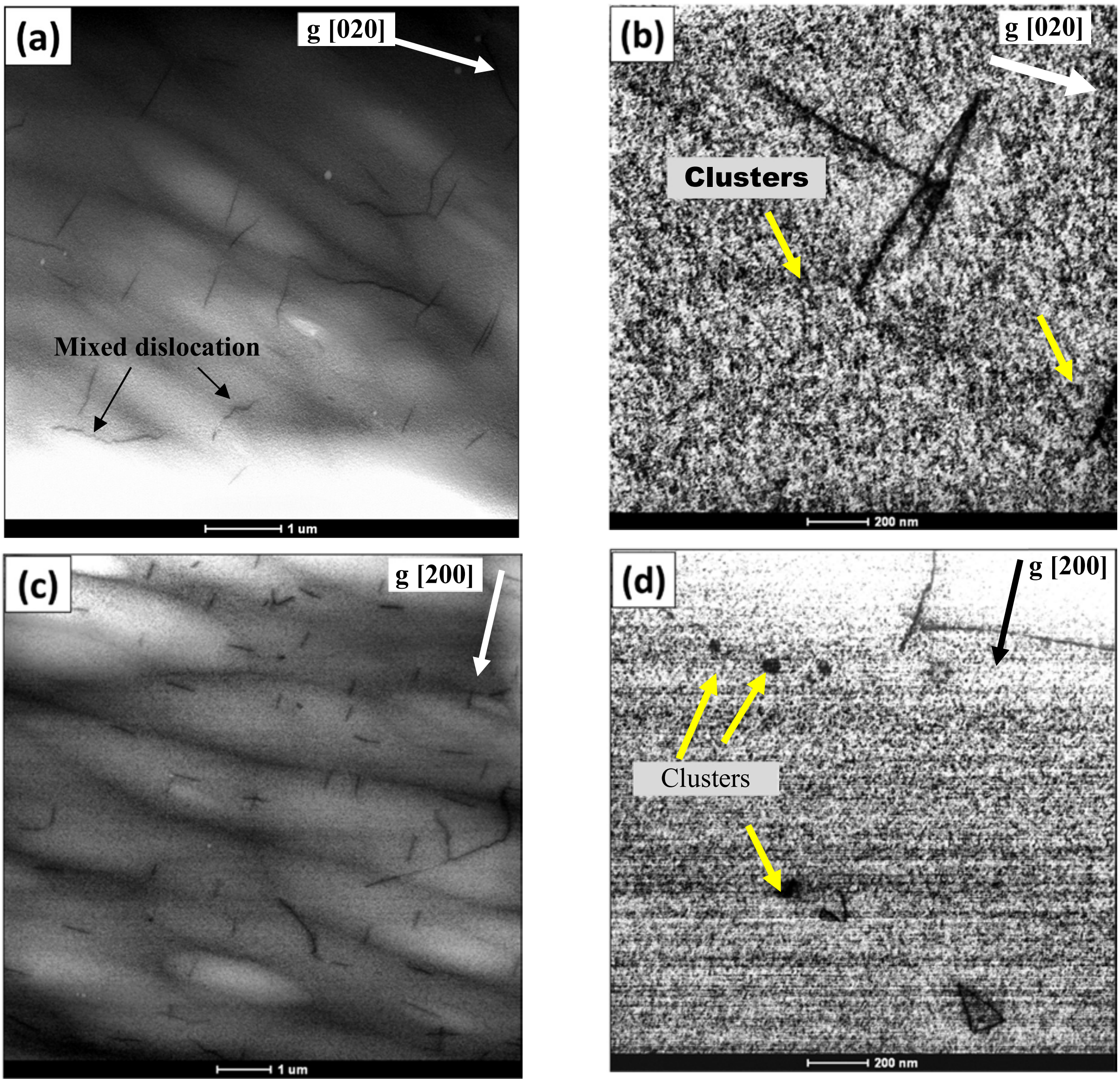

FIG. 21. Transmission electron micrographs of annealed after 80MeV Au irradiation with 1.3×10^{14} *Au-cm*$^{-2}$ *fluence (a) near surface region, (b) high magnification micrograph of near surface region (c) 2 µm in depth from surface and (d) high magnification micrograph at 2 µm depth*

From FIG. 21 (a) it is observed that dislocation lines with length ranging from 0.4 to 2 µm are present. The density of segments of these dislocation lines, in the surface region is found to be 2.9×10^{8}cm^{-2}. In addition to the dislocation lines, mixed dislocations are also seen, which are combination of edge and screw dislocations. Apart from these dislocations, small clusters are also formed after Au irradiation which can be very well seen in FIG. 21 (b) shown by arrow. FIG. 21 (c) shows the presence of dislocation lines and mixture of edge and screw dislocations along with a lot of small defect clusters (shown at higher magnification in FIG. 21 (d)). The dislocation line density at 2 µm depth from the surface is 6.1×10^{8}cm^{-2} which is more than the dislocation density at the surface. A careful analysis of the electron micrograph showed the presence of small (30 - 80 nm) clusters as shown by arrow heads in W-foil after gold irradiation which were excluded in dislocation line density measurement. From FIG. 21 (d) it may be observed that there is presence of many small clusters as shown.

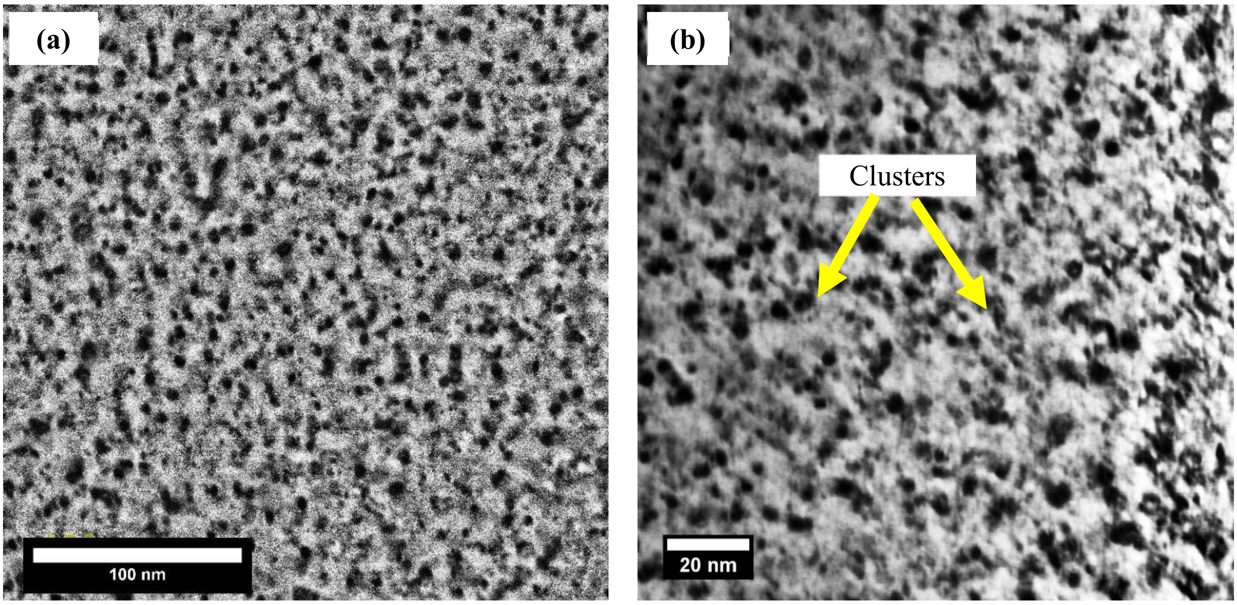

FIG. 22. (a and b): Transmission electron micrographs of annealed tungsten foil after 80MeV Au irradiation with 1.3×10^{14} Au-cm^{-2} fluence, (a) micrograph showing a number of clusters of various sizes, (b) high magnification micrograph showing clusters.

From FIG. 22 (a) it is observed that there is a formation of vacancy clusters in various size ranges. From FIG. 22 (b) it may be observed that there is presence of many small clusters. The clusters sizes were measured in the range of 2.2 m to 12 nm. The clusters density was $1.3{\times}10^{12}$ cm^{-2} which is significantly higher than the density of dislocations presented in the tungsten foil after irradiation.

4.2.3 PAS analysis for Au irradiated tungsten foils

The point defects and defect clustering in the 80 MeV Au irradiated samples were studied using both positron lifetime and Doppler broadening measurements. The mean penetration profile for the 270 keV positrons was roughly about 17 µm, which is much beyond the implantation range of 80 Au ions in tungsten foil. Annihilation data fitting done for two-component lifetimes shows τ_1= 130.4 ± 4.9 ps with 51.8 ± 4.3 % intensity and τ_2 = 250.5 ± 7.5 ps with 44.17 ± 4.3 % intensity. This may be due to the convolution of 107.3 ps, of the un-irradiated sample with defects. To resolve this, we have de-convolved the data with three components, by keeping the τ_1 fixed at 107.3 ps. This yielded three lifetime components, τ_1 = 107.3 ps with 18.3 ± 3.6 % intensity, τ_2 = 154 ± 2.3 ps with 41.0 ± 7 % intensity and τ_3 = 259.6 ± 8.7 ps with 36.6 ± 3.9 % intensity. While comparing with un-irradiated samples, the intensity of the first component of bulk lifetime has reduced from 70 % to 18 %, which indicates formation of defects throughout the sample. The additional lifetime of 154 ps is indicative of dislocations [13] with a significant intensity of 41 %. The third component indicates the formation of 6-7 vacancy clusters [14].

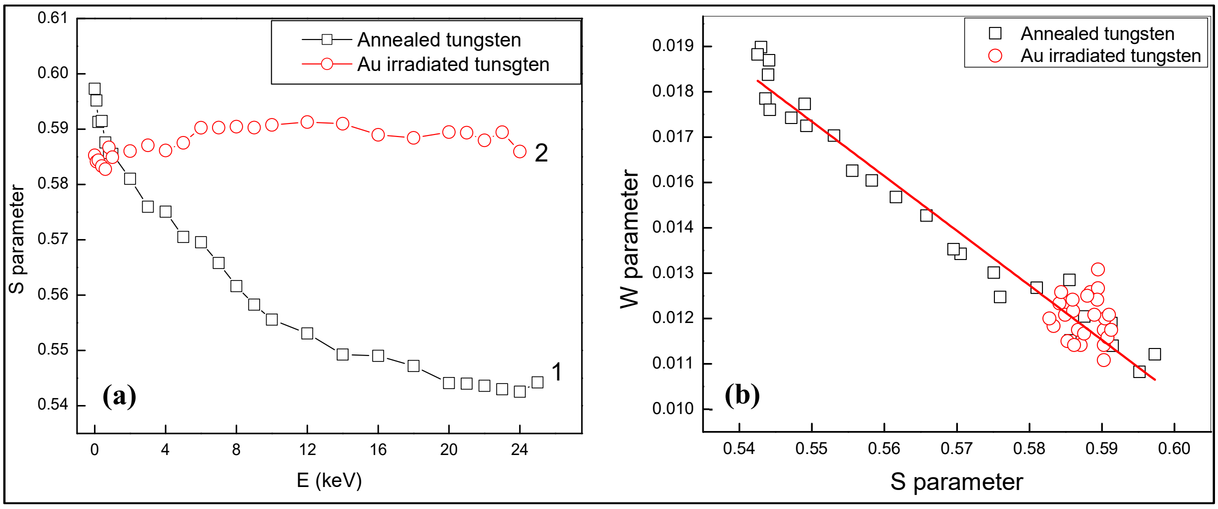

FIG. 23. (a) S-E curve for annealed tungsten foil (labelled '1'), 80MeV Au irradiated tungsten foil (labelled '2'), and (b) W-S plot of positron energy 0-25keV of annealed (1873K) tungsten foil, 80MeV Au irradiated tungsten foil.

The Doppler-broadening studies (slow beam) have been carried out for positron energies up to 25 keV. The contribution from the low-momentum part, the S-parameter, as a function of positron beam energy is plotted in FIG. 23 (a) for 80 MeV Au irradiated sample. The comparison with the un-irradiated recrystallized foil is also shown. The high S-parameter for the un-irradiated sample is due to the positrons annihilating at or the near surface regions. As the energy increases, the percentage of positrons diffusing back to the surface reduces and thus shows reduced S-parameter. At higher beam energies, the saturation of S-parameter indicates nearly defect-free bulk state of the annealed foils. After irradiation, the S-parameter shows the saturation at all beam energies up to 25 keV. It can be inferred that the 80 MeV Au irradiation cause the formation of high defect densities in the sample [15]. .

The contribution from the high (W-Parameter) and low (S-Parameter) momentum annihilation of the un-irradiated and irradiated foil samples is shown in FIG. 23 (b). The high momentum contribution shows the contribution from the core electrons is indicative of the chemical environment within the sample. The un-irradiated and Au irradiated samples fall on the same line indicating that the gold irradiation did not change the chemical environment of the sample, which is not expected at such low fluences of Au (1.3×10^{14} ions-cm^{-2}).

4.2.4 TEM analysis of boron irradiation (10 MeV) in tungsten foil

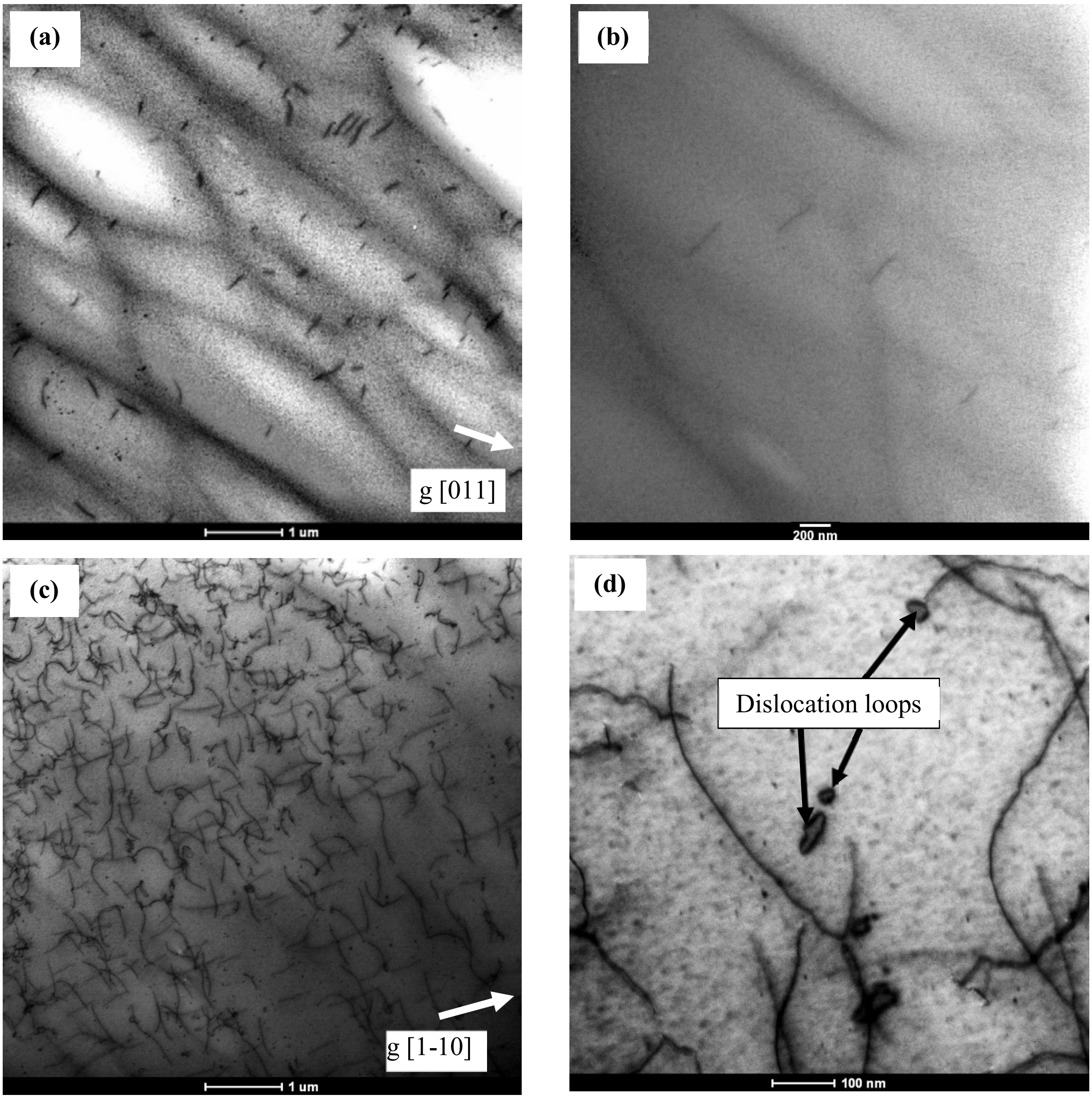

FIG. 24. Transmission electron micrographs of annealed (1873K) tungsten foil after 10MeV B irradiation with 1.3×10^{14} B-cm^{-2} fluence, (a) near surface region showing dislocation lines of different length, (b) high magnification view near surface region, (c) two micro-meter in-depth from surface region showing various sized dislocation lines and (d) high magnification view of two μm in-depth from surface.

From FIG. 24 (a) it is observed that 10 MeV B ion irradiation led to the formation of dislocation lines and line density of the order of 9.0×10^{8}cm^{-2}. In comparison with the case of annealed foil, dislocation lines lengths were found to reduce while the line density was found be higher. A few dislocations with uniform size are observed in FIG. 24 (b). The dislocations observed from FIG. 24 (c) indicate that the line density is significantly increased to 1.9×10^{10}cm^{-2} in comparison with density near surface region. The dislocation line size varied ranging from 0.08 μm to 1.1 μm. From FIG. 24 (a, c and d) it is also observed that there is presence of defects in the form of few dark dots in micrograph which may be small clusters. The size of dark dot clusters was found to be in the range of 20-60 nm with density 7.5×10^{8}cm^{-2} shown in FIG. 24 (a) and 8-35 nm with density 9.3×10^{9}cm^{-2} in FIG. 24 (c). From FIG. 24 (d) it may be noted that there is presence of dislocation loops of the size of 31 nm to 70 nm as shown with arrows in FIG. 24 (d).

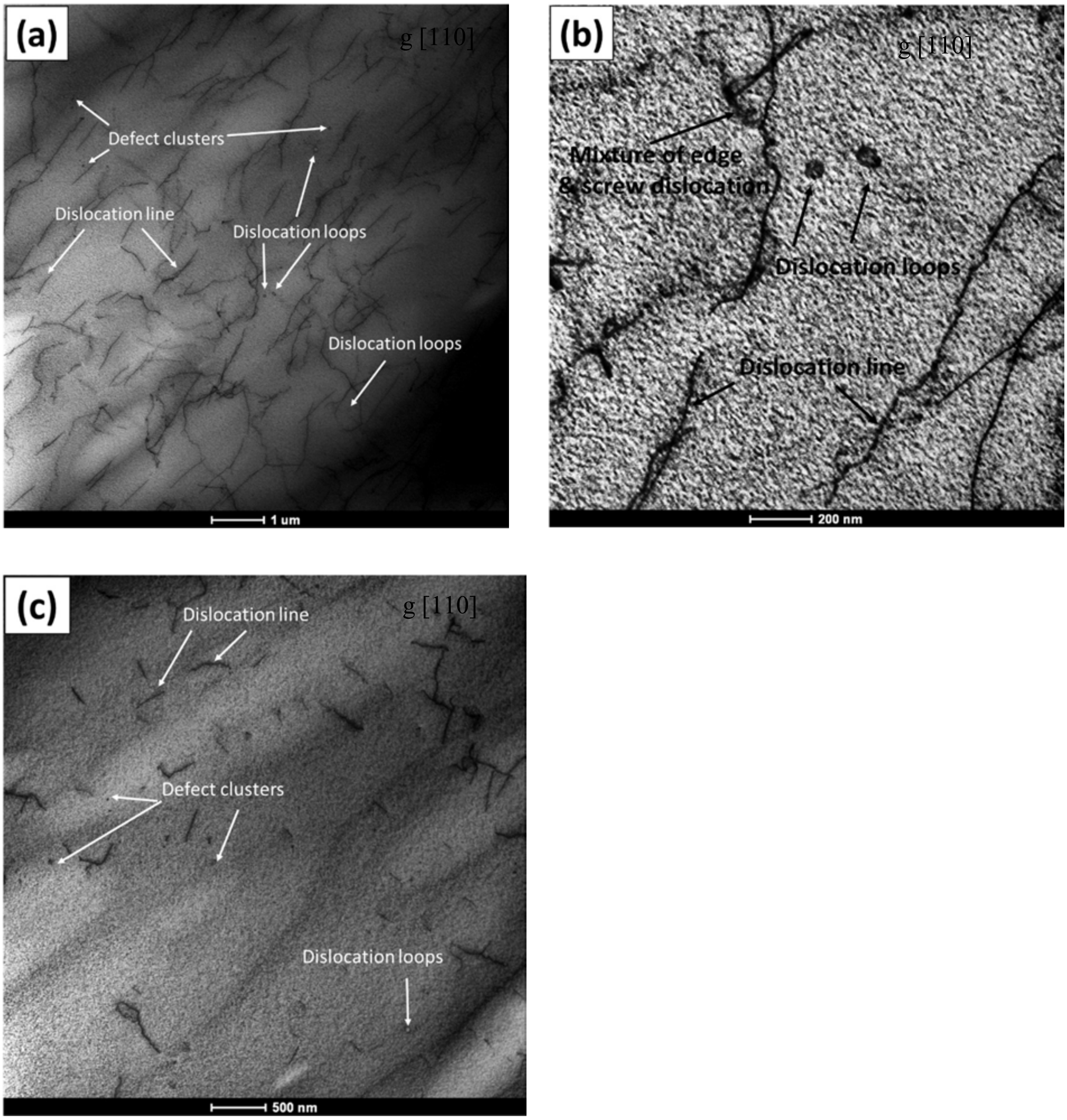

FIG. 25. Transmission electron micrographs of annealed (1873K) tungsten foil after (a) 10MeV B irradiation with 1.0×10^{15} B-cm^{-2} fluence, (b) high magnification micrograph of FIG. 25 (a) showing dislocation loops, (c) high magnification micrograph of FIG. 25(a) showing small dislocation lines, dislocation loop, and defect (vacancy) clusters.

From FIG. 25 (a) it is observed that 10 MeV B ion irradiation led to formation of dislocation lines ranging from 50 to 900 nm and density of 7.9×10^{8} cm^{-2}. Compare to Au irradiation while the line length was reduced the line density was found to be higher. It is observed from FIG. 25 (b) that the dislocation loops also were observed along with the dislocation lines. The loop sizes varied from 35 nm to 80 nm and were not circular in shape. The deviation from circular shape of dislocation loops indicates that the burger's vector of the loops is not in the foil plane (200). FIG. 25 (c) shows the presence of dislocation lines and small clusters in high magnification micrograph.

4.2.5 PAS analysis for B irradiated tungsten

Similar to gold irradiated sample, the point defects in the boron irradiated samples were studied using both positron bulk-life time and Doppler-broadening measurements. The range of 10 MeV B ions in W foil was about 4.5 μm, which made the bulk lifetime measurements possible. The bulk lifetime measurements showed two lifetime components for both low and high fluence irradiation cases. The bulk lifetime data of boron irradiated samples are shown in TABLE 5. The data is fitted with free first lifetime component as well as fixed τ_1 similar to that of un-irradiated one. This was done to understand the change in the intensity of the component which is a measure of the defect created in the samples. It can be seen that with fluence, τ_1 intensity reduces from 70% to 41%. The intensity of the second component (τ_2) increases from 27 % to 55 % indicating increased vacancy cluster formation with irradiation. It should also be noted that τ_2 reduced from 237 ps to 207 ps, which might be due to the decomposition of 4-5 vacancy clusters into single-like vacancies. It is also to be kept in mind that there was no lifetime component corresponding to 154 ps, indicating the formation of lesser number of dislocation formation in contrast to 80 MeV Au irradiation. However, further studies need to be carried out to quantify the sensitivity of positrons to dislocations in tungsten.

TABLE 5. LIFETIME DATA FOR UN-IRRADIATED AND 10 MeV BORON IRRADIATED TUNGSTEN FOILS

Fluence (ions cm^{-2})	τ_1 (ps) with intensity I_1 (%)	τ_2 (ps) with intensity I_2 (%)	Remarks
0	107.3±1.7 (70± 1.77)	237.3±5.6 (27.232 ± 1.78)	Annealed at 1838 K
1.3×10^{14}	117.1±2.4 (58±2.4 %)	232.0±4.6 (38.19 ± 2.4 %)	
1.3×10^{14}	107.3 (46.5±3.27 %)	212.3 ±7.6 (48.31 ± 7.5)	τ_1 is fixed similar to un-irradiated case
1×10^{15}	117.7 ± 2.6 (50.53 ± 2.57)	219 ± 3.5 (45.811 ± 2.56)	
1×10^{15}	107.3 (41.56 ± 0.53)	207.3 ± 1.0 (55.16 ± 0.53)	τ_1 is fixed similar to un-irradiated case

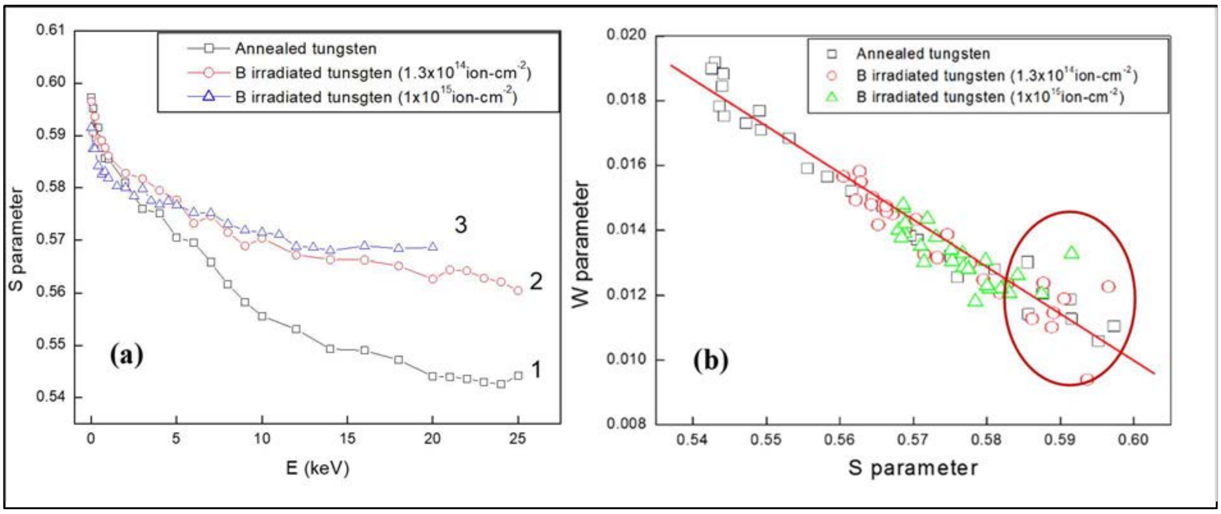

FIG. 26. (a) S-E curve for annealed (1873 K) tungsten foil (labelled '1'), tungsten foil after 10MeV B irradiation with 1.3×10^{14} ion-cm^{-2} (labelled '2') and 1×10^{15} ion-cm^{-2} (labelled '3') fluence, and (b) W-S plot of positron energy 0-25keV of annealed (1873 K) tungsten foil, 10MeV B irradiated tungsten foil.

The S-parameter obtained from Doppler-broadening studies is shown in FIG. 26 (a). It can be seen that the S-parameter shows a higher value in comparison to the un-irradiated samples indicating the formation of defects. It is also evident that the annihilation from the near-surface region of the irradiated samples is similar to that of the un-irradiated one indicating rather un-distorted tungsten surface. The S-parameter shows saturation towards the samples shows a constant defect formation within the positron penetration range. It has also kept in mind that the beam penetration depth is only several nano-meters while 10 MeV B ions have a range up to 4.5 μm.

The S-W parameter plots of the boron irradiated samples also lie in the same straight line as that of the un-irradiated foil (*cf.* FIG. 26 (b)). This indicates rather chemically similar lattice before and after irradiation even of a fluence of 1×10^{15} ions-cm^{-2}.

5. LOW ENERGY IRRADIATION - H, D AND HE IN TUNGSTEN FOIL

The pre-damaged tungsten foils using gold and boron ions were further irradiated with 100 keV deuterium and 250 keV helium ions to study the deuterium trapping at defects and in presence of helium at such high energies. The maximum range of the gaseous ions are roughly about 600 nm which is about 9 times smaller than the range of the damaging ions. The energy of the gaseous ions is chosen in such a way that their ranges overlap. We have kept a high flux ratio between deuterium and helium at 100, i.e., $\Gamma_{\mathrm{D}}= 5\times10^{17}$ ions-cm^{-2} and $\Gamma_{He}= 5\times10^{15}$ ions-cm^{-2}. This specifically allows us to explore whether the observed reduction in the deuterium trapping in presence of helium at lower energies is valid at higher energies and higher flux ratios.

5.1 100 keV Deuterium irradiation in tungsten TEM analysis

FIG. 27 (a) it is observed that the 100 keV D ion irradiation with the fluence of 5×10^{17} D-cm^{-2} in W-foil was lead to formation of dislocation lines, dislocation loops and dislocation network with length ranging from 120 to 1900 nm and increased line density in as annealed foil sample (line length range 200 nm to 900 nm and dislocation density 3.6×10^{8} cm^{-2}).

The dislocation line networks were observed in the STEM electron micrograph as shown in FIG. 27 (b). It was observed that the small sized line dislocations are entangled. It is also observed from FIG. 27 (c) that the loop sizes varied from 50 nm to 100 nm and were circular in shape. The circular shape of indicates that the burger's vectors of the loops are along the foil plane (200). The networking of small dislocations was observed, but large or extended dislocations were dispersed in microstructure, moreover, the dislocation loops were found near long dislocation segments.

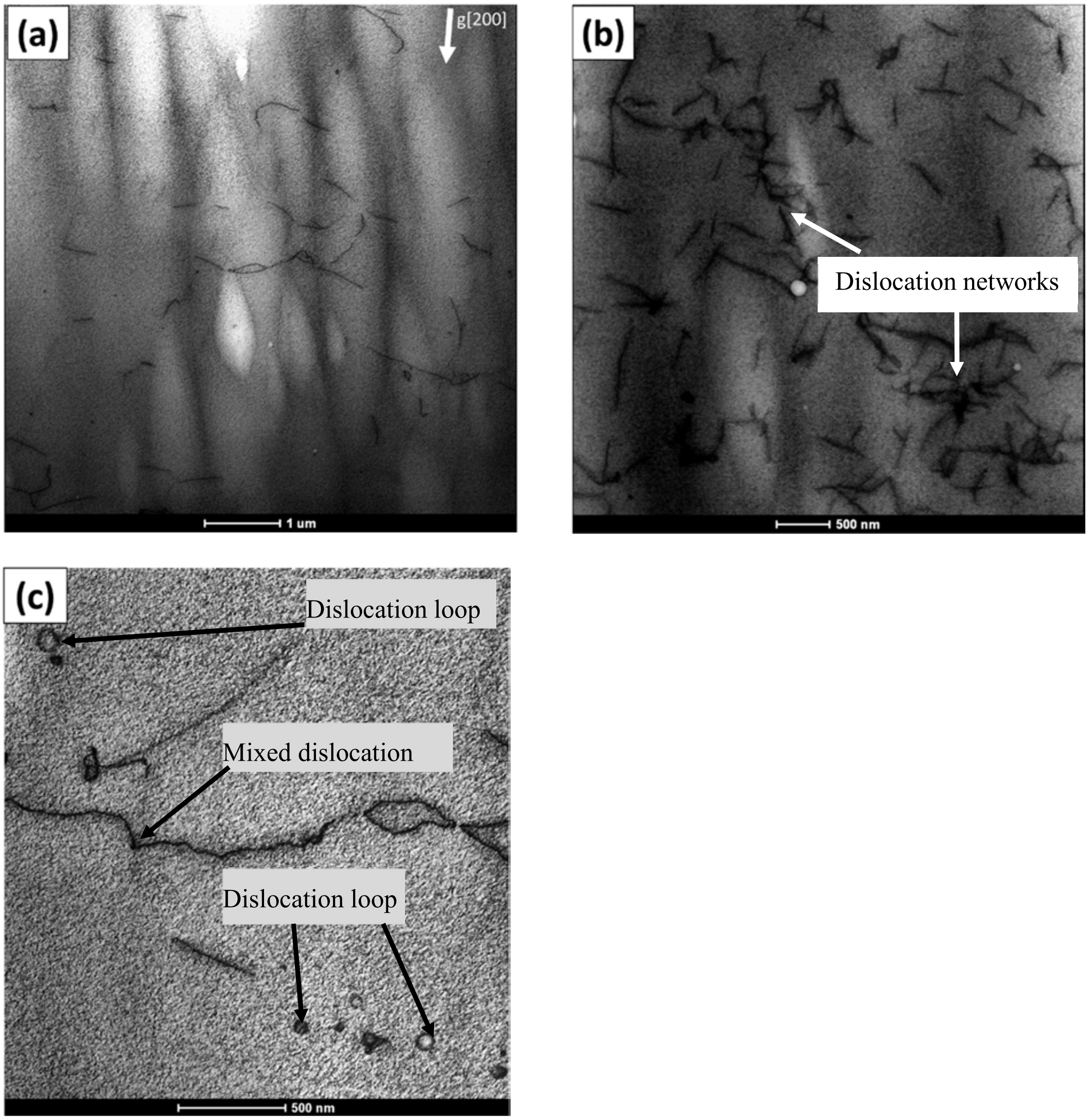

FIG. 27. Transmission electron micrographs of annealed (1873K) tungsten foil after (a) 100 keV D irradiation with 5.0×10^{17} D-cm^{-2} fluence, (b) high magnification micrograph showing dislocation network, (c) high magnification micrograph showing dislocation lines and dislocation loops.

5.2 PAS analysis for D irradiated tungsten

FIG. 28 (a) shows the S-E plots of un-irradiated and 100 keV D ion irradiated tungsten foils. An enlarged view of the S-Parameter values between 6 to 25 keV is shown in the inset, (b): the S-W parameter space of both un-irradiated and 100 keV D ion irradiated W foils.

Point defects in 100 keV deuterium irradiated samples were investigated using the variable energy positron Doppler broadening spectroscopy. Since the range of 270 keV positrons used in the bulk lifetime measurements are much larger (17 μm) than the maximum range of 100 keV D ions (600 nm) , the data cannot accurately reflect the effective change in the lifetime and hence not shown here. The S-E plots of the recrystallized and D ion irradiated tungsten is shown in FIG. 28 (a). It is observed that the S-E plot for D ion implanted tungsten the value of S decrease up to 8 keV and then increases from up to 20 keV of positron energy. This indicates that the defect distribution is inhomogeneous with depth or concentration of defects gradient. The broad maximum of S-parameter between 10 keV to 20 keV energy range which is shown in the inset of FIG. 28 (a).

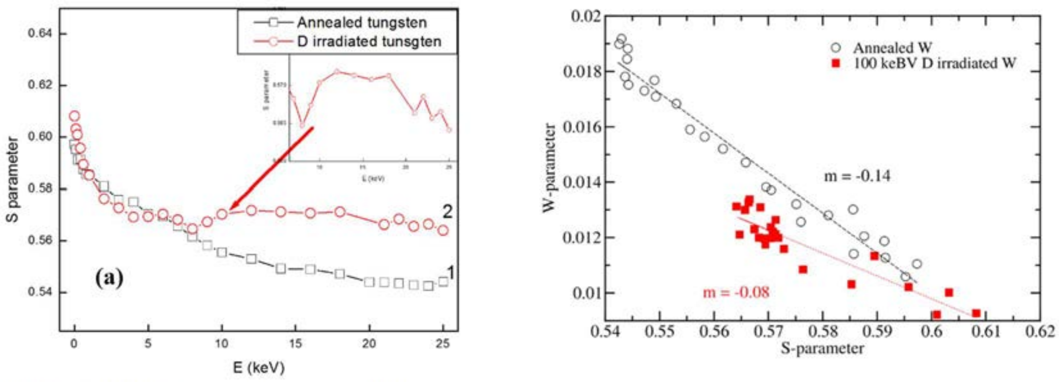

FIG. 28. (a) S-E curve for annealed tungsten foil (labelled '1'), 100 keV D irradiated tungsten foil (labelled '2'), and (b) W-S plot of positron energy 0-25 keV of annealed tungsten foil, 100 keV D irradiated tungsten foil.

The slightly higher value of S-parameter at low energies indicate the change in the surface annihilation states compared to the un-irradiated samples. The maximum in S-parameter indicates a defect rich zone created due to irradiation. From the depth profile of the implanted positrons as given by **Error! Reference source not found.**, this corresponds to 100 to 300 nm.

The S-W parameter space of the un-irradiated and irradiated foils are shown in FIG. 28 (b). It can be seen that, the D irradiated samples fall on a straight line with different slope (R = -0.91) compared to the un-irradiated sample (R = -0.98). The change in the W parameter indicates that the positrons are annihilating from a different core electron population other than the tungsten matrix, indicative of a different chemical environment. This may be indicating the presence of deuterium rich vacancies or D decorated dislocations formed due to irradiation. Such a change in the chemical environment may be due to the high fluence (5×10^{17} ions-cm^{-2}) of D ions used in our experiments.

5.3 Helium irradiation (250 KeV) in tungsten foil

From FIG. 29 (a, b) it is observed that the dislocation lines of small size length and large size length were observed. The 250 keV He ion irradiation with the fluence of 5×10^{15} He-cm^{-2} in W-foil was lead to formation of dislocation lines with length ranging from 40 nm to 1000 nm and increased line density 1.05×10^{9} after He irradiation as compared with annealed foil sample (line length range 200 nm to 900 nm and dislocation density of 3.6×10^{8} cm^{-2}).

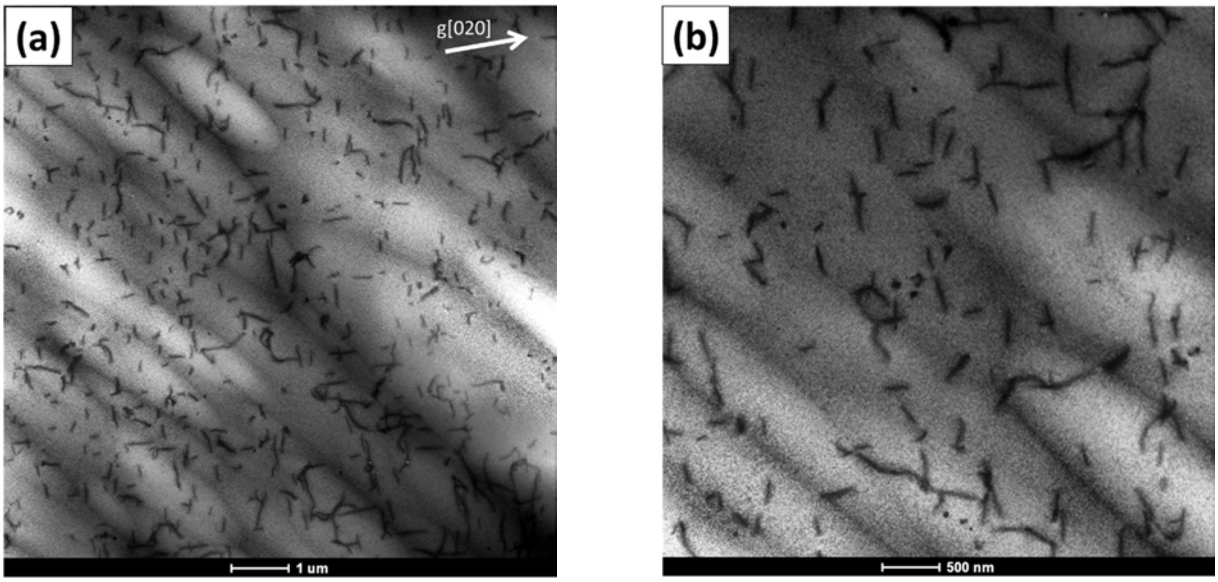

FIG. 29. Transmission electron micrographs of annealed tungsten foil after (a) 250 keV He irradiation with 5.0×10^{15} *He-cm*$^{-2}$ *fluence, (b) high magnification micrograph of FIG. 29 (a) showing dislocation lines.*

5.4 PAS analysis of helium irradiated Tungsten

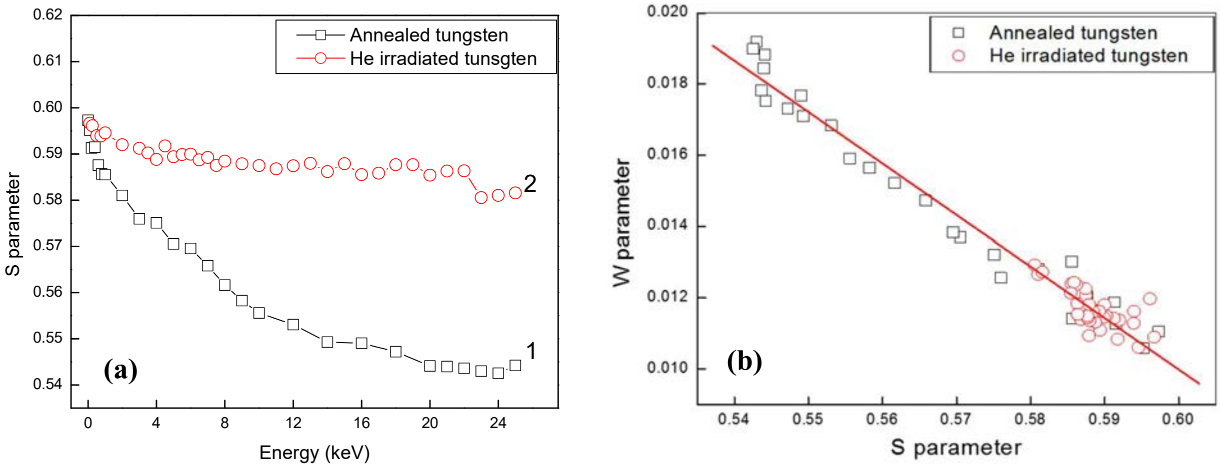

FIG. 30. (a) S-E curve for annealed tungsten foil (labelled '1'), 250 keV He irradiated tungsten foil (labelled '2'), and (b) W-S plot of positron energy 0-25 keV of annealed tungsten foil, 250 keV He irradiated tungsten foil.

FIG. 30 shows the S-E and S-W plots of recrystallized tungsten before and after 250 keV He irradiation. The saturation of S-parameter indicates that there is a homogeneous distribution of defects throughout the probing range. From the S-W parameter space it can be seen that both the un-irradiated and irradiated samples lie in the same curve. This indicates the helium atoms did not change the chemical environment of the sample, which is consistent to lower helium fluence (5×10^{15} ions-cm^{-2}) in contrast to deuterium (5×10^{17} ions-cm^{-2}).

5.5 Surface morphology and topography (SEM and AFM)

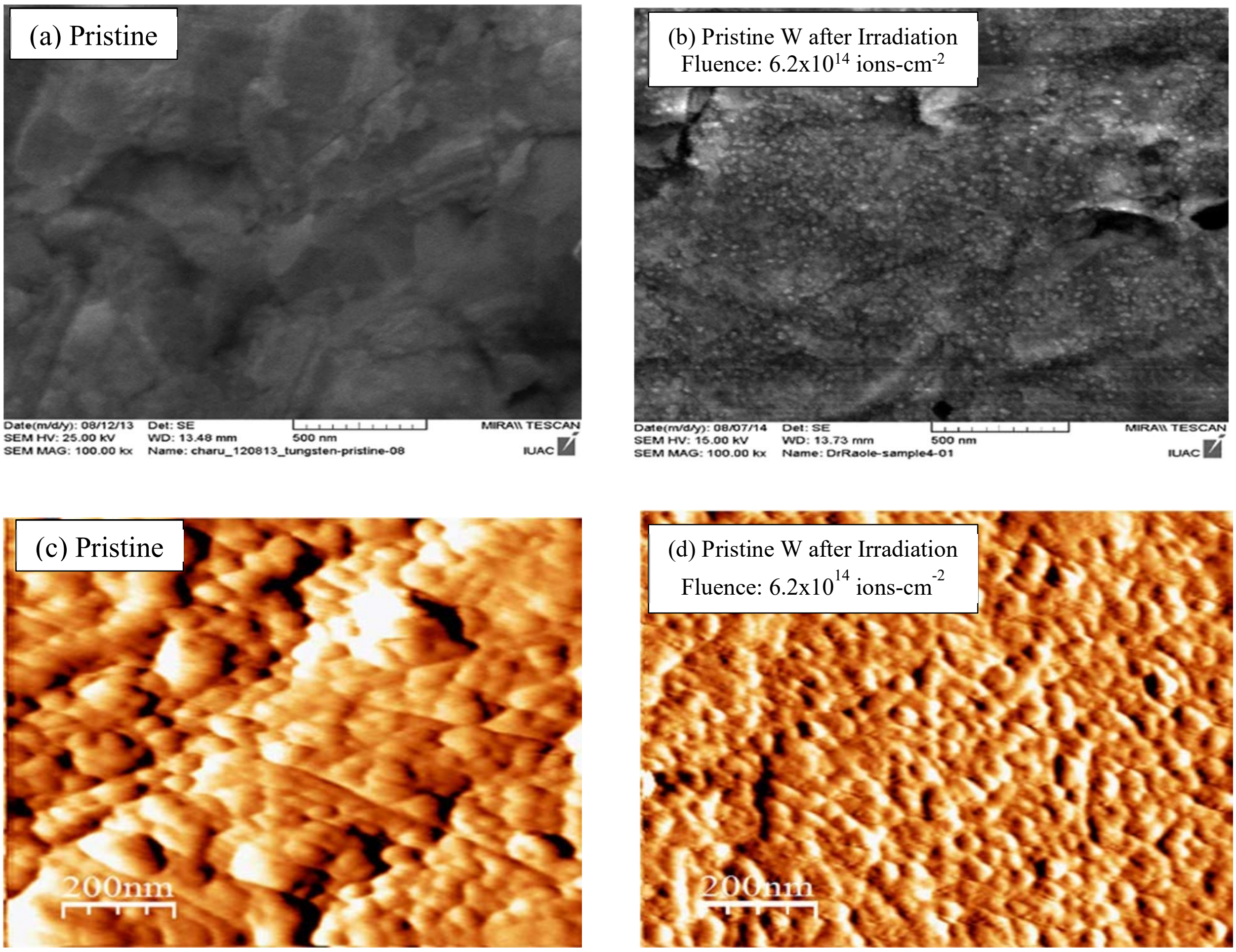

FIG. 31. (a) & (b) SEM and (c) & (d) AFM micrographs of pristine and Au-irradiated bulk tungsten sample

SEM of pristine tungsten show smooth morphology, while grainy structure is seen after Au-irradiation. AFM shows the nano-structuring after irradiation. The origin is not known and needs further investigation as this change has been observed only in the pristine samples so far.

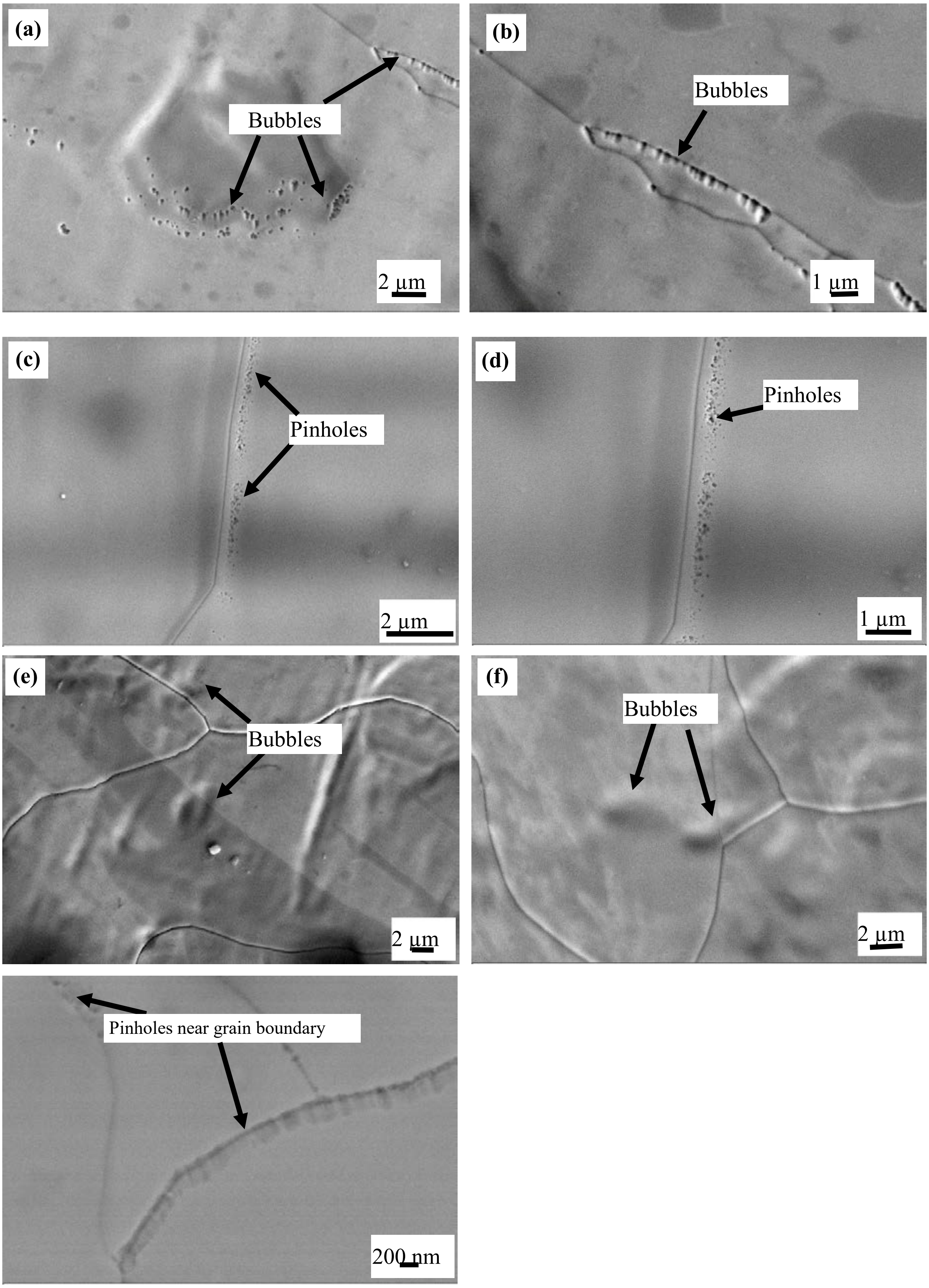

FIG. 32. Scanning electron micrograph of (a, b) 100 keV D ion implanted surface, (c, d) 250 keV He implanted surface, (e) D ion implanted surface with pre-irradiated 80MeV Au, and (f, g) D ion implanted surface with pre-irradiated Au+He.

It is observed from FIG. 32 (a, b) that D implantation leads to formation of small sized bubbles (0.1 to 0.5 µm) in grain and near grain boundary (shown by arrow heads). The bubble formation probably attributed to generation of vacancy due to D irradiation, followed by gas driven bubble formation by continuous high-flux D-implantation. On the other hand, the 250 keV He implantation leads to formation of pinholes of 20 to 100nm size near grain boundary in tungsten surface. The pinhole features, which are shown by arrow heads, may be due to rupturing of small blisters due to residual stress in tungsten foil and stress introduced by helium gaseous ion implantation (*cf.* FIG. 32 (c) and FIG. 32 (d). The 100 keV D implantation in 80 MeV irradiated tungsten foil leads to formation of bubbles of 1.5 to 2.5 µm size shown by arrow heads in FIG. 32 (e). The size of observed bubbles is larger (0.1-0.5 µm) as compared with 100 keV D implanted surface may be because of coalescence of bubbles due to residual stress by 80MeV Au ion pre-irradiation in foil. From FIG. 32 (f, g) it may be noticed that the 100 keV D implantation in foil pre-irradiated with Au (80 MeV) followed by 250 keV He leads to formation of bubbles in grain (*cf.* FIG. 32 (f)) and pinholes along the grain boundary (*cf.* FIG. 32 (g)).

5.6 Resistivity measurement for overall defects study

Four probe DC resistivity measurements were done from 300 K to 10 K temperature. Resistivity at different temperatures is shown for pristine, annealed and ion irradiated samples. Pristine sample shows maximum resistivity while sample annealed at 1838 K shows minimum resistivity. The residual resistivity ratio-RRR (R 300K /R 10K) for different samples is shown in FIG. 33 (b). Overall defects present in the sample are inversely proportional to RRR ratio.

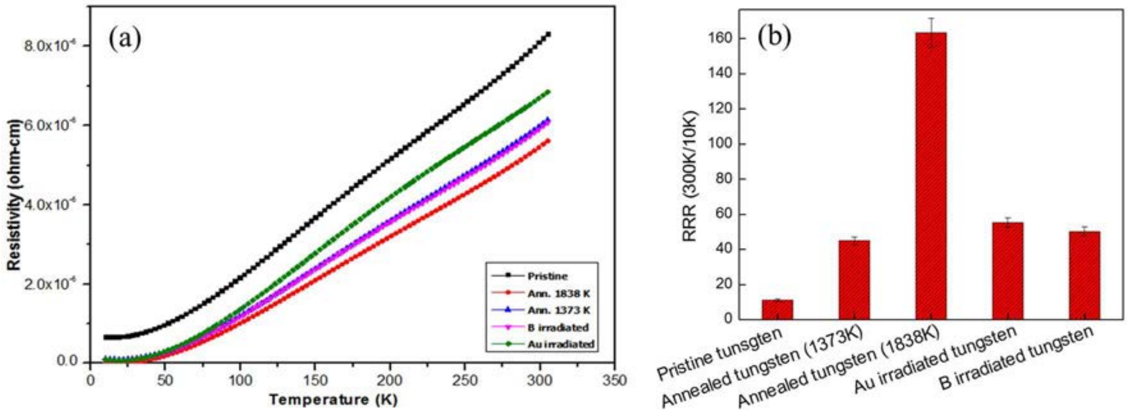

FIG. 33. Resistivity values shown in (a) and RRR values shown in (b) at different temperatures for pristine, annealed (at 1373 K & 1838 K), B and Au irradiated samples.

Annealing of tungsten foils shows significant change in the RRR. Annealing at 1373 K predominantly removes point defects while there is no recrystallization or grain growth. That is, the grain boundary fraction may be remaining relatively unchanged in comparison to pristine samples, while there is partial annealing of defects within crystallites. This could be attributed to the change in the defect scattering of electrons predominantly within the crystallite.

There is significant change in resistivity for samples annealed at 1838 K. Due to recrystallization, there is an effect due to both - defect annealing and grain growth.

The RRR values (ratio of resistivity at 300 K to 10 K) shown in FIG. 33 (b) are consistent with the resistivity curves shown in FIG. 33 (a) and the logic mentioned above. After irradiation, RRR values are observed to be more than pristine and annealed (1373 K) samples but less than recrystallized sample, which indicates that overall concentration of defects in B and Au irradiated samples are much less than pristine but more than the defects present in recrystallized samples.

6. TRAPPING OF H AND D IN IRRADIATED TUNGSTEN

TABLE 6. PARAMETERS FOR SELF-ION IRRADIATION IN BULK TUNGSTEN

Sample	Sample ID	W implantation fluence (ions-cm^{-2})	Damage due to W ion implantation at surface and total (dpa)	Hydrogen fluence (ions-cm^{-2})	Damage due to H ion implantation at surface and total (dpa)
Plansee	P1 mask	-	-	1×10^{18}	0.09 (0.74)
Plansee	P1	4.5×10^{15}	10 (17)	1×10^{18}	0.09 (0.74)
Plansee	P2	4.5×10^{14}	1 (1.7)	1×10^{18}	0.09 (0.74)

Tungsten samples have been irradiated with 7.5 MeV $W^{4+}$with beam current of ~100 nA using a 1.7 MV tandetron accelerator at room temperature. The fluence was adjusted such that implantations produced displacement damage of 1 dpa and 10 dpa at sample surface. These pre-irradiated samples with W^{4+} were subsequently irradiated with 100 keV H_2^+ ions at room temperature using a 150 kV accelerator. The beam current of H_2^+ ions was ~4 μA and the irradiation fluence amounted to 1×10^{18} H atoms-cm^{-2}. The samples which were implanted up to 10 dpa were masked with pristine samples during irradiation. These masks have been used for obtaining the depth profile of hydrogen in undamaged samples. The sample identification “P1 mask” refers to the sample which was used to mask P1 during hydrogen implantations. The details of irradiation parameters for different samples are given in TABLE 6.

Elastic Recoil Detection Analysis (ERDA) was used to obtain the depth profiles of hydrogen in tungsten pre-damaged and un-damaged samples. ERDA experiments were carried out using 4.5 MeV helium ions with typical beam currents of ~15 nA. The H recoils were detected at angle of 30° with respect to the beam direction and an aluminium absorber of thickness 20μm was used to block the forward scattered He ions. The SIMNRA program [16] was used to obtain hydrogen depth profiles.

The hydrogen depth profiles obtained using SIMNRA program is shown in FIG. 34 (a). As observed from FIG. 34 (b) the hydrogen concentration in P1 mask sample is considerably lower than in samples which are pre-damaged. The concentration profile as obtained from SIMNRA (FIG. 34 (b)) shows that most of the hydrogen is located within the first 100 nm and is shallower than the projected range of implanted hydrogen FIG. 34 (a). This could be due to hydrogen trapping in its self-generated defects.

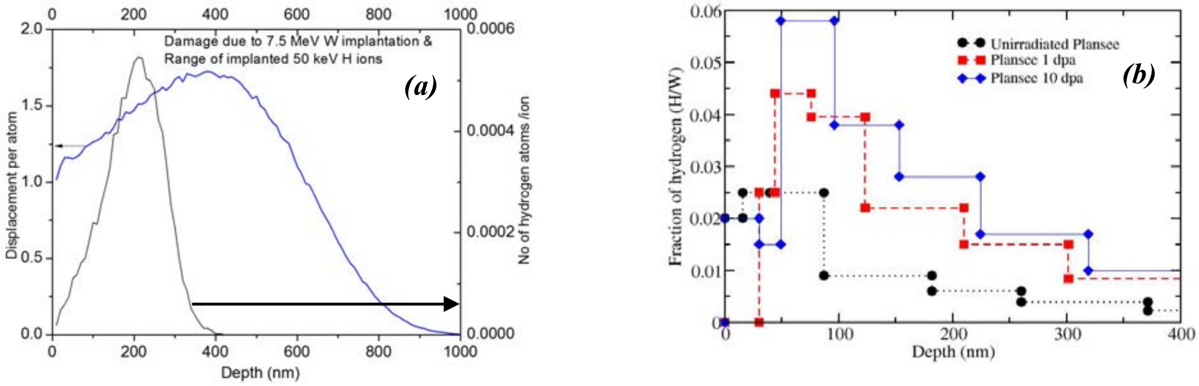

FIG. 34. (a) Displacement damage due to 7.5 MeV implantation to the fluence of 4.5×10^{14} *W ions-cm*$^{-2}$ *as obtained from SRIM program and (b) Hydrogen depth profile measured by Elastic recoil detection analysis (ERDA)*

6.1 High resolution TEM of irradiated tungsten foil

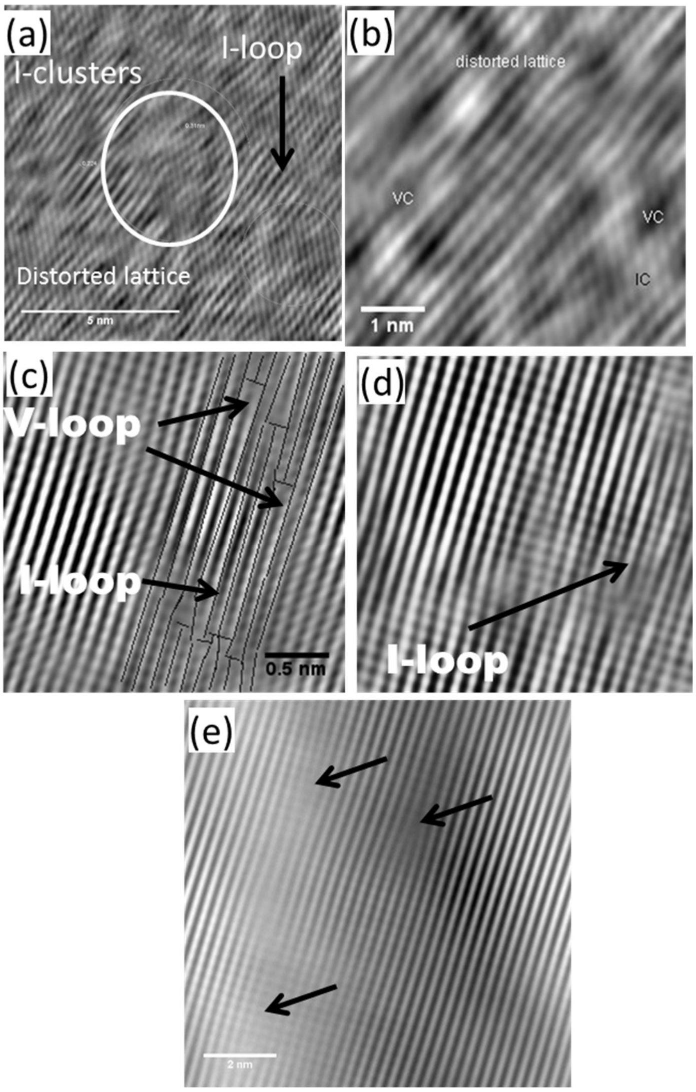

FIG. 35. High resolution transmission electron micrographs of resolved lattice (a-b) showing defect clusters in Au (1.3×10^{14} *ion-cm*$^{-2}$) *irradiated tungsten, (c-d) showing dislocation loops in B* (1.3×10^{14} *ion-cm*$^{-2}$) *irradiated tungsten and (e) showing dislocations in He* (5.0×10^{15} *ion-cm*$^{-2}$) *irradiated tungsten.*

FIG. 35 (a, b) show the interstitial (I) clusters and loops in resolved lattice image formed after 80MeV Au ion irradiation. The lattice spacing was measured and lattice strain was calculated using Δd/d value for I-cluster and dislocation I-loop which were found to be -0.38 and -1.19, respectively. In FIG. 35 (a) heavily distorted lattice are also seen. FIG. 35 (c and d) show the interstitial and vacancy dislocation loops (I-loops and V-loops) in tungsten after B ion irradiation and the lattice strain for I-loop was found to be -0.81 and for V-loop was +0.45. In case of helium ion irradiated tungsten foil (FIG. 35 (e)), strain due to dislocations was about -0.49. The negative and positive values of strain indicate the compressive and tensile nature of strain in the normal lattice of tungsten, respectively. From FIG. 35 (a-e) it may be concluded that the formation of interstitial loops in tungsten after Au ion irradiation the lattice were highly strained (-1.19), which was compressive in nature in normal lattice. The formation of I-loops and clusters in tungsten due to Au ion irradiation may cause of high strain in lattice, which was clearly seen the peak broadening in XRD pattern in case of Au irradiation (*cf.* FIG. 20 plot-3).

6.2 D trapping in pre-damaged tungsten with Au, B, and He ions

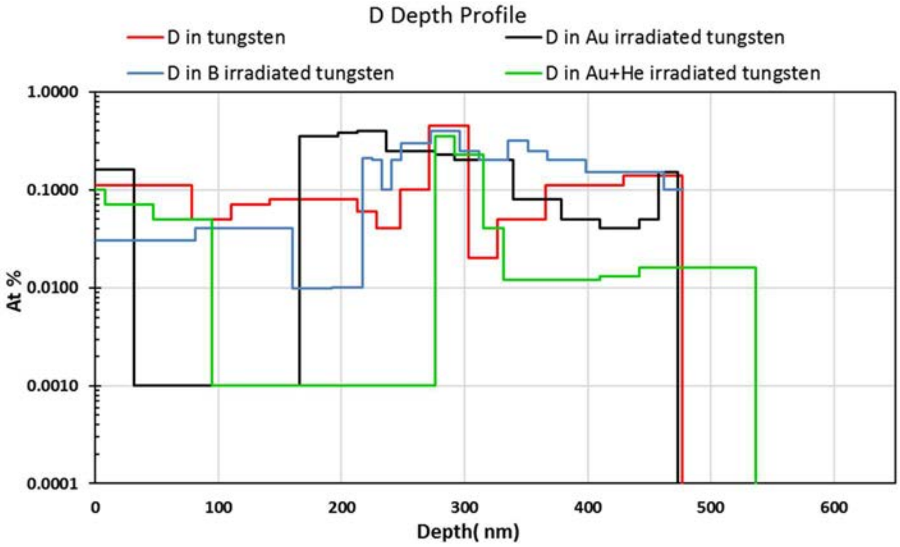

FIG. 36. Deuterium depth profile in tungsten foils measured by elastic recoil detection analysis (ERDA)

FIG. 36 shows the deuterium depth profile obtained from Elastic recoil detection analysis (ERDA). Deuterium profile in Au irradiated tungsten shows that the D concentration increases after 150 nm depth. The depth profile of D in ERDA results shows that the after exposure of helium in tungsten foil pre-irradiated with Au, the trapping of deuterium was reduced significantly.

6.3 D trapping in presence of impurity (La_2O_3)

FIG. 37 shows the deuterium depth profile obtained from Elastic recoil detection analysis (ERDA). The results show that deuterium trapping is not pre-damage/defect dependent any more, as the impurity plays an important role in D trapping in tungsten lattice. This implies that the mechanism of D trapping in tungsten alloy is different from as in pure tungsten.

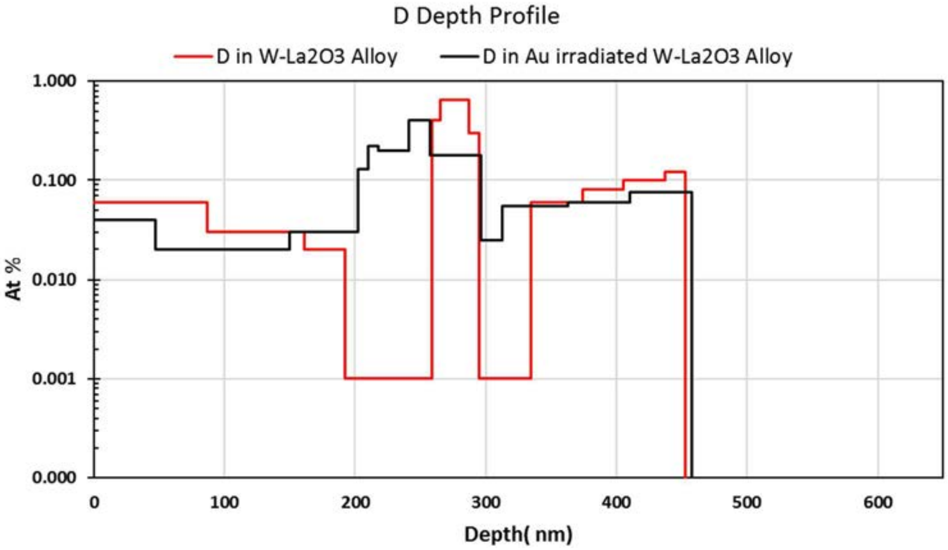

FIG. 37. Deuterium depth profile measured by elastic recoil detection analysis (ERDA)

6.4 Secondary Ion Mass Spectroscopy

The deuterium and helium depth profiles were measured using secondary ion mass spectroscopy.

The sputtering yield of 15 keV Cs^+on tungsten at 23° with respect to surface normal is about 7. By taking into account the surface roughness of the foil was about 380 nm, measured using contact profilometry method over an area 500 mm^2, the sputtering yield within 3 times roughness is considered to be angle averaged. By assuming a linear scaling of the roughness with area, for the beam raster area the roughness was about 14 nm. An increase sputtering yield of varying between a factor of 1.5 to 2 is assumed within three times this roughness. The sputtering time is converted to depth by assuming the areal density of 1.5×10^{15}atoms-cm^{-2}. The corresponding depth profile of 100 keV D atoms in recrystallized tungsten foil within one day of the irradiation is shown in FIG. 38.

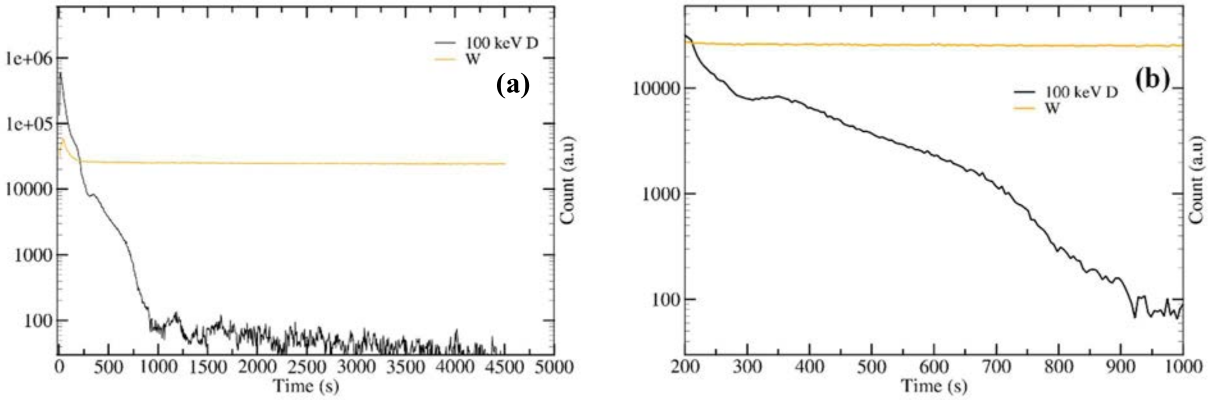

FIG. 38. (a) Depth profile (SIMS) of 100 keV deuterium atoms in tungsten foil within 1 day of irradiation and (b) enlarged view between 150 nm to 600 nm.

The total deuterium content of the sample was estimated from the experimental data by including the calibration of the field aperture as well as the particle counter. This normalized to the total atoms (both W and D) present in the given layer yields the total D concentration in the layer. A huge surface concentration of D atoms was observed in all the trials. An enlarged view of the depth profile between 150 nm to 600 nm is shown in FIG. 38 (a). A bump in the concentration profile is observed between 250 nm to 400 nm. The mean range of 100 keV D in tungsten calculated using binary collision models of SRIM was about 427 ± 139 nm for 5000 particle trials.

The deuterium depth profile measured after two weeks and three weeks of irradiation is shown in FIG. 39 (a). The surface concentrations as well as the net D content (not shown) are found to decrease with time. The rest of the deuterium depth profiles discussed here are measured after two weeks of irradiation. A comparison of depth profiles on undamaged foils, foils pre-damaged with 80 MeV gold ions and foils pre-damaged with 10 MeV boron ions is shown in FIG. 39 (b). The damaging fluence in all the cases was 1.3×10^{14} ions-cm^{-2}. In both the cases a prominent surface peak is present and the peak is shifted towards inside for the foils pre-damaged with 80 MeV Au ions. The surface as well as the total deuterium content is found to be higher in the case of gold irradiation.

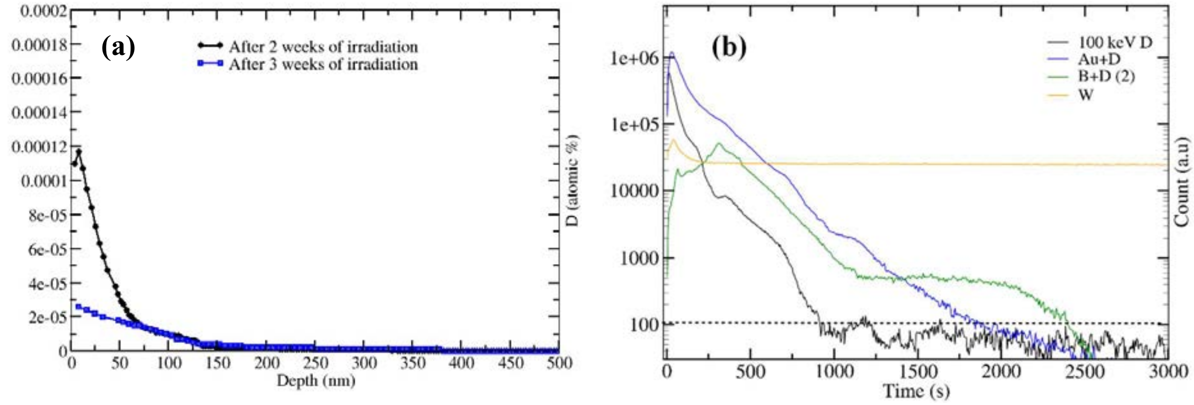

FIG. 39. (a) Deuterium depth profile (SIMS) measured after two weeks and three weeks of irradiation and (b) Deuterium depth profiles in un-damaged W foil, foils damaged with 10 MeV boron ions and with 80 MeV gold ions for a damage fluence of 1.3×10^{14} *ions-cm*$^{-2}$.

The deuterium depth profiles in the case of foils pre-damaged with 10 MeV boron shows a rather broad peak towards inside the sample. The ratio of deuterium content in pre-damaged with gold to un-irradiated sample was ~6.5. These results are preliminary, however it is clear from FIG. 36 and FIG. 39 (b) that there is enhancement in trapping of D in Au irradiated tungsten samples.

In the case of boron, while the ERDA results FIG. 36 shows enhancement of D trapping, the same cannot be confirmed by the SIMS results shown in FIG. 39 (b).

There is a puzzling result of reduced trapping of D in samples with Au irradiation followed by He as compared to samples irradiated only with Au. The SIMS and ERDA results seem to be consistent.

In general the experiments with D trapping need to be continued further for more insights into the trapping mechanism and nature of defects.

7. DISCUSSION

Understanding of the formation and evolution of defects in ion-irradiated tungsten is the essential objective of this study. In line with this objective, a study of how the defect structure is affected by initial microstructure, projectile-mass and energy has been carried out.

The annealing of tungsten foils at high temperatures in vacuum leads to a significant increase in the size of grains. The characterization of recrystallized tungsten foil (annealed at 1873 K) leads to the following observations

1. Reduced dislocation density in grains due to annealing out of dislocations.
2. Dislocation line defects are dispersed and uniformly distributed in the foil.
3. PAS lifetime intensity show 70% defect free foil and 30% is due to 3-4 vacancy clusters.

Such foils with low defects and bigger crystallite size are more suitable for the study of defects formed and their quantification.

7.1 Defect formation - Qualitative and quantitative aspects:

The qualitative and quantitative estimate of defect formation of Au and B ion-irradiated tungsten using TEM analysis is given in TABLE 7.

It may be observed that in the case of Au, the most dominant defects were vacancy clusters. We have not observed dislocation loops however, dislocation lines were seen. The long dislocation-segments observed near the surface region and at 2 μm depth from the surface in case of Au may be mixed dislocations (edge and screw) or extended dislocations by cross-slip.

In the case of boron, the cluster density is much smaller and the most prominent defects were dislocation lines.

The change in dislocation density from the surface region to 2 μm depth for both, Au and B ion irradiated tungsten, show similar trend of increasing dislocation density for the fluence of 1.3×10^{14} ions-cm^{-2}.

The range of 80 MeV Au ion in tungsten as calculated by SRIM is ~4.5 μm which shows continuously increasing density of defects up to ~4 μm. In case of boron also, a similar profile is observed.

TABLE 7. SUMMARY OF CHARACTERIZATION OF DEFECTS TYPE AND THEIR MEASUREMENTS

S. No.	Energy/Ion type	Fluence ($\times10^{14}$ ions-cm^{-2})	Type of defects	Density (cm^{-2})	Size (nm)
1	80MeV Au (at surface region)	1.3	Dislocation line	2.9×10^{8}	400-2000
2	80MeV Au (at 2μm depth)	1.3	Dislocation line	6.1×10^{8}	400-3000
3	80MeV Au (at 2μm depth)	1.3	Defect clusters	1.3×10^{12}	2.2-12
4	10MeV B (at surface region)	1.3	Dislocation line	9.0×10^{8}	100-420
5	10MeV B (at surface region)	1.3	Defect Clusters	7.5×10^{8}	20-60
6	10MeV B (at 2μm depth)	1.3	Dislocation line	1.9×10^{10}	80-1100
7	10MeV B (at 2μm depth)	1.3	Defect clusters	9.3×10^{9}	8-35
8	10MeV B (at 2μm depth)	1.3	Dislocation loops	6.9×10^{8}	30-70
9	10MeV B (at surface region)	10.0	Dislocation line	7.9×10^{8}	50-900
10	10MeV B (at surface region)	10.0	Dislocation loops	7.2×10^{7}	35-80

Boron irradiation with higher fluence leads to the formation of dislocation loops on the surface. Small sized dislocation-segments in B irradiation indicates that there is less formation of mixed dislocations (*cf.* FIG. 40 (a)) but this may need more statistical studies.

Size variation of line dislocations seen in TEM analysis after different ion irradiation in tungsten is shown in FIG. 40 (b). Annealed sample also has been included for the comparison. High mass ions show higher size of dislocation as compared to size shown for low mass ion irradiation.

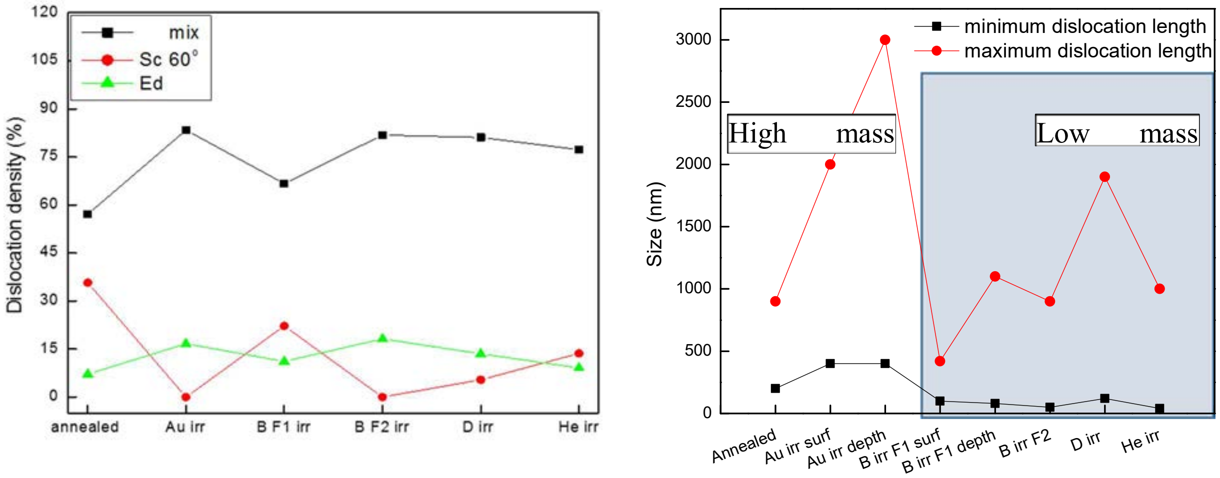

FIG. 40. (a) Variation in density of dislocation type - mix, screw with 60 degrees (Sc 60) and Edge(Ed) - in tungsten foil after different ions irradiation. B F1 is for fluence (1.0×10^{14} ions-cm^{-2}) and BF2 is for Fluence (1.3×10^{14} ions-cm^{-2}) and (b) Variation in size of dislocations in tungsten foil after different ions irradiation

DBPAS shows the S-parameter at different energies, which explains indirectly, the presence of defects at different depths (based on the profile given by Makhov, described in section 4 above). Also W-S curve show that all the irradiations except that with D did not cause any change in the local chemical environment throughout the positron range (FIG. 41). In the case of D the change in slope may be due to a change in chemical environment which seems to be consistent due to its high value of fluence. This indicates D forming defects with vacancies.

In D-irradiated tungsten, small dislocation networks are seen whereas, dislocation loops of size ranging from 50 nm to 100 nm are observed near long segments of dislocations which are of larger size than that of formed due to boron irradiation. The larger size dislocation loops in this case may be attributed to the increase in temperature of the sample during high (25-70 µA) current.

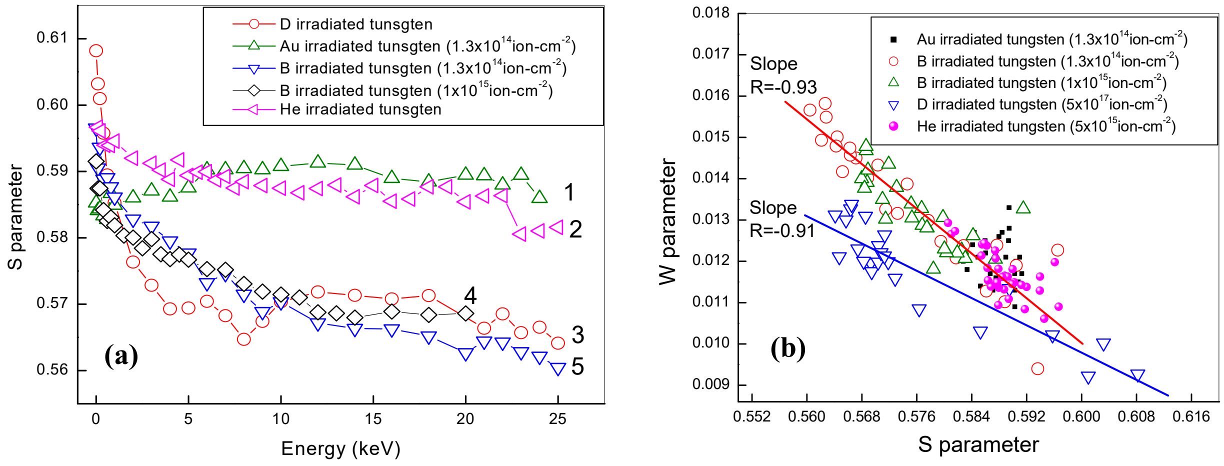

FIG. 41. (a, b). (a) S-E curve for tungsten foil after 80MeV Au irradiation (labelled '1'), 250keV He irradiation (labelled '2'), 10MeV B irradiation with fluence of 1.3×10^{14} ion-cm^{-2} (labelled '5'), 1×10^{15} ion-cm^{-2} (labelled '4'), 100 keV D irradiation (labelled '3') and (b) W-S plot of positron energy 0-25keV of 80MeV Au, 10MeV B, 250 keV He, 100 keV D irradiated tungsten foil.

As mentioned in section 5.3, helium irradiation leads to short and long segments of dislocation (in size range of 40 to 1000 nm) with the density of 1.0×10^{9} cm^{-2}. No dislocation loops were observed. The reason needs to be understood by further work. It may be recalled that in the case of Au also, no dislocation loops are seen. The changes in the S-W plot for Au and He irradiated tungsten imply different nature of defects

Role of fundamental parameters on Defect formation:

From the above discussion it is clear that there is a difference in the defects formed by Au and B-irradiation. The types of defects formed due to Au are mainly dislocations and vacancy clusters, whereas in the case of boron irradiation, in addition to dislocations and vacancy clusters, dislocation loops are also observed. The dominance of cluster formation in Au may be attributed to fragmentation of clusters formed due to high PKA energies. MD simulations suggest that the fragmentation can happen after 150 keV.

It may be recalled that the PKA due to 80 MeV Au have significant contribution from 30-300 keV energy range, whereas in the case of boron it is from 30-100 keV (FIG. 10). It is also important to note that there is a large number of low energy PKA (~ 1-10 keV) formed per incident ion in both cases (in fact boron creates almost 4 times larger number compared to Au). Given these facts, the instances of creation of radiation cascades which leave behind a cluster of vacancies (~10 or more) are much more dominant in Au. Since the migration energies of vacancies are more than 1.5 eV and the samples are irradiated at room temperature, the migration can be considered to be negligible within the timescale of irradiation. Thus, the vacancies formed could have remained in the core region of the cascade in the form of a cluster.

In the case of boron, the cascades are predominantly from the lower energy PKA (as compared to gold) and it is more likely that a sparse distribution of Frenkel-pairs is formed at the end of cascade. The number of FP seems to be approximated well by $FE = 2 \times E_{PKAkeV}$ (FIG. 3). The interstitial migration energies on the other hand are of the order to 0.4 eV. Therefore, the interstitials can migrate within a single cascade to form clusters. The average energy of atoms participating in a thermal spike could be ~0.5 eV and in multiple adjacent cascades, they can coalesce to form dislocation loops at low energy cascades as in the case of boron. Although this is possible in high energy cascades as well, there is a high likelihood that adjacent multiple cascades can restructure the local neighborhood to leave out small crystallites/interstitial dislocations with vacancy clusters.

We believe that the reason why the dislocation loops are not seen in Au irradiated samples is that, dense cascades are formed due to high nucleation rate. High nucleation rate leads to stabilize the clusters or dislocation loops in matrix rather than growth of them [17–20].

Results with He irradiation show a similarity with Au, as far as PAS analysis is considered (FIG. 41 (a)). Prima facie, it seems surprising as it indicates that the damage is more or less constant throughout the depth. However, considering the higher dose of He and the correspondingly larger defects density the PAS is not expected to look different than due to Au, given the equally high density of clusters formed.

From the same figure, the D irradiation and boron seem to follow a similar behaviour, except a small hump observed in D. The latter indicates (S-curve) that the defect concentration is gradually decreasing with depth. From the deuterium depth profiling using ERDA and SIMS it can be seen that a high concentration of D exists up to 300 nm. The different slope in the W-S curve of D (FIG. 41 (b)) can be attributed the change in local chemical environment caused by the large dose of D.

7.2 Trapping of H-isotopes in Tungsten

Au, B and He ion irradiation lead to the strain in the lattice. This strain is calculated by $\Delta d/d_0$ for I-loop, V-loop, I-cluster and the nature (compressive or tensile) and magnitude of it can affect the movement of D in lattice. However, other factors such as presence of dislocations and other complex defects also contribute to the restriction of movement of D and so it is difficult to explain the main reason of restriction of mobility of D in W lattice.

8. CONCLUSION

We have carried out computer simulation and ion-irradiation experiments to study the radiation damage in polycrystalline, bulk tungsten sample and in recrystallized tungsten foils. The highlights of this study are:

1. Atomistic simulations reveal that at higher PKA energies (> 50 keV), the collision cascades lead to the formation of large vacancy clusters at the core of the cascades and dislocation nucleation at the periphery of the cascades. We have also observed fragmentation of cascades at energies more than 150 keV. The PKA energy of B ions is closer to that produced by neutrons.
2. S-E plot seems to distinguish very well the damage produced by B as compared to that by Au. However, PAS data shows that damage due to He is also similar to that by Au
3. High energy, heavy ion-irradiation (80 MeV Au) leads to the formation of high defect density in the form of dislocation lines and vacancy clusters. However, no loop formation was observed in TEM analysis.
4. Boron irradiation (10 MeV B) leads to the formation of dislocation lines, loops and clusters. However there was no conclusive evidence of enhanced D trapping.
5. Sequential bombardment of He and D indicate that even at low fluence of He, the D trapping is significantly suppressed.

REFERENCES

[1] SUBHASH, P. V, THOMAS, S., MISHRA, S., FEDER, R., DEEPAK, Neutronic Analysis of X-Ray Survey Spectrometer for ITER Using Attila, Kalinga Institute of Industrial Technology, India (2013).

[2] WAREING, T., MCGHEE, J., EYES ONLY - Discontinuous finite element Sn methods on 3-D unstructured grids, Nucl. Sci. Eng. to Appear (1999) 1.

[3] GREENWOOD, L.R., SMITHER, R.K., SPECTER: Neutron Damage Calculations for Materials Irradiations, (1985).

[4] NORDLUND., K., Molecular dynamics simulation of ion ranges in the 1–100 keV energy range, Comp.Mater.Science, **3** 4 (1995) 448.

[5] STUKOWSKI, A., Visualization and analysis of atomistic simulation data with OVITO–the Open Visualization Tool, Model. Simul. Mater. Sci. Eng. **18** 1 (2010) 015012.

[6] JAMES F ZIEGLER, MD ZIEGLER, J.B., James F Ziegler, MD Ziegler, JP Biersack, Nucl. Instruments Methods Phys. Res. Sect. B Beam Interact. with Mater. Atoms **268** 11 (2010) 18181823.

[7] KANJILAL, D. et al., Testing and operation of the 15UD Pelletron at NSC, Nucl. Inst. Methods Phys. Res. A **328** 1–2 (1993) 97.

[8] TRIVEDI, T., PATEL, S.P., CHANDRA, P., BAJPAI, P.K., Ion Beam Facilities at the National Centre for Accelerator based Research using a 3 MV Pelletron Accelerator, Phys. Procedia **90** November 2016 (2017) 100.

[9] OLSEN, J. V., KIRKEGAARD, P., PEDERSEN, N.J., ELDRUP, M., PALSfit: A new program for the evaluation of positron lifetime spectra, Phys. Status Solidi Curr. Top. Solid State Phys. **4** 10 (2007) 4004.

[10] MAKHOV, A.F., Electron penetration in Solids, Sov. Phys. Solid State 2 2 (1961) 2172.

[11] VEHANEN, A., SAARINEN, K., HAUTOJÄRVI, P., HUOMO, H., Profiling multilayer structures with monoenergetic positrons, Phys. Rev. B **35** 10 (1987) 4606.

[12] TROEV, T., POPOV, E., NANKOV, N., YOSHIIE, T., Model calculation of positron states in tungsten containing hydrogen and helium, J. Phys. Conf. Ser. **207** (2010).

[13] DE VRIES, J., Positron Lifetime Technique With Applications In Materials Science, University of Delft (1987) 159 pp.

[14] TROEV, T., POPOV, E., STAIKOV, P., NANKOV, N., YOSHIIE, T., Positron simulations of defects in tungsten containing hydrogen and helium, Nucl. Instruments Methods Phys. Res. Sect. B Beam Interact. with Mater. Atoms **267** 3 (2009) 535.

[15] BARTHE, M.-F., Positron Annihilation Spectroscopy to Characterize Irradiation Induced Vacancy Type Defects in Materials for Nuclear Fission and Fusion, EPJ Web Conf. **115** (2016) 03004.

[16] MAYER, M., SIMNRA User's Guide, Garching, Germany (1997) IPP 9/113 pp.

[17] WATANABE, H., FUTAGAMI, N., NAITOU, S., YOSHIDA, N., Microstructure and thermal desorption of deuterium in heavy-ion-irradiated pure tungsten, J. Nucl. Mater. **455** 1–3 (2014) 51.

[18] HUANG, X., SHEN, Y., LI, Q., XU, Z., ZHU, J., Microstructural evolution of CLAM steel under 3.5MeV Fe13+ ion irradiation, Fusion Eng. Des. (2016) 1.

[19] ABE, H., NARAMOTO, H., SONODA, T., KINOSHITA, C., Formation and growth process of defect clusters in magnesia under ion irradiation, Nucl. Instruments Methods Phys. Res. **128** (1997) 176.

[20] BAYU AJI, L.B., WALLACE, J.B., KUCHEYEV, S.O., Effects of collision cascade density on radiation defect dynamics in 3C-SiC, Sci. Rep. **7** September 2016 (2017) 1.

DEUTERIUM AND HELIUM RETENTION IN RADIATION DAMAGED TUNGSTEN

Yu. M. GASPARYAN, O. V. OGORODNIKOVA, M. S. ZIBROV, V. S. EFIMOV,
A. S. SHUBINA, S. A. RYABTSEV, A. A. PISAREV

National Research Nuclear University MEPhI (Moscow Engineering Physics Institute)
Moscow, 115409, Russia

Abstract

New experimental data on D and He interaction with radiation damage in W have been obtained using, mainly, thermal desorption spectroscopy in the frame of this project. Strong influence of radiation damage on D and He retention has been demonstrated. Detrapping energies for D in single vacancies and vacancy clusters have been derived from a series of experiments with keV D ion irradiation using a special TDS procedure, which is free of any additional unknown parameters. Radiation damage produced by 20 MeV W ions have been also analysed as one of the most reliable proxy of neutron irradiation. A remarkable D retention has been observed even after irradiation at rather high temperatures up to 800 K. The effect of the incident flux on D retention have been demonsrated, which is most significant at elevated temperatures. Helium desorption from radiation damage produced by MeV ions was measured and it was observed only at very high temperatures, above 2000 K.

1. INTRODUCTION

Unlike current fusion devices that work with deuterium, ITER and future reactors will use D-T mixture as a fuel, and the total tritium amount in the machine should be controlled below the safety limit (1 kg for ITER [1]), as well as tritium permeation into the cooling system.

Tungsten will be used as plasma facing material (PFM) in the divertor area of ITER and it is also considered for future fusion reactors. The solubility of hydrogen in tungsten is very low [2], but the high heat of solution usually correlates with a high binding energy with radiation defects [3]. Therefore, hydrogen retention in the bulk of tungsten is very sensitive to presence of defects and can be rather high at high levels of radiation damage.

A significant amount of helium can be also accumulated in PFM as a result of fusion reactions in plasma and radioactive decay of tritium trapped in the wall. Presence of helium in the lattice can significantly affect hydrogen isotope behavior and thermo-mechanical properties of PFM.

This work was focused on experimental determination of qualitative and quantitative characteristics of hydrogen and helium interaction with radiation defects.

2. EXPERIMENTAL DEVICES

The main experimental technique was thermal desorption spectroscopy (TDS) available in two different devices: the TDS stand [4] and the ion beam facility MEDION [5].

The TDS stand is used for analysis of samples exposed in other installations. The base pressure in the system is 2×10^{-9} mbar. The heating of the samples is due to radiation from a U-shaped heater made of 50 μm W foil, and the temperature is controlled by a W-Re thermocouple directly welded to the sample. The linearity of the sample heating during TDS is controlled by a loop feedback system based on a proportional-integral-derivative (PID) control. The desorption flux of deuterium containing (HD, D_2, HDO, D_2O) and other molecules is measured by a quadrupole mass-spectrometer (QMS) Pfeiffer Vacuum QME 200. The calibration of the QMS was done routinely after each experiment using a system including two leak valves and a baratron as described in [4].

The ion beam facility MEDION gives the opportunity to perform the full cycle of the experiment (including pre-annealing, irradiation, and TDS) in one chamber without contact with air. The base pressure in the main chamber is below 5×10^{-9} mbar, and it increases to about 10^{-8} mbar during irradiation due to leaking of D_2 gas from the ion source. A quadrupole mass-spectrometer (QMS) is installed in the target chamber, which allows in situ TDS analysis. The absolute QMS sensitivity for helium is calibrated after each experiment by using a helium leak. The relative QMS sensitivities for other gases were determined by using the same procedure as in the TDS stand. The sample in the MEDION facility is usually a thin strip (15×50 mm^2), which is mounted on two water-cooled electrical feedthroughs and can be resistively heated by DC current. Only a small central part (3 mm in diameter) of the sample is subjected to irradiation to minimize the influence of non-uniformity of the temperature over the sample. The sample temperature near the beam strike area is measured by a spot-welded W-Re thermocouple.

3. RESULTS AND DISCUSSION

3.1. Deuterium interaction with vacancies and vacancy clusters

Experimental TDS spectra are often compared with numerical calculations, which use a number not well known adjusting parameters. However, one can avoid uncertainty connected with these parameters if to determine the H detrapping energy (E_{dt}) from the shift of the desorption maximum (T_m) in a series of TDS measurements performed with identical samples, but with different heating rates (β), in conditions of high recombination rate on the surface. The equation or determination of E_{dt} is

$$\ln\left(\frac{\beta}{T_m^2}\right) = \ln\left(A\frac{k}{E_{dt}}\right) - \frac{E_{dt}}{k}\frac{1}{T_m} \qquad (1)$$

where A – a constant depending on parameters of the material and trapping sites, k – Boltzmann constant.

Applicability of this method was theoretically investigated in [6, 7]. This method was used also for investigation of D interaction with single vacancies and small vacancy clusters in tungsten [7,8]. All experiments were performed in the MEDION ion-beam facility. The sample was cut from a 25 µm thick hot-rolled polycrystalline W foil with the purity of 99.97 wt.% produced by Plansee. It was cleaned in an ultrasonic bath with gasoline, acetone, and ethanol. In order to minimise the concentration of intrinsic defects in the sample (dislocations, grain boundaries), the sample was annealed at 1800 K for 30 min. Each series of experiments was performed using one sample, which was annealed before every next irradiations. A good reproducibility of the experimental results was observed without any memory effects, and the shifts of the peak position were measured much more precisely than in other experiments peformed with several samples in one series.

Primary defects were produced in those experiments by 10 keV D^+ ion beam at room temperature with the fluence of 3×10^{19} D/m^2. In this conditions, the TDS spectrum (FIG.1) consists of a very broad peak near 430 K, a shoulder near 610 K, and a faint shoulder near 720 K; so the detailed analysis of the spectrum is very difficult. However, it is possible to obtain well separated low temperature and high temperature peaks.

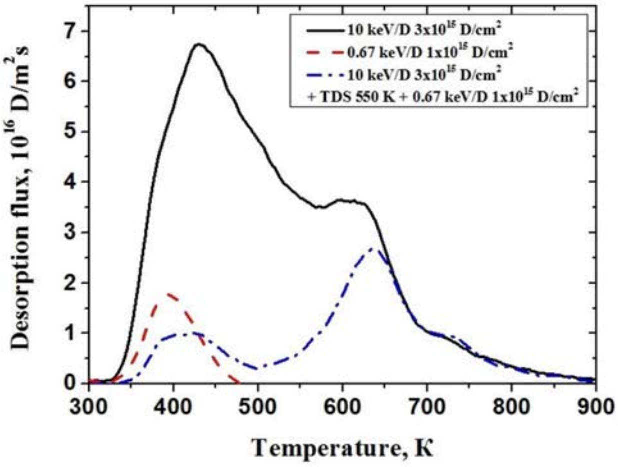

FIG. 1. A comparison of three TDS spectra of D_2 molecules from recrystallized W: 1) the sample was irradiated by 10 keV/D ions to the fluence of 3×10^{19} D/m^2; 2) the sample was implanted with 0.67 keV/D ions to the fluence of 10^{19} D/m^2; 3) the sample was irradiated by 10 keV/D ions to the fluence of 3×10^{19} D/m^2, then annealed at 550 K for 5 min, and then implanted with 0.67 keV/D ions to the fluence of 10^{19} D/m^2 [9].Reproduced courtesy of Elsevier [4455780391559].

The separation of the high temperature peaks was possible due to annealing of the sample at 550 K for 5 min after implantation and subsequent implantation of low energy D ions. The peak at about 600 K was attributed in [7] to single vacancies. Annealing to 550 K was sufficient to remove a substantial part of D from vacancies, but growth of vacancy clusters was not expected, as vacancies in W are still immobile at 550 K [10]. Subsequent implantation with 2 keV D_3^+ (0.67 keV/D) ions to the low fluence 10^{19} D/m^2 populated existing vacancies with D without producing additional displacement damage. The low fluence was also important to avoid multiple occupation of vacancies. No more than two atoms in one vacancy is expected at this fluence [7]. This procedure was repeated several times, and TDS measurements were done with different heating rates in the range of 0.15-4 K/s. Figure 2a shows the family of TDS spectra obtained for different heating rates, and Figure 2b shows the temperature dependence of the peak position.

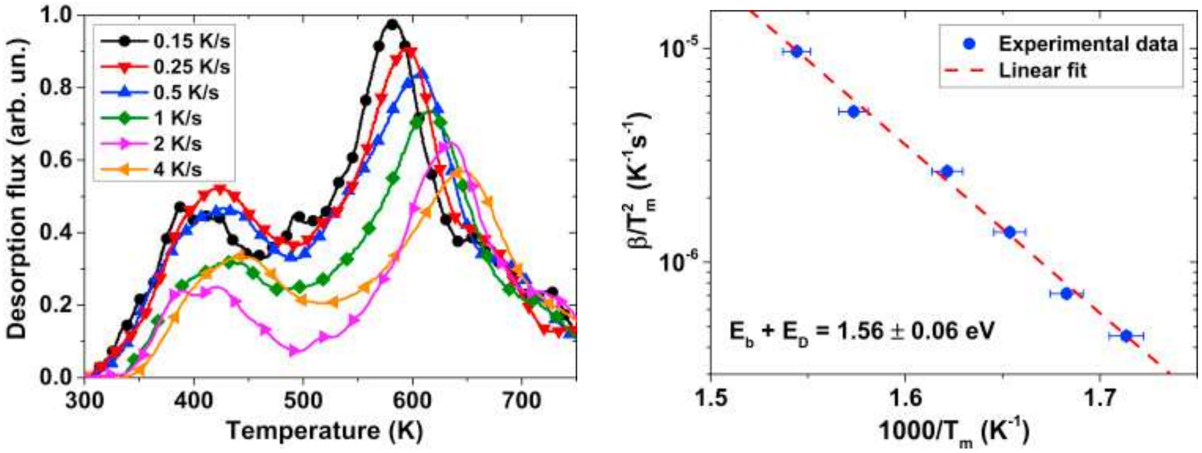

FIG. 2. a) TDS spectra of D_2 from W irradiated by 10 keV/D ions to the fluence of 3×10^{19} D/m^2, subsequently annealed at 550 K for 5 min, and then implanted with 0.67 keV/D ions to the fluence of 1×10^{19} D/m^2. b) Semilogarithmic plot of β / T_m^2 versus $1/T_m$ for the peak corresponding to the D release from vacancies in W [7].

Although the presence of the low-temperature peak near 400 K indicates existence of additional trapping sites with a lower binding energy, numerical simulations indicate that these defects do not influence the position of the high temperature peak, as they are rather weak and almost do not influence D transport and release. Figure 2b shows the semilogarithmic plot $\beta/T_m{}^2$ versus $1/T_m$ for the peak corresponding to the D release from vacancies. The best linear fit according to the least squares analysis taking into account the experimental uncertainties is also shown; it corresponds to the detrapping energy of (1.56±0.06) eV.

Similar experiments were made to investigate D interaction with vacancy clusters (FIG.3). To produce clusters, tungsten sample was annealed at 800 K after irradiation by 10 keV D^+ ion beam. Then it was filled with deuterium by low energy irradiation. Mobility and agglomeration of vacancies above 600 K was observed earlier by Eleveld et al. [10] using positron annihilation technique. In our experiments [11] on TDS measurements performed after annealing to different temperatures after implantation, it was observed that peaks corresponding to the D release from vacancy clusters appeared at annealing temperatures higher than 550 K. The detrapping energy of D from vacancy clusters was calculated to be (2.10±0.02) eV.

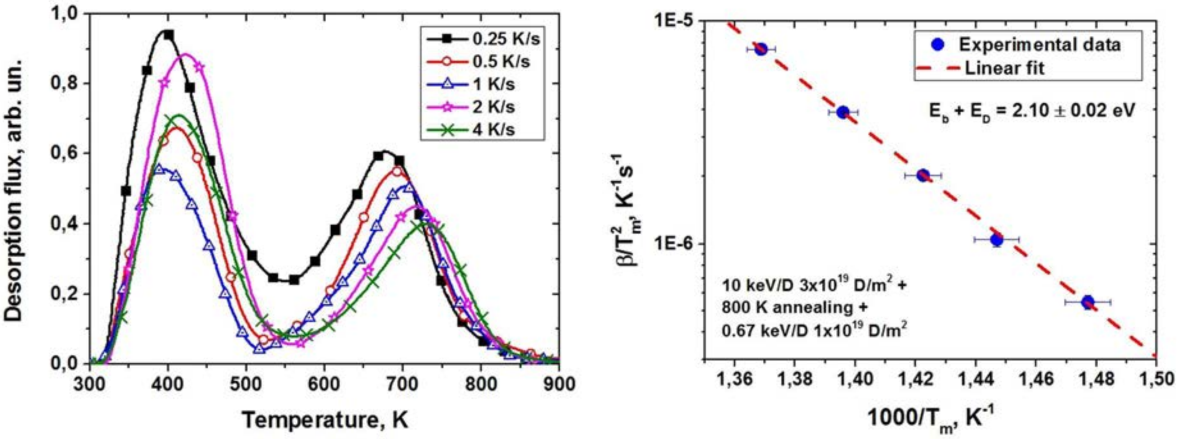

FIG. 3. a) Thermal desorption spectra of D_2 *molecules from W irradiated by 10 keV/D ions to the fluence of* 3×10^{19} *D/m*^{2}*, subsequently annealed at 800 K for 5 min, and then implanted with 0.67 keV/D ions to the fluence of* 1×10^{19} *D/m*^{2}*. The TDS heating rates varied in the range of 0.25-4 K/s. Spectra are plotted in arbitrary units. b) Semi-logarithmic plot of* $\beta / T_{\mathrm{m}}{}^2$ *versus* $1/T_m$ *for the peak corresponding to the D release from vacancy clusters in W [8].*

The detrapping energy of 1.56 eV for single vacancies is in a good agreement with that obtained by Fransens et. al. (1.55 eV) using the perturbed angular correlation technique [12], and it is also close to that obtained from various DFT calculations [13-15] (for a first and a second H atoms in a vacancy).

The values for vacancy clusters is also reasonable. For example, Poon et. al. in [16] successfully modeled deuterium-cluster interaction using the value of 2.10±0.05 eV for the trap energy. According to “adsorption model”, discussed in [17], the mechanism of H isotope trapping in a large cluster is similar to chemisorption on the surface. In this case the detrapping energy of H isotope from vacancy cluster can be estimated as $E_{dt} = E_s + E_D - Q_c$, where $Q_c = -(0.3\text{-}0.8)$ eV is the surface chemisorption heat, $E_D = 0.4$ eV – the activation energy for D diffusion in the metal, and $E_S = 1.04$ eV – the heat of solution of a H isotope [2]. The value of E_{dt} for vacancy clusters estimated in this way is 1.7-2.2 eV. The value derived from our experiments is in this range, although the size of the clusters is assumed to be rather small (4-10 vacancies).

3.2. TDS analysis of damage produced by 20 MeV W ions

Ion irradiation with energetic heavy ions is currently recognized as the only non-activating method to simulate the fast neutron damage produced in fusion reactors. One of the most adequate ways was implemented in IPP (Garching, Germany), where 20 MeV W^{6+} ions were used for damage production. Heavy W ions do not contaminate the sample and produce a dense collision cascade with a low ratio of low-energy to high-energy primary knock-on atoms in in contrast to light ions [18, 19]. A number of experiments has been already done on this topic [18-25]. Here, we present TDS analysis of pre-damaged samples exposed to the D atomic flux described in [26]. This work was done in collaboration with IPP (Garching, Germany) and Jožef Stefan Institute (Ljubljana, Slovenia) to estimate the binding energy of D with radiation-induced defects.

Samples (12×15×0.5 mm^3) were cut from a polycrystalline W rod with the purity of 99.98 % and grains oriented preferentially normal to the surface (European ITER reference W) [18]. All samples were mechanically polished to a mirror-like finish, ultrasonically cleaned in acetone bath and degassed at 1000 K for 20 minutes before any irradiation.

Radiation damage in tungsten samples was produced by W ions in four steps by four different energies to get the uniform profile of damage; it was identical for all damaged samples. The first irradiation was done by 20 MeV W^{6+} ions with the fluence of 1.4×10^{18} W/m^2, then the sample was irradiated by 8 MeV W^{6+} with the fluence of 3.06×10^{17} W/m^2, then - by 4 MeV W^{6+} ions with the fluence of 1.97×10^{17} W/m^2, and finally - by 2 MeV W^{6+} ions with the fluence of 1.38×10^{17} W/m^2. The damage profile was calculated in the same way as in [18], where the SRIM code was used with the "full cascade option" and with the displacement threshold energy E_{th} = 90 eV. With these assumptions calculations predict a flat damage profile in the surface layer of about 2 µm deep with a damage level of 0.9 dpa.

After damaging by fast ions, the samples were exposed to the flux of thermal D atoms (0.2 eV), which was created by the hydrogen atom beam source, HABS (JSI, Slovenia) [21], where hydrogen molecules thermally dissociate in the hot capillary. The incident flux of D atoms was 3.0×10^{19} D/m^{2}s. The temperature and fluence were varied in the range of 600 – 800 K and 3.8×10^{23} – 2×10^{24} D/m^2 respectively.

To demonstrate the influence of radiation damages on D retention, two samples were simultaneously exposed to D atomic flux at the temperature of 600 K with the fluence of 2×10^{24} D/m^2 (FIG.4). One of them was preliminary damaged by W ions as described above.

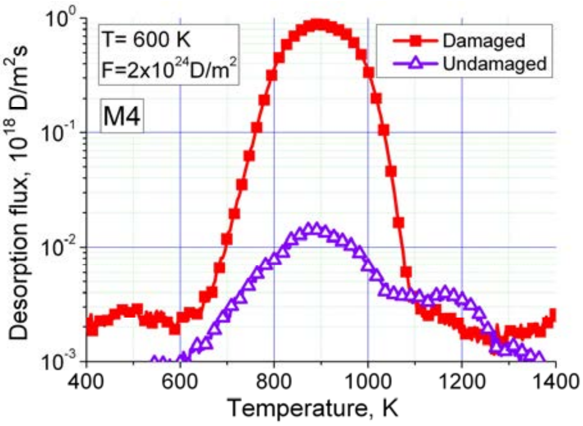

FIG. 4. TDS spectra of D_2 molecules from two samples (1 – undamaged sample, 2 – sample damaged by W ions) exposed to D atomic flux up to the fluence of 2×10^{24} D/m^2 at the temperature of 600 K [26]. Reproduced courtesy of Elsevier [4455780652241].

One can clearly see the increase of the deuterium accumulation in the damaged sample in comparison with the undamaged one, which is attributed to radiation defects. The TDS spectrum for the damaged sample consists of one broad peak in the interval from 600 to 1100 K with the maximum at 920 K. In the case of the undamaged sample, the temperature range of deuterium release is similar, but the release rate is much smaller. Additionally, the small peak with the maximum at 1200 K can be seen. High temperatures of deuterium release indicate that both samples have traps with a high binding energy, and these defects can be produced during manufacture of material and during irradiation. The total deuterium amount released in TDS from the damaged sample was about 2×10^{20} D/m^2. If to assume the uniform distribution of D atoms in the damaged layer of 2.0 µm, one can estimate the concentration of about 0.2 at.%. These numbers agree well with NRA data [25].

Another series of experiment was performed with variation of the exposure temperature: 600, 700, and 800 K. Figure 5 collects TDS spectra for damaged W exposed at three different temperatures (600, 700, 800 K) with the fluence of 3.8×10^{23} D/m^2 and the TDS spectrum for the experiment at 600 K with the higher fluence of 2×10^{24} D/m^2, because the higher fluence was needed to saturate all defects at 600 K.

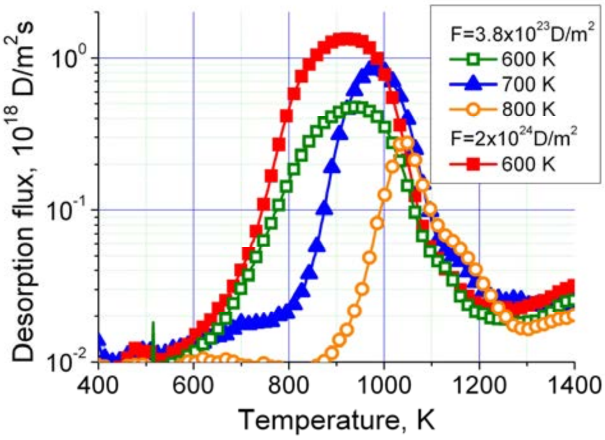

FIG. 5. TDS spectra of D_2 molecules for four damaged samples (0.9 dpa) exposed to D atomic flux at various conditions: 1- 600 K, 2×10^{24} D/m^2; 2- 600 K, 3.8×10^{23} D/m^2; 3- 700 K, 3.8×10^{23} D/m^2; 4- 800 K, 3.8×10^{23} D/m^2 [26]. Reproduced courtesy of Elsevier [4455780652241].

One can see that a remarkable deuterium amount was accumulated in damaged W even at the highest temperature of 800 K. This is an indication that a part of defects produced under irradiation by W ions have a high binding energy.

To estimate parameters of D interaction with radiation defects, TDS spectra were simulated using the computer code DIFTRAP developed in MEPhI and based on kinetic rate equations. The uniform distribution of traps for deuterium in the damaged area was assumed. Additionally only one kind of traps was assumed in simulations at the first stage. The trap density and the detrapping energy were fitting parameters. The Frauenfelder's value [2] was taken for the diffusivity. The recombination coefficient was also varied to get a better agreement with experimental data. A good agreement with the experimental curve for exposure at 600 K (FIG.6) was achieved using the detrapping energy of 1.7-1.9 eV with different combinations of the trap density and the recombination coefficient.

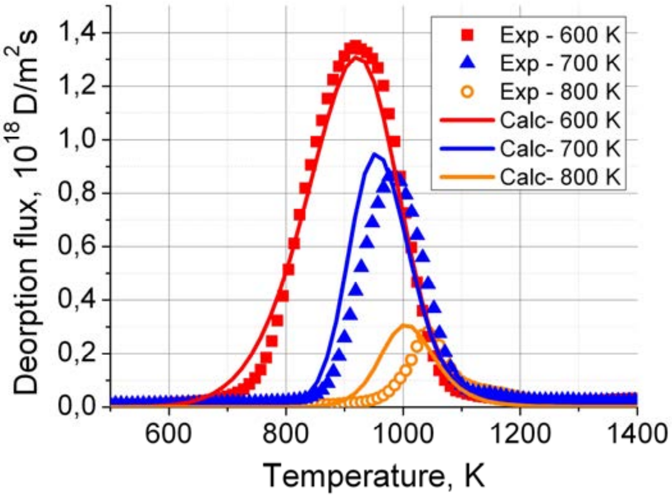

FIG. 6. The comparison of experimental TDS spectra with the spectra calculated using the DIFTRAP code. The experimental curves are given by dotes, the calculated curves are given by lines. Temperatures of exposure is specified in the figure. Parameters of calculations: $K_r=4\times10^{-24}\times\exp[-0.3\ eV/kT]$ 1/m^{4}s, $E_t=1.69$ eV [26]. Reproduced courtesy of Elsevier [4455780652241].

The correct peak position for experiments at 700 and 800 K can be achieved if to increase the detrapping energy by 0.05-0.15 eV. This can be explained by transformation of defects at elevated temperatures. For example, vacancies or small vacancy clusters can agglomerate in larger clusters or small voids.

Thus, the assumption about traps with the energy of 1.7-2.0 eV and the uniform profile gives a reasonable agreement with the experiments. Defects with a smaller energy should be also produced, but do not play significant role at high temperatures.

3.3. The effect of incident flux on D accumulation in radiation damage

A more detailed modelling of experimental data about the D depth profile in pre-damaged W after exposure to either thermal atoms or D_2 gas was also done using several types of traps (see [17] for details). A good agreement with experiments was achieved using the fixed set of parameters, namely de-trapping energies of 0.9, 1.45, 1.9, 2.2, and 2.4 eV and trap densities of 1, 0.5, 0.4, 0.06, and 0.01 at.%, respectively. Frauenfelder's solubility and diffusivity values [2] were used in calculations. These data are again in reasonable agreement with DFT calculations and our experimental data obtained for keV ion irradiation.

It was also shown analytically and confirmed experimentally that deuterium trapping in presence of defects of high density in W depends on the ion energy and ion flux [17]. Figure 7 demonstrates comparison of various experimental data in the range of 10^{19}-10^{24} D/m^{2}s with modelling.

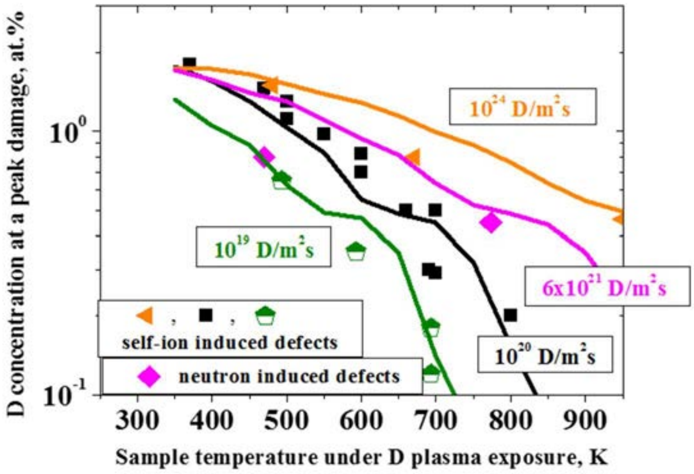

FIG. 7. The D concentration after the exposure of damaged W (0.3-0.5 dpa) to D atomic beam with a flux of 10^{19} D/m^{2}s and to plasma beams with fluxes of 10^{20} D/m^{2}s, 10^{21} D/m^{2}s, and 10^{24} D/m^{2}s. Experimental data are shown as symbols and theoretical data as solid lines [17]. Reproduced courtesy of Elsevier [4455780276226].

The effect of the incident flux is very strong for elevated temperatures, when the D concentration in defects is far from saturation. In this case, the D trapped amount depends strongly on the solute D concentration, which is determined by the incident flux. At lower temperatures, it is difficult for D to release from traps, and they are close to saturation. Therefore, the D concentration in traps depends weakly on the solute D concentration, and the influence of the incident flux is also small.

3.4. Helium desorption from damaged W

The solubility of helium in tungsten is almost zero (for helium: $E_S^{He}\approx5.5$ eV [27]), and the detrapping energy of He from radiation defects is also very high. Helium atoms are known also to agglomerate efficiently into clusters around initially point defects, and this leads to formation of bubbles. Interaction of He with point defects formed by keV ion irradiation was investigated in details in [28].

TDS spectra have a multipeak structure (in the range of 1200-1800 K) that is explained by trapping of several atoms in one trap and different detrapping energies for different number of atoms in the trap. Here, we analysed He desorption from radiation defects produced by MeV particles.

For these experiments, our TDS setup was adopted for measurements up to 2500 K. The samples were cut from the polycrystalline tungsten sheet with the thickness of 25 microns, then ultrasonically cleaned and re-crystallized at 2000 K for 30 minutes.

In the first series of experiments, re-crystallized W samples pre-damaged by 20 MeV W ions (1.4×10^{18} W/m^2, 0.89 dpa) were irradiated by 1MeV ^{3}He ions with the fluence of 10^{20} He/m^2. The dynamics of He release from the samples was measured by TDS. Additionally, the total He amount was measured before and after TDS using the ^{3}He(D,p)^{4}He nuclear reaction. The heating rate was 2 K/s in all TDS measurements, and the maximum temperature was 2470 K. All irradiations and NRA measurements were made in the accelerator at IPP, Garching.

The ^{3}He release was at the level of background in both experiments, and only release of D implanted during NRA measurements was clearly observed in spite of much lower fluence. This means that the sensitivity of our measurements was good, but He desorption was very small even at maximal temperatures. To observe an effect of long time heating, the pre-damaged sample was additionally kept at the maximal temperature for 30 minutes after TDS.

NRA measurements after TDS for the re-crystallized sample confirmed a very low He desorption. The total He amount in the sample after heating (TDS) was found to be almost the same as just after He implantation. The He amount in the pre-damaged sample decreased by about 90 %, and this was attributed to the long heating after TDS, but not to additional damage produced by W ions.

Simulations of these experimental data using a 1-D diffusion code demonstrated that all experimental observations can be well explained assuming a flat profile of traps with the detrapping energy of 4-4.5 eV and homogeneous distribution of He inside in traps [29]. This number is close to the value obtained in earlier experiments of Kornelsen et al. [28]. Much higher temperatures of He release in comparison to [28] are explained by multiple re-trapping process on the way to the surface due to a very high concentration of defects.

To confirm the role of re-trapping, another series of experiments was done with only ^{4}He irradiation (0.3 MeV or 1.0 MeV) of the samples with low fluences in the range of $(3\text{-}100)\times10^{18}$ He/m^2. The samples were heated up 2470 K and kept at maximal temperature for 5 minutes. Helium desorption was monitored during both stages and the results are summarized in Figure 8.

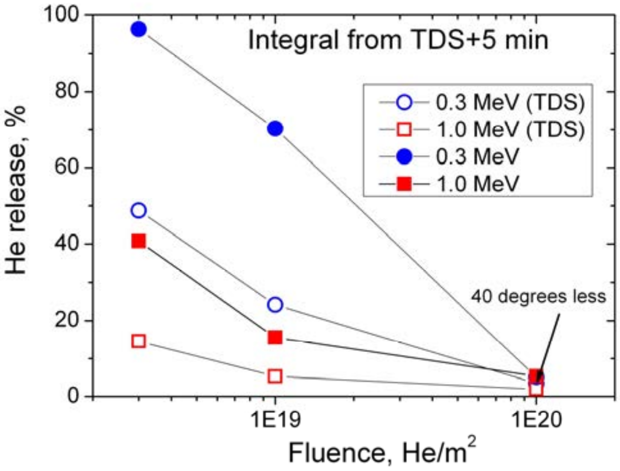

FIG. 8. The fluence dependence of total helium losses during TDS up to 2470 K (open symbols) and TDS together with 5 min storage at the maximal temperature (solid symbols) for two irradiation series with 0.3 MeV and 1.0 MeV ^{4}He ions. Reproduced courtesy of Elsevier [4455771381631].

One can clearly see that He desorption decresed strongly with the increase of the ion energy and the total fluence. Both factors increase the concentration of defects and, as a result, the efficiency of re-trapping process. Even at the lowest concentration of defects, only a half of implanted helium atoms desorbed during the linear heating phase (TDS) and another half desorbed only after additional heating.

Thus, He release from radiation defects in the bulk of tungsten in fusion devices will be almost impossible. Due to presence of He atoms in tungsten at so high temperatures, one should also expect that He will affect the annealing of radiation defects and re-crystallization processes.

SUMMARY

New experimental data on D and He interaction with radiation damage in W have been obtained using, mainly, thermal desorption spectroscopy in the frame of this project. Strong influence of radiation damage on D and He retention has been demonstrated.

Detrapping energies for D in single vacancies and vacancy clusters have been derived from a series of experiments with keV D ion irradiation. A special procedure was used to separate the peaks in TDS spectra. These data are also independent on other unknown characteristics of defects due to variation of the heating rate in experiments.

Radiation damage produced by 20 MeV W ions have been also analysed as one of the most reliable proxy of neutron irradiation. A remarkable D retention has been observed even after irradiation at rather high temperatures up to 800 K. The detrapping energies derived from experiments are in a good agreement both with DFT data and with our experiments with keV ion irradiation. Therefore, one should, probably, not expect much different energies for D in defects produced by fusion neutrons. The effect of the incident flux on D retention have been also demonsrated, which is most significant at elevated temperatures.

Helium desorption from radiation damage produced by MeV ions was measured and it is possible above 2000 K. At high levels of radiation damage, a significant amount of He was in the samples even after long time heating at 2470 K. Thus, He release from radiation defects in the bulk of tungsten in fusion devices will be almost impossible.

REFERENCES

[1] SHIMADA, M., PITTS R.A., CIATTAGLIA, S., et al. J. Nucl. Mater., **438** (2013) S996.

[2] FRAUENFELDER, R. , J. Vac. Sci. Technol., **6** (1969) 388.

[3] GORODETSKY, A.E., ZAKHAROV, A.P., SHARAPOV, V.M., ALIMOV, V.Kh. Nucl. Mater., 93-94 (1980) 588.

[4] RUSINOV, A.A., GASPARYAN, Y.M., PERELYGIN, S.F., et al. Instruments and Experimental Techniques, **52** (2009) 871-876.

[5] EFIMOV, V.S., GASPARYAN, Y.M. AND PISAREV, A.A. Study of the Fine Structure of the Spectra of Deuterium Thermal Desorption from Tungsten. Journal of Surface Investigation. X-ray, Synchrotron and Neutron Techniques **7** (2013), 472–478.

[6] ZIBROV, M.S., SHUBINA, A.S., GASPARYAN, Y.M., PISAREV, A.A. Problems of Atomic Science and Technology, ser. Thermonuclear Fusion, **38** (2015) 32-41 (in Russian).

[7] ZIBROV, M., RYABTSEV, S., GASPARYAN, Y., et al. J. Nucl. Mater., **477** (2016) 292.

[8] RYABTSEV, S., ZIBROV, M., GASPARYAN, Y., et al. Nucl. Instrum. Methods Phys. Res. B, **382** (2016) 101.

[9] ZIBROV, M., RYABTSEV, S., GASPARYAN, Y., PISAREV, A. Physics Procedia, **71** (2015) 83.

[10] ELEVELD, H., VAN VEEN, A., Journal of Nuclear Materials, 212–215, Part B (1994) 1421.

[11] RYABTSEV, S., ZIBROV, M., GASPARYAN, Y., PISAREV, A. Journal of Surface Investigation. X-ray, Synchrotron and Neutron Techniques **10** (2016), 658.

[12] FRANSENS, J.R., KERIEM, M.S.A.E., PLEITER, F., Journal of Physics: Condensed Matter, **3** (1991) 9871.

[13] YOU, Y.-W., KONG, X.-S., WU, X.-B., et al., AIP Advances **3** (2013) 012118.

[14] HEINOLA, K., AHLGREN, T., NORDLUND, K., KEINONEN, J., Physical Review B, **82** (2010) 094102.

[15] JOHNSON, D.F., CARTER, E.A., Journal of Materials Research, **25** (2010) 315-327.

[16] POON, M., HAASZ, A.A., DAVIS, J.W., Journal of Nuclear Materials, **374** (2008) 390-402.

[17] OGORODNIKOVA, O. V., J. Appl. Phys, **118** (2015) 074902.

[18] OGORODNIKOVA, O.V., SUGIYAMA, K., J. Nucl. Mater. **442** (2013) 518.

[19] TYBURSKA, B., ALIMOV, V.KH., OGORODNIKOVA, O.V., et al., Journal of Nuclear Materials, **395** (2009) 150.
[20] ALIMOV, V.KH., HATANO, Y., SUGIYAMA, K., et al. Journal of Nuclear Materials **438** (2013) S959–S962.
[21] MARKELJ, S., OGORODNIKOVA, O.V., PELICON, P., et al., J. Nucl. Mater. **438** (2013) S1027.
[22] OGORODNIKOVA, O.V., GASPARYAN, Y., EFIMOV, V., et al., Journal of Nuclear Materials, **451** (2014) 379–386.
[23] CIUPIŃSKI, L., OGORODNIKOVA, O.V., PŁOCIŃSKI, T., et al. Nucl. Instr. & Meth. in Phys. Res. B., **317** (2013) 159–164.
[24] OGORODNIKOVA, O.V., TYBURSKA, B., ALIMOV, V.Kh., ERTL, K., Journal of Nuclear Materials, **415** (2011) S661.
[25] OGORODNIKOVA, O.V., MARKELJ, S., VON TOUSSAINT, U. Journal of Applied Physics, **119** (2016) 054901.
[26] GASPARYAN, Y., OGORODNIKOVA, O.V., EFIMOV, V., et al. J. Nucl. Mater., **463** (2015) 1013.
[27] WILSON, W. D., BISSON, C. L.. Radiation Effects, **19** (1973) 53.
[28] KORNELSEN, E.V., VAN GORKUM, A.A., J. Nucl. Mater., **92** (1980) 79.
[29] Y. GASPARYAN et al., in preparation.

DEFECT-HYDROGEN ISOTOPE INTERACTIONS IN NEUTRON-IRRADIATED TUNGSTEN, AND EFFECTS OF ALLOYING ELEMENTS AND CRYSTAL ORIENTATION ON DEFECT FORMATION UNDER SURROGATE IRRADIATIONS

Y. HATANO[1], T. TOYAMA[2], H. T. LEE[3], Y. UEDA[3], Y. OYA[4], M. YAJIMA[5], N. OHNO[6]

[1]Hydrogen Isotope Research Center, University of Toyama
Toyama, 930-8555, Japan

[2]Institute for Materials Research, Tohoku University,
Ibaraki, 311-1313, Japan

[3]Graduate School of Engineering, Osaka University
Osaka, 565-0871, Japan

[4]Collage of Science, Shizuoka University
Shizuoka,

[5]National Institute for Fusion Science
Gifu, 509-5292, Japan

[6]Graduate School of Engineering, Nagoya University
Aichi, 464-8603, Japan

Abstract

In this study, trapping and transport of hydrogen isotope were examined for tungsten (W) specimens irradiated with neutrons in a fission reactor. In addition, the effects of rhenium (Re) on defect accumulation and the influence of crystal orientation on displacement threshold energy were studied using surrogate irradiation with high energy heavy ions and electrons. The contents of this report are the following.

- Positron annihilation spectroscopy study on defect-hydrogen isotope interactions in neutron-irradiated W;
- Kinetics of hydrogen isotope penetration into neutron-irradiated W;
- Effects of Re addition on hydrogen isotope retention in W after damaging with heavy ions; and
- Crystal orientation dependence of displacement damage in W.

1. INTRODUCTION

Tritium (T) retention in plasma-facing materials (PFMs) and consequent accumulation of T in a vacuum vessel are important issues for safety assessment of a future fusion reactor and T economy in it. Tungsten (W) is currently recognized as a leading candidate of a PFM. During the service as a PFM, W will be exposed to plasma of deuterium (D) , tritium (T) and helium (He) ions and irradiated with high energy (14 MeV) neutrons produced by fusion reactions. The high energy neutrons induce displacement damage in W throughout the bulk, and variety of defects are formed.

The effects of neutron-induced defects on hydrogen isotope retention in W was firstly investigated in the Japan-US Fusion Research Collaboration TITAN Project Task 2–1 (2007–2012) [1–8]. In this project, W disks were irradiated with neutrons in a fission reactor called High Flux Isotope Reactor (HFIR) at Oak Ridge National Laboratory at around 50 °C and then exposed to D plasma in a linear plasma device called Tritium Plasma Experiment (TPE) at Idaho National Laboratory at 100–500 °C. Nuclear reaction analysis (NRA) and thermal desorption measurements performed after the plasma exposure showed orders-of-magnitude increase in D retention by neutron irradiation. Thermal desorption of D from neutron irradiated W continued to very high temperature (~ 900 °C) in comparison with non-irradiated specimen. The D release at high temperature indicated presence of strong traps, and the analysis of desorption curve showed the binding energy between D atom and trap site is ~1.8 eV in average [6]. However, types of radiation-induced defects playing dominant roles in trapping were not identified, and the effects of neutron irradiation at higher temperature were not clarified.

The influence of neutron irradiation at elevated temperatures (500–1200 °C) on microstructures, mechanical properties and hydrogen isotope retention of W and W alloys has been investigated in the subsequent Japan-US Fusion Research Collaboration PHENIX Project [9,10]. In parallel, a new linear plasma device called Compact Divetor Plasma Simulator (CDPS) was installed in a radiation-controlled area of International Research Center for Nuclear Materials Science, Institute for Materials Research (IMR-Oarai), Tohoku University [11]. The measurements of D retention in neutron-irradiated W and defect characterization by positron annihilation spectroscopy have been started.

In this CRP report, Japanese activities on hydrogen isotope behavior in neutron-irradiated W are described in two chapters; this chapter and the one summarized by M. Shimada. The former present Japanese domestic activities including research in IMR-Oarai, and the latter reports the accomplishments of Japan-US Fusion Research Collaboration PHENIX Project.

The contents of this chapter are as follows:

1. Introduction
2. Positron annihilation spectroscopy study on defect-hydrogen isotope interactions in neutron-irradiated W [12];
3. Kinetics of hydrogen isotope penetration into neutron-irradiated W [11];
4. Effects of Re addition on hydrogen isotope retention in W after damaging with heavy ions [13];
5. Crystal orientation dependence of displacement damage in W; and
6. Summary

2. POSITRON ANNIHILATION SPECTROSCOPY STUDY ON DEFECT-HYDROGEN ISOTOPE INTERACTIONS [12]

Positron annihilation spectroscopy (PAS) is a powerful tool to characterize defects having open volume such as vacancies and vacancy clusters. Defect formed in W by electron and ion irradiations and hydrogen isotope trapping at those defects have been examined by angular correlation of annihilation radiation [14] and Doppler broadening spectroscopy [15,16]. However, interactions of hydrogen isotopes with neutron-induced defects in W have not been examined. In this study, size of vacancy type defect induced by neutron irradiation in W and D trapping at the defect were examined by positron lifetime measurement. In addition, positron annihilation with electron of D was directly confirmed by coincidence Doppler broadening spectroscopy.

The specimens used were disks of pure W (99.99% purity, 3 mm diameter and 0.2 mm thickness) prepared from a rod supplied by A. L. M. T. Co., Japan. After polishing into mirror-like finish, the specimens were heated in a vacuum for 0.5 h at 1300 °C to remove stress possibly induced during polishing. Then, the specimens were irradiated with neutrons in HFIR under the framework of TITAN Project at ~300 °C for 48 h and shipped to IMR-Oarai after sufficient reduction of radioactivity. The irradiation dose corresponded to ~0.3 displacement per atom (dpa). The surfaces of irradiated specimens were cleaned by immersing into NaOH aqueous solution. Positron lifetime t_L and Doppler broadening of annihilation γ-rays were examined before and after heating these specimens in D_2 gas at 0.1 MPa and 300 °C for 100–300 h. The specimens subjected to similar heat treatments but in a vacuum were also examined for comparison.

Results of t_L measurements are summarized in Figure 1. The average lifetime, $t_{L,ave}$, for non-irradiated specimen was 118 ps and this corresponds to positron annihilation in the bulk of W. Neutron irradiation resulted in increase in $t_{L,ave}$, to 332 ps. Analysis of positron lifetime spectra showed presence of two components. The value of t_L for a short-life component was 268 ps and that for long-life component was 453 ps. According to Troev et al. [17], the former corresponds to the annihilation at a cluster of 6 vacancies (V_6) and the latter to the annihilation at a vacancy cluster larger than V_{37}. It is clear that neutron irradiation at 300 °C resulted in the formation of vacancy and relatively large vacancy clusters. No significant change was observed in positron lifetime spectra after heat treatment at 300 °C in vacuum for 100 h. This is because the specimen was already kept at 300 °C for 48 h during neutron irradiation. On the other hand, significant reduction in positron lifetime was observed after heat treatment under D_2 gas atmosphere. The reduction in positron lifetime was ascribed to deuterium trapping at vacancy-type defect and consequent increase in electron density in that defect. This change in positron lifetime due to D uptake is the direct evidence of hydrogen isotope trapping in vacancy-type defect. Note that both short-life and long-life components decreased after exposure to D_2 gas. This means both small and large vacancy clusters acted as traps against D.

Figure 2 shows the ratio curves to non-irradiated W obtained by coincidence Doppler broadening spectroscopy. After neutron irradiation, the intensity in a low momentum region ($< 4.3\times10^{-3}\ m_0c$ where m_0 is the rest mass of electron/positron and c is the speed of light) increased, while that at a high momentum region decreased. This change was attributed to increase in annihilation probability with valence electrons in vacancy and vacancy clusters. After exposure to D_2 gas, significant decrease in the ratio was observed in the low momentum region together with clear increase in the high momentum region. The change indicates annihilation of positrons with deuterium electrons. In other words, the observed change in the ratio curve is also the evidence of hydrogen isotope trapping at vacancy-type clusters.

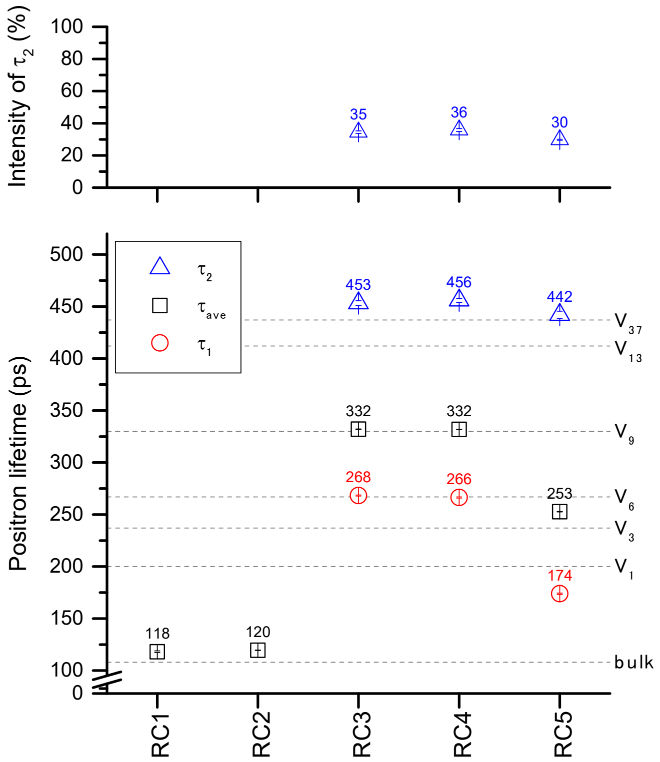

FIG. 1. Results of positron lifetime measurements. RC1: non-irradiated, RC2: RC1 was annealed in D_2 gas at 300 °C, RC3: RC1 was neutron-irradiated at ~300 °C to dose of ~0.3 dpa, RC4: RC3 was annealed in vacuum at 300 °C, RC5: RC3 was annealed in D_2 gas at 300 °C. This figure was reproduced courtesy of Elsevier [4406771259502] from [12] T. Toyama et al., Deuterium trapping at vacancy clusters in electron/neutron-irradiated tungsten studied by positron annihilation spectroscopy, J. Nucl. Mater., 499 (2018) 464.

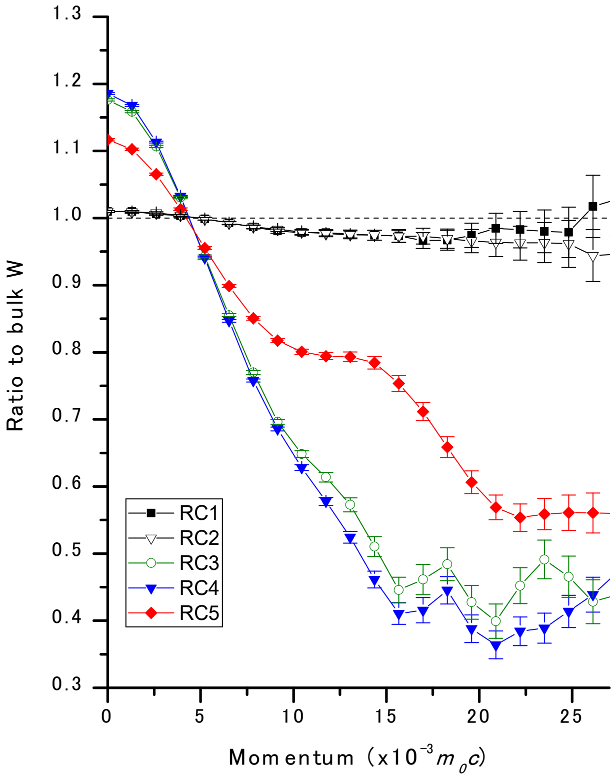

FIG. 2. Ratio curves of coincidence Doppler broadening measurements (ratio to well-annealed pure W). RC1: non-irradiated, RC2: RC1 was annealed in D_2 gas at 300 °C, RC3: RC1 was neutron-irradiated at ~300 °C to dose of ~0.3 dpa, RC4: RC3 was annealed in vacuum at 300 °C, RC5: RC3 was annealed in D_2 gas at 300 °C. m_0 is the rest mass of electron/positron and c is the speed of light. This figure was reproduced courtesy of Elsevier [4406771259502] from [12] T. Toyama et al., Deuterium trapping at vacancy clusters in electron/neutron-irradiated tungsten studied by positron annihilation spectroscopy, J. Nucl. Mater., 499 (2018) 464.

3. KINETICS OF HYDROGEN ISOTOPE PENETRATION INTO NEUTRON-IRRADIATED TUNGSTEN

Neutron irradiation induces defect almost uniformly throughout the bulk of plasma-facing components (PFCs) in contrast to ion irradiation which generally produces defect only in a shallow region near a specimen surface. Therefore, hydrogen isotope transport in neutron-irradiated W occurs via long-distance diffusion under trapping effects. Consequently, it takes many hours for neutron-irradiated W to get saturated with hydrogen isotopes even under exposure to high flux plasma, and the retention of hydrogen isotopes in neutron-irradiated W has long transient time. The understanding of kinetics of hydrogen isotope penetration into neutron-irradiated W is important for evaluation of in-vessel tritium inventory in pulsed-operation fusion devices. In this study, the penetration kinetics of D into neutron-irradiated W was examined by exposing irradiated specimens to D plasma using CDPS [11] at 290 °C for 25, 100, 400 min and measuring the retention by thermal desorption spectroscopy (TDS).

Disk-type specimens (6 mm diameter and 0.5 mm thickness) prepared from a rod of pure W (99.99 mass%, A.L.M.T. Co., Japan) were polished into mirror-like finish and annealed in a vacuum (10^{-6} Pa) at 900 °C for 1 h. Then, the specimens were irradiated with neutrons to 0.06 dpa at 290 °C in the Belgian Reactor 2 (BR2) at the Belgian Nuclear Research Centre. After shipping the specimens to

IMR-Oarai, the surfaces of samples were electro-polished to remove impurities and oxide layers formed during neutron irradiation and post-irradiation handling. The polished specimens were exposed to D plasma at the flux and incident energy of 5.4×10^{21} $m^{-2}s^{-1}$ and 100 eV, respectively. The D retention was measured using TDS at a temperature ramp rate of 0.5 °C s^{-1}.

The correlation between D retention and plasma exposure time is shown in Figure 3. It is clear that the retention is in proportional to the square root of plasma exposure time. Such variation of retention with exposure time can be explained as follows.

Neutron irradiation induces defect uniformly throughout the bulk of specimen, as previously mentioned. The defect induced by neutron irradiation acts as a strong trap against hydrogen isotope atom, and the binding energy between D atom with defect is reported to be as high as 1.8 eV [6]. Therefore, D atom entering the specimen immediately gets trapped if it meets an unoccupied trap. Under such conditions, relatively clear interface is formed between the near-surface region where the majority of traps are occupied with D and the deeper region where the majority of traps are empty, as proposed in [18] and experimentally observed for ion-irradiated W in [19] (see Figure 1 in [19]). The rate of inward movement of this interface, $\mathrm{d}x/\mathrm{d}t_{\mathrm{exp}}$ [m s^{-1}] where x is the thickness of the near-surface region where the majority of traps are occupied [m] and t_{exp} is the exposure time [s], is determined by the diffusion rate of mobile D atoms (D atoms in a solid solution state), as shown in Figure 4. Namely,

$$\frac{\mathrm{d}x}{\mathrm{d}t}N_{\mathrm{t}} = D\frac{C_0}{x},$$

where N_{t} is trap density [m^{-3}], D is the diffusivity, and C_0 is the concentration of mobile D in the sub-surface region which is determined by the balance of incident flux and the rate constant for D reemission. Therefore,

$$x = \sqrt{\frac{2DC_0t_{\mathrm{exp}}}{N_{\mathrm{t}}}}. \text{ [18]}$$

Because the probability of trap occupancy is almost unity in the region shallower than the interface, the retention of D is expressed as xN_{t}. Therefore, the retention is proportional the square root of t_{exp}, as observed in Figure 3.

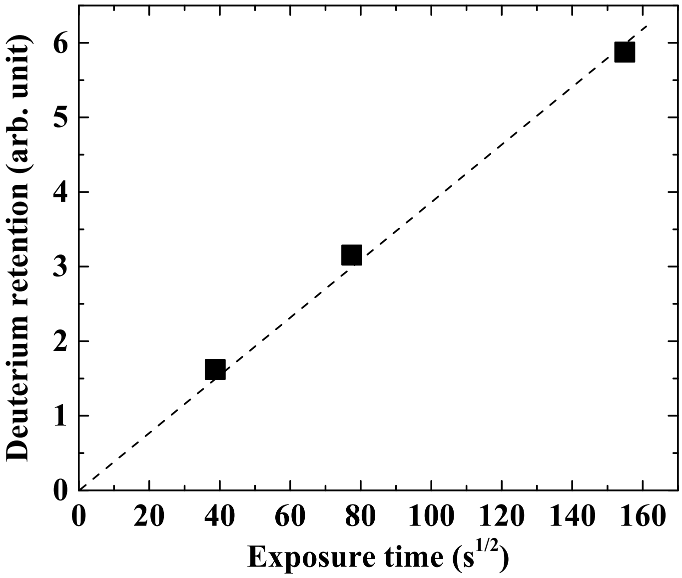

FIG. 3. Correlation between plasma exposure time and deuterium retention in neutron-irradiated tungsten after exposure to deuterium plasma at 290 °C.

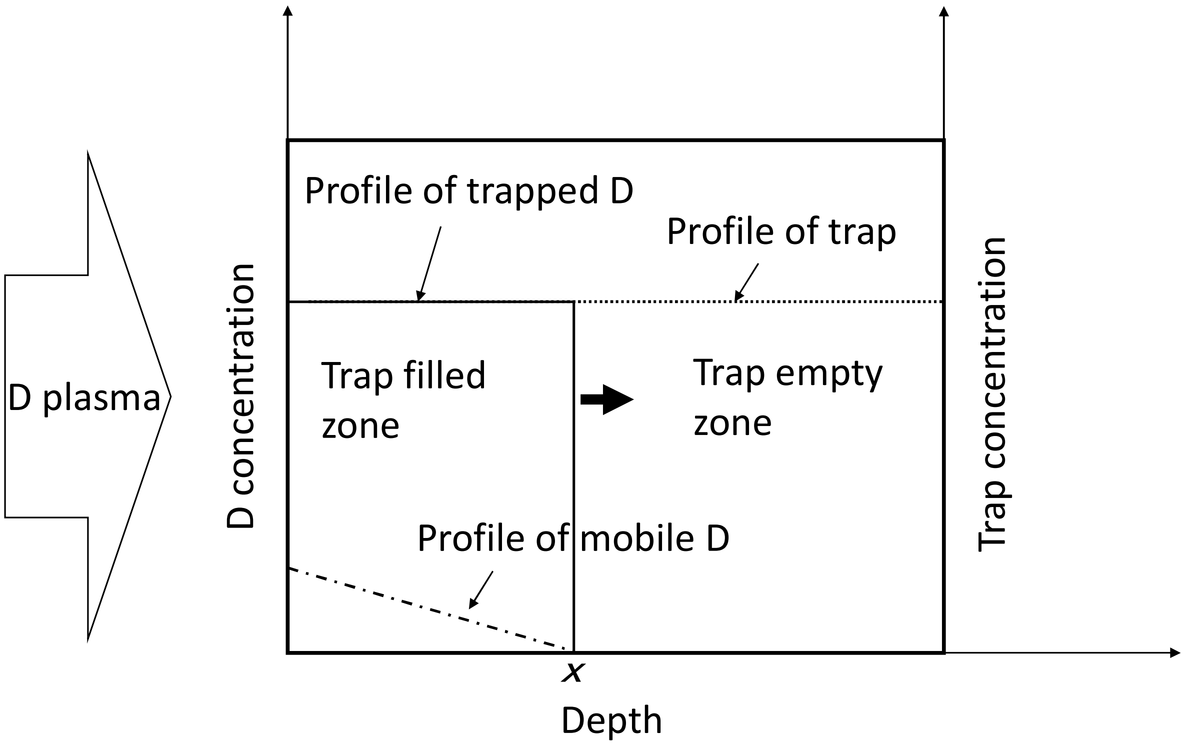

FIG. 4. Schematic description of depth profiles of mobile and trapped deuterium atoms in neutron-irradiated tungsten under exposure to deuterium plasma.

4. EFFECTS OF RHNIUM ADDITION ON HYDROGEN ISOTOPE RETENTION IN TUNGSTEN AFTER DAMAGING WITH HEAVY IONS AT ELEVATED TEMPERATURES [13]

Neutron irradiation of W results in formation of Re and Os through nuclear transmutation. Tanno et al. [20] and Fukuda et al. [21,22] reported that formation of voids during neutron irradiation is strongly suppressed by addition of Re in W before irradiation and formation of Re in W during irradiation. Such modification of defect structure should influence on hydrogen isotope retention. In this study, the synergetic effects of Re addition and high temperature irradiation were examined by irradiating W and W-5%Re specimens with 6.4 MeV Fe ions at 250–1000 °C [13].

The specimens were 1 mm thick warm-rolled W plate (99.95 mass% purity, Goodfellow Cambridge Ltd, UK) and 0.5 mm thick warm-rolled W-5%Re alloy plate (99.99 mass% purity, A.L.M.T. Co., Japan). After polishing the surfaces to mirror-like finish, the specimens were annealed in a vacuum (10^{-5} Pa) at 950 °C for 1 h to relieve stresses possibly induced in the polishing process. These specimens were irradiated with 6.4 MeV Fe ions at temperatures of 250, 500, 800, and 1000 °C to the fluence of 3.2×10^{18} Fe/m^2 in the accelerator DuET, Kyoto University. The damage profile evaluated using the program SRIM 2008.03 [23] indicated that the damage level reached 0.5 dpa at the Bragg peak located at a depth of 1.2 μm. Some specimens irradiated at 250 °C were subjected to post-irradiation annealing in a vacuum (10^{-5} Pa) at 800 °C for 1 h; this duration of annealing was comparable with the time period of the Fe ion irradiation. Then the specimens were exposed to D_2 gas at 400 °C and 0.1 MPa for 10 h to fill radiation-induced defects with D.

The depth profiles of D in the damaged specimens were evaluated using NRA at the Max-Planck-Institut für Plasmaphysik. The details of analysis were described elsewhere [13]. After the NRA measurements, the D retention in W and W-5%Re specimens irradiated with Fe ions at 800 °C was examined using TDS at the IFERC, Japan Atomic Energy Agency (presently National Institute for Quantum and Radiological Science and Technology). The temperature ramp rate was set to be 0.5 °C s^{-1}. The specimens irradiated at 1000 °C were subjected to positron lifetime measurement in IMR-Oarai.

Figure 5 shows depth profiles of D in the irradiated W and W-5%Re specimens. The concentration of D was high in the near-surface region up to the depth of ~2 μm, indicating the trapping of D at radiation-induced defects. The concentration of trapped D, $C_{\text{D-trap}}$, decreased as the irradiation temperature, $T_{\text{Fe-irr}}$, increased. The correlation between $C_{\text{D-trap}}$ at the damage peak and $T_{\text{Fe-irr}}$ is shown in Figure 6. The value of $C_{\text{D-trap}}$ in W-5%Re was comparable with that in W after irradiation at 250 °C. $C_{\text{D-trap}}$ in both materials decreased with increasing $T_{\text{Fe-irr}}$, but far stronger reduction was observed for W-5%Re than W; $C_{\text{D-trap}}$ in W-5%Re at $T_{\text{Fe-irr}} = 1000$ °C was 1/180 of that at $T_{\text{Fe-irr}} = 250$ °C, while $C_{\text{D-trap}}$ in W at $T_{\text{Fe-irr}} = 1000$ °C was smaller than that at $T_{\text{Fe-irr}} = 250$ °C just by a factor of 3. The difference observed for W between $T_{\text{Fe-irr}} = 250$ and 1000 °C (a factor of 3) was comparable with that observed in [24]. This figure shows also the values of $C_{\text{D-trap}}$ in the W and W-5%Re specimens subjected to the post-irradiation annealing at 800 °C after the irradiation at 250 °C. As reported in [24], the value of $C_{\text{D-trap}}$ in W specimen after the irradiation at 800 °C was slightly lower (by a factor of 2) than that after the post-irradiation annealing at 800 °C. On the other hand, the W-5%Re specimens showed far larger difference between dynamic annealing during the irradiation and post-irradiation annealing; $C_{\text{D-trap}}$ after the irradiation at 800 °C was lower than that after the post-irradiation annealing by a factor of 50.

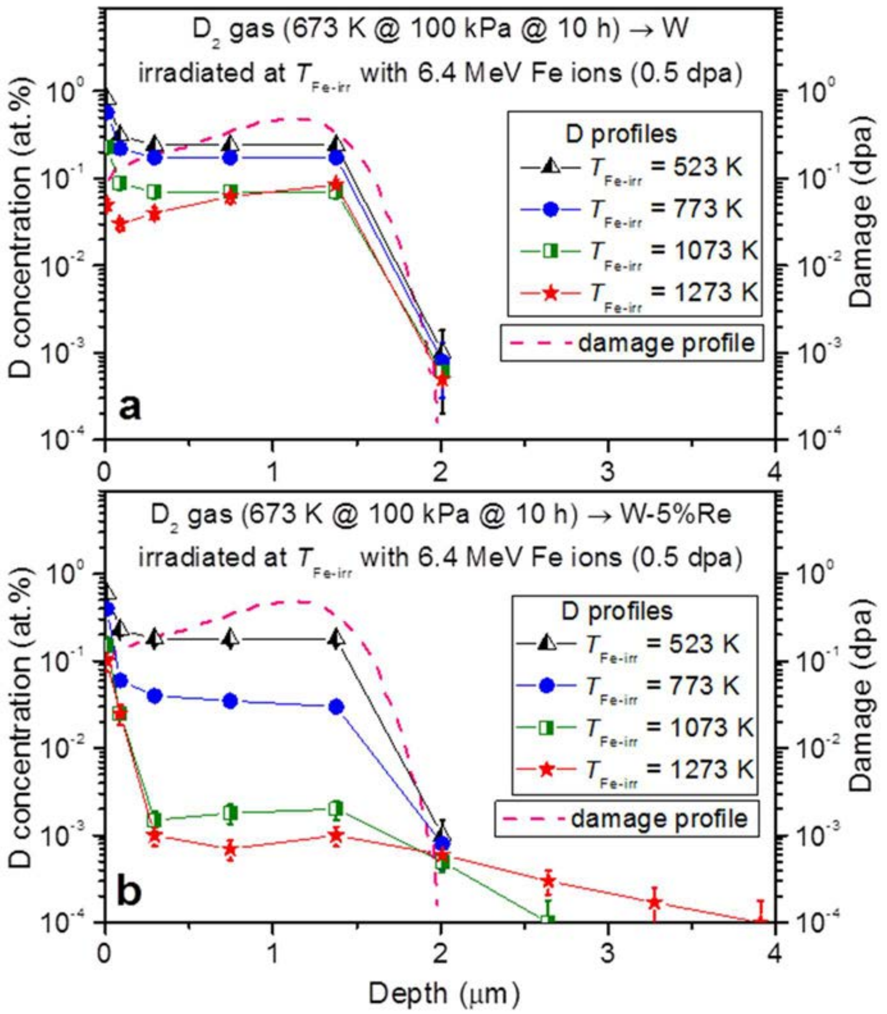

FIG. 5. Depth profiles of D retained in W (a) and W-5%Re (b) irradiated at various temperatures with 6.4 MeV Fe ions to the peak damaged level of 0.5 dpa and then exposed to D_2 gas at temperature of 400 °C and pressure of 0.1 MPa for 10 h. Temperatures of irradiation with 6.4 MeV Fe ions, $T_{Fe\text{-}irr}$, are indicated in the legends. In both panels, a calculated damage depth profile is also shown. This figure was reproduced courtesy of Elsevier [4406780298729] from [13] Y. Hatano et al., Deuterium retention in W and W-Re alloy irradiated with high energy Fe and W ions: Effects of irradiation temperature, Nucl. Mater. Energy, ***9*** *(2016) 93.*

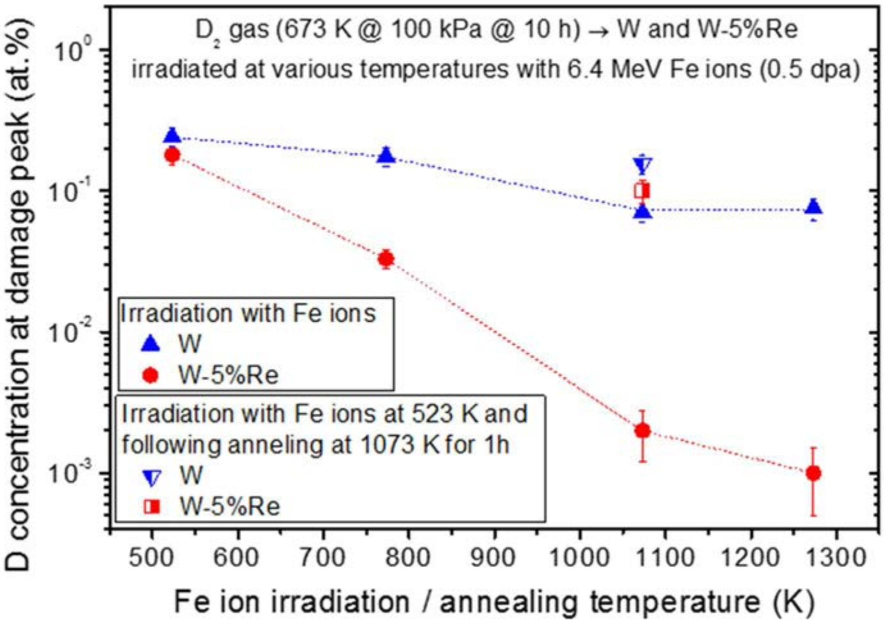

FIG. 6. Concentration of deuterium at a depth of the damage peak in W and W-5%Re irradiated at various temperatures with 6.4 MeV Fe ions to the peak damage level of 0.5 dpa and then exposed to D_2 gas at a temperature of 400 °C and a pressure of 0.1 MPa for 10 h, as a function of Fe ion irradiation temperature. Additionally, the D concentration at the damage peak in W and W-5%Re, initially irradiated at 250 °C with 6.4 MeV Fe ions to the peak damage level of 0.5 dpa and then annealed in vacuum at 800 °C for 1 h, after D_2 gas exposure under the same exposure conditions is shown. This figure was reproduced courtesy of Elsevier [4406780298729] from [13] Y. Hatano et al., Deuterium retention in W and W-Re alloy irradiated with high energy Fe and W ions: Effects of irradiation temperature, Nucl. Mater. Energy, ***9*** *(2016) 93.*

TDS spectra of D released from the W and W-5%Re specimens irradiated at 800 °C are shown in Figure 7. A broad desorption peak at 430-700 °C was observed for both specimens. The values of D retention in the W specimen evaluated using the NRA and TDS techniques were $(7\pm1)\times10^{19}$ D/m^2 (NRA) and $(2\pm1)\times10^{19}$ D/m^2 (TDS), whereas for the W-5%Re specimen these values were $(6\pm2)\times10^{18}$ D/m^2 (NRA) and $(4\pm2)\times10^{18}$ D/m^2 (TDS). The TDS measurements were performed about 3 months after the NRA measurements, and hence desorption of D at weak traps was possible before the TDS measurements.

The values of positron lifetime in W and W-5%Re specimens before irradiation were 133.9±0.5 and 137.7±0.5 ps, respectively. Troev et al. [17] has reported the positron lifetime in W matrix is 108 ps and that in a monovacancy is 200 ps. The values of positron lifetime observed before irradiation seem to be average values determined by the matrix of W and intrinsic defects such as dislocations and vacancies induced during fabrication processes at relatively low concentrations. After the irradiation of W to 0.5 dpa at 1000 °C, the lifetime spectrum was fitted well using two components, 125±1 ps and 470±20 ps; the average lifetime was 168.0±0.5 ps. The value for the short-life component (125±1 ps) is close to the positron lifetime in the non-irradiated specimens, while that for long-life component (470±20 ps) corresponds to relatively large vacancy clusters. According to Troev et al. [17], the positron lifetime in the cluster of 37 vacancies is 437 ps; The irradiated W specimen appears to contain vacancy clusters larger than V_{37}. In contrast, the W-5%Re specimen showed no significant increase in positron lifetime after the irradiation under the same conditions; the positron lifetime in the W-5%Re specimen irradiated at 1000 °C was 138.9±0.5 ps. These observations suggest that Re significantly suppressed the accumulation of vacancy clusters. According to Tanno et al. [20] and Fukuda et al. [21,22] who observed microstructures of W and W-Re alloys with a transmission electron microscopy (TEM) after neutron irradiation at elevated temperatures, the void concentration in W-Re alloys was significantly lower than that in W, while the former contains precipitates consisting of W and Re. Our results of positron lifetime measurements were consistent with their observations. As previously mentioned, the positron lifetime in a monovacancy is 200 ps [17] and significantly longer than that in the matrix of W-5%Re. Negligible increase in positron lifetime after the irradiation at 1000 °C indicates that Re suppressed also the accumulation of monovacancies.

As described above, the W and W-5%Re specimens irradiated with Fe ions at different temperatures were exposed to D_2 gas under the same conditions (400 °C and 0.1 MPa). The TDS spectra in Figure 7 showed the main peaks for W and W-5%Re in the same temperature range, indicating that the binding energy of D atom and a trap is comparable between W and W-5%Re. In addition, according to Benamati [25] et al., the permeability values of H and D through W and W-5%Re were comparable with each other. It is therefore appropriate to consider that the solubility of D in W and W-5%Re are also comparable with each other, as well as the diffusivity. Therefore, solely the difference in the concentration of trap sites can explain the far lower $C_{\text{D-trap}}$ in W-5%Re than in W after the irradiation at high temperatures. In other words, lower $C_{\text{D-trap}}$ was due to lower concentration of radiation-induced defects acting as trapping sites. The positron lifetime measurements indicated the significantly lower concentration of vacancy-type defects (monovacancies and vacancy clusters) in W-5%Re than in W after the irradiation at 1000 °C. It was therefore concluded that vacancy-type defects played dominant roles in D trapping after high temperature irradiation and the significantly reduced D retention observed for W-5%Re was due to suppressed accumulation of vacancy-type defects during high temperature irradiation.

Suzudo et al. [26,27] reported that Re atom in W forms a mixed dumbbell with an interstitial W atom. The rotation energy barrier of the W–Re dumbbell is so low that Re interstitials have 3-dimensional motion instead of the 1-dimensional motion of W self-interstitial atoms, and the interstitials with 3-dimensional motion have a greater probability for recombination with vacancy [26,27]. The mechanism proposed by Suzudo et al. [26,27] is applicable also for the case of this study.

The post-irradiation annealing of W-5%Re specimen at 800 °C after the irradiation at 250 °C resulted in far high $C_{\text{D-trap}}$ in comparison with the irradiation at 500–1000 °C. This observation indicates that dynamic annealing under irradiation plays a critical role in the reduction of concentrations of vacancy-type defects by Re addition. Further investigation is necessary to understand the detailed mechanisms underlying the enhanced recovery of vacancy-type defects by Re addition under dynamic annealing.

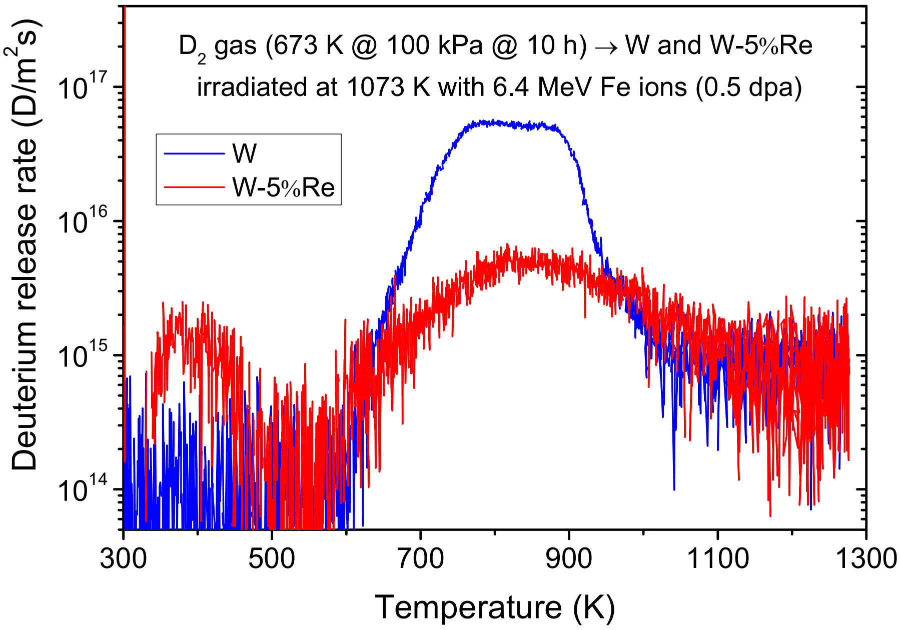

FIG. 7. Thermal desorption spectra of deuterium for W and W-5%Re irradiated at 800 °C with 6.4 MeV Fe ions to the peak damaged level of 0.5 dpa and then exposed to D_2 gas at a temperature of 400 °C and a pressure of 0.1 MPa for 10 h. This figure was reproduced courtesy of Elsevier

[4406780298729] from [13] Y. Hatano et al., Deuterium retention in W and W-Re alloy irradiated with high energy Fe and W ions: Effects of irradiation temperature, Nucl. Mater. Energy, ***9*** *(2016) 93.*

5. CRYSTAL ORIENTATION DEPENDENCE OF DISPLACEMENT DAMAGE IN TUNGSTEN

The threshold displacement energy (TDE) is the minimum kinetic energy needed to permanently displace an atom from its lattice site. It is one of the most basic parameters in radiation damage studies and used in all radiation damage models to calculate a dpa value. The TDE is crystal orientation dependent and density functional theory (DFT) and molecular dynamics (MD) simulations have recently calculated such anisotropic values for W [28]. In any collision, the energy and momentum transfer from a primary knock-on atom is not limited to a single crystallographic direction. Therefore in experiments, the concept of a threshold surface [29] is invoked to approximate the orientation dependent TDEs. The standard experimental method for the determination of threshold surfaces in metals is by electron irradiation and subsequent observation of the resulting radiation damage. For W, the most cited experimental work is by Maury et al. [30]. They first damaged W using a high-voltage electron microscope (HVEM), and monitored the resulting damage and annealing *in-situ* by residual electrical resistivity measurements. Due to the relative thick specimens used (10–30 μm), the energy straggling of the incoming electrons is not negligible. In this respect, direct observation of defect clusters using a HVEM using thinner specimens can be advantageous for determining TDEs [31] (i.e. microscopy). Here, the point defects created during electron irradiation migrate and agglomerate into clusters large enough to give sufficient contrast for imaging. While defect evolution in W at low [32] and high [33] temperatures has been reported following 2 MeV electron irradiation, no systematic microscopy study on the crystal orientation dependence on the threshold displacement energy exist to date. To fill this gap, we have performed *in-situ* microscopy experiments with W with the observation axis along the [110] and [100] orientation using the HVEM at Osaka University. In this study, we focused on the qualitative aspects of the observed radiation damage to estimate the threshold displacement energy as a function of crystal orientation. Our approach is to confirm the generation of Frenkel pairs by observation of point defect clusters in the microscopic image as a function of crystal orientation, temperature, and accelerating voltages.

Figure 8 shows TEM images at room temperature under 2.0 MeV irradiation as function of total irradiation time, *t*. The observation axis was approximately along the [110] and [100] direction. The diffraction patterns are shown in the first column. The formation of point-defect clusters can be clearly identified as black dots indicated by the white arrows for both crystal orientations. These point-defect clusters likely correspond to coalesced W self-interstitial atoms and/or dislocation loops. The point-defect clusters are mainly visible in the periphery of the irradiated spot at this temperature. The absence of point defect clusters in the center likely indicates loss by point-defect reactions and/or transport. The dynamics of W self-interstitial atoms and coalesced dislocation loops have been studied by Amino et al. [34] and Swinburne et al. [35], respectively. Incorporating their findings in a quantitative treatment is out of scope of the present study. It is anticipated however that numerous processes like mutual annihilation, annihilation at the surfaces, interaction with impurity atoms, defect absorption at internal sinks, and diffusion will affect the surviving point-defect clusters. Whatever the exact mechanism(s), it can be seen that the point-defect clusters are observed throughout the measurement time suggesting continuous creation of point defects. From such observations, we conclude the threshold displacement energy must be <71 eV for both (100) and (110) orientations. The value for (110) orientation is in good agreement with 75±5 eV as reported by Maury et al. [30]. Our values should be considered as upper limits since it is known that if the temperature is too high and/or the specimen is too thin, an apparent threshold displacement energy is measured which can be considerably higher than the real value. No point defect-clusters were visible at 1.5 MeV irradiation for both orientations (images not shown).

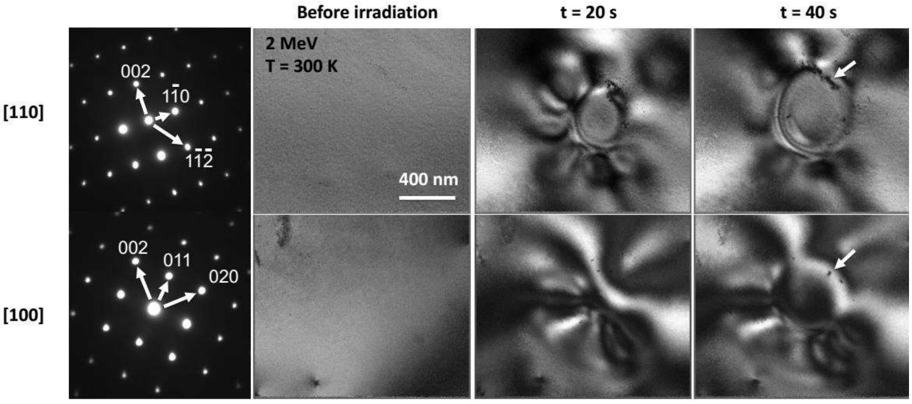

FIG. 8. TEM images showing the presence and evolution of defect clusters produced by 2.0 MeV electron irradiation at 300 K. The observation axis is approximately along [110] and [100]. Defect clusters are seen as black dots as indicated by white arrows. The diffraction patterns are shown in the first column.

6. SUMMARY

Neutron irradiation of W in a fission reactor at elevated temperature (300 °C) resulted in formation of vacancy clusters with a variety of sizes. Deuterium trapping at small and large vacancy clusters were directly confirmed by the reduction in positron lifetime and the change in ratio curves obtained by coincidence Doppler broadening measurements. The retention in neutron-irradiated W under D plasma exposure increased in proportional to the square root of exposure time, as the result of long-range transport in the bulk of irradiated W under the strong trapping effects of neutron-induced defects. The addition of Re into W as an alloying element led to significant reduction in the trap density after the irradiation of high energy Fe ions at high temperatures (≥ 500 °C). Confirmation of this preferable effects of Re by neutron irradiation is necessary. The irradiation of high energy electrons at different crystal orientation of W showed that the threshold displacement energy must be <71 eV for both (100) and (110) orientations.

ACKNOWLEDGEMENTS

This work was supported by JSPS KAKENHI Grant Number JP18H03688 and JP15K18309, NIFS LHD Project (NIFS13KOBF026) and Network-type Collaboration Project (NIFS17KNWF003). A part of this work was performed under the Inter-university Cooperative Research Program of the Institute for Materials Research, Tohoku University (Proposal No. 18M0022 and 18M0027) and Joint Usage/Research Program on Zero-Emission Energy Research, Institute of Advanced Energy, Kyoto University (ZE30A-16). The authors would like to express their sincere thanks to Professors T. Hinoki and S. Kondo at Kyoto University, Japan, for their support in Fe ion irradiation, Dr. K. Sugiyama at Max-Planck-Institut für Plasmaphysik, Germany, for his help in NRA measurements, Drs. M. Oyaidzu and T. Hayashi at QST, Japan, for their help in TDS analysis, Dr. T. Kuwabara and Mr. M. Takagi at Nagoya University, Japan, for their contributions to CDPS construction and operation, and Professors T. Nagase, H. Yasuda and Dr. E. Taguchi at Research Center for Ultra-high Voltage Electron Microscopy, Osaka University for their support with the UHVEM experiments.

Parts of this article are reprinted from the *Journal of Nuclear Materials* **499**, 464 (2018) and *Nuclear Materials and Energy* **9**, 93 (2016) with permission from Elsevier [444527133677, 4445280021311].

REFERENCES

[1] SHIMADA, M., HATANO, Y., CALDERONI, P., ODA, T., OYA, Y., SOKOLOV, M., ZHANG, K., CAO, G., KOLASINSKI, R., SHARPE, J. P., First result of deuterium retention in neutron-irradiated tungsten exposed to high flux plasma in TPE, J. Nucl. Mater., **415** (2011) S667.

[2] SHIMADA, M., CAO, G., HATANO, Y., ODA, T., OYA, Y., HARA, M., CALDERONI, P., The deuterium depth profile in neutron-irradiated tungsten exposed to plasma, Phys. Scr., **T145** (2011) 014051.

[3] OYA, Y., SHIMADA, M., KOBAYASHI, M., ODA, T., HARA, M., WATANABE, H., HATANO, Y., CALDERONI, P., OKUNO, K., Comparison of deuterium retention for ion-irradiated and neutron-irradiated tungsten, Phys. Scr., **T145** (2011) 014050.

[4] SHIMADA, M., HATANO, Y., OYA, Y., ODA, T., HARA, M., CAO, G., KOBAYASHI, M., SOKOLOV, M., WATANABE, H., TYBURSKA-PÜSCHEL, B., UEDA, Y., CALDERONI, P., OKUNO, K., Overview of the US–Japan collaborative investigation on hydrogen isotope retention in neutron-irradiated and ion-damaged tungsten, Fusion Eng. Des., **87** (2012) 1166.

[5] HATANO, Y., SHIMADA, M., OTSUKA, T., OYA, Y., ALIMOV, V. Kh., HARA, M., SHI, J., KOBAYASHI, M., ODA, T., CAO, G., OKUNO, K., TANAKA, T., SUGIYAMA, K., ROTH, J., TYBURSKA-PÜSCHEL, B., DORNER, J., YOSHIDA, N., FUTAGAMI, N., WATANABE, H., HATAKEYAMA, M., KURISHITA, H., SOKOLOV, M. A., KATOH, Y., Deuterium trapping at defects created with neutron and ion irradiations in tungsten, Nucl. Fusion, **53** (2013) 073006.

[6] HATANO, Y., SHIMADA, M., ALIMOV, V. Kh., SHI, J., HARA, M., NOZAKI, T., OYA, Y., KOBAYASHI, M., OKUNO, K., ODA, T., CAO, G., YOSHIDA, N., FUTAGAMI, N., SUGIYAMA, K., ROTH, J., TYBURSKA-PÜSCHEL, B., DORNER, J., TAKAGI, I., HATAKEYAMA, M., KURISHITA, H., SOKOLOV, M. A., Trapping of hydrogen isotopes in radiation defects formed in tungsten by neutron and ion irradiations, J. Nucl. Mater., **438** (2013) S114.

[7] HATANO, Y., SHIMADA, M., OYA Y., CAO, G., KOBAYASHI, M., HARA, M., SHI, J., MERRILL, B. J., OKUNO, K., SOKOLOV, M. A., KATOH, Y., Retention of hydrogen isotopes in neutron irradiated tungsten, Mater. Trans., **54** (2013) 437.

[8] SHIMADA, M., CAO, G., OTSUKA, T., HARA, M., KOBAYASHI, M., OYA, Y., HATANO, Y., Irradiation effect on deuterium behaviour in low-dose HFIR neutron-irradiated tungsten, Nucl. Fusion, **55** (2014) 013008.

[9] KATOH, Y., CLARK, D., UEDA, Y., HATANO, Y., YODA, M., SABAU, A. S., YOKOMINE, T., GARRISON, L. M., GERINGER, J. W., HASEGAWA, A., HINOKI, T., SHIMADA, M., BUCHENAUER, D., OYA, Y., MUROGA, T., Progress in the U.S./Japan PHENIX Project for the technological assessment of plasma facing components for DEMO reactors, Fusion Sci. Technol., **72** (2017) 222.

[10] SHIMADA, M., OYA, Y., BUCHENAUER, D. A., HATANO, Y., Hydrogen isotope retention and permeation in neutron-irradiated tungsten and tungsten alloys under PHENIX Collaboration, Fusion Sci. Technol., **72** (2017) 652.

[11] OHNO, N., KUWABARA, T., TAKAGI, M., NISHIMURA, R., YAJIMA, M., SAGARA, A., TOYAMA, T., SUZUKI, K., KURISHITA, H., SHIKAMA, T., HATANO, Y., YOSHIDA, N., Development of a compact divertor plasma simulator for plasma-wall interaction studies on neutron-irradiated materials, Plasma Fusion Res., **12** (2017) 1405040.

[12] TOYAMA, T., AMI, K., INOUE, K., NAGAI, Y., SATO, K., XU, Q., HATANO, Y., Deuterium trapping at vacancy clusters in electron/neutron-irradiated tungsten studied by positron annihilation spectroscopy, J. Nucl. Mater., **499** (2018) 464.

[13] HATANO, Y., AMI, K., ALIMOV, V. Kh., KONDO, S., HINOKI, T., TOYAMA, T., FUKUDA, M., HASEGAWA, A., SUGIYAMA, K., OYA, Y., OYAIDZU, M., HAYASHI, T., Deuterium retention in W and W-Re alloy irradiated with high energy Fe and W ions: Effects of irradiation temperature, Nucl. Mater. Energy, **9** (2016) 93.

[14] ROZING, G. J., WEEBER, A. W., MIJNARENDS, P. E., VAN VEEN, A., DE VRIES, J., SCHUT, H., 2D-ACAR measurements in tungsten with voids decorated with deuterium, Mater. Sci. Forum, **105–110** (1992) 1205.

[15] ELEVELD, H., VAN VEEN, A., Void growth and thermal desorption of deuterium from voids in tungsten, J. Nucl. Mater., **212–215** (1994) 1421.

[16] 'T HOEN, M. H. J., MAYER, M., KLEYN, A. W., SCHUT, H., ZEIJLMANS VAN EMMICHOVEN, P. A., Reduced deuterium retention in self-damaged tungsten exposed to high-flux plasmas at high surface temperatures, Nucl. Fusion, **53** (2013) 043003.

[17] TROEV, T., POPOV, E., STAIKOV, P., NANKOV, N., YOSHIIE, T., Positron simulations of defects in tungsten containing hydrogen and helium, Nucl. Instrum. Meth. Phys. Res. B, **267** (2009) 535.

[18] WAMPLER, W. R., DOERNER, R. P., The influence of displacement damage on deuterium retention in tungsten exposed to plasma, Nucl. Fusion, **49** (2009) 115023.

[19] ALIMOV, V. Kh., HATANO, Y., SUGIYAMA, K., ROTH, J., TYBURSKA-PÜSCHEL, B., DORNER, J., SHI, J., MATSUYAMA, M., ISOBE, K., YAMANISHI, T., The effect of displacement damage on deuterium retention in tungsten exposed to D neutrals and D_2 gas, J. Nucl. Mater., **438** (2013) S959.

[20] TANNO, T., HASEGAWA, A., FUJIWARA, M., HE, J.-C., NOGAMI, S., SATOU, M., SHISHIDO, T., ABE, K., Precipitation of solid transmutation elements in irradiated tungsten alloys, Mater. Trans., **49** (2008) 2259.

[21] FUKUDA, M., TANNNO, T., NOGAMI, S., HASEGAWA, A., Effects of Re content and fabrication process on microstructural changes and hardening in neutron irradiated tungsten, Mater. Trans., **53** (2012) 2145.

[22] FUKUDA, M., YABUUCHI, K., NOGAMI, S., HASEGAWA, A., TANAKA, T., Microstructural development of tungsten and tungsten–rhenium alloys due to neutron irradiation in HFIR, J. Nucl. Mater., **445** (2014) 460.

[23] ZIEGLER, J. F., http://www.srim.org/

[24] OGORODNIKOVA, O. V., GASPARYAN, Yu., EFIMOV, V., CIUPINSKI, Ł., GRZONKA, Annealing of radiation-induced damage in tungsten under and after irradiation with 20MeV self-ions, J. Nucl. Mater. **451** (2014) 379.

[25] BETAMATI, G., SERRA, E., WU, C. H., Hydrogen and deuterium transport and inventory parameters through W and W-alloys for fusion reactor applications, J. Nucl. Mater., **283–287** (2000) 1033.

[26] SUZUDO, T., YAMAGUCHI, M., HASEGAWA, A., Stability and mobility of rhenium and osmium in tungsten: first principles study, Modelling Simul. Mater. Sci. Eng. **22** (2014) 075006.

[27] SUZUDO, T., HASEGAWA, A., Suppression of radiation-induced point defects by rhenium and osmium interstitials in tungsten, Sci. Rep., 6 (2016) 36738.

[28] DE BACKER, A., SAND, A., ORTIZ, C. J., DOMAIN, C., OLSSON, P., BERTHOD, E., BECQUART, C. S., Primary damage in tungsten using the binary collision approximation, molecular dynamic simulations and the density functional theory, Phys. Scr., **T167** (2016) 014018.

[29] JAN, R. V., SEEGER, A., Zur Deutung der Tieftemperatur-Elektronenbestrahlung von Metallen Phys. Stat. Sol., **3** (1963) 465.

[30] MAURY, F., BIGET, M., VAJDA, P., LUCASSON, A., LUCASSON, P., Frenkel pair creation and stage I recovery in W crystals irradiated near threshold, Rad. Eff., **38** (1978) 53.

[31] HOHENSTEIN, M., SEEGER, A., SIGLE, W., The anisotropy and temperature dependence of the threshold for radiation damage in gold — comparison with other FCC metals, J. Nucl. Mater., **169** (1989) 33.

[32] AMINO, T., ARAKAWA, K., MORI, H., Activation energy for long-range migration of self-interstitial atoms in tungsten obtained by direct measurement of radiation-induced point-defect clusters, Philos. Mag. Lett., **91** (2011) 86.

[33] FUKUZUMI, S., YOSHIIE, T., SATOH, Y., XU, Q., MORI, H., KAWAI, M., Defect structural evolution in high purity tungsten irradiated with electrons using high voltage electron microscope, J. Nucl. Mater., **343** (2005) 308.

[34] AMINO, T., ARAKAWA, K., MORI, H., Detection of one-dimensional migration of single self-interstitial atoms in tungsten using high-voltage electron microscopy, Sci. Rep., **6** (2016) 26099.

[35] SWINBURNE, T. D., ARAKAWA, K., MORI, H., YASUDA, H., ISSHIKI, M., MIMURA, K., UCHIKOSHI, M., DUDAREV, S. L., Fast, vacancy-free climb of prismatic dislocation loops in bcc metals, Sci. Rep., **6** (2016) 30596.

HIGH-FLUX PLASMA EFFECT ON TUNGSTEN DAMAGED BY HIGH-ENERGY IONS

B. I. KHRIPUNOV, V. S. KOIDAN, A. I. RYAZANOV

National Research Center “Kurchatov Institute”
Moscow, 123182, Russia

Abstract

The main objective of the work was to investigate experimentally the complex effect of radiation damage and plasma on tungsten suggested as plasma facing material for a long-operating fusion reactor providing high neutron fluence. The use of charged particles (heavy ions) accelerated to MeV-range energies was adopted as a method to produce high-level damage in tungsten relevant to those expected in ITER and DEMO reactors. Experiments have been performed in two stages: production of radiation damage in tungsten, first, and exposure of the damaged material to high-flux plasma simulating conditions of a reactor operating in steady-state, second. Different ion species were taken for the damage production, namely, Helium ions and Carbon ions accelerated to energy of 3-10 MeV so that the damage was generated in the surface layer of 3-6 microns at 1-60 displacements per atom (dpa). Irradiations with protons induced the damage about 0.01-0.05 dpa to 50 micron depth. The samples of irradiated tungsten were subjected to steady-state deuterium plasma and the consequences of plasma-surface interaction were analyzed and compared for the damaged and undamaged materials. Erosion of the surface and deuterium retention were studied after plasma exposure. Experimental work was supported by computations of the defect production in the ion-irradiated tungsten to help interpretation of the obtained experimental results.

1. INTRODUCTION

A full assessment of tungsten as of a plasma facing material for a fusion reactor should have an extensive experimental basis including, in particular, behavior of the irradiated material in plasma environment. Radiation defects produced in PFMs by 14 MeV-neutrons during long operation of D-T fusion reactor are supposed to be relevant to high-level damage and they are supposed to range from 1 to a few tens *dpa*. The problem finds still rising scope of the research (ex. [1-4]). The results of experimental investigation of deuterium plasma effect on damaged tungsten undertaken at Kurchatov Institute a few years ago are presented in this report.

The anticipated consequences of primary concern are changes in tungsten microstructure due to accumulation of defects produced by high-energy particles. These would change the material response to the plasma impact. The main aim of the study was to find out the influence of the radiation damage occurring in tungsten on the result of the plasma effect with the main attention to the erosion of radiation-damaged material and to hydrogen isotope retention.

Analysis of tungsten microstructure was made at different stages of the experiments - after irradiation by high-energy particles and during plasma exposures. Erosion of the irradiated material in deuterium plasma was evaluated; its relation to irradiation, to the accumulated defect level and to changes of microstructure was analyzed. An important issue of hydrogen isotope retention in irradiated tungsten (tritium accumulation) was also examined in the work: analyses of hydrogen isotopes was performed by nuclear reactions methods and by **T**hermo-**D**e**S**orption to establish the penetration depth and the quantity of the retained isotope after exposure of damaged tungsten to plasma fluence 10^{26} m^{-2}. Temperature may have an important role in accumulation of radiation damage, so appropriate experiments were done at an elevated temperature in order to obtain data on tungsten erosion yield and deuterium retention.

The first part of the work (production of radiation damage in tungsten) was performed on the cyclotron (NRC KI), the plasma exposure experiments were conducted also at NRC KI on the LENTA linear plasma simulator, analysis of the hydrogen isotope content was made on the facilities at Lomonosov University and at MEPhI.

2. EXPERIMENTAL PROCEDURE AND PERFORMANCE

Experimental procedure includes two stages. At the first stage, the damage was produced by fast ions accelerated on the cyclotron at Kurchatov Institute (1-60 MeV) to simulate neutron radiation effect.

The experiments were conducted on tungsten W (99.95% wt.) (Russian grade) and W Plansee – the ITER candidate grade. The ion species used in these experiments were fast helium ions He^{2+} accelerated to 3.5-4.5 MeV to achieve fluences of 10^{21}-$3\cdot10^{22}$ ion/m^2, carbon ions C^{3+} at an energy of 10 MeV and protons of 3.7 MeV in average, 10^{22} m^{-2}. The primary damage in a few micron surface layer of the material fell into the interval from 0.1 to about 60 *dpa* thus covering the whole range supposed to be of interest for fusion research.

The irradiated samples were then subjected to steady-state deuterium plasma on the LENTA linear plasma device which is used for divertor and SOL simulations of tokamak. The plasma ion energy on the surface was chosen by bias potential so that erosion condition (250 eV over 180 eV of sputtering threshold) was obtained and that being relevant to divertor plasma condition in tokamak. The loss of material from the tungsten surface by sputtering was detected, the surface microstructure suffered important modification as it has been shown by surface analysis. The plasma processing of the damaged samples was performed in an exposure sequences: successive multiple exposures resulted in the surface progress shift to depth due to sputtering finally reaching the depth of the fast ion range. D-ion fluence of $F=10^{25}$-10^{26} D_{ion}/m^2 was achieved on the W surface.

To date, we have obtained tungsten samples damaged to the level evaluated in displacements per atom as falling within an interval from 0.1 to 60 dpa. This interval covers practically whole range corresponding to the fusion reactor forecast for the ITER and DEMO projects. It becomes possible to study materials at so high damage level due to the use of accelerated MeV-range heavy ions for their production.

3. PRODUCTION OF RADIATION DAMAGE IN TUNGSTEN

Analysis of the resulting radiation damage was performed by calculation (SRIM) providing primary defect profiles in the surface layer in dependence on irradiation dose and ion energy [5]. Three kinds of irradiations tested in our experiments are illustrated in Figures 1- 3. Generation of defects in tungsten by Helium ions (4 MeV, $1.1\cdot10^{22}$ ion/m^2) and the implanted Helium content is shown in Figure 1. The damaged layer is about 6 micron thick,. The produced defects correspond to about 10 dpa in average with maximal concentration at the depth of He-ion range D_{max}= 66.8 dpa.

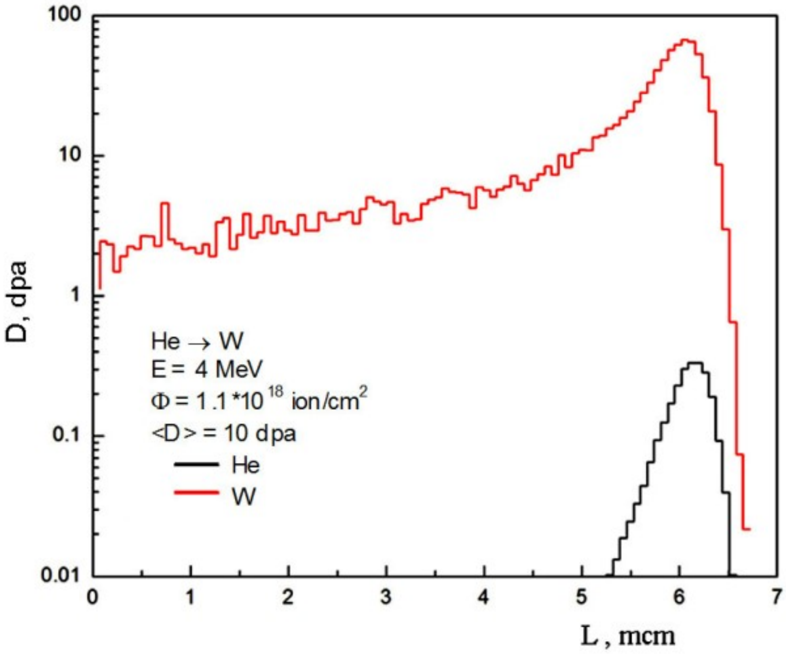

FIG. 1. Primary defect distribution in tungsten irradiated by He-ions (1.1 × 10^{22} m^{-2}; 4 MeV; D_{max}=66.8 dpa) and implanted He concentration (at.%).

Similar result for irradiations conducted with 10 MeV ions $^{12}C^{3+}$ is given in Figure 2 for 10^{21} ion/m^2 fluence. In this case the damaged layer is ~3.5 micron thick. The average defect level in this layer is <D> = 4.2 dpa.

For the light Hydrogen ions (protons) the picture changes essentially. Protons were accelerated in the cyclotron to 32 MeV (optimal for the maximum beam current), then the beam came through aluminum-water moderator and finally impinged on the tungsten target at an average energy of ~4 MeV. Tungsten was damaged to depth about 100 microns in this case; the achieved proton fluence was 10^{21} p/m^2 (see Figure 3). The samples were ready for handling in the experiments after 2.5 months to drop down the induced activity.

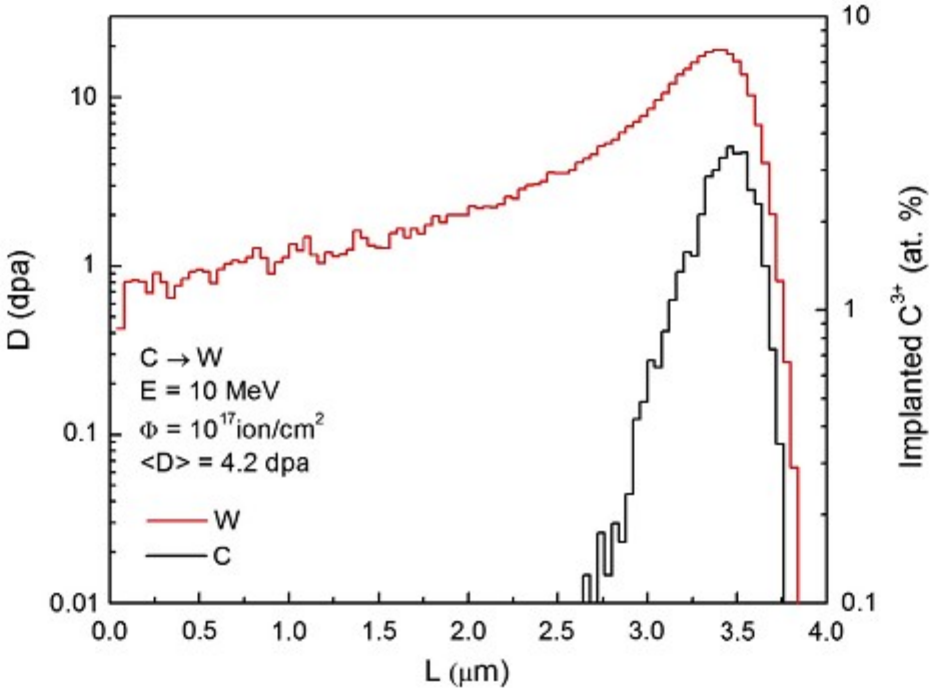

FIG. 2. Primary defect distribution in tungsten irradiated by $^{12}C^{3+}$ ions at 10 MeV to fluence of 10^{21} C_{ion}/m^2. <D> = 4.2 dpa average over damaged layer 3.5 μm thick. Reprinted under licence CC BY-NC-ND 4.0 from Physics Procedia 71 (2015) 63-67.

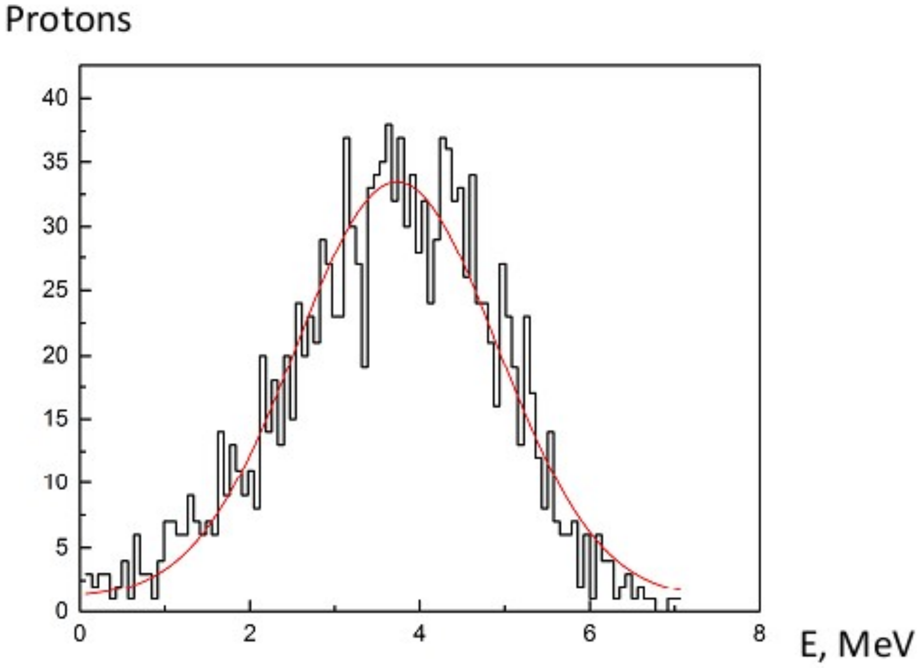

FIG. 3. Proton beam energy spectrum.

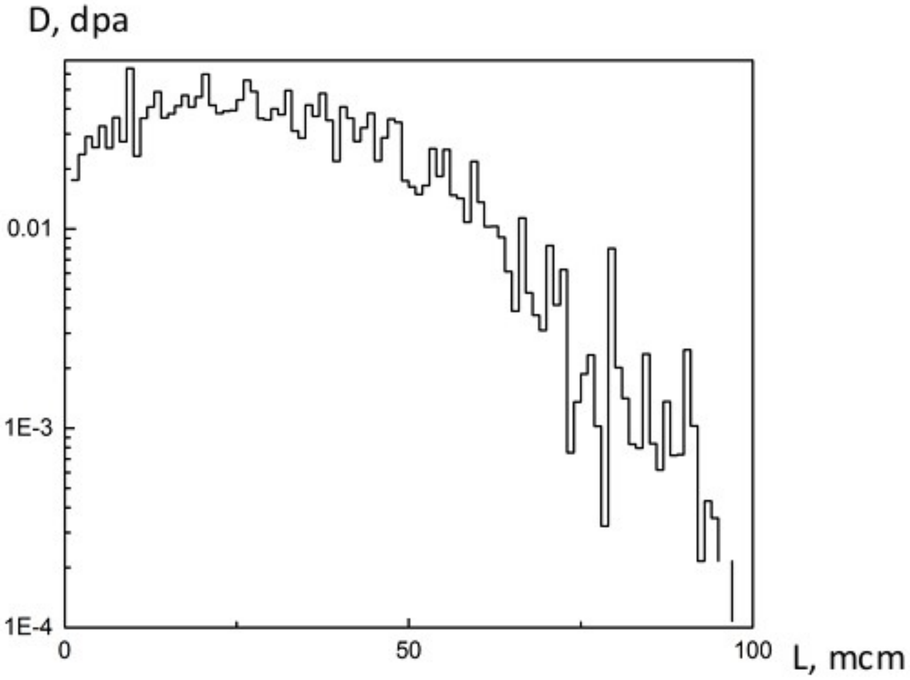

FIG. 4. Primary defects produced in tungsten by irradiation with protons (E_{av} = 3.7 MeV, 10^{22} p/m^2).

4. IRRADIATION AND PLASMA EFFECTS ON TUNGSTEN

4.1. Swelling, microstructure.

The evidence of important radiation damage of the studied material after irradiations was revealed by observations of swelling effect. Swelling was registered on the irradiated tungsten by surface profiling measurements. Profilometry has shown 0.1-2 % swelling for C-irradiated tungsten and 2-3 % for He-irradiated material [6]. Example of tungsten surface profiling is given in Figure 5. Shown are **S**canning **E**lectron **M**icroscopy image of the sample irradiated with C-ions (10 MeV, 10^{21} C_{ion}/m^2**.** <D> = 4.2 dpa) taken around the boundary of the irradiated area and the corresponding surface profile. 0.2 micron elevation of the irradiated region is seen in the Figure 5.

Comparison of irradiated and unirradiated tungsten samples shows that considerable changes occur in surface microstructure and in damage layer microstructure as it was found by SEM technique. $^4He^{2+}$-ion irradiations of polycrystalline tungsten W 99.95 wt.% (Russian grade) have been performed to doses from 10^{21} m^{-2} to 10^{23} m^{-2} at 3.5-4 MeV (corresponding to the alphas generated in DT fusion reaction). By this, defects were produced to depth of $^4He^{2+}$ range in tungsten of about 6 μm (Figure 1). At high helium fluences given above, the damaged layer acquires a particular porous structure shown in Fig. 5, the pores and cavities supposed to be filled with helium. For example, experimental peak profile of the implanted helium (**RBS** analysis by 7.2 MeV protons) was also much larger ($\Delta \sim$ 2-3 μm) than that expected from calculation ($\Delta \sim$ 0.5-1 μm) (see Figure 1) [6]. This result is readily explained by strong changes of the material structure in the damaged layer.

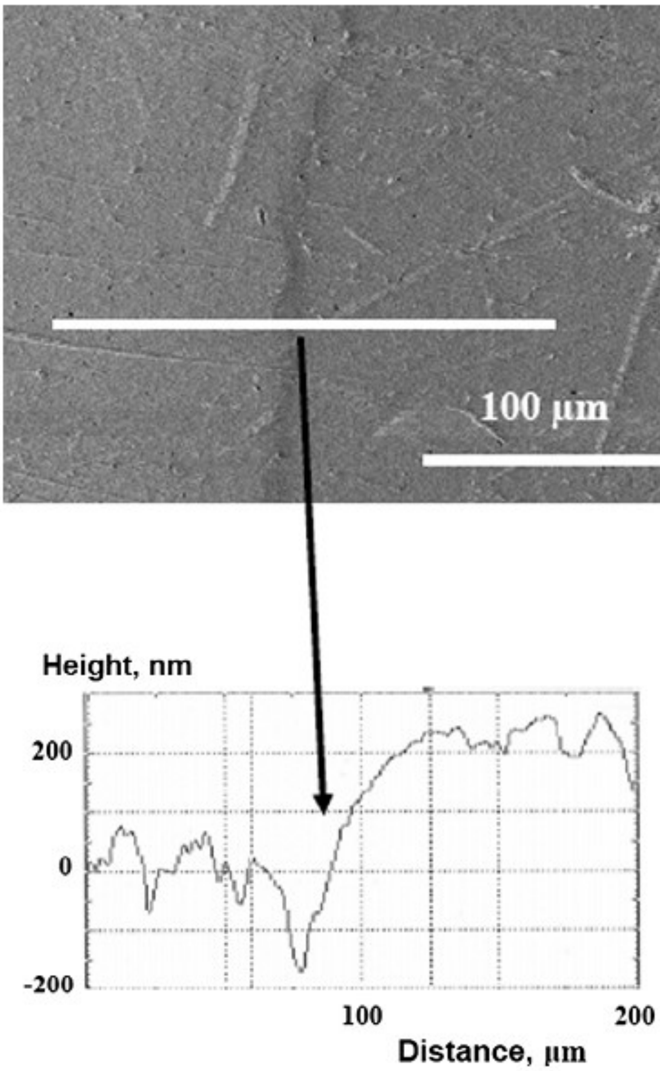

FIG.. 5. Boundary of C-ion irradiated area on tungsten sample: the irradiated area is to the right; the left hand part was masked from irradiation. Surface profile shows elevation of the irradiated area.

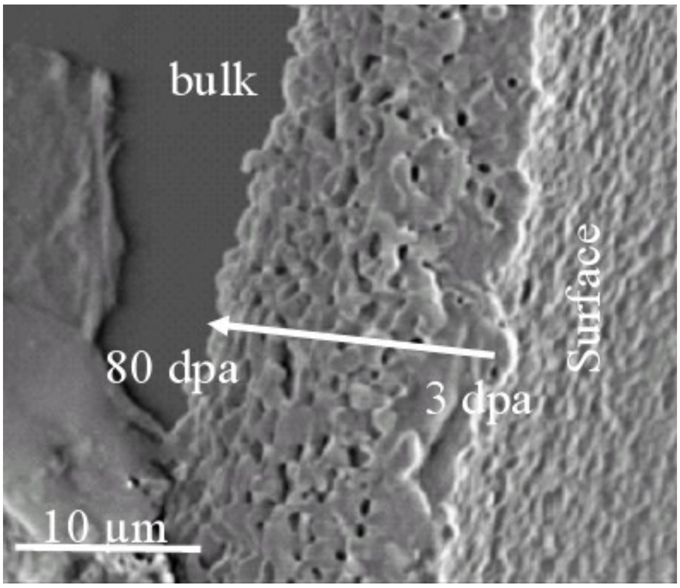

Fig. 6. Surface layer of tungsten (fracture) damaged by He-ions (3×10^{22} m^{-2}, 3.5-4 MeV): from 3 dpa at the surface to 80 dpa at 6 micron depth.

4.2. Erosion in deuterium plasma, deuterium retention.

The structure of the damaged material and the presence of helium have a major influence on the performance of the material under plasma exposure. The results of plasma experiments with He-irradiated tungsten presented below have been also reported elsewhere [6-10].

Sequential exposures have been carried out to investigate changes in the damaged layer under durable plasma action. Plasma parameters were taken so that erosion condition was realized. Erosion of tungsten at each exposure step was 0.5-1.5 μm, therefore the whole damaged layer could be taken off by erosion in several step sequences. By this, relation of erosion rate and surface microstructure with the level of damage at the corresponding layer could be examined.

An example of plasma exposed surface of He-irradiated tungsten sample ($3 \cdot 10^{22}$ He/m^2; 3,5 MeV) is presented in Figure 7 (SEM). The photo corresponds to the exposure stage where the erosion depth was about 3.6 μm (~ 15 dpa). Exposure parameters were: deuterium ion flux (2-3) × 10^{17} ion/cm^2s; plasma density 2 × 10^{12} cm^{-3}, electron temperature 6-8 eV, ion energy 250 eV (bias). A cellular structure was formed during erosion with helium escaping from the pores.

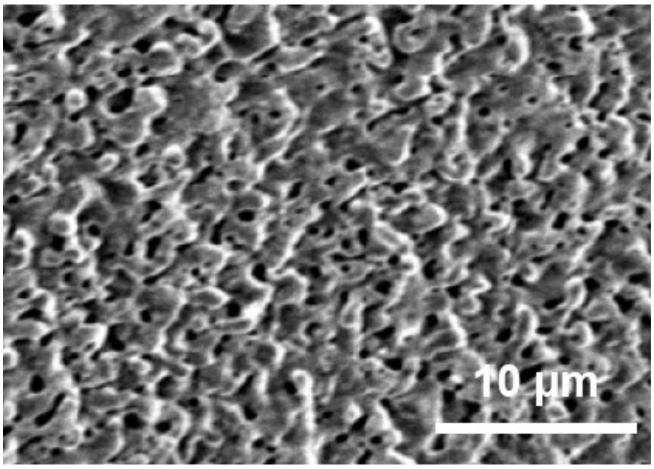

Fig. 7. He-irradiated tungsten surface (3 × 10^{18} cm^{-2}, 3.5 MeV) after deuterium plasma exposure, 3.6 μm eroded.

Erosion yield of the damaged tungsten in deuterium plasma was evaluated by weight loss at $Y_{d\text{-}w} \cong (1\text{-}4) \cdot 10^{-3}$ at/ion. No correlation of damage and erosion rate was found so far for the ITER relevant damage levels.

Taking into account these particular properties of helium present in tungsten (see also [11]) the work was continued with another ion species. Irradiations of tungsten were made with carbon ions $^{12}C^{+3}$ accelerated to 10 MeV [12]. In this case, the total ion fluence reached $\Phi = 2 \times 10^{21}$ m^{-2}. The resulting levels of damage were equivalent to those obtained in He-ion case.

Erosion of C-irradiated samples has been also studied in deuterium plasma at the levels of 10-20 dpa. Both low temperature case (below 100C) and elevated temperature case (500 C) of tungsten were under study. Irradiation conditions corresponded to the following data: C ions at 10 MeV, (1-2) × 10^{21} ion/m^2. Plasma exposures of these samples were conducted in conditions close to those for He-irradiated samples: D-plasma at 250 eV, 2 × 10^{25} D/m^2. Two-fold exposure showed the measured values of erosion yield of about $Y_{d\text{-}w} = 3 \times 10^{-3}$ at/ion at ~1 μm depth and about $Y_{d\text{-}w} = 5 \times 10^{-3}$ at/ion deeper by 0.5 μm. The effect is illustrated in Figure 8 where a cross section of C-irradiated tungsten after d-plasma exposure is presented as taken after erosion to 1 μm. The structure of the damaged layer is definitely different from that of the bulk material, and appearance of cavities may be supposed.

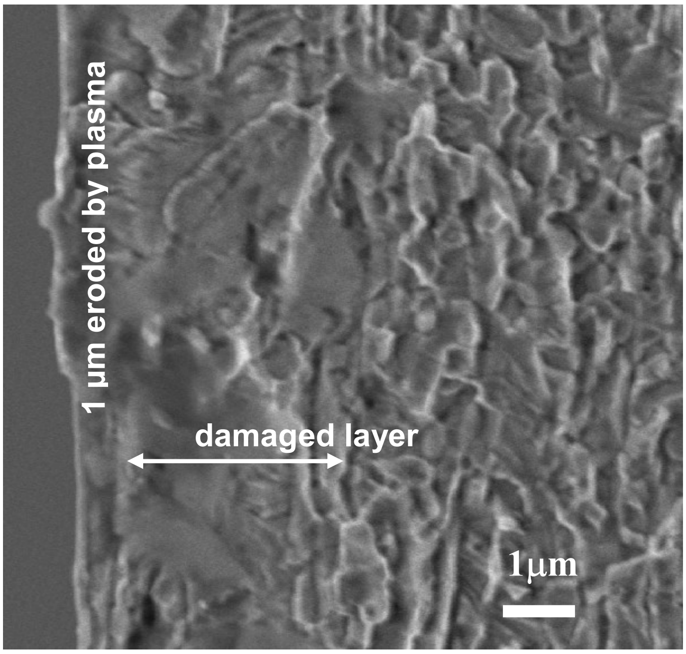

FIG. 8. C-irradiated tungsten cross section (10 MeV, 2 × 10^{21} m^{-2}) after deuterium plasma (1 µm eroded). Reprinted under licence CC BY-NC-ND 4.0 from Physics Procedia 71 (2015) 63-67.

The samples irradiated with carbon ions (C^{3+}, 10 MeV, 1.5 × 10^{21} m^{-2}) at T_{irrad} = 500 C were also exposed to deuterium plasma. The temperature of the material was also controlled at 500 C during plasma operation till the plasma fluence F = (1-1.2) × 10^{25} D/m^2 was reached. Erosion depth in this case was 0.8 micron, and erosion yield evaluation gave $Y_{d\text{-}w}$ = 4.3 × 10^{-3} at/ion. The obtained value does not differ much from the earlier results for other irradiation and plasma exposure conditions. The surface structure of the sample processed at 500 C does not show much difference compared to the low temperature case after erosion.

Gas uptake (D, He) in the ion-irradiated and plasma exposed tungsten was measured by nuclear methods and by **TDS** spectroscopy. **E**lastic **R**ecoil **D**etection **A**nalysis was applied to measure concentration of the trapped deuterium and hydrogen content. Increased content of the retained deuterium (1.8-20%) was found in the surface layer of irradiated tungsten (100-150 nm deep) (see also [13]). Significant D uptake was found in He-irradiated tungsten at the ion range depth (2·10^{21} D/m^2).

Spectacular effect was found in the comparison of deuterium retention in the studied tungsten for two ions species (He, C) used for damage production at similar damage levels and plasma conditions (Figures 9, 10). The ERDA analysis has shown very similar depth distributions of deuterium concentration at the surface facing the plasma at close values of damage (2-3 dpa). The data shown in Figures 9, 10 were taken for very close plasma conditions: two curves in Figure 9 represent D distributions for C-irradiated tungsten (10 MeV, Φ = 2 × 10^{21} m^{-2} both), and two others in Figure 10 represent distributions for He-irradiated samples (E = 3-4 MeV, Φ = 3 × 10^{22} m^{-2} and E = 3.2 MeV, Φ = 3.2 × 10^{22} m^{-2} correspondingly). Close maximal values of 6-8 % at. (at 20-30 microns) and total quantities of the retained deuterium (from 1.65 × 10^{20} m^{-2} to 1.85× 10^{20} m^{-2}) were found to occur.

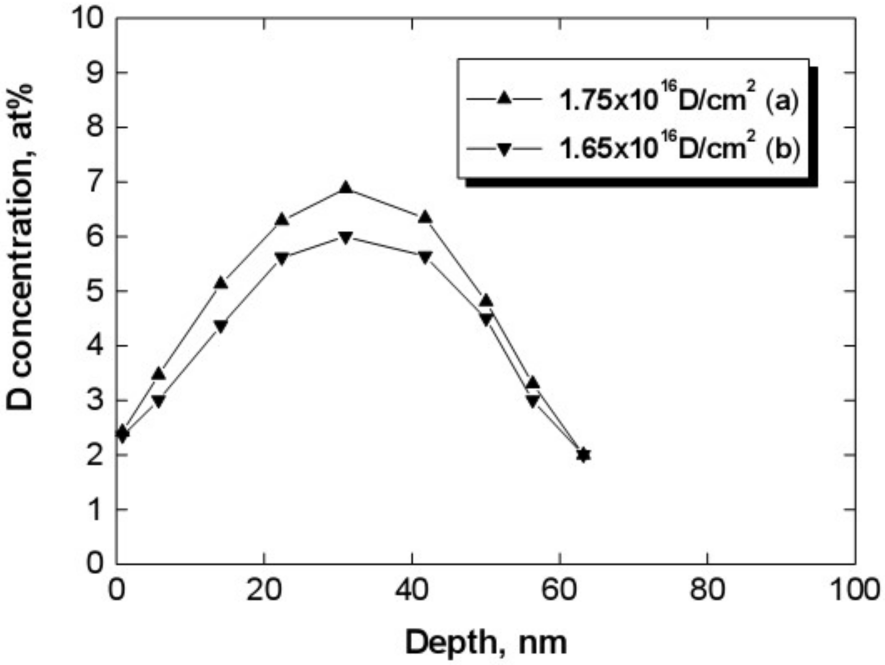

FIG. 9. Deuterium concentration (ERDA) in C-damaged (10 MeV, $\Phi = 2\cdot10^{21}$ C^{3+}/m^2) plasma exposed tungsten at room temperature: 2 dpa at the surface, (a) plasma fluence $F= 1\cdot10^{25}$ D/m^2, 0.5 micron eroded; (b) $F = 2\cdot10^{25}$ m^2, 0.9 micron eroded.

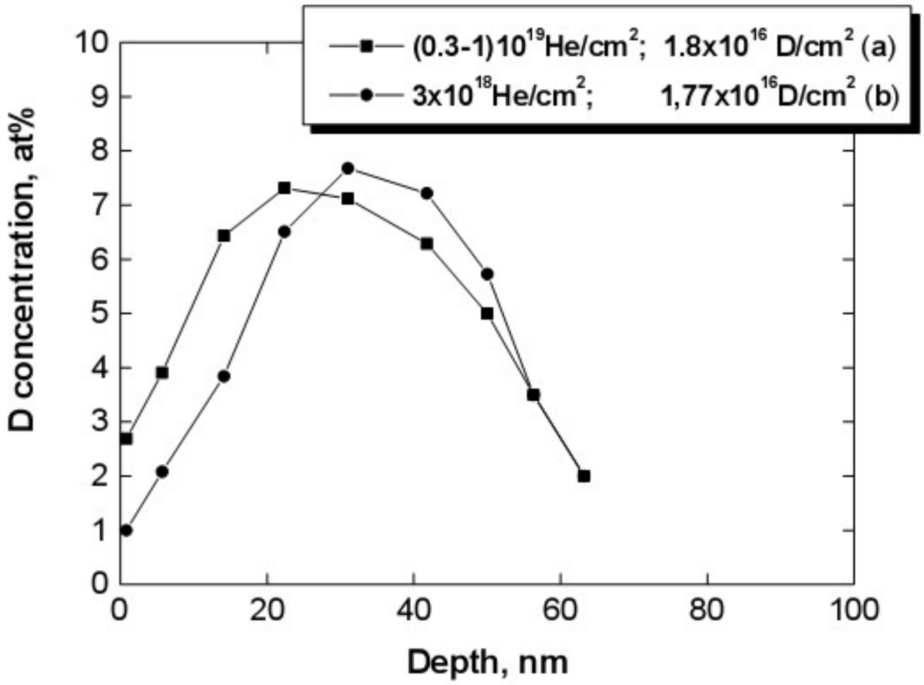

FIG. 10. Deuterium concentration (ERDA) in He-irradiated plasma exposed tungsten (RT): 2 dpa at the surface; (a) plasma $F = 2.9\cdot10^{25}$ D/m^2, 1.2 micron eroded; (b) $F = 1.0\cdot10^{25}$ D/m^2, 0.7 micron eroded. Reprinted courtesy of Elsevier [4452620771602].

The ITER candidate material W Plansee was also tested. Irradiations were performed with He ions (4.2 MeV, $1.5\cdot10^{22}$ He^+/m^2) and protons ($E_{av} = 3.7$ MeV, $\Phi = 10^{22}$ m^{-2}). He-irradiated tungsten surface microstructure after D plasma exposure ($0,8\cdot10^{26}$ D/m^2 at 250 eV) is given in Figure 11. Strong development of grain boundaries has been observed. The effect may be important for analysis of hydrogen isotope trapping in the material (increase of grain boundary diffusion).

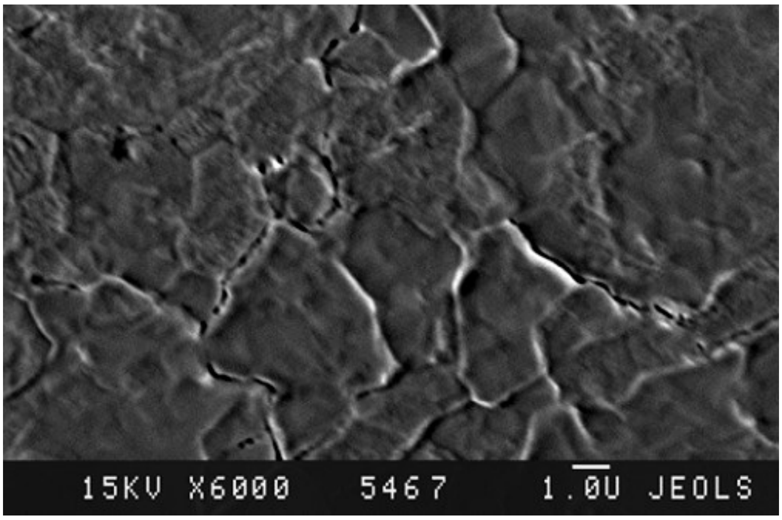

FIG. 11. Surface of He-irradiated W plansee after D-plasma (E_i=250 eV; F=2,8·10^{21} D_{ion}/m^2s; Φ=0,8·10^{26} D_{ion}/m^2).

TDS analysis of plasma exposed W Plansee (Figure 12) has shown important retention in He-irradiated material (D_{av} = 1.5 dpa) and low retention for proton-irradiated material (0.05 dpa). The latter has shown to be just slightly different from the unirradiated material (Figure 12).

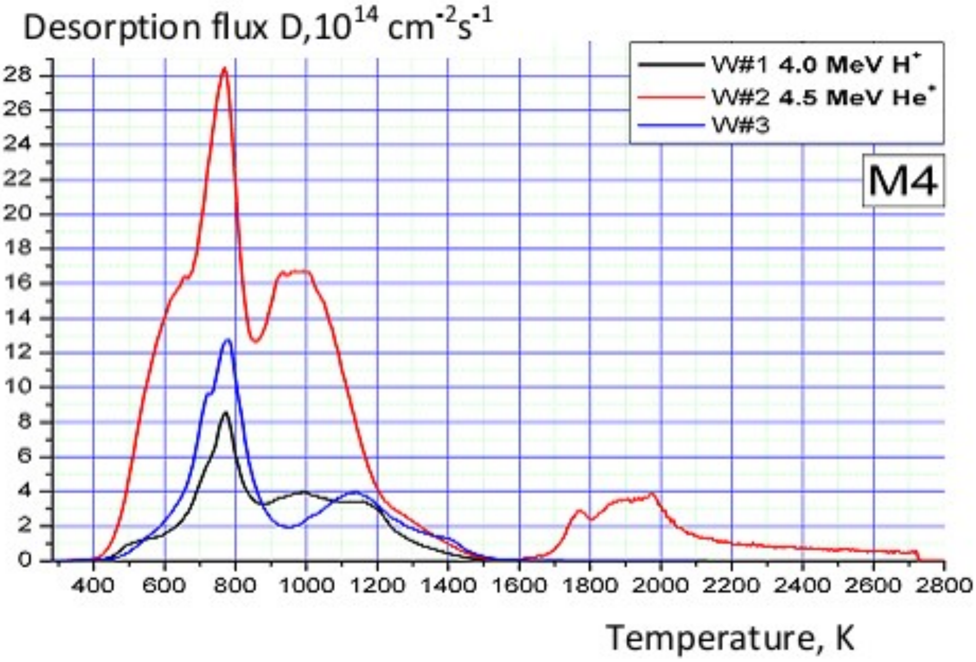

FIG. 12. TDS spectrum of W Plansee irradiated with He (W2) and with protons (W1) after D-plasma exposure (W3 – unirradiated) .

5. SUMMARY

Deuterium plasma impact on tungsten at high level of radiation damage has been investigated. Damage of the material was produced by high-energy ions $^{12}C^{+3}$ (10 MeV), protons (4 MeV) and $^{4}He^{+2}$ (3-4 MeV) from accelerator to simulate neutron effect. The level of radiation damage relevant to fusion reactors was reached on tungsten samples. The primary defects generation obtained experimentally ranged in 1- 60 dpa interval in the surface layer of 3.5-6 µm .

Swelling effect was observed both on He- and C-irradiated tungsten at maximal damage. Tungsten showed linear deformation 2-3 % in He-irradiations and 0.1-2 % in C-irradiations.

Strong microstructure modifications of tungsten was detected after plasma exposure of the irradiated material surface – micron-sized structure, cracks, blisters, delamination, bubbles, large cavities with accumulated helium (in case of He-irradiations) in damaged layer. Erosion yield of irradiated tungsten was evaluated at $Y_{D\text{-}W} \cong (1\text{-}4)\cdot 10^{-3}$ in deuterium steady-state plasma in simulated SOL conditions. No correlation of damage and erosion rate was found so far for ITER relevant damage levels. Blistering effect took place enhancing erosion.

Deuterium retention in irradiated tungsten was analyzed in plasma-induced erosion dynamic condition at 250 eV of D-ions energy. Deuterium was concentrated in the 100-150 nm layer at different levels of damage from 1.8 to 20 % at. Increased concentration of deuterium uptake ($2\cdot 10^{21}$ D/m^2) in the layer around the He-ions range was measured. Implanted Helium accumulation 8-10% at. was detected at the depth of ion range as a 2-3 μm wide peak. He- and C-irradiations gave close distributions of the retained deuterium for 2-3 dpa at the surface at room temperature. Proton irradiated W Plansee (0.05 dpa) showed minor difference as to deuterium retention compared to unirradiated material.

Important increase in deuterium retention in He-irradiated tungsten Plansee at 10-30 dpa was found by TDS. On the other hand, the material damaged by protons to 0.05 dpa has shown almost the same retention as the unirradiated material.

The experiments performed as well as the results obtained appear to be efficient in providing data on radiation-damaged materials at high level of damage under plasma impact for evaluations of neutron effect and tritium retention in a fusion reactor PFMs.

ACKNOWLEDGMENTS

The authors are grateful to Prof. Linke for providing the samples Plansee for this work. Also we are grateful to MEPhI group Prof. Pisarev A, A., Gasparyan Yu. M., Efimov V.S. for providing the TDS data. This work was supported in part by Russian Foundation for Basic Research, Projects № 13-08-00692–a and № 15-08-04409-a.

REFERENCES

[1] WAMPLER, W., DOERNER, R., The influence of displacement damage on deuterium retention in tungsten exposed to plasma, Nuclear Fusion **49** (2009) 115023.

[2] HATANO, Y., SHIMADA, M., ALIMOV, V., SHI, J., HARA, M., NOZAKI, T., OYA, Y., KOBAYASHI, M., OKUNO, K., ODA, T., CAO, G., YOSHIDA, N., FUTAGAMI, N., SUGIYAMA, K., ROTH, J., TYBURSKA-PÜSCHEL, B., DORNER, J., TAKAGI, I., HATAKEYAMA, M., KURISHITA, H., SOKOLOV, M., Trapping of hydrogen isotopes in radiation defects formed in tungsten by neutron and ion irradiations, Journal of Nuclear Materials **438** (2013) S114.

[3] ROTH, J., SCHMID, K., Hydrogen in tungsten as plasma-facing material, Physica Scripta **T145** (2011) 014031.

[4] OGORODNIKOVA, O., TYBURSKA, B., ALIMOV, V., ERTL, K., The influence of radiation damage on the plasma-induced deuterium retention in self-implanted tungsten, Journal of Nuclear Materials **415** (2011) S661.

[5] RYAZANOV, A., SEMENOV, E., Radiation damage formation in fusion structural materials due to elastic and inelastic processes, Journal of Nuclear Materials **417** (2011) 1074.

[6] KHRIPUNOV, B., GUREEV, V., KOIDAN, V., KORNIENKO, S., LATUSHKIN, S., PETROV, V., RYAZANOV, A., SEMENOV, E., STOLYAROVA, V., DANELYAN, L., KULIKAUSKAS, V., ZATEKIN, V., UNEZHEV, V., Study of ion-irradiated tungsten in deuterium plasma, Journal of Nuclear Materials **438** (2013) S1014.

[7] KHRIPUNOV, B., GUREEV, V., S KOIDAN, V., LATUSHKIN, S., PETROV, V., RYAZANOV, A., SEMENOV, E., STOLYAROVA, V., UNEZHEV, V., DANELYAN, L., KULIKAUSKAS, V., ZATEKIN, V., Plasma impact on materials damaged by high-energy ions, Physica Scripta **T145** (2011) 014052.

[8] RYAZANOV, A. I., KOIDAN, V. S., KHRIPUNOV, B. I., LATUSHKIN, S. T., PETROV, V. B., DANELYAN, L. S., SEMENOV, E. V., UNEZHEV, V. N., Investigations of Radiation Damage Effects on ITER Structural and Plasma-Facing Materials, Fusion Science and Technology **61** (2012) 107.

[9] KOIDAN, V. S., ET AL., IAEA FEC-23, (2010), CD Rep. FTP/3-3Rb.

[10] KHRIPUNOV, B., BRUKHANOV, A., GUREEV, V., KOIDAN, V., KORNIENKO, S., LATUSHKIN, S., PETROV, V., RYAZANOV, A., SEMENOV, E., STOLYAROVA, V., UNEZHEV, V., DANELYAN, L., KULIKAUSKAS, V., ZATEKIN, V., VOSTRIKOV, V., ROMANOVSKY, E., Plasma effect on tungsten damaged by high-energy alpha particles: Erosion and deuterium trapping, Journal of Nuclear Materials **415** (2011) S649.

[11] MIYAMOTO, M., NISHIJIMA, D., UEDA, Y., DOERNER, R., KURISHITA, H., BALDWIN, M., MORITO, S., ONO, K., HANNA, J., Observations of suppressed retention and blistering for tungsten exposed to deuterium–helium mixture plasmas, Nuclear Fusion **49** (2009) 065035.

[12] KHRIPUNOV, B., GUREEV, V., KOIDAN, V., KORNIENKO, S., LATUSHKIN, S., PETROV, V., RYAZANOV, A., SEMENOV, E., STOLYAROVA, V., DANELYAN, L., KULIKAUSKAS, V., ZATEKIN, V., UNEZHEV, V., Erosion and deuterium retention in ion-irradiated tungsten under plasma exposure, Journal of Nuclear Materials **463** (2015) 258.

[13] HU, A., HASSANEIN, A., Modeling hydrogen isotope behavior in fusion plasma-facing components, Journal of Nuclear Materials **446** (2014) 56.

ACROSS-SCALE SELF-HEALING MECHANISMS FOR RADIATION DAMAGE IN NANO-CRYSTAL TUNGSTEN

X. LI, Y. XU, Y. ZHANG, C. S. LIU

Key Laboratory of Materials Physics, Institute of Solid State Physics, Chinese Academy of Sciences, Hefei, 230031, PR China

Abstract

Radiation damage not only seriously degrades the mechanical properties of tungsten (W) but also enhances hydrogen retention in the material. Introducing a large amount of defect sinks, e.g., grain boundaries (GBs) is an effective method of improving resistance of W to irradiation damage. Here, combining molecular dynamics (MD) simulations, molecular statics (MS) calculations and the object kinetic Monte Carlo (OKMC) method, we provide across-scale self-healing mechanisms for radiation damage in nano-crystal W from the view of the fundamental interaction of the radiation-created vacancies (Vs), self-interstitial atoms (SIAs). These mechahnisms include GB-enhanced diffusion and annihilation of the V and SIA, interstitial-emission (IE) induced annihilation, coupling of the segregation and SIA motion along the GB, and interstitial reflection (IR) by the locally dense GB region. First, we find that, SIAs are preferentially trapped into the GB over vacancies (Vs) during irradiation, with the V dominated near the GB and SIA highly localized at the GB. The GB serves as a sink both for Vs and SIAs near itself by reducing their formation energy and diffusion energy barrier. Second, we propose a MS method for calculating the IE-induced annihilation. The SIA only needs to migrate over a small distance from the GB/surface to recombine with the V nearby at a small energy barrier. During the process, the annihilation region around a static SIA at the GB/surface propagates or extends greatly to the adjacent bulk area. The annihilation is via the IE from the GB/surface or coupled vacancy hop with the IE. The ratio of the SIA-GB/surface binding energy to the trapping-radius of the GB/surface for the SIA is proposed to be a better qualitative indicator for the difficulty in the IE than the binding energy. Third, the single SIA trapped at the GB firstly moved along the GB quickly and clustered to be di-SIA therein, reducing its mobility to a value comparable to that that for the V diffusion in the bulk. Then, the bulk V was recombined via coupled motion of the di-SIA along the GB, the hop of the V towards the GB and the accompanying interstitial emission (IE). Fourth, the SIA-cluster was observed to be reflected back into the grain interior when approaching the locally dense GB region. Correspondingly, the energy landscape for the SIA near a locally dense region is featured by a shoulder, different to the downhill energy landscape of the SIA near a locally loose region as indicative of the sink role of the GB. The reflection of a SIA-cluster of parallel <1 1 1> crowdions by the GB enhances annihilation of bulk Vs. Finally, we also present relevant atomic data on the interaction among the V, SIA and the GB.

1. INTRODUCTION

As a potential first-wall fusion reactor material, tungsten (W) will be subjected to high radiation flux of 14MeV-neutrons and high ion bombardment fluxes of low-energy (～100 eV) deuterium, tritium and helium at a typical operation temperature of 1000K [1, 2]. Fusion neutrons produce collision cascades, introducing large quantities of vacancies (Vs) and interstitials (SIAs), into W. These defects and their clusters not only affect the mechanical properties of W, but also introduce trap sites for implanted hydrogen isotopes and helium [3–6].

To improve the performance of nuclear materials, the effective way known is to introduce high density of defects sinks into the material. Interfaces, e.g. grain boundaries (GBs) in nano-crystals (NCs) have been demonstrated to be good sinks for point defects both experimentally and theoretically, enhancing defect diffusion and annihilation [7–45]. Extensive experimental efforts have been made to prepare and develop highly radiation-resistant W materials [7–12]. It is found that, the most preferable microstructure is a nano-structure that contains nano-sized dispersoids and/or nano-sized grains. Neutron and He-ion irradiation experiments indicate superior resistance of nano-structured W to radiation hardening [7, 8]. Irradiated nano-structured W (equiaxed grain sizes: 50-200 nm) has a much smaller density of voids compared with commercially pure W (average grain size: 20 μm). Similar enhanced radiation-resistant performance is also observed in other nano-structured systems, such as molybdenum [13] and vanadium [14].

Often, the radiation tolerance of NCs strongly depends on fundamental processes in such systems, i.e., the diffusion, segregation and annihilation of SIAs and Vs near the GBs. Qualitatively, the radiation-tolerance of NCs could be attributed to the trapping of radiation-induced defects (SIAs, Vs) by the GBs in NCs which consequently decreases the formation of the large immobile defect clusters. The detailed mechanism could be complex due to the inherently multi-scale nature of the radiation damage, multiple levels of the defect mobility and possible presence of multiple types of GBs in NCs. Hierarchy is the key feature of the defect and its evolution. The processes we wish to study (e.g., diffusion and annihilation of defects after a cascade event near the surface) often take place on much longer time scales. To overcome this "time-scale problem" [46], one needs to use multiscale/across-scale simulation techniques. In addition, once one type of defects is preferentially confined to the GB, the process along the GB may influence the diffusion, segregation and annihilation of the defects near the GB. In other words, there may exist a coupling of some sort, for instance, of the segregation/diffusion process of the SIA and the V, which promotes the SIA-V annihilation.

In this paper, using molecular dynamics (MD), molecular statics (MS), object kinetic Monte Carlo (OKMC), we present across-scale self-healing mechanisms for radiation damage in NC W by investigating the diffusion, segregation, annihilation of the V and SIA near the GB at different scales. We also provide relevant atomic data on the interaction among the V, SIA and the GB. These fundamental interaction processes are illustrated in Fig. 1. Here, we focus on the processes near the GB and within the GB.

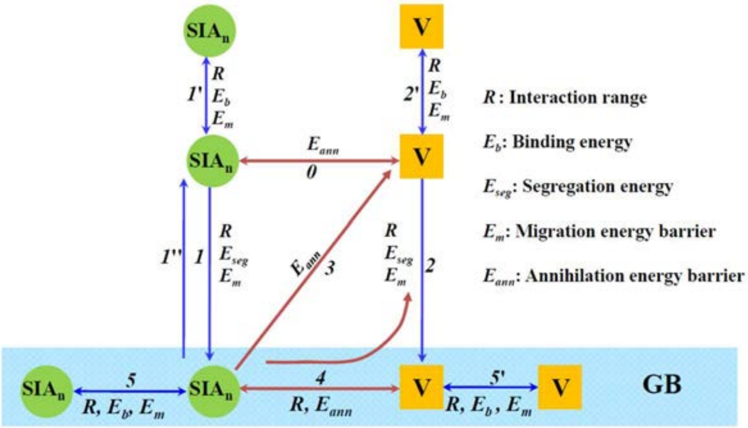

FIG. 1. Illustration of the possible interaction processes among the SIA-cluster (SIA_n), vacancy (V) and the GB. The SIA_n is indicated by the light green sphere and the orange square is for the V. The atomic processes include annihilation of the SIA_n with the V in the bulk (process 0), segregation of the SIA_n and V (processes 1 and 2), reflection of the SIA_n by the GB (process 1''), SIA_n-V annihilation near the GB via emission of the SIA_n (process 3), SIA_n-V annihilation within the GB (process 4). The curved arrow illustrates possible coupling among processes 2–4. Processes 1' and 2' are the clustering of the bulk SIA and V, respectively. Processes 5 and 5' are the clustering of the SIA and V, respectively within the GB. The energetic and kinetic parameters for these processes include binding energy (E_b), segregation energy (E_{seg}), migration energy barrier (E_m), and annihilation energy barrier (E_{ann}). R denotes interaction range of two defects or a defect with the GB.

2. COMPUTATIONAL METHOD

2.1. GB Models and Atomic Potential

Body-centered cubic (bcc) W was chosen as a typical model system. In addition, bcc Fe and face-centered cubic (fcc) Cu were chosen as comparison models. These metals have distinct SIA configurations of <1 1 1> crowdion in W, and <1 1 0> dumbbell in Fe, <1 0 0> dumbbell in Cu, respectively. Different levels of SIA-GB binding energies in these systems act as another factor for choosing the model systems, as revealed in some GBs and surfaces in these systems [32–45]. The GB studied in this work is a Σ5(3 1 0)/[0 0 1] symmetric tilt GB in bcc W and Fe. For fcc Cu, a Σ11(1 1 3)/[1 $\bar{1}$ 0] symmetric tilt GB was used. The two GBs have been frequently modeled in studying radiation effects [32–45]. To explore the generality of the simulation results, a total of 46 GBs in W were also modeled by using a different interatomic potential. These GBs have distinct periodical structural units along the GB with various lengths.

For MD simulations, a block with a slab geometry was used. The thickness of each slab was at least twice the cutoff radius of atomic interaction. The free atoms were sandwiched between two slabs of fixed atoms on each side of the GB plane. The dimensions of the free region were approximately equal in all three directions. The fixed atoms were allowed to move rigidly during the structural relaxation. The atoms in the outmost three layers of the moving region were coupled with a velocity-rescaling thermostat to extract the cascade energy and maintain the system temperature at 600 K. The velocity-Verlet method was used for the numerical integration.

The creation and relaxation procedures are refereed to Refs. [35–44]. Periodic boundary conditions were applied in the three directions of the GB systems. The GB energy was minimized through the rigid-body translations of one grain relative to the other in the two directions parallel to the GB, followed by atomic relaxation in all the three Cartesian directions at 0 K. Assuming the length of the minimal periodical structural units in the two directions parallel to the GB plane is *px* and *py*, respectively, and the corresponding translation step is *stepx* and *stepy*, one has to perform *Nx*×*Ny* (*Nx*=*px*/*stepx*, *Ny*=*py*/*stepy*) structural relaxations. Although a small step leads to a high resolution of the potential energy variation surface as a function of the translation vector. In most of the GB structural relaxation, a value of 0.5 Å was employed for both stepx and stepy. Parts of the relaxed GB structures are shown in Fig. 2.

Besides for the GB stuctures, low-index surfaces (1 0 0) and (1 1 0) were also built to investigate annihilation mechanism in nano-porous (NP) W. The model size has been checked to be large enough to avoid the interaction of a defect with the free surface in the direction normal to the GB plane, and the interaction of the defect with the other free surface in the surface model.

Both the bond-order potential (BOP) that includes three-body contributions and angular dependence [47] and the embedded-atom method (EAM) [48] were used for investigating the V-SIA interaction near the GB in W. The inter-atomic potential proposed by Mendelev *et al* as part of their EAM potentials [49] (Potential 2 in Ref. [49]) was used to model the inter-atomic interaction in Fe. The EAM potential [50] was also used to describe the atomic interaction in Cu.

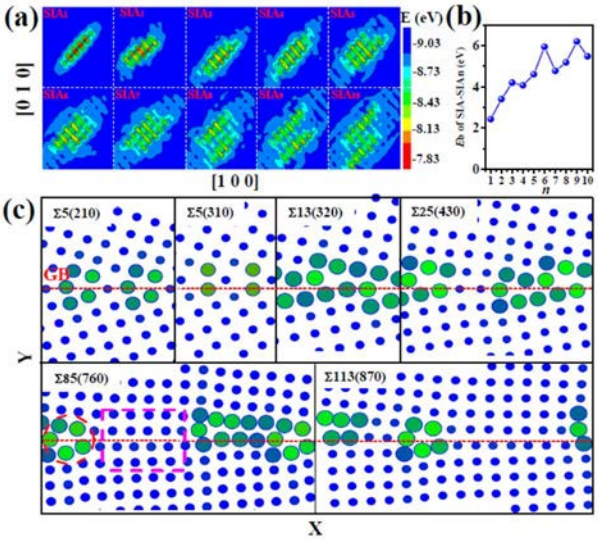

FIG. 2. GB models for MD, MS and OKMC simulations of the V-SIA$_n$ behavior near the GB in W. (a) Configurations of the SIA$_1$–SIA$_{10}$ in bulk W. Here, a SIA$_n$ is characterized by the potential energy contour. The correspondence of the color to the energy is presented in the color bar on the right side. (b) Binding energy (E_b) of a SIA with a SIA$_n$ in bulk W. (c) Atomic GB models for calculating the energetic and kinetic behavior of the SIA$_n$ near the GB. Here, the atoms are colored with their potential energies. The red dashed line indicates the GB position. To highlight the GB region, the atoms that have energy deviation higher than 0.1 eV from the bulk value, are represented by bigger sized spheres. For the GBs Σ5 (2 1 0), Σ5 (3 1 0), Σ13 (3 2 0), Σ25 (4 3 0), Σ85 (7 6 0) and Σ113 (8 7 0), the axis X is along the [1 $\bar{2}$ 0], [1 $\bar{3}$ 0], [2 $\bar{3}$ 0], [3 $\bar{4}$ 0], [6 $\bar{7}$ 0] and [7 $\bar{8}$ 0] directions, respectively. Correspondingly, the axis Y is along the [2 1 0], [3 1 0], [3 2 0], [4 3 0], [7 6 0] and [8 7 0] directions, respectively.

2.2. Definition of Defect Formation Energy Near the GB and Surface

The V/SIA formation energy at site α was defined as:

$$E_f^\alpha = E_1^a - E_0 \pm E_{coh}, \tag{1}$$

where positive sign corresponds to the V and a negative one corresponds to the SIA. E_{coh} is the cohesive energy per atom in a perfect bulk, which is −8.89, −4.12 and −3.54 eV in W, Fe and Cu, respectively. E_1^a and E_0 denote the total energies of the simulation cell with and without the V or SIA, respectively. The initial site of the SIA near the GB/surface was obtained by adding $0.25a\times\vec{e}$ to the position of a lattice site; here a is the lattice constant, $\vec{e}$ is the unit vector along <1 1 1> in W, <1 1 0> in Fe and <1 0 0> in Cu. The energy of the system with a V or SIA was minimized by using the steepest descent method. The reduction in the defect formation energy compared to the bulk value was termed as the defect binding energy with the GB/surface or the defect segregation energy. A positive value of the segregation energy indicates that it is energetically favorable for a defect to segregate to the defect sink. A negative value of V formation energy often indicates the instability of the site [32, 35–38, 40, 41, 43].

The SIA$_n$ formation energy in the bulk was defined as:

$$Ef_{SIAn}^{bulk} = E_{SIAn}^{bulk} - E_{bulk} - nE_{coh}, \tag{2}$$

where E_{SIAn}^{bulk} and E_{bulk} are the total energies of the bulk simulation cell with and without the SIA$_n$, respectively. E_{coh} is the cohesive energy per atom of a perfect bcc lattice, which is −8.90, −6.82, and −4.12 eV for W, Mo, and Fe , correspondingly.

The binding energy of one SIA to the SIA$_n$ was defined as:

$$Eb^{bulk}_{SIA-SIAn} = Ef^{bulk}_{SIAn+1} - Ef^{bulk}_{SIAn} - Ef^{bulk}_{SIA} \, . \tag{3}$$

For the SIA$_n$ at site α near the GB, its formation energy was defined as:

$$Ef^{GB,\alpha}_{SIAn} = E^{GB,\alpha}_{SIAn} - E_{GB} - nE_{coh} \, , \tag{4}$$

where $E^{GB,\alpha}_{SIAn}$ and E_{GB} are the total energies of the GB system with and without the SIA$_n$ at site α, respectively.

The binding energy of the SIA$_n$ to the site α at the GB was defined as:

$$Eb^{GB}_{SIAn-GB} = Ef^{bulk}_{SIAn} - Ef^{GB,\alpha}_{SIAn} \, . \tag{5}$$

V formation energy was defined as:

$$E^{f,\alpha}_{V} = E^{\alpha}_{V} - E + E_{coh} \, , \tag{6}$$

where E^{α}_{V} and E are the total energies of the system with and without a V at site α, respectively.

To put a SIA$_n$ at the site near a GB, an atom in the vicinity of the GB was selected as the reference point. Then, the bulk coordinate system [1 0 0]-[0 1 0]-[0 0 1] was transformed to the GB coordinate system, e.g. [0 0 1]-[1 $\overline{3}$ 0]-[3 1 0] in Σ5 (3 1 0)/[0 0 1]. Assuming $\vec{e}_x$, $\vec{e}_y$ and $\vec{e}_z$ are three unit and orthogonal vectors in the GB coordinate system, the position of the atom in the new system is [$r \bullet \vec{e}_x$, $r \bullet \vec{e}_y$, $r \bullet \vec{e}_z$] where *r* is the atom position in the bulk. The initial configuration of the SIA$_n$ near the GB was thus created using above notations for bulk SIA$_n$, which was then relaxed at 0 K via the steepest descent method.

To move the SIA/V from one of its locations to another nearest location, the SIA/V jumped $(\sqrt{3}/2a_0/N)\vec{e}_{111}$ each time. Here, a_0 is the lattice constant and *N* for the SIA varies from four to seven and for the vacancy is one; $\vec{e}_{111}$ is the unit direction vector along <111> pointing towards the GB. For the SIA, $\vec{e}_{111}$ has a specific direction while for the V, $\vec{e}_{111}$ has several directions starting from the V, e.g. eight directions in the bulk along the line from the V to its first nearest neighboring atoms. After moving the SIA/V, the initial and final configurations were relaxed by using the steepest descent method, which then acted as the end configurations of the nudged elastic band (NEB) method (a widely used standard algorithm that explores the potential energy surface at 0 K [51]). After the relaxation of the initial path, the minimum energy path was then determined. The number of images along the diffusion path is 30.

2.3. Details for MS Investigation of the SIA Segregation, Emission and Annihilation Near the GB/Surface

2.3.1. Details for MS calculation of the kinetics for the IE-induced annihilation

First, the transition region lying between the bulk region and the trapping region of the GB/surface for the SIA was determined by calculating the SIA formation energy near the GB/surface. Then, a SIA within the transition region was forced to migrate towards the GB/surface according to their well-known respective migration mechanisms until the SIA was trapped by the GB/surface. For each movement of the SIA, the migration path was optimized by using the NEB method [51] known as a standard algorithm for finding the minimum energy path of transitions. Consequently we obtained the energy landscape along the path and the potential well for the SIA near the GB/surface. During the last transition, the system moved from a meta-stable state S2 to a stable state S1 at the sink (Fig. 3). The state images on the path from S2 to S1 were recorded after each NEB optimization in order to construct an initial SIA emission path. We obtained the system configuration $\vec{R}_{\sin k}$ as a SIA is trapped at the sink (state S1 in Fig. 3), and $\vec{R}_{near}$ as the SIA is located at a meta-stable state S2 (Fig. 3).

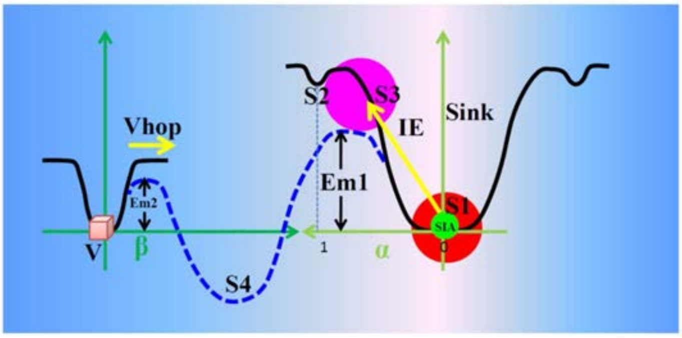

FIG. 3. Illustration of the annihilation of a V near the GB/surface with a SIA trapped at the GB/surface via V-hop or SIA emission. The black curves centered on the V and SIA represent the energy landscape of the V and SIA, respectively as they are far apart. The dash blue curve illustrates the energy landscape as the V and SIA approaches to each. The red cubic and green sphere represent the V and SIA, respectively. Em1 and Em2 are the annihilation energy barriers induced by the IE and V hop, respectively. S1 and S2 denote the system states with a SIA at the GB/surface and near the GB/surface, respectively. S3 denotes the temporal state image lying between S1 and S2, while S4 denotes the system state after the annihilation of the V-SIA. Note that, state S3 is unstable without a V nearby and it is only used for constructing an initial IE-annihilation path. The red and pink spheres represent the annihilation region around a static SIA and partially emitted SIA from the GB/surface, respectively. Symbols α and β denote the degree for the SIA emission and V hop, respectively. A value of zero for α/β corresponds to a static SIA/V, while a value of one corresponds to the movement of the SIA/V to its nearest state from the current state. Reproduced courtesy of Elsevier [4450861388662].

One could construct an initial IE path by:

$$\vec{R}_{IE} = \vec{R}_{\sin k} + \alpha(\vec{R}_{near} - \vec{R}_{\sin k}), \tag{7}$$

where α denotes the emission degree ranging from 0 to 1 and $\vec{R}_{IE}$ is the system configuration after the SIA is partially emitted. A zero value of α corresponds to a static SIA at the GB/surface, while a one value of α corresponds to the complete emission of the SIA from state S1 to S2. As α is larger than zero and less than one, the SIA was partially emitted.

Then, we determined the annihilation sites around the path by introducing a V near the path and calculating the system energy after relaxation at 0 K. The annihilation was confirmed by comparing the system energy with a SIA and V to that of a perfect system or directly visualizing the system configuration after relaxation. The annihilation energy barrier was obtained by using the NEB method [51]. The calculation region was gradually extended until no annihilation sites were found.

2.3.2. Details for MS calculation of the annihilation volume as a function of the annihilation energy barrier

To characterize the annihilation ability of a SIA trapped at the GB/surface, we calculated the annihilation volume (V_{ann}), which was defined as the number of sites at which a V recombines with the SIA. The V_{ann} of a static SIA at the GB/surface was determined via calculating the V formation energy of the sites around the SIA. In this case, α in Eq. 7 is zero. The annihilation energy barrier is zero and the SIA spontaneously recombines with a V located within the annihilation region.

As α in Eq. 7 is not zero, the V_{ann} is actually the cumulative number of annihilation sites as a function of the annihilation energy barrier. For a specific V, it has multiple paths to be recombined with the SIA with different energy barriers. The path with the lowest annihilation energy barrier was chosen as the most favorable one. The V_{ann} was thus defined as:

$$V_{ann} = V_{ann}(E_{ann}) = \sum\{E^{i}_{ann} < E_{ann}, i = 1, Nv\}, \tag{8}$$

where E_{ann} is the variable of the annihilation energy barrier, E^{i}_{ann} is the lowest annihilation energy barrier for a certain V near the SIA, N_v is the number of sites at which Vs were produced and further annihilated via the IE. After the partial emission of the SIA from a GB/surface, the front atom composed of the SIA was allowed to jump one step to as far as the third nearest neighbors of the annihilation region. From the view of the V, the V of the first, second and third nearest neighbors of the annihilation region was allowed to jump one step to arrive at one of the sites of the annihilation region.

2.3.3. Computational details for MS simulations of the SIA_n behavior at the GB

The migration of the single SIA and SIA_2 at the GB was calculated by using the NEB method. The stable locations for the SIA and SIA_2 at the GB were firstly obtained by calculating the formation energy of the possible configurations. The initial configuration was produced by inserting an atom at the center of two nearest atoms. However, the initial migration path was hard to create, since the migration mechanism of the SIA and SIA_2 at W GBs is very complex and unknown intuitively, as suggested by the diffusion of the SIA at copper GBs [52]. Here, we developed a method that efficiently calculated the migration of the SIA and SIA_2 along W GBs. We took advantage of the knowledge that the repulsive interaction of the SIA with the surrounding atoms on the migration path leads to a high migration energy barrier along this path. The shorter the distance of the atom moves, the lower the migration energy barrier may be. Thus, a SIA initially residing at the open space was forced to move to another stable site from one stable site. During this process, several atoms were induced to move. Assuming the initial and final states for these atoms to the collector *C1* $\{A_i, i=1, N\}$ (N is the number of atoms involved) and *C2* $\{A_j, j=1, N\}$, respectively, then the favorable guessed migration path $A_i \rightarrow A_j$ was obtained by minimizing the distance between A_i and *C2*. The path was further relaxed by using the NEB method. The favorable migration path for the SIA_2 was similarly obtained.

2.4. Details for the OKMC Investigation of the Dynamic Behavior of the SIA_n Near the GB

Figure 4 shows the models used for the OKMC simulation of the behavior of the SIA_n and V and relevant simplified physical pictures of the interaction among the SIA_n, V and GBs. For OKMC simulations, a square-shaped grain was built with periodic boundary conditions imposed in all three dimensions. The GB was placed at the center of the cell. In the bulk, the V and SIA undergo three dimensional walk along eight directions in a body-centered cubic cell. At the GB, the V and SIA move two dimensionally. In the vicinity of the GB, the V and SIA have two motion degrees, segregation into the GB or escape from the GB. The annihilation rate of the V–SIA pair depends on the location of the V and SIA. For the vacancy diffusion in the bulk, only transitions from the vacancy to its eight first-nearest neighbors were included in the model. A relatively sliding SIA cluster was approximated by a tightly bound string which moves one-dimensionally. The real energy landscape of the V near the GB (the energy variation of the system with the V distance from the GB) was approximated by a squared potential well. The energy barrier near the GB was assigned to be one half of the bulk value considering GB-enhanced diffusion or annihilation of the defect. The width of the well was defined as the interactive range of the defect with the GB. The depth of the well is the energy reduction as the defect segregates into the GB from the bulk (binding energy). The event rates for the defect object were calculated by $r = v_0 \exp(-E_a / k_B T)$, where v_0 is the vibration frequency of atoms in metals and was generally assumed to be 10^{12}/s. The Boltzmann constant k_B has a value of 8.617×10^{-5} eV/K. E_a and T are activation energy and system temperature, respectively. Three typical temperatures, 10, 563 and 850 K, were selected based on experimental conditions [7, 8]. At 10 and 563 K, the SIA in the bulk region became activated whereas the V remained immobile. At 850 K, both the SIA and the V became activated [37]. The grain size was chosen to 50 nm.

During the OKMC simulations, we found it challenging to bridge the timescale as the system contains multiple objects with different levels of mobility. On one hand, the challenging comes from the large gap between the mobility of the single SIA and that for the V as both of them locate at the homogeneous space, e.g., in the bulk and at the GB. The timescale spans from 10^{-12} s to one hour at the considered temperatures. Given this, the behavior of the defects was simulated separately. By analyzing the motion trajectories of the SIA/V, the possible dynamic annealing picture was deduced. On the other hand, the preferential segregation of the SIA to the GB leads to its separation from both the bulk V and the remaining SIA in the bulk. The subsequent evolution timescale of the system relates to the mobility of the SIA in the bulk, at the GB and the mobility of the V in the bulk. During the time that one type of defects jumps one step, another type of defects jumps *N* step (for example, at 850 K, the SIA jump 10^{12} steps along the GB of Σ5(2 1 0) as bulk V jumps one step). As *N* exceeds the maximal step of OKMC simulations, e.g., 10^7, the defect was artificially cooled. The system was considered to have reached equilibrium. By adopting this approximation, the annihilation fraction and the SIA-clustering fraction at the GB were underestimated.

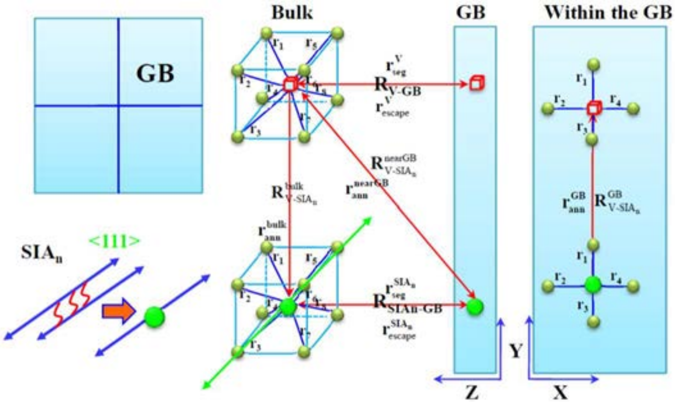

FIG. 4. Schematic illustration of the models used for the OKMC simulation of the macroscopic behavior of the SIA$_n$ and V and relevant simplified physical pictures of the interaction among the SIA$_n$, V and GBs. The blue line indicates the GB position and L denotes the grain size. Axis Z is normal to the GB, while axes X and Y are parallel to the GB. The red cubic and green spheres represent a V and a SIA$_n$, respectively. $R^{bulk}_{V-SIA_n}$ and $R^{GB}_{V-SIA_n}$ stand for the distance from the V to the SIA$_n$ that are both in the bulk and at the GB, respectively. $R^{nearGB}_{V-SIA_n}$ denotes the distance of the bulk V to the SIA$_n$ trapped at the GB. R_{V-GB} and R_{SIA_n-GB} denote the distance to the pure GB from the V and the SIA$_n$, respectively. The symbols r1, r2, r3, r4, r5, r6, r7, r8 denote the rates along eight directions in a body-centered cubic cell for the V diffusion in the bulk. For SIA$_n$, however, r3 and r5 are the rates for the SIA$_n$ moving forward and backward along <111> as illustrated by the green double-headed arrow, while r1, r2, r4, r6, r7, r8 are rates for SIA$_n$ rotation in the bulk. The symbols r_1, r_2, r_3, r_4 are rates for the V and SIA$_n$ migration along four directions within the GB. The symbols r^V_{seg} and $r^{SIA_n}_{seg}$ denote the segregation rates for a V and a SIA$_n$, respectively. The corresponding rates for a V and an SIA$_n$ to migrate out of the GB are represented by r^V_{escape} and $r^{SIA_n}_{escape}$. The annihilation rates for a V-SIA$_n$ in the bulk, near the GB and at the GB are denoted by r^{bulk}_{ann}, $r^{near\mathrm{GB}}_{ann}$ and r^{GB}_{ann}, respectively.

3. BASIC SEGREGATION AND ANNIHILATION OF THE V AND SIA NEAR THE GB

Many of the results presented here were discussed in detail previously [35–44]. Here we give main results from these calculations.

3.1. Primary Radiation Damage in Bcc W GB

We start with the simulation of displacement cascades near a Σ5(310)/[001] symmetric tilt GB in bcc W at 600 K. The system was initially relaxed at 600 K for 10 picoseconds (ps) with a time step of 2 femtoseconds (fs) to reach thermal equilibrium. Then, an atom at 35 Å on one side of the GB and located at the center of the plane parallel to the GB plane was selected as the primary knock-on atom

(PKA); the atom was given 6 keV of kinetic energy with its velocity directed perpendicularly toward the GB. The PKA induced a collision cascade and a smaller time step of 0.1 fs was used for an additional 2 ps after which the time step was increased back to 2 fs for about 10 ps to remove defects near the GB. Several typical snapshots of defect generation and annihilation are shown in Fig. 5.

It can be seen that for the applied PKA, the cascade center basically locates at the GB plane (Fig 5(a)). At about 0.5 ps, the cascade reaches its maximal size of about 3 nm. Comparing Fig. 5(a) with (b) or (b) with (c), one sees that radiation-generated SIAs move towards the GB, and after about 4 ps all the SIAs are annihilated or trapped into the GB. However, the motion of Vs has not been observed. Three Vs survive near the GB (Fig. 5(d)) and they still remain immobile during the subsequent simulations at 600 K. This special defect structure, with V dominated near the GB and SIA highly localized at the GB, has been observed previously in W [53], Ni [54] and Cu [32]. It will strongly modify the GB structure and thus affect further evolution of defects in the GB neighborhood, such as the annihilation of the Vs that survive near the GB at the MD time-scale. Apparently, the GB region is extended. The semi-influence range of the GB extends to about 10 Å locally (Fig. 5(d)) from 5 Å of the pristine GB, which can be attributed to the trapped SIAs at the GB.

In the following sections, we show how Vs and SIAs segregate into the GB and how the surviving Vs near the GB above are annihilated by investigating energetics and kinetics of V/SIA segregation and V-SIA annihilation near the GB, mainly using MS.

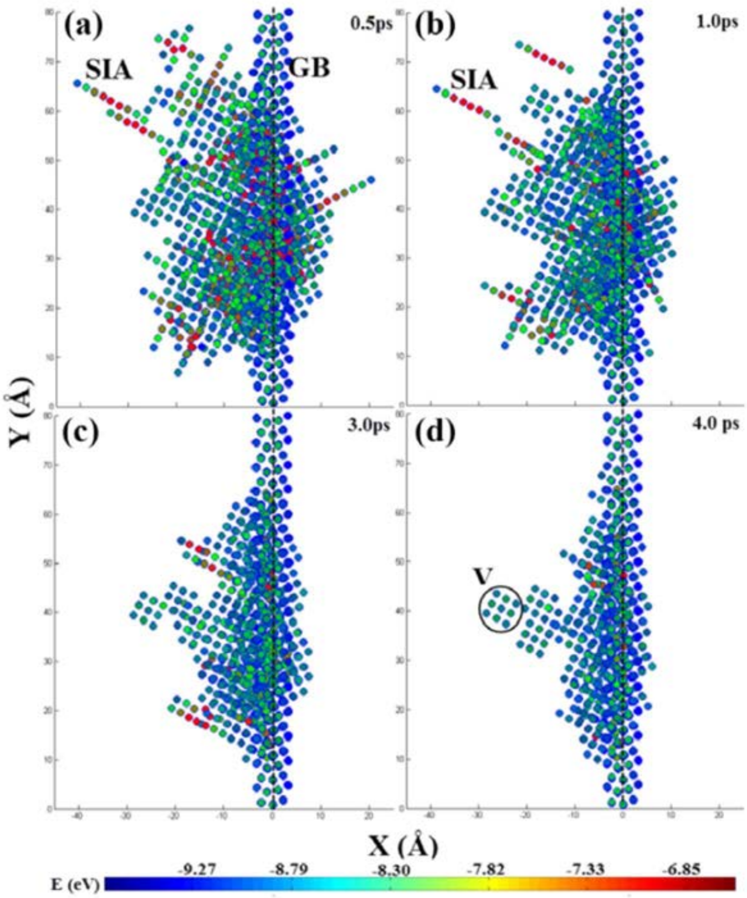

FIG. 5. Representative snapshots of a MD simulation of displacement cascades near a Σ5 (310)/[001] symmetric tilt GB in W at 600K. Here the GB is indicated by a dashed red line. SIA is for interstitials and V represents vacancies. Atoms are colored by their potential energy; atoms with energy deviation from the bulk value less than 0.2 eV are treated as non-defective and are not shown. In this display scheme, a vacancy is characterized as a 14-atom cluster, because of the increase in energy of the 8 first nearest neighboring atoms and 6 second nearest neighboring atoms of the vacancy. The axes X and Y are along [310] and [$\overline{1}$ 30], respectively.

3.2. Energetics of V and SIA Segregation Near the Pure GB

The present MD simulations in W have clearly demonstrated that SIAs are quickly and easily trapped at the GB, but Vs are immobile in the time scale of MD. In order to show energetically whether a SIA/V has a tendency to flow into a W GB, we calculate the single V/SIA formation energies at various locations near the GB. During the calculation, first step is to create one V or SIA near the GB. To introduce a V, a host atom at a particular site α within 40 Å of the GB was removed and then an energy minimization algorithm such as the steepest descent method was used to minimize the energy of the GB structure. While for the introduction of a SIA, we first search a perfect bcc unit cell from the site α, if it was found, then an initial configuration of the crowdion along a <111> direction was created. If there exists no such a perfect unit cell like in the two nearest layers of the GB where the coordinate number is lower compared with that in the bulk, an atom was inserted in the center of two nearest neighbors. After that, the simulation cell was relaxed, using the same algorithm as in the case of V.

Figure 6 shows the V/SIA formation energy profile near the GB. It exhibits some noteworthy and remarkable features. First, we note that the formation of both the V/SIA is always endothermic within a certain range of the GB, 9.4 Å (26.5 Å) for the V/SIA. And the defect energy generally decreases as the defect moves from the bulk to the GB. Thus, it is energetically favorable for a V/SIA to reside at the GB. The decrease in formation energies implies an attractive interaction between the V/SIA and the GB. Thus, the defects formed in the bulk can migrate to the GB at elevated temperatures, forming defect denuded zones near the GB [15, 55, 56].

More remarkably, there is a big difference in the sink strength for Vs/SIAs. The V formation energy decreases only by ~0.86 eV, but the reduction is as much as 7.5 eV for the SIA in the GB core. This is a surprisingly large reduction in the SIA formation energy, approximately 74% of the value in the bulk and 23% for the V. The larger amount of reduction in formation energies indicates that the system energy is decreased more through SIAs occupying GB sites, rather than Vs. In other words, SIAs will preferentially locate at the GB.

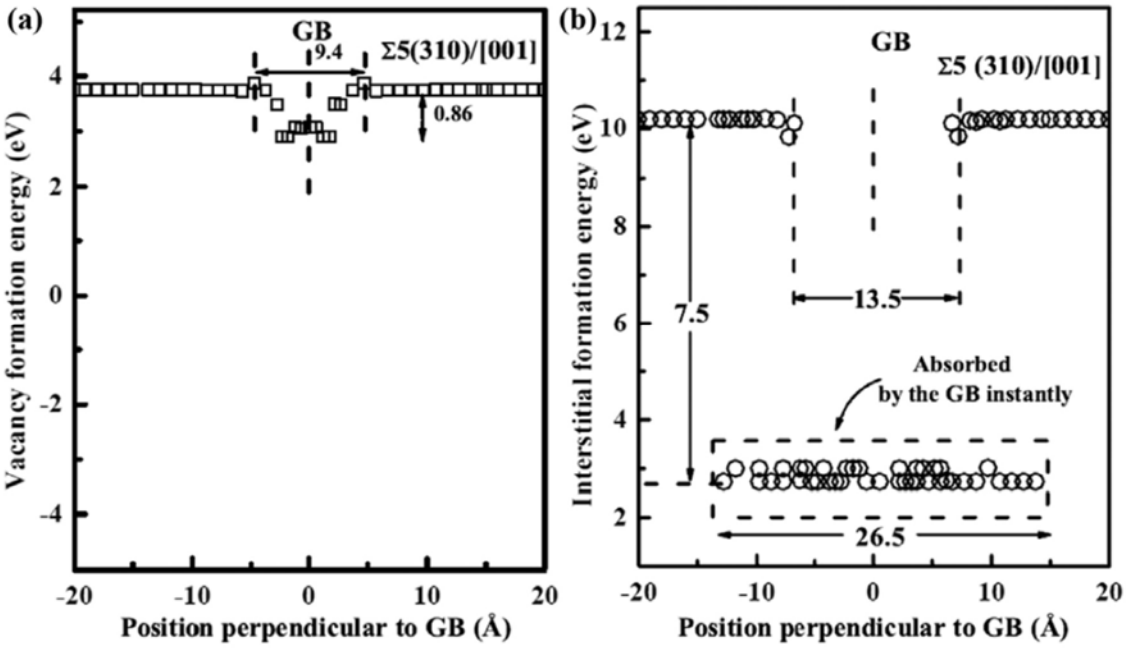

FIG. 6. Defect formation energy profiles of a pristine symmetric Σ5(310)/[001] GB in W for (a) Vs and (b) SIAs.

We also find that the trapping sites for Vs and SIAs exhibit rather different features. For Vs, there exists a transition region between the bulk and the GB core, where a V locates at the meta-stable site. And a V must overcome barriers jumping from one trapping site to another with lower energy. Thus, the segregation of Vs near the GB should be described by the Layer-by-Layer Model [57]. For SIAs, however, there exist several layers near the GB during which a SIA will be instantly trapped into the GB via a barrier-free process, as observed in the minimization of the GB energy. Out of this region (within the dashed box in Fig. 6(b) that has a range of about 26.5 Å), the SIA only with certain orientation will spontaneously segregate into the GB, which may arise from the anisotropic stress field of the GB. Just like previously reported, SIAs in Ni change their direction as they approach the GB, because of the stress field near the GB [58]. Therefore, the interaction of SIAs with the GB in W is orientation-dependent. In addition, there are two types of sites for the SIA at the GB core, one meta-stable with energy about 0.25 eV higher than stable ones.

For the other two GBs of W (Σ13(320)/[001] and Σ25(430)/[001]), we obtain similar results. The GB influence range for Vs (SIAs) is 9.5 Å, 14.4 Å (19.6 Å, 18.5 Å) for Σ13 and Σ25, respectively, and the segregation energy is 1.75 eV, 2.00 eV (7.8 eV, 7.9 eV). Thus, it clearly demonstrates that the GB indeed serves as a sink for irradiation-produced Vs (SIAs), and the GB has a preferential absorption of SIAs over Vs.

3.3. Kinetics of V and SIA Segregation Near the Pure GB

Next, we investigate the kinetic process for Vs and SIAs jumping from the W bulk to the GB. Using the nudged-elastic-band (NEB) method [51], we calculate the V and SIA diffusion barriers towards the GB as displayed in Fig. 7(a). Two nearest ones, within all sampled defect configurations completely relaxed for calculating defect formation energy above, have been used as the initial and final states. Between the two states are inserted 28 images. Parts of defect configurations are employed to construct defect migration paths. One typical path for V diffusion is shown in Fig. 7(b).

Figure 7(a) suggests that the defect diffusion barriers are greatly reduced when Vs (SIAs) come close to the GB. For Vs, the barrier in the bulk is as high as about 1.8 eV, while it is as low as 1.2 eV, 0.7 eV and 0.5 eV in the several layers near the GB. In particular, the SIA energy barrier is reduced to zero, because SIAs within a certain range of the GB are instantly trapped at the GB; that is why one typical path only for V diffusion is given in Fig. 7(b). Just as the diffusion path shows, a V overcomes a low energy barrier of 0.42 eV to move towards the GB; meanwhile, the system energy reduces 0.86 eV when the V locates at the GB. While for the SIA near the GB, it diffuses to the GB via a barrier-free process, leading to a reduction of 7.5 eV in the system energy once it is trapped at the GB (Fig. 6). Thus, kinetically it becomes easier for Vs and SIAs to diffuse towards the GB with the reduced defect diffusion energy barrier near the GB as alternative driving force, besides the lowered defect formation energy in the neighboring region of the GB as mentioned above (Fig. 7).

Therefore, energetically or kinetically GBs are sinks for Vs and SIAs with the preference for SIAs, due to exceptionally larger segregation energy, an extremely lower diffusion barrier, and a much wider interactive range for the SIA.

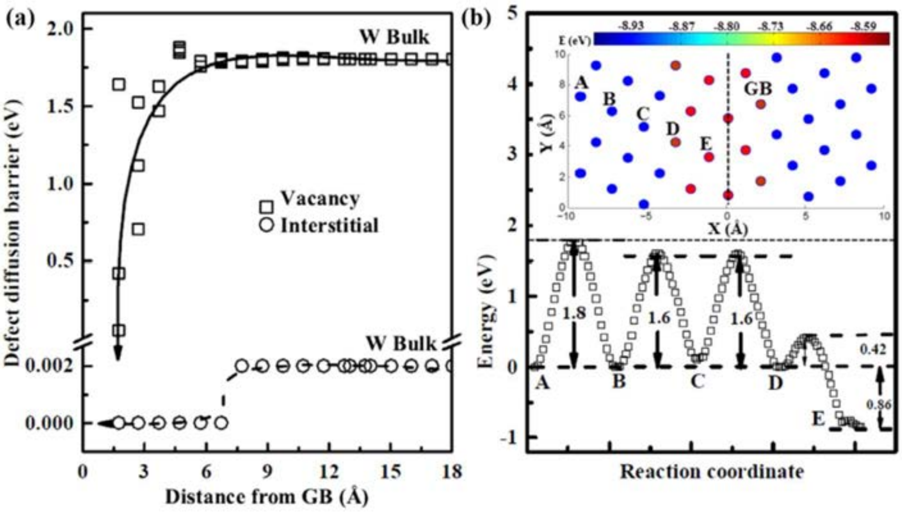

FIG. 7. The diffusion of Vs and SIAs near the pristine GB. (a) The V and SIA diffusion energy barriers as a function of distance from a pristine GB. The arrow lines are only to guide the eyes. (b) One path for V diffusion from the bulk to the GB. The system energy at A has been selected as the reference energy. After the V migrating from A to E, the system energy decreases by 0.86 eV. The axes X and Y are along [310] and [$\bar{1}$ 30], respectively.

3.4. Modifications of the GB by the Segregated SIAs

Our MS calculations above have shown that SIAs are preferentially trapped into the GB. It is consistent with the observation in the MD simulations that a special defect structure forms with V dominated near the GB and SIA highly localized at the GB after several ps. In order to elaborate the interaction between the V in the vicinity of the GB and the GB that has trapped SIAs, we intentionally placed one SIA near the GB. And then the system was relaxed at 300 K for 10 ps to allow the SIA to find the lowest energy site. By the end of the MD simulation, the added SIA became incorporated into the GB. Then the steepest descent method was used to minimize the energy and structure of the GB. Alternatively, we also inserted eight SIAs at once near the GB in another system with possible clustering of SIAs at the GB in consideration. During the relaxation of these systems, the SIAs were spontaneously trapped into the GB and reside at the sites with low energy as indicated in the dashed box in Fig. 6(b). After the GB structure with the SIAs is optimized, the V formation energy within a certain range of the GB is calculated.

Figure 8 shows V formation energy profiles in the vicinity of the loaded GB with SIAs. It can be seen, the most noticeable difference in the behavior of Vs between the loaded GB and the pristine GB is the greatly reduced formation energy, as exemplified in Fig. 8(a). What is more, the influence range of the GB extends from 9.4 Å in the pure GB to 11.6 Å for the GB loaded with one SIA and 19.2 Å for the GB having eight SIAs. Another prominent feature is the appearance of the sites with negative V formation energies surrounding the SIA trapped at the GB for the two loaded GBs. This indicates an exothermic process to create a V at one of these sites and the resulting reduction in the system energy. Further investigation shows that, the annihilation actually occurs between the V located at one of these sites and an SIA trapped at the GB, leading to the healing of the damaged GB. Note that the structural optimization is preformed at 0 K when calculating the V formation energy, and thus the annihilation above is a barrier-free process. Therefore, the sites with negative V formation energies in Fig. 8 are unstable; all of these sites form a spontaneous annihilation region around the SIAs trapped at the GB. It means that irradiation-created Vs at these sites or the Vs coming from bulk to these sites will be instantly annihilated with the SIA. Besides, the surviving Vs near the GB in MD simulations (Fig. 5(d)) have to overcome some energy barriers to be recombined with the SIA. Thus, the energy barrier of the V diffusion near the region is calculated using NEB method, as shown in Fig. 9. The configurations that are fully relaxed for calculating V formation energies in Fig. 8 have been used as the initial and final states.

Comparing Fig. 9 and Fig. 7(a), we find that the barrier of V diffusion towards the GB is further reduced after the GB traps some SIAs. And when the V enters the spontaneous annihilation region, it is instantly recombined with the SIA. That is why the annihilation energy barrier has been defined as the one that a V overcomes before reaching the border of the annihilation region. To clearly show the change of the system energy as one V approaches the GB with SIAs, we designed one diffusion-annihilation path as displayed in Fig. 9. A V initially created at *A*, overcomes the barriers of 1.8, 1.1, 0.74 eV sequentially and then overcomes a low barrier of 0.34 eV, annihilating one SIA at the GB. The annihilation induces a reduction of 5.7 eV in the system energy. Therefore, the Vs near the GB with SIAs localized at the GB in Fig. 5(d) can be annihilated via a low-barrier process.

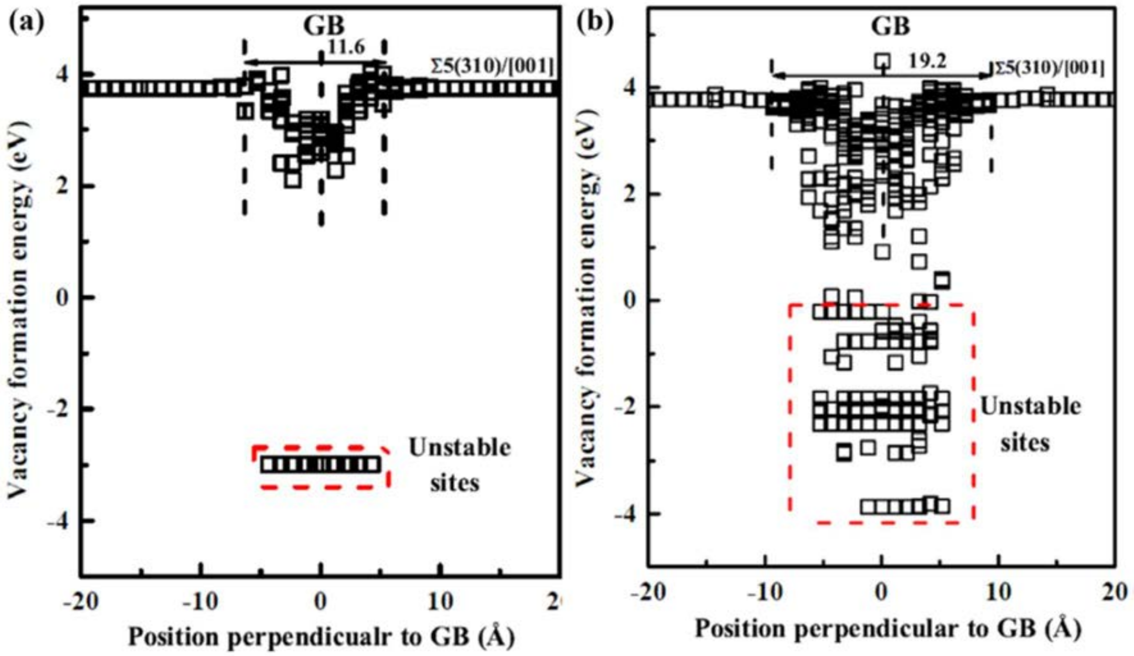

FIG. 8. V formation energy profile of a GB loaded with one (a) and eight SIAs (b).

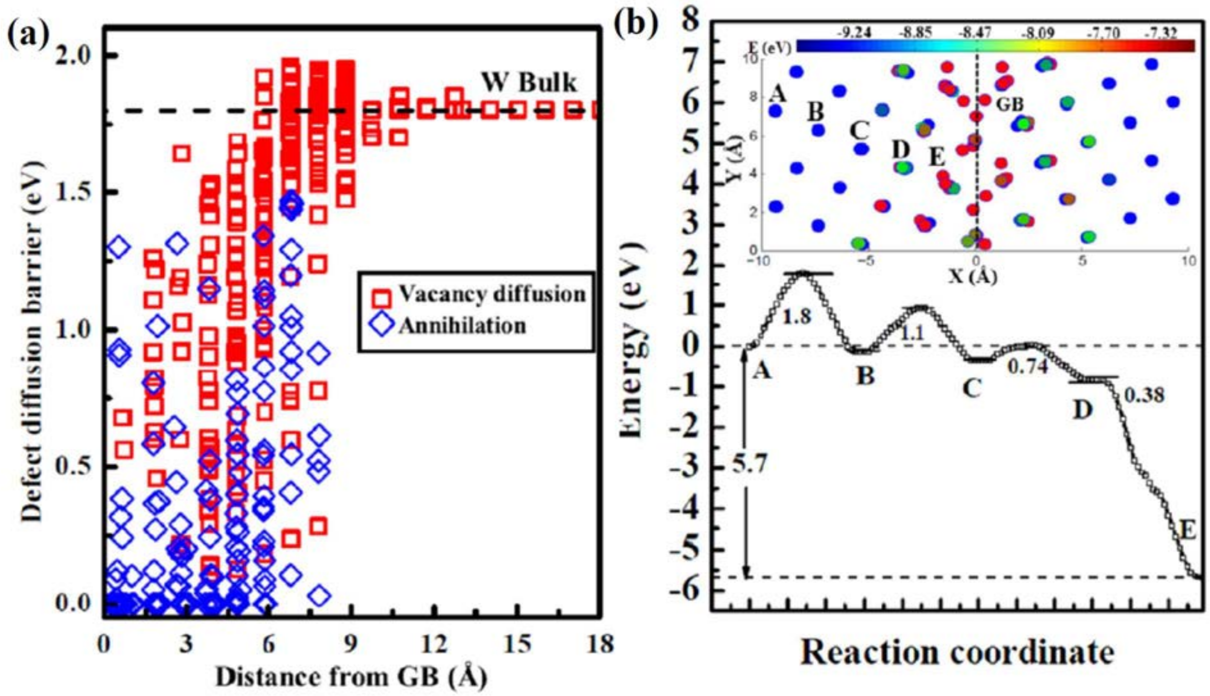

FIG. 9. (a) The V diffusion and annihilation barriers as a function of distance from a GB loaded with eight SIAs. (b) One annihilation path for the V near the GB with SIAs trapped at the GB. The axes X and Y are along [310] and [$\overline{1}$ 30], respectively.

4. STATIC EMSSION OF INTERSTITIALS

4.1. V-SIA Annihilation Near the GB/Surface Induced by the Spontaneous IE

To obtain the binding energy (E_b) of the SIA with the GB/surface, we calculated the SIA formation energy profile (Eq. 1) near the GB/surface in W, Fe and Cu, as presented in Fig. 10. Fig. 10(a) suggests that the system energy decreases sharply as the SIA is within the several layers of the GB/surface coming from the bulk. Thus, there is an energetic driving force for the SIA to segregate to both the GB [32–38, 41, 43, 44] and the surface [40]. The examination of the structure with a SIA before and after relaxation suggested that the SIA produced near the GB/surface spontaneously segregated to the core of the GB/surface during the structural relaxation at 0 K, which has been observed near W and Fe GBs [35, 37, 53]. It can also be seen, E_b depends on the system. E_b is over 7.0 eV in NC and NP W, and ranges from 1.5 to 3.0 eV in NC/NP Fe and Cu. Figure 10(b) suggests that for different W GBs, E_b varies from about 7 to 10 eV. Therefore, all the investigated W GBs modeled by both the BOP and EAM potential strongly bind with the SIA. Although E_b is as small as 1.5 eV for the SIA near a Cu GB, the SIA still needs about 10^{13} s to come out of the GB at a typical experimental temperature of room temperature. Therefore, these values of the E_b are large enough for the GB/surface to tightly bind the SIA. Once the SIA is trapped by the GB or surface, it is indeed hard for the SIA to be emitted from a pure GB/surface.

Due to the higher mobility of the SIA compared to the V, the preferential segregation of the SIA to the GB/surface will leave amount of Vs behind near the GB/surface before the segregation/annihilation of the V [32, 35, 37, 40, 53, 54]. To explore the effect of the V on the SIA behavior near the GB/surface, we introduced a V near the stable SIA with lowest SIA formation energy and calculated the V formation energy. We found that the sites near the SIA become unstable as indicated by a negative value of the V formation energy. Examination of the structure before and after relaxation suggests that the V created at one of such sites spontaneously recombines with the SIA during the structural relaxation at 0 K. Such sites compose of a spontaneous annihilation region (SAR). As shown in Fig. 11(a)–(c), the SAR was found at one GB in W, Fe and Cu with different structures. At surface (1 0 0) in the three metals, the SAR is composed of five spontaneous annihilation sites (Fig. 11(d)–(f)). Such small size of the SAR could be ascribed to the open site of the SIA at the surface where the stress around a SIA could be well released. Further calculations on more GBs in W by using the EAM potential [48] suggest that SAR always forms at the investigated 46 W GBs with distinct structures, as indicated by the formation of the unstable sites near the SIA at these GBs (Fig. 11(g)). Figure 11(h)–(m) shows the SAR in six typical W GBs. The SAR was also found around the SIA in W, Fe and Cu bulks [35, 37].

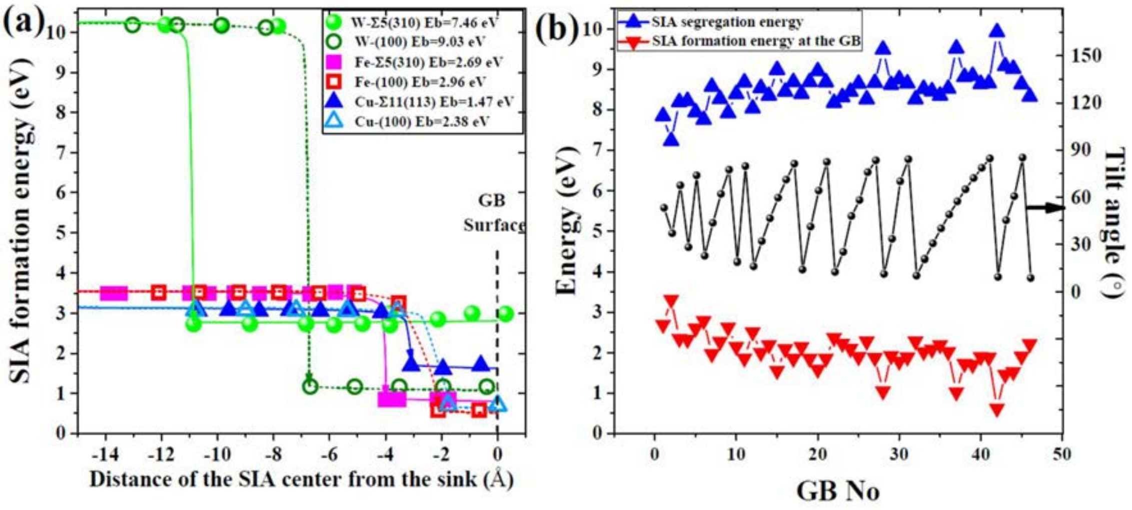

FIG. 10. (a) SIA formation energies as a function of the distance of the initial SIA center from the GB/surface. (b) Variation of the SIA formation energy, segregation energy and tilt angle with the GB number in W. Reproduced courtesy of Elsevier [4450861388662].

To show how the SIA recombines with the V that is located within the SAR, we connected the initial positions of the atoms involved in the annihilation to the final positions of these atoms. As shown in Fig. 11(a)–(f) and (h)–(m), the annihilation process exhibits as the emission of the SIA from the GB/surface towards the V, similar to that observed in Cu [32] and Fe [34]. Depending on the position of the V, the length of the atomic chains involved in the annihilation varies from 1 to 3. The annihilation at the surface involves only two atoms.

In the above visualization method, the intermediate processes of the annihilation were neglected. The recombination was further visualized by displaying the atomic configurations during the annihilation. As shown in Fig. 12(a)–(c), the V near W Σ5(3 1 0)/[0 0 1] remains immobile while the SIA gradually moves towards the V from the GB. In Fig. 12(d), the SIA recombines with the V and then the damaged GB becomes a healed one. Therefore, the annihilation here is indeed via the IE mechanism. Since the annihilation occurs spontaneously, we defined such IE as a spontaneous IE (SIE). The SIE works similarly near the GBs in Fe (Fig. 12(e)–(h)) and in Cu (Fig. 12(i)–(l)) and also near the surface as shown in Fig. 12(m)–(p) for the annihilation near Cu surface (1 0 0). Similar annihilation processes were found near all 46 GBs in W modeled by the EAM potential. Figure 12(q)–(n1) shows the results near three low-Σ high-angle GBs of Σ5(2 1 0), Σ5(3 1 0), Σ13 (3 2 0), one low-angle GB of Σ85(7 6 0), and one GB of Σ109 (10 3 0) with long periodical structural units along the GB. The energy barrier in all the annihilation processes near these GBs/surfaces is zero, as shown by the energy profiles during the annihilation (Fig. 12(o1)). Therefore, it is expected that the SIE may work universally at the GB/surface in W, Fe and Cu. The annihilation in W and Fe bulks (Refs. [37] and [35]) was also found to follow similar processes, involving collective motion of multiple atoms as suggested by the highly correlated displacements curves with time during the annihilation.

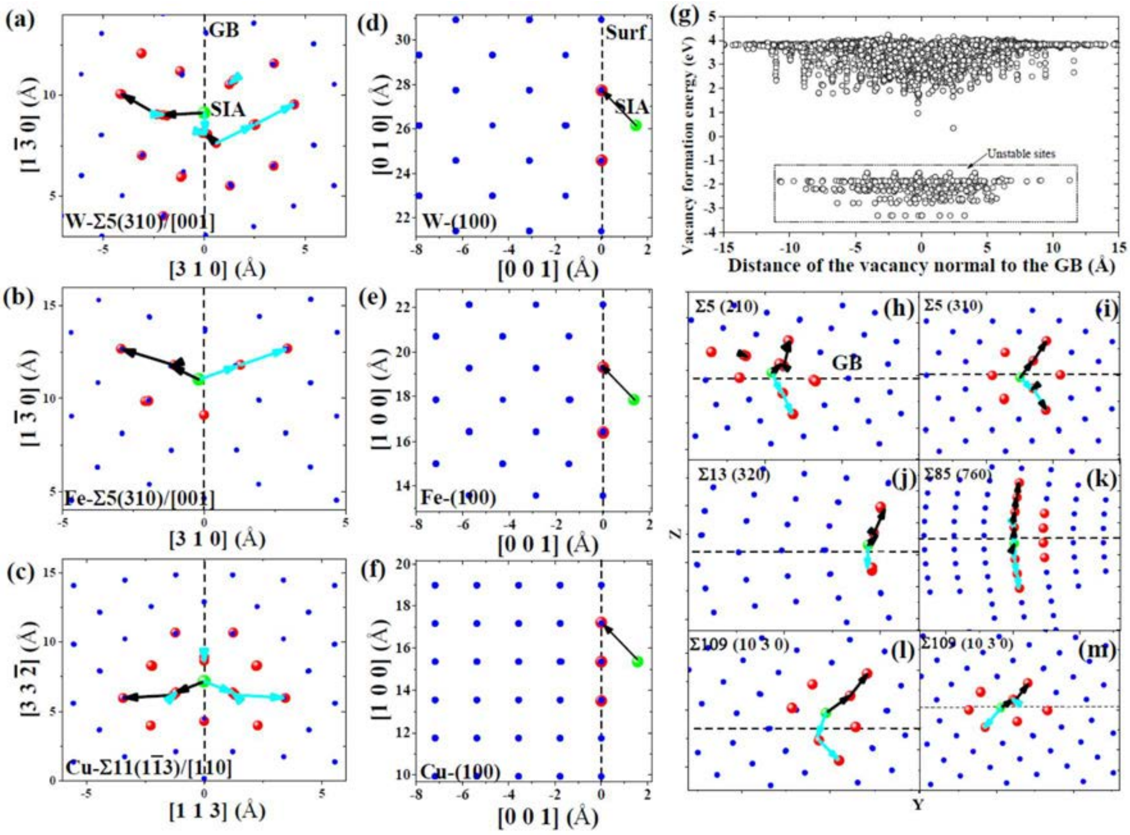

FIG. 11. Spontaneous annihilation region around a SIA (a)–(c) at a GB and (d)–(f) at a surface in W, Fe and Cu. (g) Vacancy formation energy profiles near the GB in W calculated by using the EAM potential. (h)– (m) Spontaneous annihilation region around a SIA at several GBs in W obtained by using the EAM potential. For a (h k 0) GB with a [0 0 1] tilt axis, axis Y is along [k -h 0] and Z is along [h k 0]. In (a)–(f) and (h)–(m), the red sphere represents the site at which a V spontaneous recombines with a SIA trapped at the GB/surface during the GB/surface structural relaxation at 0 K. The green sphere represents the SIA. The lines with arrows were drawn by connecting the atom positions in an initial state to the atom positions in the final state after the annihilation process. The atoms with displacements less than 0.5 Å are considered to be immobile during the annihilation and are not shown. Reproduced courtesy of Elsevier [44508613886662].

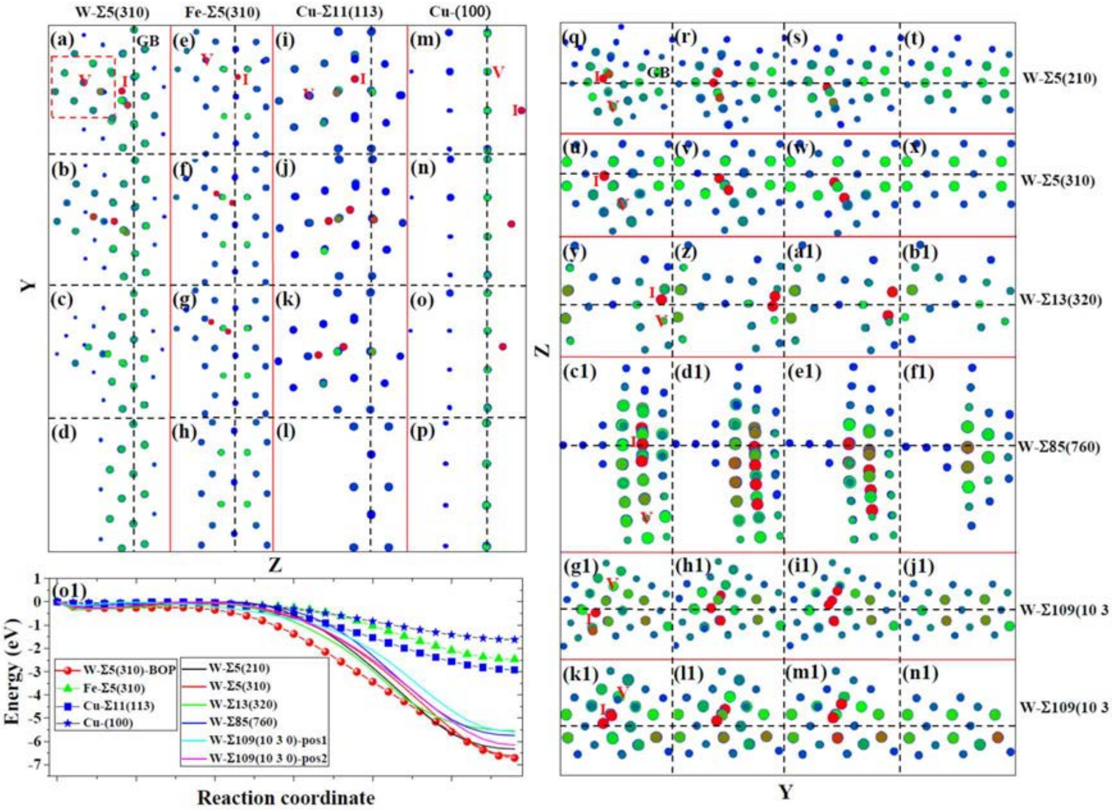

FIG. 12. (a)–(d) Snapshots for the spontaneous annihilation process near the GB Σ5(3 1 0)/[0 0 1] in W, (e)–(f) near the GB Σ5(3 1 0)/[0 0 1] in Fe, (i)–(l) near the GB Σ11(1 1 3)/[1 $\bar{1}$ 0] in Cu, and (m)–(p) near Cu surface (1 0 0). (q)–(n1) results near several GBs in W calculated by using the EAM potential. For a (h k 0) GB with a [0 0 1] tilt axis, axis Y is along [k -h 0] and Z is along [h k 0]. Atoms are colored by their potential energies. The atoms with energy deviation from the bulk value less than 0.05 eV are treated as non-defective and are not shown. To outline the defective atoms, atoms with energy deviation from the bulk value larger than 0.3 eV are represented by big spheres. In this display scheme, a V is represented by an atom cluster composed of its nearest neighboring atoms, as shown by the dash red square in (a). A SIA is often shown as a high energy atom, as marked by symbol I. (o1) Energy profiles on the annihilation paths. Reproduced courtesy of Elsevier [4450861388662].

4.2. V-SIA Annihilation Near the GB/Surface Induced by the Thermally-activated IE

Next we explore whether the V out of the SAR could be annihilated at a low energy barrier and the associated atomic process near the GB/surface. We calculated the energy landscape on a designed IE-induced annihilation path (Eq. 7) near the GB/surface in W, Fe and Cu, as presented in Fig. 13. The landscape on the V-hop induced annihilation path is also given for comparison; the landscape exhibits a similar downhill energetic feature indicating that the SIA-loaded GB/surface enhances the migration and annihilation of the V. Previously, the energy landscape has been calculated for a V-SIA pair colliding in the bulk or along the GB in Fe where the motion mechanism of the V/SIA was known (Fig. 3 in Ref. [35]) and for the V-hop towards the SIA trapped at the GB in W and Fe [35, 37]. Yet the landscape for the SIA to migrate out of the GB/surface to move towards the bulk V has never been obtained except for the ones near Fe Σ3 <1 1 0> {1 1 1} calculated by the ABC method [34] and that near Cu GBs calculated by the TAD method [32]. It can be seen, the energy landscapes for the IE-induced annihilation near the GB/surface are similar. Different to the SIE within the SAR, the SIA has to overcome a certain energy barrier to recombine with the V nearby. Thus, we distinguished thermally activated IE (AIE) from the SIE. The system consequently arrives at a more stable state as demonstrated by the appearance of the deeper potential well adjacent the SIA potential well at the GB/surface.

Therefore, there is a thermodynamic driving force for the SIA trapped at the GB/surface to be emitted from the GB/surface and induce the annihilation. Meanwhile, we noted that the energy barrier for the AIE-annihilation is not necessarily higher than the bulk V hop energy barrier but significantly lower than the energy barrier for the SIA to overcome to be emitted from a pure GB/surface (Fig. 10), implying the AIE-induced annihilation could be kinetically favorable to occur. Note that, the energy landscape for the IE-induced annihilation obtained here is different to that obtained by the ABC method in Fe where the SIA emission process near Σ3<110>{111} GB was claimed to be composed of three steps (Fig. 2 in Ref. [34]). The possible reason for the discrepancy is that the annihilation in Ref. [34] may be induced by the coupling motion of the V hop and the IE, since the V was not explicitly kept static during the ABC calculation. Other possible reasons may arise from the different GB structures in Ref. [34] to ours. Figures 14–16 showing the annihilation near the typical W GB/surface support the former speculation.

As shown in Fig. 14(a) and (b), the V near W GB of Σ5(2 1 0)/[0 0 1] recombines with the SIA by overcoming different energy barriers along various IE-annihilation paths and then the system energy reduces by 6.5-7 eV. The annihilation energy barriers for the AIE-induced annihilation along several paths e.g. paths A, B, C, E and F are much lower the V migration energy barrier in bulk W, implying that the AIE-induced annihilation could preferentially occur at an elevated temperature. Note that, the annihilation mechanism was initially artificially-designed as the AIE. The real mechanism could be different after the annihilation path was relaxed by the NEB method. We thus further examined the annihilation process along these low-energy barrier paths. Figure 14(c)–(f) shows the annihilation process along path C as an example. It can be seen, the SIA moves towards the V nearby slowly while the V nearly remains static until the SIA-V is recombined. Therefore, the annihilation along theses paths is indeed induced by the IE with a certain energy barrier. We also found that double saddle points appear on the energy landscape of some annihilation paths, e.g. path D, similar to that in Ref. [34]. Different to the direct IE-induced annihilation along path C, both the motion of the V and SIA was observed during the annihilation as shown in Fig. 14(g)–(j). Therefore, the annihilation along path D involves the coupling motion of the V-hop and IE. The investigation on the annihilation near another small-angle GB Σ85(7 6 0)/[0 0 1] (Fig. 15) suggests that the V near the SIA could also be annihilated at a low energy barrier (Fig. 15(a) and (b)) via the similar coupling motion of the V and IE (Fig. 15(c)–(g)), besides for the annihilation induced by the direct IE (Fig. 15(h)–(l)). In addition, the GB migration was observed during the annihilation along the two paths A and C.

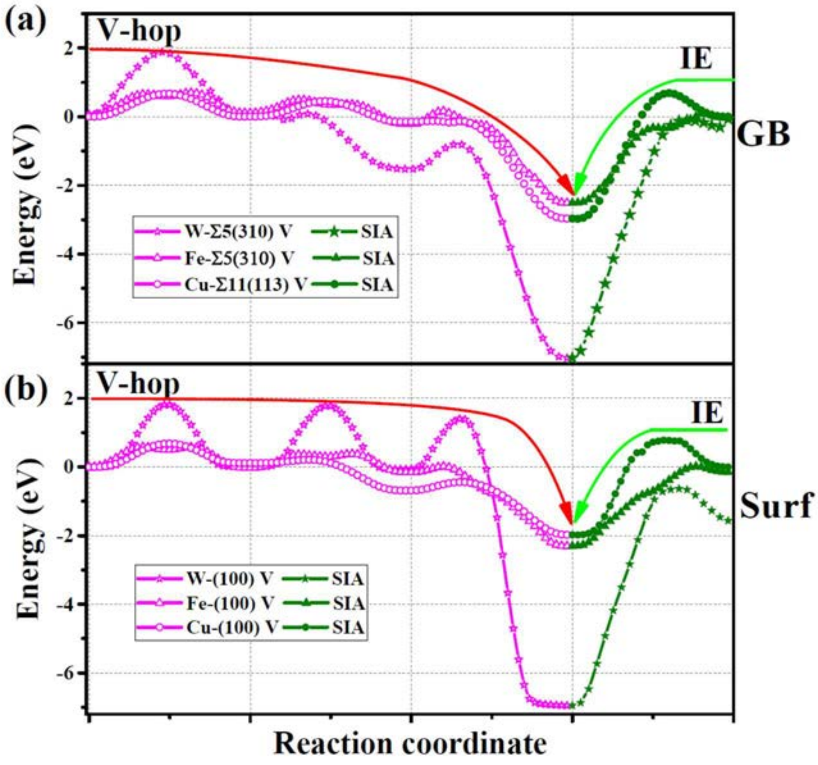

FIG. 13. Energy landscapes for a single colliding V-SIA pair near a GB/surface. The energy of a system prior to annihilation serves as reference. Reproduced courtesy of Elsevier [4450861388662].

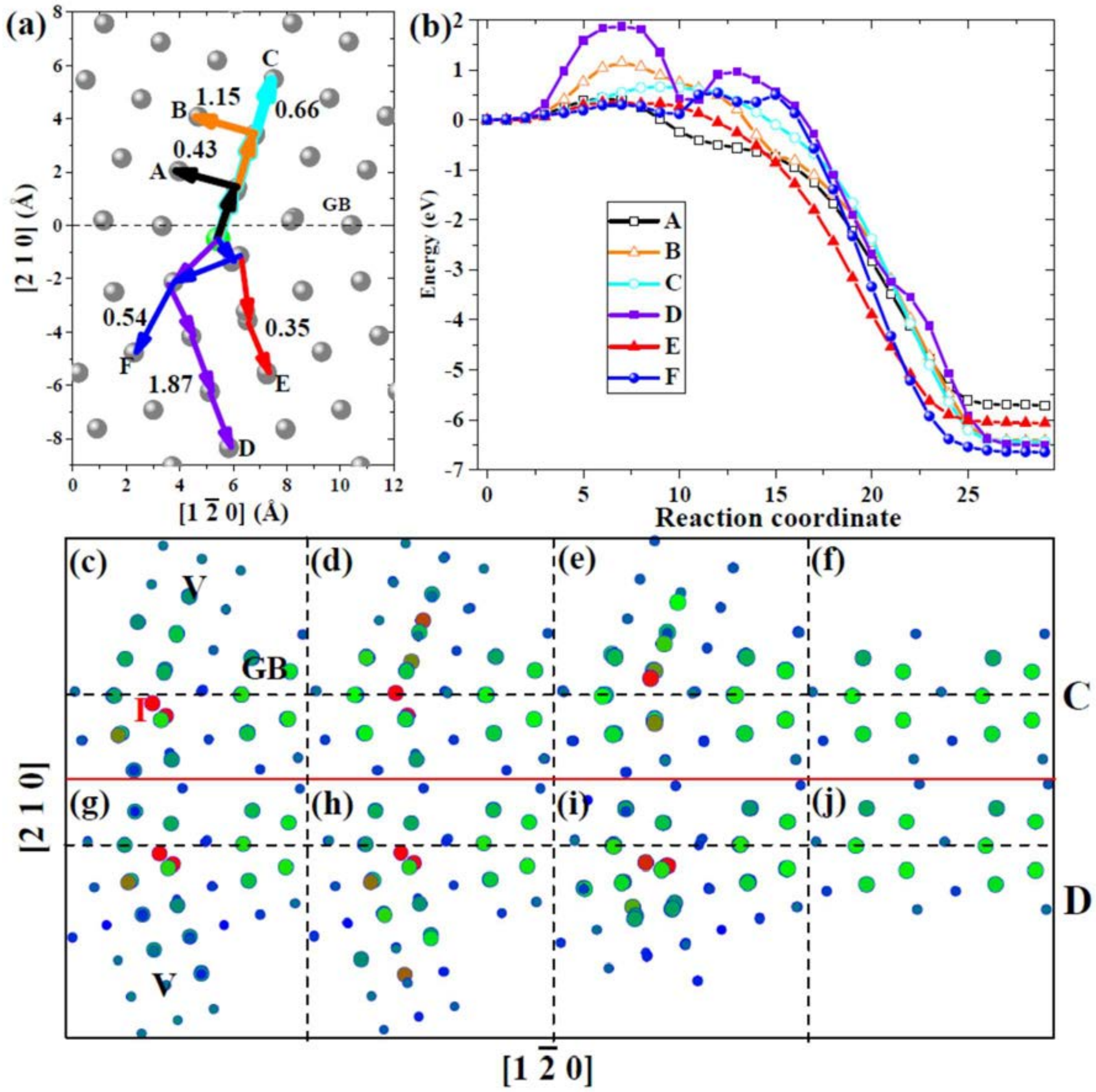

FIG. 14. (a) Illustration of an annihilation path induced by the thermally-activated IE near Σ5(2 1 0)/[0 0 1] in W. Annihilation energy barriers are marked on the path. The annihilation path is given by connecting the initial positions to the final positions of the atoms involved. The atoms with displacements less than 0.5 Å are considered to be immobile during the annihilation. The large green sphere represents a SIA trapped at the GB. (b) Energy landscapes for V-SIA annihilation. The energy of a system prior to annihilation acts as reference. (c)–(j) Snapshots for the annihilation process near the GB. Reproduced courtesy of Elsevier [4450861388662].

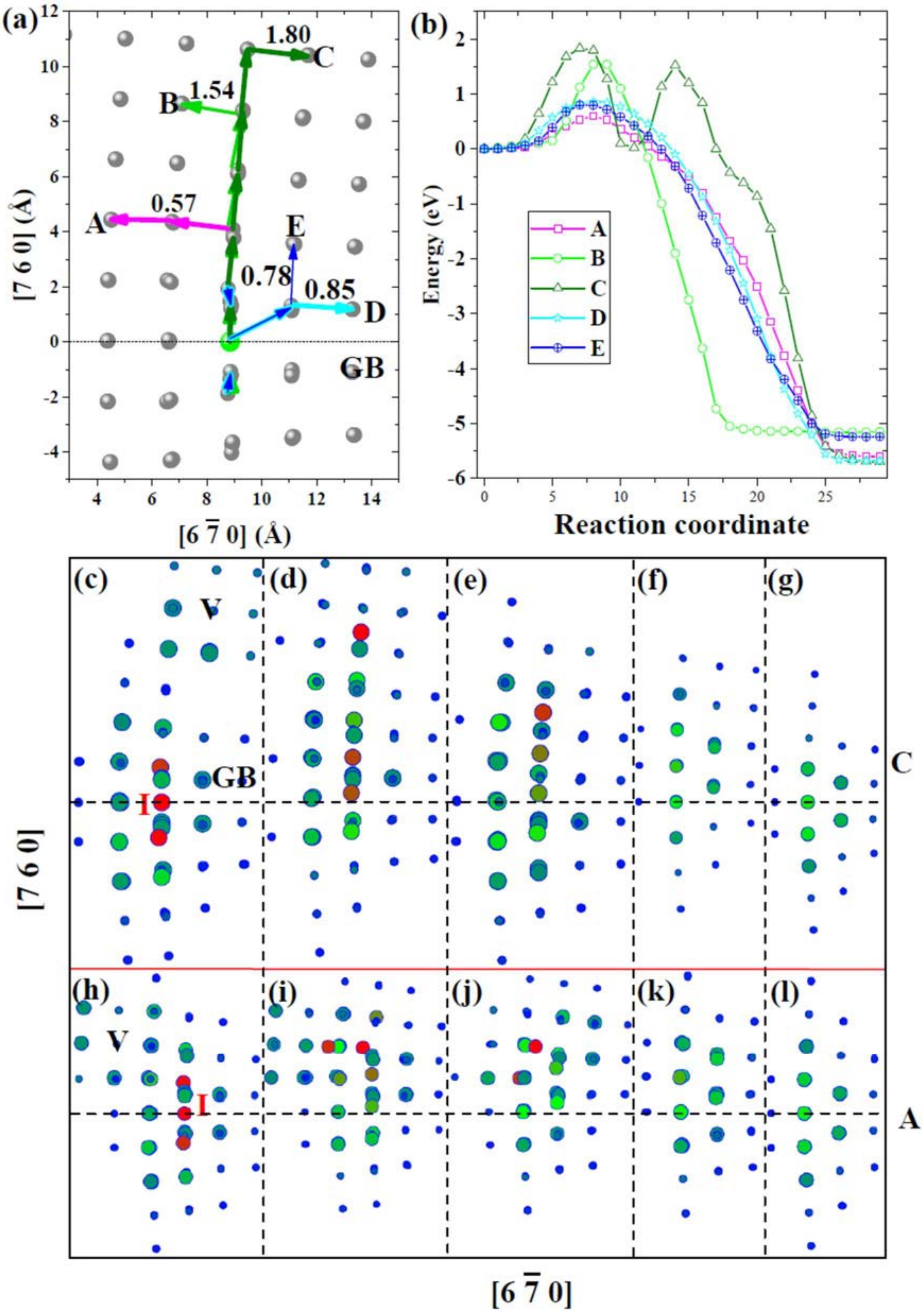

FIG. 15. (a) Illustration of an annihilation path induced by the thermally-activated IE near Σ85(7 6 0)/[0 0 1] in W. The visualization method is identical to that in Fig. 6. (b) Energy landscapes for V-SIA annihilation. The energy of a system prior to annihilation acts as reference. (c)–(l) Snapshots for the annihilation process near the GB. Reproduced courtesy of Elsevier [4450861388662].

Figure 16 summarizes the energy barrier for the annihilation induced by the designed IE as a function of the distance of the V normal to the GB/surface. It can be seen, the V-hop and IE mechanisms would work at different regions. As the distance of the V is over about 10 Å from the SIA at the GB/surface, the IE-induced annihilation energy barrier is much higher than that for the V-hop in W bulk, implying that the IE only works within a local region at the GB/surface. Out of the region, it is more kinetically favorable for the V-hop towards the SIA at the GB/surface to induce the annihilation. For the V at some sites within the region, the IE-induced annihilation energy barrier is comparable to the V-hop energy barrier. In this case, the V could be annihilated via the coupled IE with the V-hop, as observed in Figs. 13–15. The enhanced migration of the V near a static SIA at the GB/surface (Fig. 21 in Ref. [44]) may also promote the coupling of the V-hop with the IE.

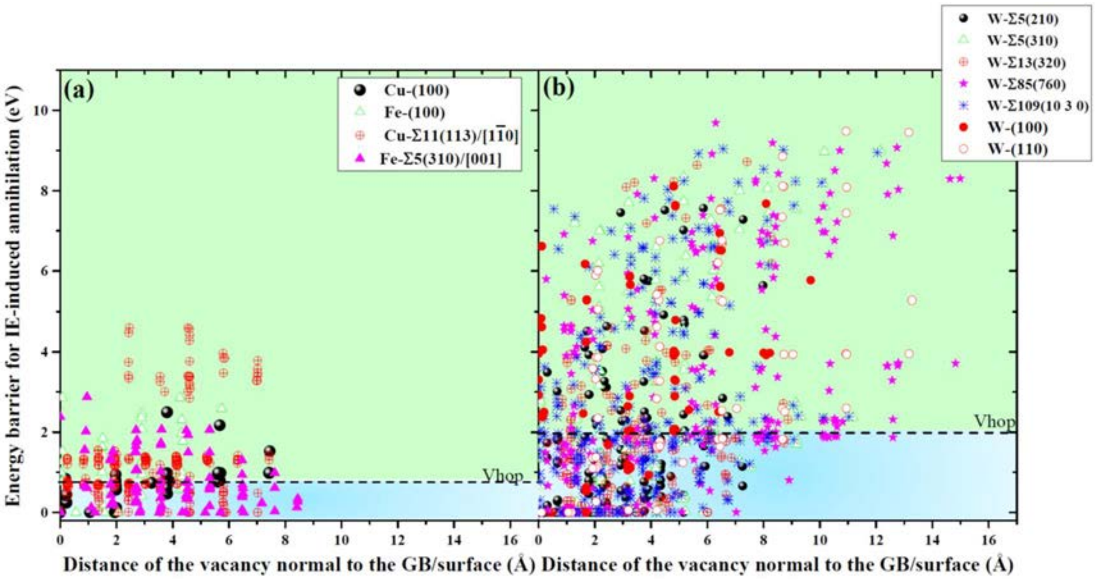

FIG. 16. IE-induced annihilation energy barrier as a function of the initial distance of the V normal to the GB/surface. Reproduced courtesy of Elsevier [4450861388662].

4.3. Propagation or Extension of the Annihilation Region Induced by the Partial IE

We have shown that the there exists low energy paths for annihilating the V near the GB/surface with the SIA trapped at the GB/surface via the direct IE or coupling of the V-hop with the IE (Figs. 13–16). We then explored the dynamic relation of the annihilation with the IE. After examining the stability of the sites around the SIA after the partial IE, we found that, for a given SIA configuration on the emission path there always existed a region surrounding the SIA where the V recombined with the emitted SIA (Fig. 22 in Ref. [44]). The annihilation was confirmed by comparing the system energy with an emitted SIA and a V nearby with the energy of a pure GB/surface. It was further confirmed by the visualization of the system configuration after relaxation. Note that, the IE-annihilation here does not spontaneously occur. Prior to the annihilation, the SIA has to overcome a certain energy barrier to be partially emitted from the GB/surface.

According to Eq. 8, we further calculated V_{ann} of a partially emitted SIA. Figure 17(a) presents V_{ann} for several values of α (Eq. 8) near Cu (1 0 0) surface. Initially, V_{ann} has a limited value of five around a static SIA as illustrated by a light red ellipse. After the partial IE, the annihilation region extends significantly towards the region nearby, as indicated by the enlarged light green and blue ellipses. Meanwhile, we noted that as the amplitude of the SIA emission (characterized by α in Eq. 7) increases, the annihilation energy barrier shows an increasing trend (Fig. 17(b)). Therefore, the favorable kinetic condition for the IE from the GB/surface is sacrificed to a certain extent to induce the propagation or extension of the annihilation region. The SAR around an initially static SIA at the GB/surface (Fig. 11) propagates or extends towards the region nearby as the SIA is partially emitted.

To show whether such picture applies to other systems, we performed similar calculations of V_{ann} as a function of the annihilation energy barrier in more GBs/surfaces to that near Cu (1 0 0) surface. As shown in Fig. 17(c), as the SIA is initially static at the surface, V_{ann} in NPs W, Fe and Cu is only five. In the GBs in W, Fe and Cu, V_{ann} is 27, 14 and 45, respectively, which is obviously larger than that in the surfaces in W, Fe and Cu. After the partial SIA emission, V_{ann} increases significantly with the annihilation energy barrier. As the annihilation energy barrier is smaller than that for the bulk V migration (in this case, the bulk V is not activated), the annihilation volume in NPs W, Fe and Cu increases to 17, 19, 47 from 5, respectively, while in NCs W, Fe and Cu, V_{ann} increases to 58, 39 and 78. Therefore, the partial IE induced annihilation could anneal the Vs in a large range near the SIA at a small energy barrier in NPs and NCs W, Fe and Cu. The IE-induced annihilation near the GB/surface in W, Fe and Cu is all kinetically favorable to occur at an elevated temperature. Similar conclusion could be drawn near more GBs in W (Fig. 17(d)) with different structures.

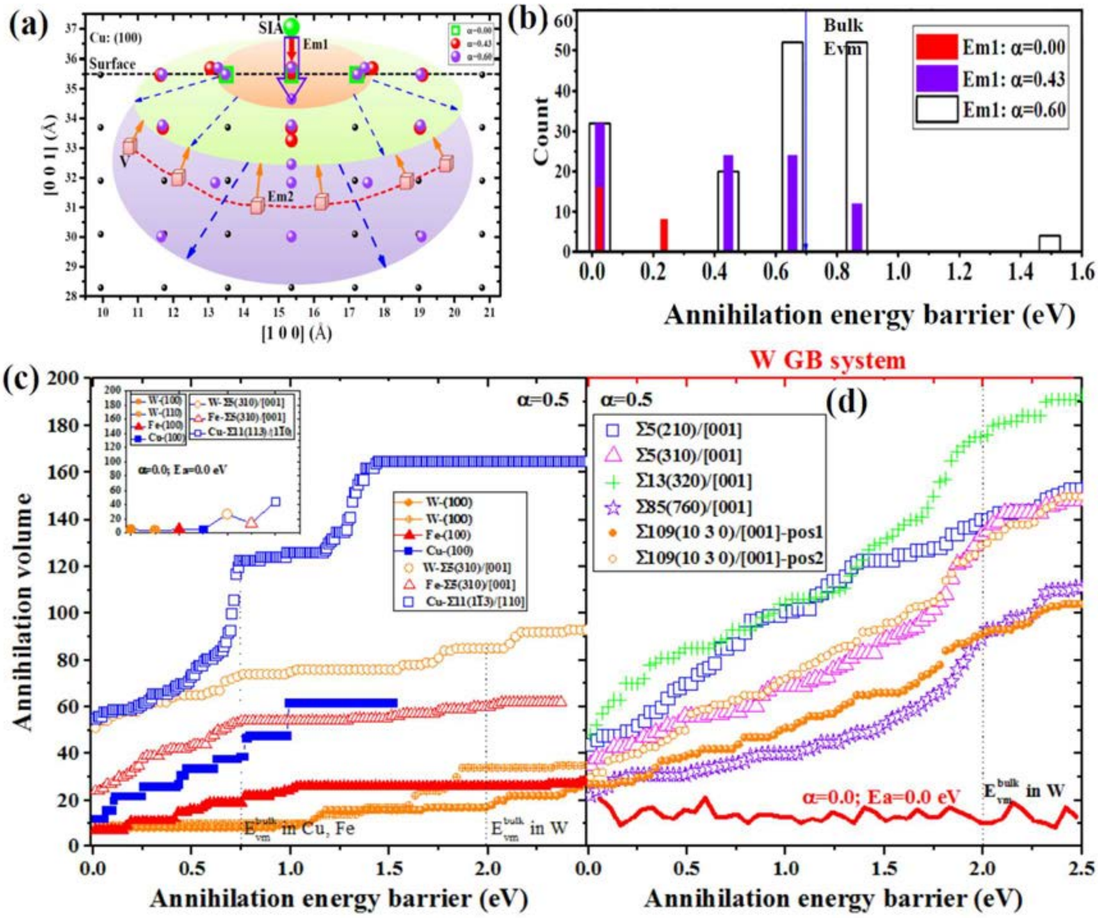

FIG. 17. (a) Illustration for the propagation/extension of the annihilation region around a SIA as the SIA is partially emitted from Cu (1 0 0) surface. Here, Em1 and Em2 have the identical meaning to that in Fig. 1(l). (b) Distribution of the number of annihilation paths on annihilation energy barrier. (c) Annihilation volume (see computational method for its definition) for a partially emitted SIA from the GB/surface in W, Fe and Cu as a function of annihilation energy barrier. The inset shows the annihilation volume for a static SIA in at the GB/surface in W, Fe and Cu. (d) Annihilation volume for a partially emitted SIA at several GBs in W as a function of annihilation energy barrier calculated by using the EAM potential. The red curve show the annihilation volume for a static SIA at these GBs. E_{vm}^{bulk} *in (c) and (d) denotes the energy barrier for the V migration in the bulk; in Cu, Fe, the bulk V migration energy barrier is about 0.7 eV, and in bulk W, the value is about 2.0 eV. Reproduced courtesy of Elsevier [4450861388662].*

4.4. Restraining Force for the IE

As mentioned in the introduction, some researchers often use the large E_b as an indicator for the difficulty in the IE from the GB. In this sense, only when E_b is below a certain level could the SIA be possibly emitted from the GB/surface (Fig. 18(a)). However, the V within the SAR around a static SIA at the GB/surface could be annihilated at a zero energy barrier via the direct IE (Figs. 11 and 12). The V out of the SAR could also be annealed via the low-energy barrier process of the IE and /or coupling of the IE with the V-hop (Figs. 13–17), although the SIA-GB/surface binding energy is very high (Fig. 10). How to understand the IE behavior near the GB/surface in a qualitative manner?

As we know, excess Vs will reside near the GB/surface in NPs and NCs after primary radiation damage due to the preferential segregation of the SIA to the GB/surface. Thus, the SIA may does not necessarily completely migrate out of a square potential well with E_b as the well depth to annihilate the V nearby, which has to overcome an energy barrier of at least E_b (Fig. 18(b)). Furthermore, E_b could be reduced with the presence of the V nearby (Figs. 13–18); in this case E_b is the energy barrier of E_{m1} in Fig. 3. In addition, the SIA potential well has the other dimension the width besides for the potential well depth E_b. Depending on the system, the half-width of the potential well varies from about 5 to 10 Å, which is apparently larger in W than ones in Fe and Cu. Since the SIA migrates a certain distance and then overcomes an energy barrier to annihilate the V, it is rational to estimate the average energy barrier for such process by the ratio of E_b to the half-width of the potential well. We defined it as the restraining force for the IE (Fig. 18(c)). By doing this, the SIA potential well at the GB/surface was approximated by a triangle potential well (Fig. 18(d)). The restraining force is the slope of the triangle potential well, which has the physical meaning as the energy barrier for the SIA to overcome as migrating over a unit length of the distance from the GB/surface to the region nearby. As shown in Fig. 18(c), NCs Cu, Fe and W have a smaller slope compared with NPs W, Fe and Cu, implying the SIA is easier to be emitted from a GB than from a surface in these systems. The emission difficulty ordered based on the slope (Fig. 18(c)) is different to that based on the value of the binding energy (Fig. 18(a)). As the SIA migrates over a distance of d from the GB/surface, it approximately overcomes an energy barrier of $d \times s$ (s is the slope). As d is one Å, the emission energy barrier is much lower than the binding energy. Thus, the IE may be much easier to occur than expected.

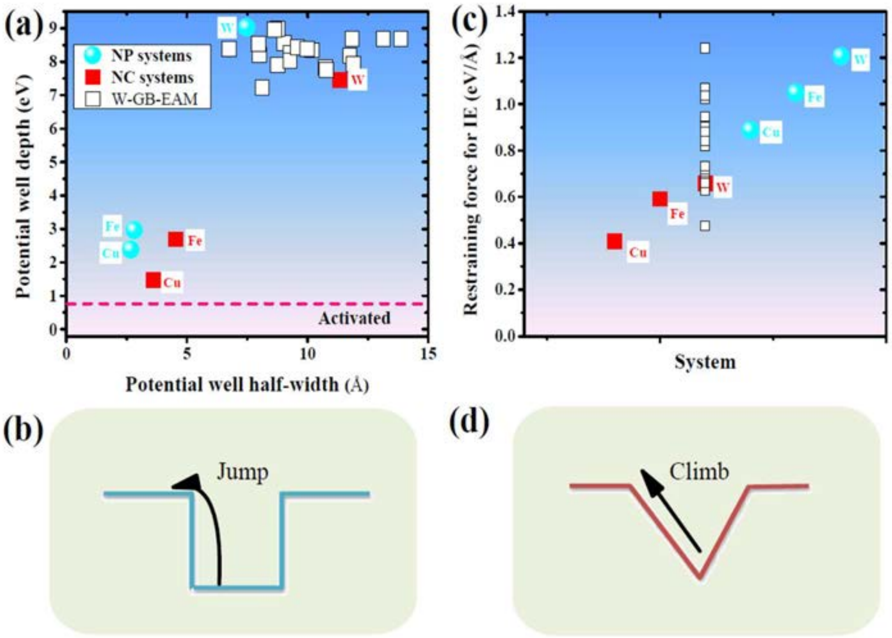

FIG. 18. (a) Distribution of the parameters for a square potential well of the SIA at the GB/surface in W, Fe and Cu in the space of the potential well depth (the SIA-GB/surface binding energy) and potential well half-width. (b) Illustration for the SIA potential well at the GB/surface as a square potential well. (c) The restraining force for the IE defined as the ratio of the potential well depth to the potential well half-width in W, Fe and Cu. (d) Illustration for the SIA potential well at the GB/surface as a triangle potential well. Here, "NC-W", "NC-Fe", "NC-Cu" denote the GB models in the three metals, respectively, and "NP-W", "NP-Fe", "NP-Cu" denote the relevant surface models in the three systems. Reproduced courtesy of Elsevier [4450861388662].

5. COUPING AMONG VACANCY SEGREGATION, INTERSTITIAL MOTION ALONG THE GB AND IE

Next, we focused on the annihilation of the V with a SIA$_n$ that segregates to the GB from the view of the energetic and kinetic properties of the V around the SIA$_n$. Special attention was paid to the effect of in-boundary process, e.g. motion of the SIA along the GB, on eliminating Vs adjacent the GB.

5.1. Static Interaction of the V-SIA$_n$ at the GB

The location and diffusion of a V near a SIA$_n$ was calculated. MS calculations show that there are common energetic features for the V near a SIA$_n$ (Fig. 19(a)), similar to the energetic property of a V around a SIA [37, 41]. The reduced E_V^f around a SIA$_n$ indicated the enhanced occupancy of the V nearby the SIA$_n$. This could be understood based on the natural attraction of a defect with its anti-defect, e.g. a V and a SIA. Particularly at certain sites around the SIA$_n$, E_V^f reduces extensively that it becomes negative. Further examination of the structural after relaxation at 0 K suggested that a V at the site within such region, actually recombined with a SIA in the SIA$_n$ spontaneously. Therefore, a spontaneous annihilation region formed around a SIA$_n$ ("SAR" in Fig. 19). Such concept has been established for the V around the bulk SIA in Fe and W [35–44], which holds for the V around the bulk SIA-cluster. Meanwhile, the annihilation mechanism could be termed as spontaneous interstitial emission ("SIE" in Fig. 19(c)).

Further calculations show that the V near the first and second nearest neighbors of the SAR could also recombine with a SIA in the SIA$_n$ at a low barrier (Figs. 19(a) and (c)). Correspondingly, the annihilation of the V with the SIA_n trapped at the GB was via the activated IE (AIE). The annihilation was a replacement process mainly along <1 1 1> (Fig. 19(b)). It was mixed with <1 0 0> in some cases where the annihilation was induced by the jump of the V to its second nearest neighbor. Therefore, the diffusion mechanism of the vacancy around a SIA_n was modified and the migration along <1 0 0> is possible besides commonly along <1 1 1>. Out of these regions, the diffusion of the V via conventional hop was also accelerated.

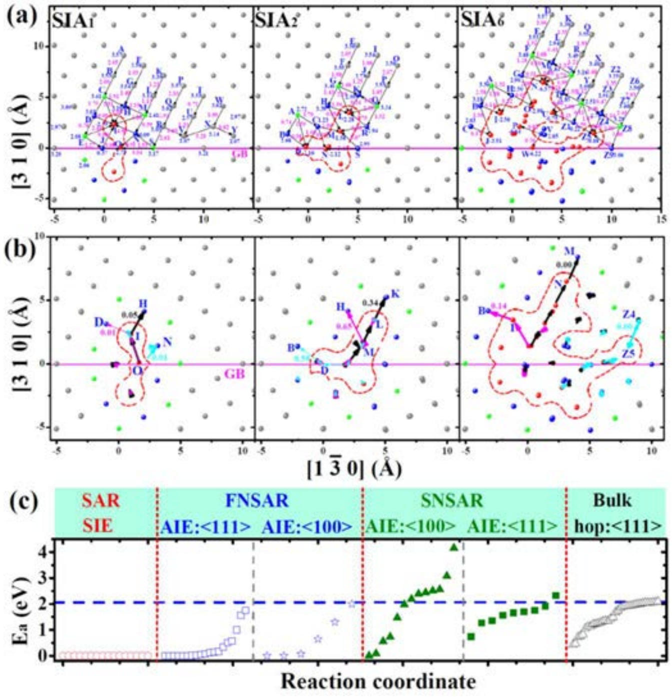

FIG. 19. (a) Energetic and kinetic properties of the V near a SIA cluster that is trapped at the GB. The area enclosed by the dashed red line contains the sites with negative vacancy formation energy (E_{vf}). The first-nearest and second-nearest neighbors of the area are represented by the blue and green spheres, respectively. The blue, green and gray sites outside this area are associated with a positive E_{vf} value. The gray spheres represent normal lattice sites with an E_{vf} equal to the bulk value. The values printed in pink are the diffusion energy barriers for the vacancy on its path, while the values printed in blue are E_{vf} at the site. (b) Recombination process of a vacancy with a SIA cluster at the pure GB Σ5 (3 1 0)/[0 0 1]. The spheres with different colors have the same meaning as that in (a). The annihilation process is visualized by joining the arrows from the initial to final location of each atom involved. The corresponding annihilation barriers are given on the path. (c) Diffusion and annihilation energy barriers (E_a) of a vacancy near the SIA cluster. Here, the symbol SIE denotes spontaneous interstitial emission and AIE denotes activated interstitial emission. The symbols SAR, FNSAR and SNSAR are short for the spontaneous annihilation region, first-nearest neighbor of the spontaneous annihilation region, second-nearest neighbor of the spontaneous annihilation region, respectively. The horizontal dashed blue line indicates the diffusion energy barrier of the bulk vacancy along <1 1 1> direction.

5.2. Diffusion of the SIA_n Along the GB

As shown in Fig. 20(a), the in-boundary process may play a role in suppressing radiation damage near the GB. Considering the preferential segregation of the SIA_n to the GB, the diffusion of the SIA_n along the GB was investigated (Figs. 20(b) and (c)). The SIA_n at the GB either directly comes from the bulk or the clustering of the single SIA at the GB. Thus, the binding of a SIA with another one was also investigated (Fig. 20(c)). We found that the diffusion direction for the SIA and SIA_2 is parallel to the tilt axis. Both the diffusion energy barrier and the binding energy depend on the GB structure. The diffusion energy barrier for the SIA is smaller compared with that for the V diffusion in the bulk except in GBs of Σ25 and Σ85. The binding energy is over 0.6 eV. Thus multiple SIAs at the GB can be clustered. Compared with the single SIA, the mobility of the SIA$_2$ is lower, which is, however, comparable to that for the V except in GBs of Σ25 and Σ85.

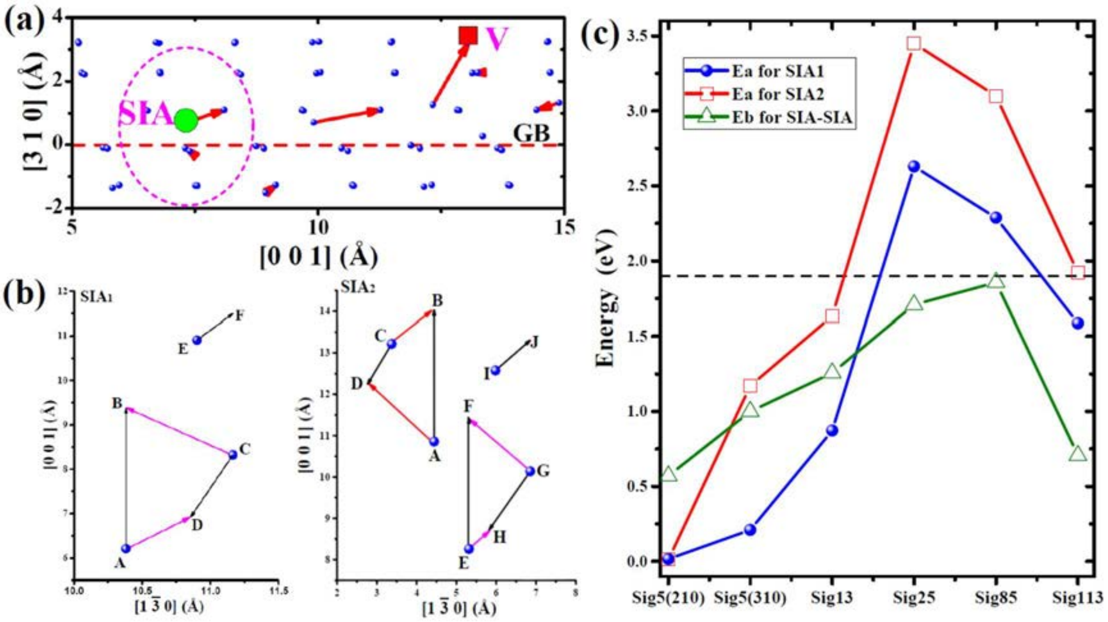

FIG. 20. (a) Annihilation of the V near the GB induced by the diffusion of the SIA along the GB and the emission. Here the green sphere and red filled square denote the SIA and the V, respectively. The red dashed line indicates the GB position. The diffusion and annihilation process is visualized by connecting the relaxed initial and final states. The dashed pink circle encloses the spontaneous annihilation region around the SIA. The annihilation was obtained by MD simulations at 1000 K. (b) Illustration of the diffusion of the single SIA and the di-SIA along the GB. Initially, a SIA at site A was forced to move to its another stable site B along path A→B, which induced the motion of the atoms C and E. Actually, the easy transition path for the SIA migration is via A→D, C→B and E→F. The favorable migration path for the di-SIA was similarly obtained. (c) Energy barriers (E_a) for the SIA and di-SIA diffusion along the GB and SIA-SIA binding energy (E_b) at different GBs.

5.3. Annihilation of the V via Dynamic SIA Emission

We termed the IE that is induced by the short-ranged interaction of the V with the SIA as the static IE, e.g., the ones in Fig. 19. The dynamic annihilation picture was investigated by the OKMC method which relates to the long-ranged diffusion of the defects and the collective/coupled motion of defects at the GB and near the GB. In the third OKMC model Sys3, the SIA energy landscape was approximated by a square-shaped potential well. The energy barrier for the SIA approaching to the GB was given by $E_a = E_a^{bulk} H(d - d_0)$. By adopting such approximation, the SIA near the GB would diffuse and get trapped by the GB spontaneously. For the SIA$_n$, the barrier was set to be twice that of the single SIA. For the V, the energy barrier near the GB was assigned to be one half of the bulk value and the GB trap range for the V was 5.0 Å. After the SIA was trapped at the GB, its annihilation radius for the V was set to be 5.0 Å, while the annihilation radius for the SIA–V in the bulk was given of 10.0 Å.

Figure 20(c) suggests that the kinetic properties of the SIA at the GB depend on the GB structure, although the diffusion barrier of the SIA in the bulk is extremely low. Based on previous knowledge from the simulations of the coupled segregation and annihilation in Fe [35], the dynamic behavior of the SIA in W could be deduced as follows. As the diffusion energy barrier of the SIA along the GB ($E_a^{SIA,GB}$) is very high (e.g. in GBs of Σ25 and Σ85), the SIA is not activated at the GB at the temperature of interest e.g. 10, 563 and 850 K. In this case, the SIA is pined at the GB after segregation from the bulk. Then, the bulk V either hops towards the GB once activated or remains immobile in the bulk as it is not activated. In this case, the annihilation of the V with the SIA is described by their static interaction

(Fig. 19). As $E_a^{SIA,GB}$ is comparable to that for the V diffusion in the bulk, e.g. in GB Σ113, it is expected that the coupled picture as proposed in Fe applies to W.

Meanwhile, we note that, in some GBs, e.g. Σ5 (2 1 0), Σ5 (3 1 0) and Σ13, $E_a^{SIA,GB}$ is much lower than the bulk value of the V diffusion. Correspondingly, the time of the SIA and V to jump one step differs by at least six orders of magnitude. In this case, the SIA migrates along the GB exceptionally quickly after segregation, while the V remains static in the bulk. The dynamic annihilation could be as illustrated in Fig. 20(a). A SIA moves along the GB carrying with a low-barrier annihilation region that extends to the bulk. As the SIA comes close enough to the V, they are annihilated via IE. This picture is supported by the trajectories for the SIA diffusion near the GB at long timescale in Fig. 21(a), where $E_a^{SIA,GB}$ was assigned to 0.35eV.

The above picture was analyzed based on the behavior of a SIA-V pair. As the system contains multiple SIAs and Vs, the mechanism is complex due to possible clustering of SIAs at the GB (Fig. 20(c)). In this case, it needs to compare the length of the free path of the SIA at the GB (determined by the concentration of the SIA at the GB or in other words by radiation dose) with the distance of the bulk V from the GB. Under the present simulation conditions (the system has 300 appm SIA-V pair initially), we found that the SIA at the GB quickly clustered at the GB after segregation (Fig. 21(b)). The cluster is mainly di-SIA, which has lower mobility than the single SIA (Fig. 20(c)). In the subsequent evolution, the cluster moved along the GB. Simultaneously, the bulk V approached the GB, which was finally annihilated via such coupled process, as illustrated in Fig. 21(c). The dynamic picture was termed as the dynamic IE which involves the motion of the SIA along the GB and the coupled motion of the di-SIA and the diffusion of the bulk vacancy. The mechanism enhances the annihilation of the V (Fig. 21(d)).

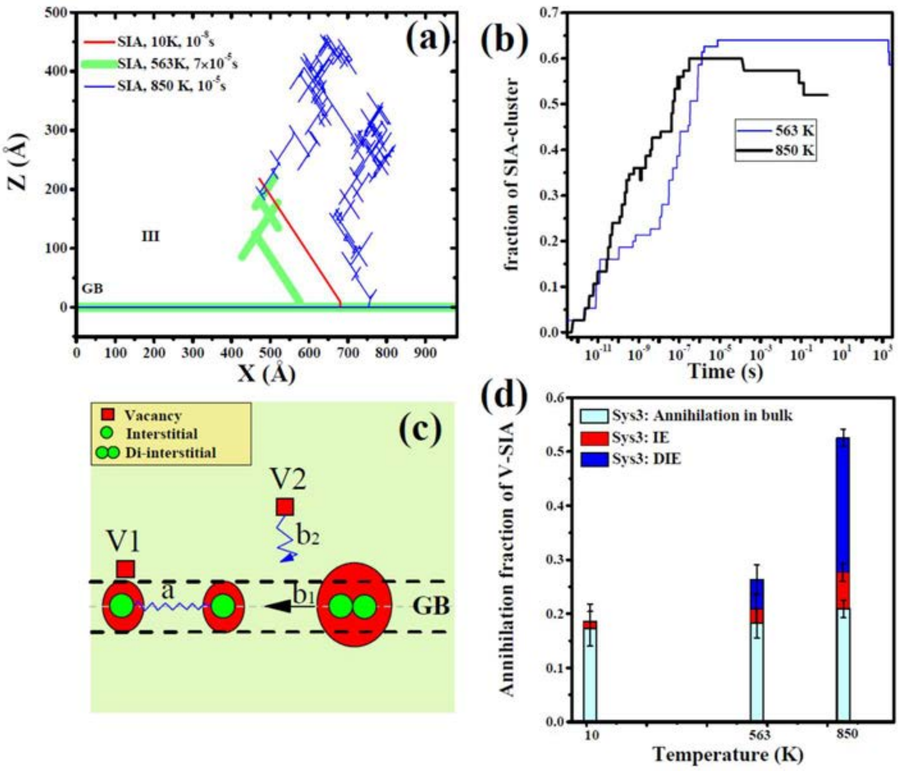

FIG. 21. (a) Typical trajectories a SIA near the GB at three typical temperatures of 10, 563 and 850 K. Here, energy landscape of the SIA is approximated by a downhill square-shaped potential well. (b) Evolution of the SIA-cluster fraction with time. (c) Illustration of the V-SIA annihilation picture near the GB. (d) Statistic results of the annihilation fraction of the V–SIA at 10, 563 and 850 K in W. Here, the symbol Sys3 represents a system; IE denotes interstitial emission; DIE is short for dynamic interstitial emission.

6. DYNAMIC REFLECTION OF INTERSTITIALS

6.1. MD Simulations of Segregation and Reflection of the SIA$_n$ Near the GB

A SIA$_n$ was intentionally put at several typical sites about 10 Å away from the GB, since the SIA$_n$ within the region may be directly trapped by the GB based on previous MS calculations of the single SIA [37, 41]. Then, the system was fully relaxed at 0 K before performing MD simulations at 300 K. After analyzing SIA$_n$ configurations and motion trajectories, the complex behavior of the SIA$_n$ near the GB was observed, including not only SIA$_n$ segregation but also its reflection that depends on the local GB structure. Figure 22 presents the selected representative snapshots from MD simulations of the SIA$_n$ near two typical pure or SIA$_n$-loaded GBs of $\Sigma5$ (3 1 0) and $\Sigma113$ (8 7 0); results for the single SIA, and the SIA$_2$ and SIA$_6$ were taken as an example.

Near the locally loose region, both the single SIA and SIA-cluster were always observed to move towards the GB via replacement-atom sequences during multiple runs of MD simulations (Figs. 22(a) and (c)). This is consistent with previous observation in MD simulations of primary radiation damage in several metals [32, 35, 37, 40, 53]. For the single SIA, it moved along <1 1 1> to approach the GB, while a SIA-cluster relatively slid along <1 1 1> before trapping by the loose region. The large segregation energy acts as an energetic driving force for the SIA$_n$ segregation. In addition, the dissociation of a SIA-cluster was also observed (e.g. SIA$_2$ in Fig. 22(c)), which never occurred before arriving at the GB. The larger binding energy of the SIA with the GB (over 7.0 eV) versus the binding energy of the SIA with a SIA$_n$ (over 2.5 eV as shown Fig. 2(b)) can give rise to the dissociation of the

SIA_n. After parts of the SIA_n dissociated into the GB, the remaining parts entered the neighboring vacant region in most cases.

However, in certain MD simulations, the remaining SIAs of the SIA_n were observed to occasionally move away from the GB following the original <1 1 1> direction. Such motion had never been observed for a single SIA near the vacant region that can at least accommodate a SIA; it may indicate that the SIA behavior near the GB relates to the GB absorption capacity for the SIA. This motion of the SIA_n was termed as the interstitial reflection (IR) by the GB. Although there are free surfaces in the direction normal to the GB that also act as sinks for the SIA_n, the surface effect was excluded by setting a large distance of the surface to the GB (over 45 Å). We speculated that the locally loose region either could not accommodate excess SIAs, consequently scattering them into the neighboring vacant region or even reflecting them back into the grain interior. Otherwise, the SIA had to overcome a certain energy barrier to enter the GB after the locally vacant region have been partially occupied by some SIAs .e.g. by the SIAs dissociated from a SIA_n.

To support the above speculation, more MD simulations were designed and performed. First, the locally loose region was artificially loaded with the SIA_n. Then, it was more frequent to observe the reflection of the newly produced SIA_n. The newly created SIA_n was reflected back into the bulk as a whole rather than dissociation. Figures 22(b) and (d) show the typical reflection of the SIA_n by the SIA_n-loaded GBs of Σ5 (3 1 0) and Σ113 (8 7 0), respectively. After the SIAn was reflected, it was finally trapped by the surface after taking a random walk for hundreds of ps near the GB at 300 K. Second, the reflection of the SIA_n was a common observation near the locally inherently dense region, as shown in Fig. 22(e) for the case of Σ113. Therefore, the local GB structure affects the role of the GB as a sink or reflector for the SIA_n, which may influence the dynamic annihilation of the bulk vacancy.

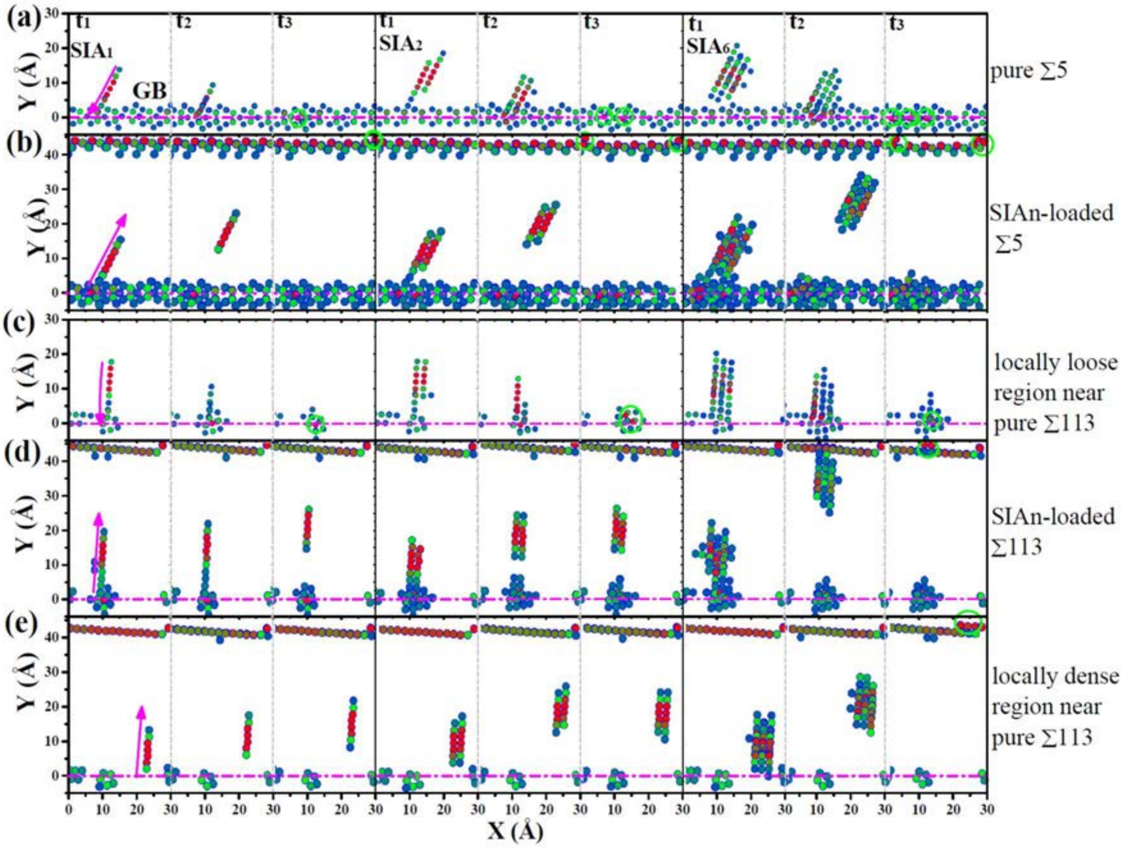

FIG. 22. Representative snapshots of the SIA and cluster near the GB from MD simulations at 300 K within a time period of 1 nano-second. For the single SIA, 2-SIA (SIA_2) and 6-SIA (SIA_6) clusters, three frames of the animation were presented, e.g. the snapshots at t1, t2 and t3 for the SIA. (a) and (b) The results near a pure and a SIA_n-loaded Σ5 (3 1 0) GB, respectively. (c) and (d) show the motion snapshots of the SIA, SIA_2 and SIA_6 near the pure and SIA_n-loaded Σ113 (870), respectively. (e) The results near the intrinsic dense region of Σ113 (870). In (a)–(e), the GB position is indicated by the pink colored dashed line. Atoms are colored according to their potential energy. Atoms with the energy deviation from the bulk energy value less than 0.1 eV are not shown. The green circle marks the SIA after it is absorbed by the GB or the surface. In (a) and (c), the pink colored arrow directed towards the vacant site at the GB, illustrates the trapping of the SIA by the GB. In (b), (d) and (e), the pink colored arrow that is along the main axis of the SIA and directed towards the surface indicate the reflection of the SIA by the GB in the subsequent evolution. In (a) and (b), axes X and Y are along directions $[1\ \bar{3}\ 0]$ and [3 1 0], respectively for Σ5(3 1 0) GB, while in (c)–(e), are respectively along directions $[7\ \bar{8}\ 0]$ and [8 7 0] for Σ113(8 7 0) GB.

6.2. Structural and Kinetic Reason for the Interstitial Segregation and Reflection Near the GB

To understand the trapping and reflection of the SIA_n by the GB, the kinetics of the SIA near the GB were investigated. To do this, a SIA was forced to move towards the GB along a specific <1 1 1> direction. Before and after each step of the move of the SIA (refer to the calculation method for moving the SIA), the GB system was relaxed, followed by the NEB [51] calculation. Meanwhile, the SIA motion trajectory was also obtained by connecting the initial atoms to the final atoms after relaxation. According to the structural periodicity along the GBs, all the non-equivalent paths for the SIA diffusion towards the GB were explored. Figures 23(a) and (b) show the obtained diffusion trajectory. Figure 23(c) shows energy landscapes of the SIA near the GB of Σ5 (3 1 0)/[0 0 1].

Near the locally pure GB, a decreasing energy landscape was obtained (Fig. 23(c)), e.g., along paths d_1 and d_2 (Fig. 23(a)). It suggested an energetically and kinetically favorable trend for the SIA to be trapped by the GB. The prediction was consistent with the aforementioned current observations in

MD simulations and in other studies [32, 35, 37, 40, 53]. The SIA first moved via a short-range replacement process. Then, it changed its direction and moved towards the vacant site at the GB. Finally, it became trapped there through the long-range replacement of the atomic sequence.

When the newly coming SIA was forced to move towards the GBs that was loaded with a SIA e.g. the one coming from the grain interior along paths d_1 or d_2., the SIA finally entered the neighboring structural unit following path d_3 (Fig. 23(a)). The trajectory suggested that the SIA was scattered by the SIA lying ahead of its course, different to that along d_1 or d_2 near a pure GB. After the locally loose region and its neighboring ones were fully occupied by the SIA (Fig. 23(b)), the newly added SIA had to kick the atom on the GB plane out to the site on the other side of the GB (the trajectory is shown by the trajectory d_4), forming a special structure of the SIA–V–SIA complex. Meanwhile, it was found that, contrary to a decreasing energy landscape for the SIA near the pure GB, the energy landscapes of the SIA near the SIA-loaded GB are first increasing and then decreasing. In this case, the SIA had to overcome a certain energy barrier to get trapped at the GB, which implies that a SIA would be reflected back as it approached the SIA-loaded GB at elevated temperature (the activation temperature could be estimated based on $t = t_0 \exp(E_a / k_B T)$, where t_0 is the vibration period of atoms in tungsten bulk and is generally assumed to be 10^{-12} s. The Boltzmann constant k_B has a value of 8.617×10^{-5} eV/K. E_a is the diffusion energy barrier and T is system temperature. The activation temperature is defined as the one at which the transition time is one second. Since the diffusion energy barrier of the SIA is as small as 0.002 eV, the activation temperature for the SIA reflection is as low as several K).

To further discover the correlation of the SIA behavior with the local GB structure, the SIA energy landscapes near more other GBs were calculated similarly, including the GBs Σ5 (2 1 0), Σ13 (3 2 0), Σ25 (4 3 0), Σ85 (7 6 0) and Σ113 (8 7 0) (Fig. 24). The SIA was forced to move along <1 1 1> until it was reflected back after relaxation. The interactions of the SIA with these GBs were found to be divided into three groups: I, II, and III (Figs. 24(a)–(d)), according to the final location and morphology of the SIA. The energy landscapes and trajectories of the corresponding types of the SIA also have unique features. If the GB structure is locally loose as marked by the pink closed atomic rings in Figs. 24(e)–(i), the SIA of type I could reside there as a localized point. This situation is similar to that near Σ5 (3 1 0)/ [0 0 1] (Fig. 23(a)). However, both increasing and decreasing energy landscapes appear as more non-equivalent paths exist near these GB structural units that extend along axis X in Figs. 24(e)–(i). For instance, the SIA of type II resided at an interstitialcy site at the GB, resulting displacement of several atoms. When being forced to move along <1 1 1>, the SIA of type III could not enter the GB core due to existence of a locally dense region ahead of its' course. In this case, the SIA finally behaved as a distorted crowdion located near the GB; the energy landscape is basically increasing. It was noted that, in Fig. 24 the SIA was not artificially loaded into these GBs to construct a locally dense structure. It is expected that the locally loose regions of these GBs being SIA-loaded would result in the shoulder appearing in the energy landscape more frequently. Therefore, the SIA near a locally loose region either barrier-freely segregates to the GB or overcomes a certain energy barrier to enter the GB. For the later, since the barrier for the SIA to move away from the GB is far less than that for the SIA approaching the GB, the SIA is reflected by the GB. Near a locally dense region, it is always kinetically favorable for the SIA to diffuse away from the region. In addition, by comparing the SIA behavior near Mo and Fe GBs (Figs. 25 and 26), it was found that the SIA_n motion style that is one-dimensional or three-dimensional affects on the SIA_n behavior near the GB. The SIA that moves three-dimensionally could more easily find a location at the GB.

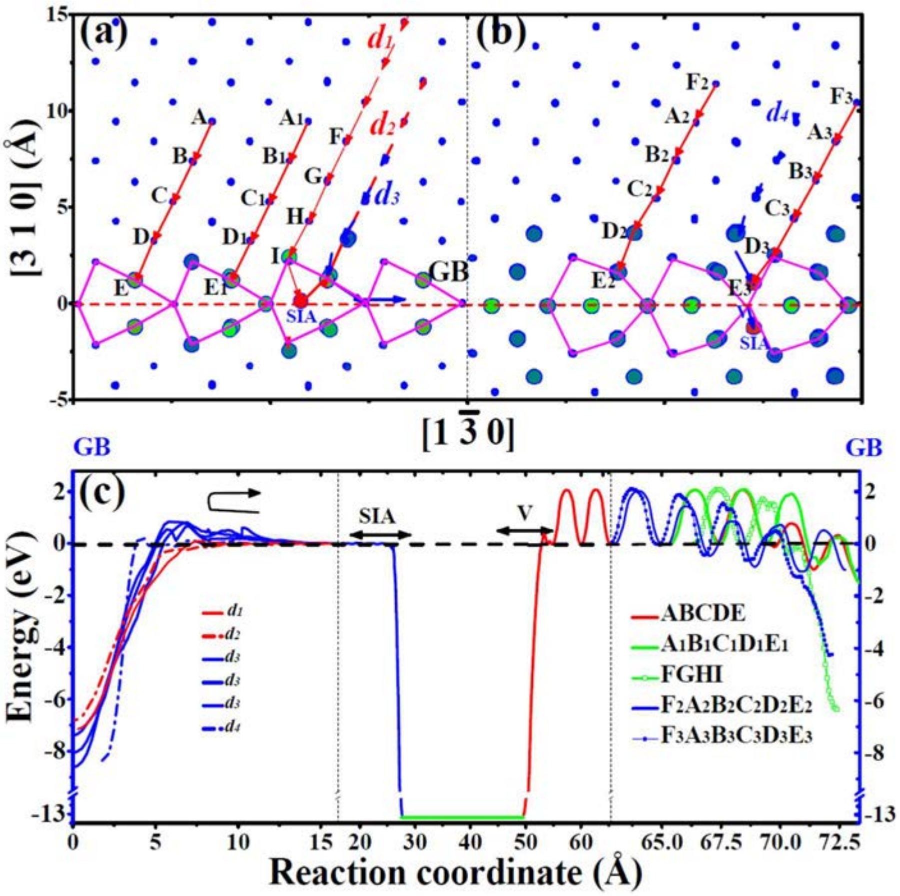

FIG. 23. Diffusion of the single SIA and V and corresponding energy landscapes near a symmetric tilt Σ5 (3 1 0)/[0 0 1] GB in W. In (a), A→B→C→D→E is the path for V diffusion near the pure GB, whereas A_1→B_1→C_1→D_1→E_1 and F→G→H→I are the paths near a GB that has absorbed one SIA. Symbols d_1 and d_2 are used to mark two diffusion and absorption trajectories of the SIA near the pure GB. d_3 marks the trajectory of the SIA near the GB loaded with one SIA. In (b), F_2→A_2→B_2→C_2→D_2→E_2 is the path for the V diffusion located near the GB where the open SIA site in (a) has been fully occupied by the SIA. F_3→A_3→B_3→C_3→D_3→E_3 is one path for the V diffusion near the GB that has absorbed another SIA by forming a dumbbell at the GB. The trajectory for this SIA is denoted by d_4. In (a) and (b), the trajectory of the SIA diffusion is shown by connecting the relaxed initial and final states. (c) Energy landscapes of the SIA and V diffusion near different local GB structures. The potential well lying between two vertical dashed black lines is the landscape for a SIA–V collision and annihilation in the bulk region.

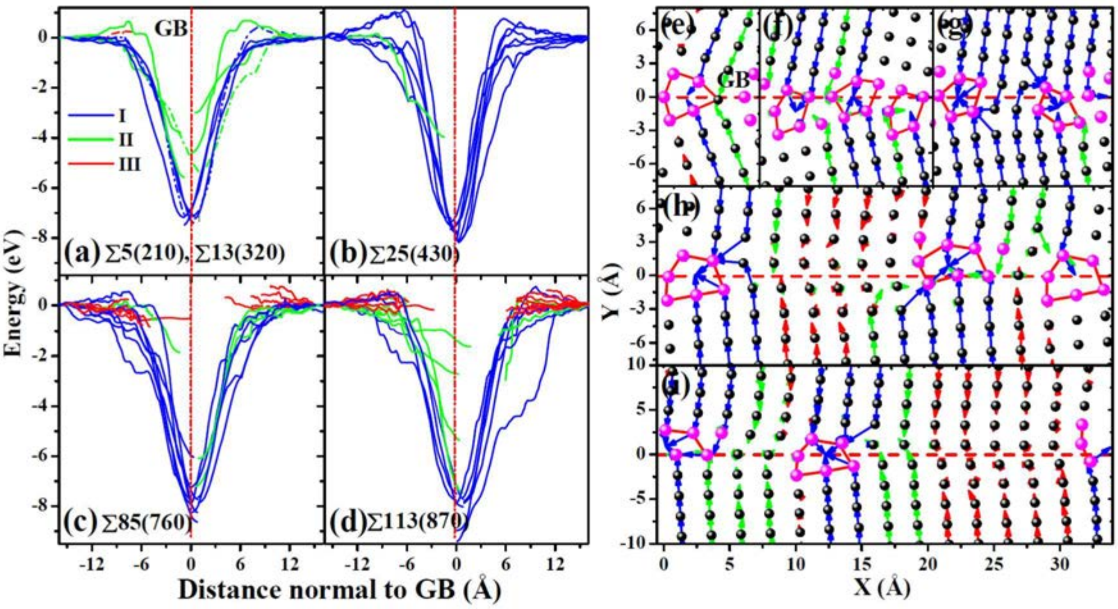

FIG. 24. (a)–(d) Energy landscapes of the SIA near symmetric tilt GBs Σ5 (2 1 0), Σ13 (3 2 0), Σ25 (4 3 0), Σ85 (7 6 0) and Σ113 (8 7 0). In (a), the dashed cures are results for Σ5 (2 1 0). I, II and III denote three types of energy landscapes divided according to the SIA morphologies near the GB. (e)–(i) Diffusion trajectories of the SIA near these GBs in W. The SIA diffusion trajectories are projected by connecting initial and final states which are colored correspondingly to the color of the energy landscape curves in (a–d). The closed pink colored atomic ring indicates the local vacant space at the GB where a SIA locates itself with its energy landscape of type I. The SIA having type II landscape will reside itself at an interstitialcy site at the GB, while the SIA with type III landscape cannot approach the GB core, due to existence of a locally dense region ahead of its' course. The vertical dashed red colored line in (a–d) and the corresponding horizontal one in (e–i) mark the GB positions. In (e)–(i), the axis X is along directions [1 $\bar{2}$ 0], [2 $\bar{3}$ 0], [3 $\bar{4}$ 0], [6 $\bar{7}$ 0] and [7 $\bar{8}$ 0] for Σ5 (2 1 0), Σ13 (3 2 0), Σ25 (4 3 0), Σ85 (7 6 0) and Σ113 (8 7 0), respectively. Correspondingly, the axis Y is along directions [2 1 0], [3 2 0], [4 3 0], [7 6 0] and [8 7 0].

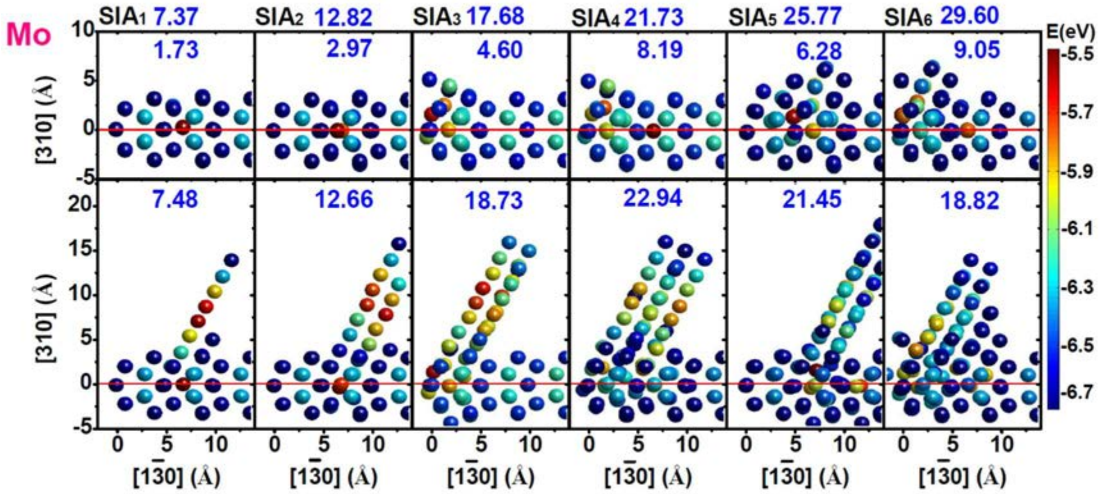

FIG. 25. Configurations of the small SIA$_n$ trapped at the pure GB Σ5 (3 1 0)/[0 0 1] and blocked near the SIA$_n$-loaded GB in Mo. The GB position is indicated by the red line. The formation energies for SIA$_1$–SIA$_6$ that are located in the bulk, trapped at the GB and blocked near the GB are given, respectively (e.g. 7.37, 1.73 and 7.48 eV for SIA$_1$). As the single SIA or SIA$_2$–SIA$_6$ are put near the pure GB, they instantly segregate into the GB and get trapped there during the relaxation of the GB structure (first row). Meanwhile, the SIA$_n$ formation energies are greatly reduced. Then, as more SIAs are inserted near the GB, they no longer spontaneously flow into the GB, but get blocked near the GB (second row). The SIA$_n$ blocked near the GB has energy comparable to that in the bulk.

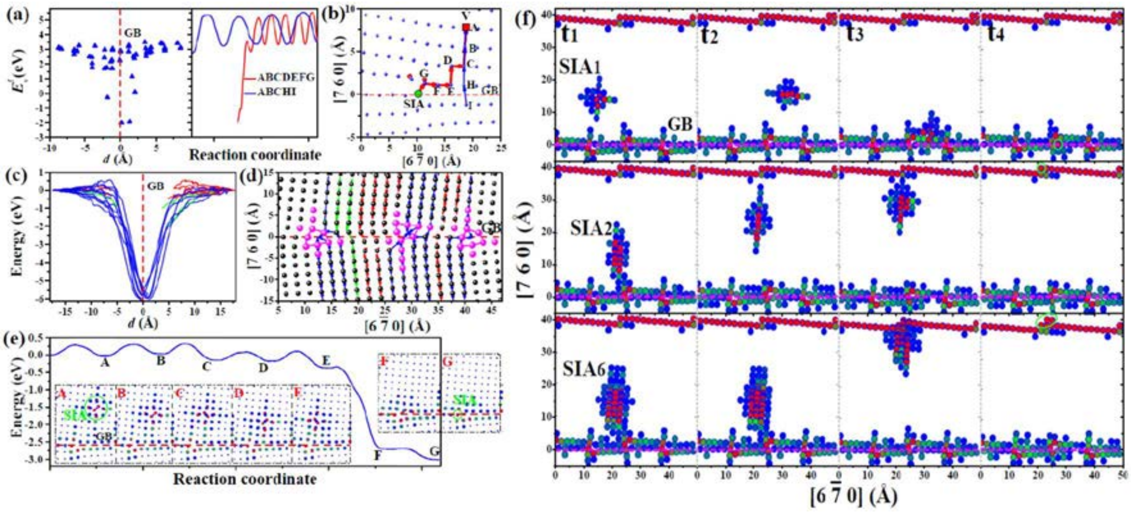

FIG. 26. (a) and (b) Three- and one-dimensional motion behavior of the V and/or SIA near a Σ85 (7 6 0) GB in W, (c) and (d) in Mo, and (e) in Fe. In (a), the left part shows the V energy profile near the GB where d is the distance of the V normal to the GB and E_v^f denotes the V formation energy. The vertical dashed red line indicates the GB position. The right part shows the energy landscape of the V along two paths A→B→C→D→E→F→G and A→B→C→H→I as marked in (b). The green sphere presents a SIA while a filled red square is for a V. The path direction is given based on motion direction of the atom during V migration towards the GB. For path A→B→C→D→E→F→G, the V spontaneously recombines with the SIA as created at site G during the following structural relaxation at 0 K. (c) shows energy landscapes of a <1 1 1> crowdion whose motion trajectories near a Σ85 (7 6 0) GB are shown in (d). The vertical dashed red line in (c) and the horizontal dashed red line in (d) indicates the GB position. The color of the landscape curves corresponds to the color of the SIA trajectories. In (c), d is the distance of the SIA center normal to the GB. (e) shows diffusion and trap of a <110> dumbbell near a Σ85 (7 6 0) GB in Fe. The SIA is marked by a dashed green circle. (f) Representative snapshots of the MD simulation of the SIA and cluster behavior near a pure Fe GB Σ85 (7 6 0)/ [0 0 1] at 800 K within a time period of one nano-second. For the single SIA, SIA$_2$ and SIA$_6$, four frames of the animation were given, e.g. the snapshots at t1, t2, t3 and t4 for the SIA. Here, the GB position is indicated by a pink dashed lin. The green circle marks the SIA after it is absorbed by the GB or the surface.

6.3. Dynamic Annihilation of the V via SIA Reflection

The reflection may influence the dynamic annihilation mechanism for the V–SIA near the GB. As shown in Fig. 23(c), if a V near the GB was placed, a nearly squared potential well appeared in the SIA energy landscape, where a V was found to spontaneously recombine with a SIA. Although the V itself could also migrate towards the GB following a decreasing energy landscape, the energy barrier for the V diffusion is far higher than the SIA diffusion barrier. The V near the GB preferentially waits for the SIA to come close to it and gets annihilated. MS calculations of the energetics and kinetics of the V around a SIA$_n$ suggested that, a spontaneous annihilation region formed around a SIA$_n$ that is initially in the bulk or reflected to the grain interior from the neighboring region of the GB.

Next, the dynamic annihilation picture at long timescale was explored by using the OKMC method. In the OKMC simulations, two types of the SIA energy landscape were considered based on MS calculations (Figs. 23 and 24). Correspondingly, two model systems were built, i.e. Sys1 and Sys2 (Fig. 27). Three typical temperatures, 10, 563 and 850 K were selected based on experimental conditions [10, 15]. In Sys1, the SIA energy landscape is increasing and then decreasing as the SIA approaches the GB: $E_a = \{(E_a^{\max} - E_a^{bulk})\exp[-((d-d_0)/d_0)^2] + E_a^{bulk}\}H(d-d_0)$, where $E_a^{\max}$ is the maximum reflection energy barrier with a value of 0.4 eV, E_a^{bulk} is the energy barrier for the SIA diffusion in the bulk with a value of 0.002 eV, d is distance of the SIA normal to the GB, d_0 is half-width of the GB sink with a value of 5.0 Å, H is the Heaviside step function whose value is zero for negative argument and one for positive argument. In Sys2, the SIA energy landscape is just climbing: $E_a = (E_a^{\max} - E_a^{bulk})\exp[-(d/d_0)^2] + E_a^{bulk}$. For the V, the energy barrier near the GB was assigned to be one half of the bulk value and the GB trap range for the V was 5.0 Å. The annihilation radius for the SIA–V in the bulk was given of 10.0 Å. The energy barrier for the SIA rotation was 0.43 eV.

Figures 27(a) and (b) shows the SIA motion trajectories under these two simplified energy landscapes. The evolution of the distance of the SIA normal to the GB suggested that, in Sys1 at 10 K the SIA approached the GB until it was reflected by the GB and then moved away from the GB (Fig. 27(a)). The "approaching-reflection" repeated. Although the energy landscape was set to be increasing and then decreasing, the SIA was not observed to be trapped by the GB during the simulation time of 10^{-7} s, similar to that in Sys2 (Fig. 27(b)) where the energy landscape is just increasing. This could be attributed to the exceptionally small value of the SIA diffusion barrier away from the GB than that for the SIA approaching the GB (about 0.002 versus 0.4 eV). Figure 27(c) suggests that the annihilation fraction of the SIA–V in Sys1 and Sys2 increased from 18% at 10 K to 25% and 30%, respectively. As the temperature increased to 563 and 850 K, the SIA behavior was similar to that at 10 K apart from having "approaching-reflection" frequent in observation. At such high temperatures, the SIA was still moving one-dimensionally locally. Meanwhile the rotation of the SIA was activated. Correspondingly, the annihilation fraction increased to over 35% and 45% respectively from 20% when the IR mechanism was not considered. This indicates that the reflection of the SIA enhances SIA–V annihilation. This could be ascribed to the reflection-extended lifetime of the SIA in the bulk. Therefore, the IR mechanism could serve as a self-healing mechanism, particularly at a low temperature, e.g. 10 and 563 K where the V is actually immobile [7].

In the above simulations, the initial objects in the system were SIA-V pairs with a concentration of 300 appm. Calculations by Zhou *et al* [59] suggest that the small SIA-cluster also has high mobility along <1 1 1> compared to the single SIA. Therefore, the IR mechanism may hold for SIA-clusters at long timescale. The difference in the dynamic picture lies in the rotation of the defects. The rotation barrier of a SIA_2 is as high as 1.307 eV [59]. Compared with the single SIA, the rotation of the cluster during the IR rarely occurs even at a high temperature of 850 K.

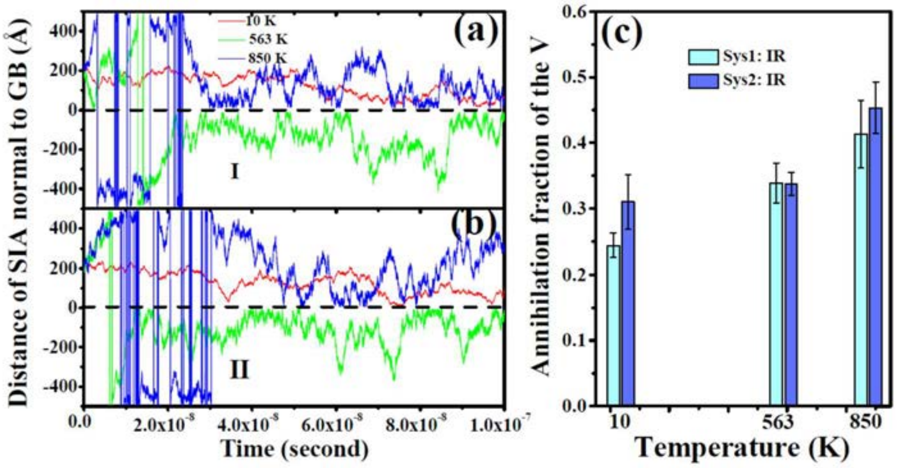

FIG. 27. (a) and (b) Typical trajectories are shown of a SIA near the GB at three typical temperatures of 10, 563 and 850 K, and (c) projects the statistic results of the annihilation fraction of the V–SIA at 10, 563 and 850 K in W. In (a), the SIA landscape near the GB is featured by a shoulder. In (b), the SIA landscape is uphill. In (a) and (b), the horizontal dashed black line indicates the GB position. Due to periodic boundary conditions, the defect reenters the system from the opposite side. In (c), the symbols Sys1 and Sys2 represent two systems designating that; IR is short for interstitial reflection.

6.4. Mechanisms Responsible For the Enhanced Radiation-performance of NC W

Nano-structured W exhibits radiation-resistance of [7, 8], particularly at the low temperature [7]. In the neutron-irradiation experiment at 563 K [7], post-irradiation examinations showed that the degree of hardening due to irradiation was significantly reduced for fine-grained W-0.3 wt%TiC (0.9 μm) compared with commercially available pure W (20 μm). Neutron-irradiation experiments at 823 and 873 K [8] suggested that the density of voids in commercially available pure W (average grain size: 20 μm) is about 4 times that in ultra-fine grained W-(0.25-0.8)wt%TiC samples with equiaxed grain sizes of 50–200 nm. Recently, Borovikov *et al* [45] proposed the coupled motion of GBs in bcc W as a possible radiation-damage healing mechanism under fusion reactor conditions. The authors in Refs. [7, 8] attributed the improved radiation-resistance of grain-refined materials under experimental conditions to the role of the GB as the effective sinks for irradiation produced defects. Li *et al* [37] ascribed the radiation-tolerance of nano-structured W to GB-enhanced segregation and annihilation of the V mainly based on static analyses. Figure 19(c) also suggests that the short-ranged interaction of the V with the SIA_n could explain the improved radiation performance of nano-structured W due to SIA_n-enhanced diffusion and annihilation. The present work, however, provides some new insights into the radiation-tolerance of nano-structured W based on dynamic and long-ranged interaction among SIAs, Vs and the GB.

The IR works near a locally dense region for one-dimensional migration SIA-type defects, like the SIA and SIA_n in W and Mo and the SIA_n in Fe. After the SIA is reflected, it can annihilate the V far away from it via the long-range migration at a low energy barrier. Besides, the annihilation volume of a SIA_n in the bulk is far larger than that for a SIA_n trapped at the GB (Fig. 28). Due to these two favorable factors, the IR can contribute a lot to eliminate the V near the GB particularly in the bulk. The working temperature for the IR is nearly the activation temperature for the bulk SIA given the high mobility of the bulk SIA_n [59]. The temperature could be extremely low, implying that the annihilation of the V with the SIA_n via the IR mechanism contributes to alleviating the radiation damage in W at low temperature, e.g. at 563 K.

The dynamic IE works without requirement of the vacancy to locate in the vicinity of the SIA but requiring the vacancy to be near the GB. After the SIA segregated at the GB, it moved along the GB. When the V in the bulk entered the low-energy barrier annihilation region around the SIA, the V was recombined. As the SIA was concentrated at the GB, during the moving and waiting of the SIA at the GB, the SIA was clustered to be di-SIA, which slows down SIA mobility along the GB (Fig. 21). Then, the annihilation proceeded via coupled motion of the di-SIA along the GB and the diffusion of the V towards the GB. The working temperature for the dynamic IE is the activation temperature for the SIA and di-SIA motion along the GB, which could be lower than the one for the diffusion of the bulk V (Fig. 20(c)), except in certain GBs. Therefore, the low-temperature radiation-resistance can also be ascribed to the recombination of the V with the SIA_n via the dynamic IE.

While the findings here are suggestive to the interpretation of material properties for future fusion reactors, a number of issues remain to be explored considering complexity of the real fusion environments. First, damage evolution in irradiated W is a complex multiscale problem involving a large number of competing effects. In the present work, we only considered the behavior of the SIA_n and V near several W GBs. Actually, under the irradiation of 14 MeV neutrons, point defects (SIA, V), defects clusters (SIA_n, V_n, SIA-type dislocation loops and voids as observed in simulation experiments [7, 8]) and high concentrations of hydrogen (H), helium are all produced. Moreover, alloying elements are created via transmutation reaction. Impurity atoms, e.g. carbon, nitrogen and oxygen, especially those that segregate to GBs, will also play a role. Triple junctions in poly- and nano-crystalline W, can substantially affect evolution of the defects. These objects may complicate the SIA_n behavior and the annihilation mechanism we have described here due to complex interactions among them.

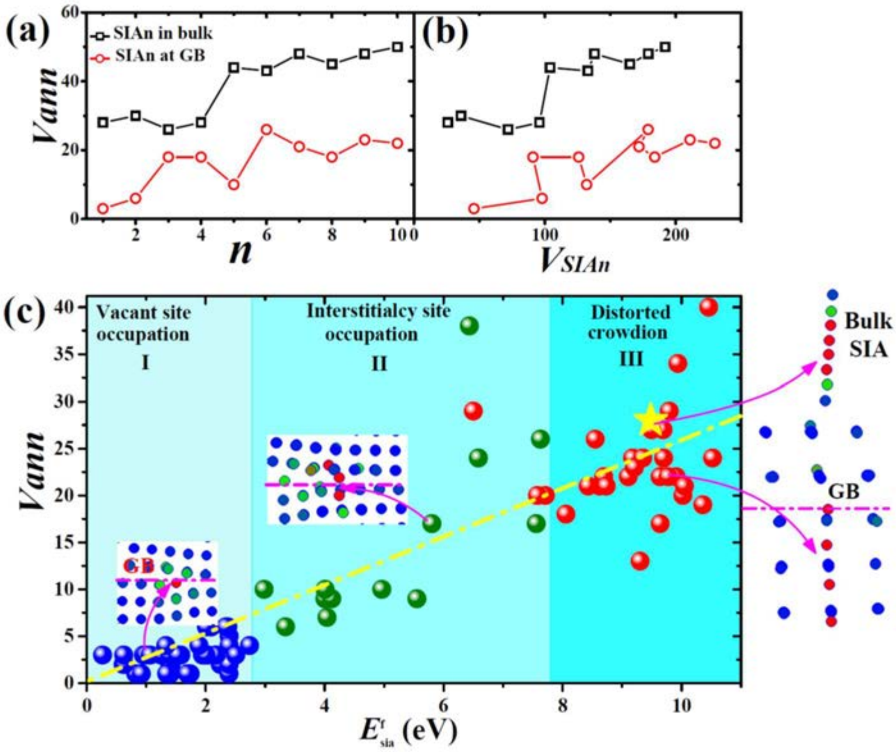

Figure 28. (a) Annihilation volume of a SIA$_n$ (V_{ann}) as a function of the number of SIA in the cluster, (b) correlation of V_{ann} with the volume of the SIA$_n$ (V_{SIAn}), and (c) the annihilation capacity of a SIA for the V as a function of the SIA morphology in W. The annihilation volume of a SIA$_n$ is defined as the number of lattices around a SIA$_n$ where a V spontaneously recombines with a SIA within the cluster. The volume of a SIA$_n$ is defined as the number of sites where the deviation of the atom potential energy from its bulk value is larger than 0.05 eV. In (c), E^{f}_{sia} denotes the SIA formation energy to measure stability of the SIA with different morphologies. The typical morphologies are given for the SIA residing at the designated vacant site, at the interstitialcy site, existing as a distorted crowdion and as a perfect <1 1 1> crowdion. The yellow dashed colored line is to guide the readers' eye.

7. ATOMIC DATASET ON THE INTERACTION OF THE VAND SIA WITH THE GB

Finally, we present relevant atomic data on the interaction among the V, SIA and the GB (Tables 1-3).

TABLE 1. SOME CHARACTERISTIC QUANTITIES DESCRIBING THE GB SERVING AS THE SINK FOR THE VACANCY AND INTERSTITIAL, AND CATALYST FOR VACANCY-INTERSTITIAL ANNIHILATION. THESE INCLUDE THE BARRIER OF VACANCY (INTERSTITIAL) DIFFUSION IN THE BULK, NEAR THE PURE GB, AND THE BARRIER OF VACANCY-INTERSTITIAL ANNIHILATION WITHIN THE SPONTANEOUS ANNIHILATION REGION AND NEAR THIS REGION. THE CORRESPONDING ACTIVATION TEMPERATURE (T_A) IS ALSO GIVEN, DEFINED AS THE TEMPERATURE THAT GIVES THE TRANSITION TIME ONE SECOND. THE TRANSITION TIME $t = t_0 \exp(E_a / k_B T)$, WHERE t_0 IS THE VIBRATIONAL PERIOD OF W ATOMS IN THE BULK AND ASSUMED TO BE 10^{-12} S. THE BOLTZMANN CONSTANT K_B HAS A VALUE OF 8.617×10^{-5} EV/K. HERE *V* (*SIA*) IS SHORT FOR THE VACANCY (INTERSTITIAL). OTHER SYMBOLS ARE DEFINED AS FOLLOWS. THE GB INFLUENCE RANGE AND THE CORRESPONDING VOLUME FRACTION ARE LISTED. THE FRACTION OF GB REGION IS CALCULATED BY $\frac{L^3 - (L-W)^3}{L^3} = x^3 - 3x^2 + 3x$, WHERE $X=W/L$ WITH *W* AS THE INFLUENCE RANGE, *L* AS THE GRAIN SIZE (HERE ASSIGNED TO BE 100 NM).

V_m^{bulk} : VACANCY DIFFUSES IN THE BULK,

V_m^{GB} : VACANCY DIFFUSES NEAR THE GB,

SIA_m^{bulk} : INTERSTITIAL DIFFUSES IN THE BULK,

SIA_m^{GB} : INTERSTITIAL DIFFUSES NEAR THE GB,

ann_{V-SIA}^{GB} : VACANCY-INTERSTITIAL ANNIHILATION WITHIN THE SPONTANEOUS ANNIHILATION REGION,

$ann_{V-SIA}^{near-GB}$: VACANCY-INTERSTITIAL ANNIHILATION NEAR THE SPONTANEOUS ANNIHILATION REGION.

	V_m^{bulk}	V_m^{GB}	SIA_m^{bulk}	SIA_m^{GB}	ann_{V-SIA}^{GB}	$ann_{V-SIA}^{near-GB}$
Barrier (eV)	1.8	0.98	0.002	0	0	0.31
T_a (K)	702	382	1	0	0	121
Range (Å)		9.4		26.5	10	11.6
Fraction (%)		3		8	3	3

TABLE 2. PARTS OF THE DEFECT PROPERTIES IN BULK W.

Value	Term	Comments
1.8 eV	Em_V_bulk	Diffusion energy barrier for a single V in W bulk
1.94 eV	Em_V$_2$_bulk	Diffusion energy barrier for V$_2$ in W bulk
2.17 eV	Em_V$_3$_bulk	Diffusion energy barrier for V$_3$ in W bulk
2.78 eV	Em_V$_4$_bulk	Diffusion energy barrier for V$_4$ in W bulk
3.12 eV	Em_V$_5$_bulk	Diffusion energy barrier for V$_5$ in W bulk
3.11 eV	Em_V$_7$_bulk	Diffusion energy barrier for V$_7$ in W bulk
0.66 eV	Eb_V-V_bulk	Binding energy of a V with a V in W bulk
1.12 eV	Eb_V-V$_2$_bulk	Binding energy of a V with a V$_2$ in W bulk
1.90 eV	Eb_V-V$_3$_bulk	Binding energy of a V with a V$_3$ in W bulk
1.79 eV	Eb_V-V$_4$_bulk	Binding energy of a V with a V$_4$ in W bulk
2.30 eV	Eb_V-V$_5$_bulk	Binding energy of a V with a V$_5$ in W bulk

1.75 eV	Eb_V-V$_6$_bulk	Binding energy of a V with a V$_6$ in W bulk
2.27 eV	Eb_V-V$_7$_bulk	Binding energy of a V with a V$_7$ in W bulk
2.27 eV	Eb_V-V$_8$_bulk	Binding energy of a V with a V$_8$ in W bulk
2.27 eV	Eb_V-V$_9$_bulk	Binding energy of a V with a V$_9$ in W bulk
2.08 eV	Eb_V-V$_{10}$_bulk	Binding energy of a V with a V$_{10}$ in W bulk
2.35 eV	Eb_V-V$_{27}$_bulk	Binding energy of a V with a V$_{27}$ in W bulk
3.17 eV	Eb_V-V$_{51}$_bulk	Binding energy of a V with a V$_{51}$ in W bulk
3.21 eV	Eb_V-V$_{76}$_bulk	Binding energy of a V with a V$_{76}$ in W bulk
3.36 eV	Eb_V-V$_{112}$_bulk	Binding energy of a V with a V$_{112}$ in W bulk
5.26 Å	W_V-V_bulk	Trapping radius of a V for a V in W bulk
6.07 Å	W_V-V$_2$_bulk	Trapping radius of a V$_2$ for a V in W bulk
6.75 Å	W_V-V$_3$_bulk	Trapping radius of a V$_3$ for a V in W bulk
6.59 Å	W_V-V$_4$_bulk	Trapping radius of a V$_4$ for a V in W bulk
6.86 Å	W_V-V$_5$_bulk	Trapping radius of a V$_5$ for a V in W bulk
6.73 Å	W_V-V$_6$_bulk	Trapping radius of a V$_6$ for a V in W bulk
7.65 Å	W_V-V$_7$_bulk	Trapping radius of a V$_7$ for a V in W bulk
7.57 Å	W_V-V$_8$_bulk	Trapping radius of a V$_8$ for a V in W bulk
7.88 Å	W_V-V$_9$_bulk	Trapping radius of a V$_9$ for a V in W bulk
7.89 Å	W_V-V$_{10}$_bulk	Trapping radius of a V$_{10}$ for a V in W bulk
8.91 Å	W_V-V$_{27}$_bulk	Trapping radius of a V$_{27}$ for a V in W bulk
10.03 Å	W_V-V$_{51}$_bulk	Trapping radius of a V$_{51}$ for a V in W bulk
11.28 Å	W_V-V$_{76}$_bulk	Trapping radius of a V$_{76}$ for a V in W bulk
12.16 Å	W_V-V$_{113}$_bulk	Trapping radius of a V$_{113}$ for a V in W bulk
0.002 eV	Em_SIA_bulk	Diffusion energy barrier for single SIA in W bulk
0.43 eV	Em_SIA_rotate	Rotation energy barrier for single SIA in W bulk
1.02 eV	Em_SIA$_2$_rotate	Rotation energy barrier for SIA$_2$ in W bulk
1.83 eV	Em_SIA$_3$_rotate	Rotation energy barrier for SIA$_3$ in W bulk
2.20 eV	Eb_SIA-SIA_bulk	Binding energy of a SIA with a SIA in W bulk
3.23 eV	Eb_SIA-SIA$_2$_bulk	Binding energy of a SIA with a SIA$_2$ in W bulk
4.71 eV	Eb_SIA-SIA$_3$_bulk	Binding energy of a SIA with a SIA$_3$ in W bulk
4.31 eV	Eb_SIA-SIA$_4$_bulk	Binding energy of a SIA with a SIA$_4$ in W bulk
5.27 eV	Eb_SIA-SIA$_5$_bulk	Binding energy of a SIA with a SIA$_5$ in W bulk
6.96 eV	Eb_SIA-SIA$_6$_bulk	Binding energy of a SIA with a SIA$_6$ in W bulk
7.40 eV	Eb_SIA-SIA$_{12}$_bulk	Binding energy of a SIA with a SIA$_{12}$ in W bulk
13.77 Å	W_SIA-SIA_bulk	Trapping radius of a SIA for a SIA in W bulk
20.62 Å	W_SIA-SIA$_2$_bulk	Trapping radius of a SIA$_2$ for a SIA in W bulk
17.91 Å	W_SIA-SIA$_3$_bulk	Trapping radius of a SIA$_3$ for a SIA in W bulk
20.64 Å	W_SIA-SIA$_4$_bulk	Trapping radius of a SIA$_4$ for a SIA in W bulk
20.68 Å	W_SIA-SIA$_5$_bulk	Trapping radius of a SIA$_5$ for a SIA in W bulk
20.65 Å	W_SIA-SIA$_6$_bulk	Trapping radius of a SIA$_6$ for a SIA in W bulk
20.71 Å	W_SIA-SIA$_{12}$_bulk	Trapping radius of a SIA$_7$ for a SIA in W bulk

TABLE 3. PARTS OF THE DEFECT PROPERTIES NEAR W GBS. EB_SIA-SIA_WITHIN_GB: BINDING ENERGY OF A SIA WITH SIA WITHIN THE GB. EM_SIA_ALONG_GB: DIFFUSION ENERGY BARRIER FOR A SIA WITHIN THE GB. EM_SIA$_2$_ALONG_GB: DIFFUSION ENERGY BARRIER FOR A SIA$_2$ WITHIN THE GB. EB_V-GB: BINDING ENERGY OF A V WITH THE GB. W_V-GB: TRAPPING RADIUS OF THE GB FOR A V. W_SIA_GB: TRAPPING RADIUS OF THE GB FOR A SIA.

GB	Eb_SIA-SIA_within_GB (eV)
Σ5(210)/[001]	0.57 eV
Σ5(310)/[001]	1.00 eV
Σ13(320)/[001]	1.26 eV
Σ25(430)/[001]	1.71 eV
Σ85(760)/[001]	1.86 eV
Σ113(870)/[001]	0.71 eV
GB	Em_SIA_along_GB (eV)
Σ5(210)/[001]	0.02 eV
Σ5(310)/[001]	0.20 eV
Σ13(320)/[001]	0.87 eV
Σ25(430)/[001]	2.63 eV
Σ85(760)/[001]	2.29 eV
Σ113(870)/[001]	1.59 eV
GB	Em_SIA$_2$_along_GB
Σ5(210)/[001]	0.02 eV
Σ5(310)/[001]	1.17 eV
Σ13(320)/[001]	1.64 eV
Σ25(430)/[001]	3.45 eV
Σ85(760)/[001]	3.10 eV
Σ113(870)/[001]	1.92 eV
GB	Eb_V-GB
Σ5(310)/[001]	0.86 eV
Σ13(320)/[001]	1.75 eV
Σ25(430)/[001]	2.00 eV
Σ5(310)/[001]	7.50 eV
Σ13(320)/[001]	7.80 eV
Σ25(430)/[001]	7.90 eV
GB	W_V-GB
Σ5(310)/[001]	4.70 Å
Σ13(320)/[001]	9.50 Å
Σ25(430)/[001]	14.40 Å
GB	W_SIA_GB
Σ5(310)/[001]	13.30 Å
Σ13(320)/[001]	19.60 Å
Σ25(430)/[001]	18.50 Å

ACKNOWLEDGMENTS

This study was part of the CRP (Coordinated Research Projects) program carried out under the sponsorship of the International Atomic Energy Agency (IAEA).

This work was supported in part by the National Magnetic Confinement Fusion Program (Grant no.: 2015GB112001), the National Key Research and Development Program of China (Grant No.: 2017YFA0402800), the National Natural Science Foundation of China (Nos.:11505215, 11735015, 51671185, 11475214, 11575229, 11505214, 51771181), and by the Center for Computation Science, Hefei Institutes of Physical Sciences.

Parts of this article have been reproduced with permission from *Nuclear Fusion* **57**, 116055 (2017); *Journal Nuclear Materials* **500**, 199 (2018); and *Nuclear Fusion* **53**, 123014 (2013).

REFERENCES

[1] CHANT, I., MURTY, K.L., Structural materials issues for the next generation fission reactors, JOM **62** (2010) 67–74.

[2] ZINKLE, S.J., BUSBY, J.T., Structural materials for fission & fusion energy, Mater. Today **12** (2009) 12–19.

[3] WRIGHT, G.M., MAYER, M., ERTL, K., DE SAINT-AUBIN, G., RAPP, J., Hydrogenic retention in irradiated tungsten exposed to high-flux plasma, Nucl. Fusion **50** (2010) 075006.

[4] TYBURSKA, B., ALIMOV, V.KH., OGORODNIKOVA, O.V., SCHMID, K., ERTL, K., Deuterium retention in self-damaged tungsten, J. Nucl. Mater. **395** (2009) 150.

[5] WAMPLER, W.R., DOERNER, R.P., The influence of displacement damage on deuterium retention in tungsten exposed to plasma, Nucl. Fusion **49** (2009) 115023.

[6] WRIGHT, G.M., WHYTE, D.G., LIPSCHULTZ, B., Measurement of hydrogenic retention and release in molybdenum with the DIONISOS experiment, J. Nucl. Mater. **390-391** (2009) 544.

[7] KURISHITA, H., KOBAYASHI, S., NAKAI, K., OGAWA, T., HASEGAWA, A., ABE, K., ARAKAWA, H., MATSUO, S., TAKIDA, T., TAKEBE, K., KAWAI, M., YOSHIDA, N., Development of ultra-fine grained W-(0.25-0.8)wt%TiC and its superior resistance to neutron and 3 MeV He-ion irradiations, J. Nucl. Mater. **377** (2008) 34–40.

[8] KURISHITA, H., AMANO, Y., KOBAYASHI, S., NAKAI, K., ARAKAWA, H., HIRAOKA, Y., TAKIDA, T., TAKEBE, K., MATSUI, H., Development of ultra-fine grained W-TiC and their mechanical properties for fusion applications, J. Nucl. Mater. **367-370** (2007) 1453–1457.

[9] XIE, Z.M., LIU, R., MIAO, S., YANG, X.D., ZHANG, T., WANG, X.P., FANG, Q.F., LIU, C.S., LUO, G.-N., LIAN, Y.Y., LIU, X., Extraodinary high ductility/strength of the interface designed bulk W-ZrC alloy plate at relatively low temperature. Sci. Rep. **5** (2015) 16014.

[10] FAN, J., HAN, Y., LI, P., SUN, Z., ZHOU, Q., Micro/nano composited tungsten material and its high thermal loading behavior. J. Nucl. Mater. **455** (2014) 717–723.

[11] YAN, Q., ZHANG, X., WANG, T., YANG, C., GE, C., Effect of hot working process on the mechanical properties of tungsten materials. J. Nucl. Mater. **442** (2013) S233–S236.

[12] HE, B., HUANG, B., XIAO, Y., LIAN, Y., LIU, X., TANG, J., Preparation and thermal shock characterization of yttrium doped tungsten-potassium alloy. J. Alloys Compd. **686** (2016) 298–305.

[13] KITSUNAI, Y., KURISHITA, H., KUWABARA, T., NARUI, M., HASEGAWA, M., TAKIDA, T., TAKEBE, K., Radiation embrittlement behavior of fine-grained molybdenum alloy with 0.2wt%TiC addition, J. Nucl. Mater. **346** (2005) 233–243.

[14] KURISHITA, H., KUWABARA, T., HASEGAWA, M., SOBAYASHI, S., NAKAI, K., Microstructural control to improve the resistance to radiation embrittlement in vanadium, J. Nucl. Mater. **343** (2005) 318–324.

[15] ROSE, M., BALOGH, A.G., HAHN, H., Instability of irradiation induced defects in nanostructured materials, Nucl. Instrum. Meth. B. **127-128** (1997) 119–122.

[16] CHIMI, Y., IWASE, A., ISHIKAWA, N., KOBIYAMA, M., INAMI, T., OKUDA, S., Accumulation and recovery of defects in ion-irradiated nanocrystalline gold, J. Nucl. Mater. **297**

(2001) 355–357.

[17] YU, K.Y., LIU, Y., SUN, C., WANG, H., SHAO, L., FU, E.G., ZHANG, X., Radiation damage in helium ion irradiated nanocrystalline Fe, J. Nucl. Mater. **425** (2012) 140–146.

[18] YU, K.Y., BUFFORD, D., SUN, C., LIU, Y., WANG, H., KIRK, M.A., LI, M., ZHANG, X., Removal of stacking-fault tetrahedra by twin boundaries in nanotwinned metals, Nat. Commun. **4** (2013) 1377.

[19] KILMAMETOV, A., BALOGH, A., GHAFARI, M., GAMMER, C., MANGLER, C., RENTENBERGER, C., VALIEV, R., HAHN, H., Radiation effects in bulk nanocrystalline FeAl alloy, Radiat. Eff. Defect. S. **167** (2012) 631–639.

[20] DIAZ DE LA RUBIA, T., ZBIB, H.M., KHRAISHI, T.A., WIRTH, B.D., VICTORIA, M., CATURLA, M.J., Multiscale modelling of plastic flow localization in irradiated materials, Nature **406** (2000) 871–874.

[21] VICTORIA, M., BALUC, N., BAILAT, C., DAI, Y., LUPPO, M.I., SCHAUBLIN, R., SINGH, B.N., The microstructure and associated tensile properties of irradiated fcc and bcc metals, J. Nucl. Mater. **276** (2000) 114–122.

[22] ODETTE, G.R., ALINGER, M.J., WIRTH, B.D., Recent developments in irradiation-resistant steels, Annu. Rev. Mater. Res. **38** (2008) 471–503.

[23] SICKAFUS, K.E., GRIMES, R.W., VALDEZ, J.A., CLEAVE, A., TANG, M., ISHIMARU, M., CORISH, S.M., STANEK, C.R., UBERUAGA, B.P., Radiation-induced amorphization resistance and radiation tolerance in structurally related oxides, Nat. Mater. **6** (2007) 217–223.

[24] ACKLAND, G., Controlling radiation damage, Science **327** (2010) 1587–1588.

[25] GRIMES, R.W., KONINGS, R.J.M., EDWARDS, L., Greater tolerance for nuclear materials, Nat. Mater. **7** (2008) 683–685.

[26] ZINKLE, S.J., GHONIEM, N.M., Prospects for accelerated development of high performance structural materials, J. Nucl. Mater. **417** (2011) 2–8.

[27] CHEN, Y., LI, J., YU, K.Y., WANG, H., KIRK, M.A., LI, M., ZHANG, X., *In situ* studies on radiation tolerance of nanotwinned Cu, Acta Mater. **111** (2016) 148–156.

[28] SUN, C., ZHENG, S., WEI, C.C., WU, Y., SHAO, L., YANG, Y., HARTWIG, K.T., MALOY, S.A., ZINKLE, S.J., ALLEN, T.R., WANG, H., ZHANG, X., Superior radiation-resistant nanoenginerred austenitic 304L stainless steel for applications in extreme radiation environments, Sci. Rep. **5** (2015) 7801.

[29] FU, E.G., CARO, M., ZEPEDA-RUIZ, L.A., WANG, Y.Q., BALDWIN, K., BRINGA, E., NASTASI, M., CARO, A., Surface effects on the radiation response of nanoporous Au foams, Appl. Phys. Lett. **101** (2012) 191607.

[30] BRINGA, E.M., MONK, J.D., CARO, A., MISRA, A., ZEPEDA-RUIZ, L., DUCHAINEAU, M., ABRAHAM, F., NASTASI, M., PICRAUX, S.T., WANG, Y.Q., FARKAS, D., Are nanoporous materials radiation resistant? Nano Lett. **12** (2012) 3351–3355.

[31] SUN, C., BUFFORD, D., CHEN, Y., KIRK, M.A., WANG, Y.Q., LI, M., WANG, H., MALOY, S.A., ZHANG, X., *In situ* study of defect migration kinetics in nanoporous Ag with enhanced radiation tolerance, Sci. Rep. **4** (2014) 3737.

[32] BAI, X.-M., VOTER, A.F., HOAGLAND, R.G., NASTASI, M., UBERUAGA, B.P., Efficient annealing of radiation damage near grain boundaries via interstitial emission, Science **327** (2010) 1631–1634.

[33] CHEN, D., WANG. J., CHEN, T., SHAO, L., Defect annihilation at grain boundaries in alpha-Fe, Sci. Rep. **3** (2013) 1450.

[34] TANG, X., GUO, Y., FAN, Y., YIP, S., YILDIZ, B., Interstitial emission at grain boundary in nanolayered alpha-Fe, Acta Mater. **105** (2016) 147–154.

[35] LI, X., LIU, W., XU, Y., LIU, C.S., PAN, B.C., LIANG, Y., FANG, Q.F., CHEN, J., LUO, G.N., LU, G., WANG, Z., Radiation resistance of nano-crystalline iron: Coupling of the fundamental segregation process and the annihilation of interstitials and vacancies near the grain boundaries, Acta Mater. **109** (2016) 115–127.

[36] LI, X., LIU, W., XU, Y., LIU, C.S., PAN, B.C., LIANG, Y., FANG, Q.F., CHEN, J., LUO, G.N., LU, G., WANG, Z., Energetic and kinetic dataset on interaction of the vacancy and self-interstitial atom with the grain boundary in α-iron, Data Brief **7** (2016) 798–813.

[37] LI, X., LIU, W., XU, Y., LIU, C.S., FANG, Q.F., PAN, B.C., CHEN, J., LUO, G., WANG, Z., An

energetic and kinetic perspective of the grain-boundary role in healing radiation damage in tungsten, Nucl. Fusion **53** (2013) 123014.

[38] LI, X., DUAN, G., XU, Y., ZHANG, Y., LIU, W., LIU, C.S., LIANG, Y., CHEN, J.-L., LUO, G.-N., Annihilating vacancies via dynamic reflection and emission of interstitials in nano-crystal tungsten, Nucl. Fusion **57** (2017) 116055.

[39] DUAN, G., LI, X., SUN, J., HAO, C., XU, Y., ZHANG, Y., LIU, W., LIU, C.S., Clustering and segregation of small vacancy clusters near tungsten (0 0 1) surface, Nucl. Instrum. Methods B **414** (2018) 29–37.

[40] DUAN, G., LI, X., XU, Y., ZHANG, Y., JIANG, Y., HAO, C., LIU, C.S., FANG, Q.F., CHEN, J.-L., LUO, G.-N., WANG, Z., Surface-structure dependence of healing radiation-damage mechanism in nanoporous tungsten, J. Nucl. Mater. **498** (2018) 362–372.

[41] LI, X., LIU, W., XU, Y., LIU, C.S., FANG, Q.F., PAN, B.C., CHEN, J., LUO, G.N., WANG, Z., Principal parameters characterizing the interactions between irradiation-induced point defects and several tilt symmetric grain boundaries in Fe, Mo and W, J. Nucl. Mater. **444** (2014) 229–236.

[42] LI, X., LIU, W., XU, Y., LIU, C.S., FANG, Q.F., PAN, B.C., WANG, Z., Energetic and kinetic behaviors of small vacancy clusters near a symmetric Σ5(310)/[001] tilt grain boundary in bcc Fe, J. Nucl. Mater. **440** (2013) 250–256.

[43] LI, X., XU, Y., DUAN, G., SUN, J., HAO, C., ZHANG, Y., LIU, W., LIU, C.S., FANG, Q.F., On the possibility of universal interstitial emission induced annihilation in metallic nanostructures, J. Nucl. Mater. **500** (2018) 199–212.

[44] LI, X., XU, Y., DUAN, G., SUN, J., HAO, C., ZHANG, Y., LIU, W., LIU, C.S., FANG, Q.F., Atomic dataset on the interstitial emission induced annihilation in metallic nanostructures, Data Brief (submitted).

[45] BOROVIKOV, V., TANG, X.Z., PEREZ, D., BAI, X.-M., UBERUAGA, B.P., VOTER, A.F., Coupled motion of grain boundaries in bcc tungsten as a possible radiation-damage healing mechanism under fusion reactor conditions, Nucl. Fusion **53** (2013) 063001.

[46] VOTER, A.F., SICKAFUS, K.E., KOTOMIN, E.A., UBERUAGA, B.P., Radiation effects in solids, Springer (2007) 1–23.

[47] AHLGREN, T., HEINOLA, K., JUSLIN, N., KURONEN, A., Bond-order potential for point and extended defect simulations in tungsten, J. Appl. Phys. **107** (2010) 033516.

[48] MARINICA, M.-C., VENTELON, L., GILBERT, M.R., PROVILLE, L., DUDAREV, S.L., MARIAN, J., BENCTEUX, G., WILLAIME, F., Interatomic potentials for modeling radiation defects and dislocations in tungsten, J. Phys.: Condens. Matter. **25** (2013) 395502.

[49] MENDELEV, M.I., HAN, S., SROLOVITZ, D.J., ACKLAND, G.J., SUN, D.Y., ASTA, M., Development of new interatomic potentials approximate for crystalline and liquid iron, Philos. Mag. **83** (2003) 3977–3994.

[50] MISHIN, Y., MEHL, M.J., PAPACONSTANTOPOULOS, D.A., VOTER, A.F., KRESS, J.D., Structural stability and lattice defects in copper: *Ab initio*, tight-binding, and embedded-atom calculations, Phys. Rev. B **63** (2001) 224106.

[51] HEYDEN, A., BELL, A.T., KEIL, F.J., Efficient methods for finding transition states in chemical reactions: Comparison of improved dimer method and partitioned rational function optimization method, J. Chem. Phys. **123** (2005) 224101.

[52] SΦRENSEN, M.R., MISHIN, Y., VOTER, A.F., Diffusion mechanisms in Cu grain boundaries, Phys. Rev. B **62** (2000) 3658.

[53] PARK, N.-Y., CHA, P.-R., KIM, Y.-C, SEOK, H.-K., HAN, S.-H., LEE, S.-C., CHO, S., JUNG, H., Radiation damage in nano-crystalline tungsten: A molecular dynamics simulation, Met. Mater. Int. **15** (2009) 447.

[54] SAMARAS, M., DERLET, P.M., VAN SWYGENHOVEN, H., VICTORIA, M., Computer simulation of displacement cascades in nanocrystalline Ni, Phys. Rev. Lett. **88** (2002) 125505.

[55] SHAIKH, M.A., Void denudation and grain boundary migration in ion-irradiated nickel, J. Nucl. Mater. **187** (1992) 303.

[56] HAN, W.Z., DEMKOWICZ, M.J., FU, E.G., WANG, Y.Q., MISRA, A., Effect of grain boundary character on sink efficiency, Acta Mater. **60** (2012) 6341–6351.

[57] LEJČEK, P., Grain boundary segregation in metals, Springer (2010) 156.

[58] SAMARAS, M., DERLET, P.M., VAN SWYGENHOVEN, H., VICTORIA, M., Movement of

interstitial clusters in stress gradients of grain boundaries, Phys. Rev. B **68** (2003) 224111.
[59] ZHOU, W.H., ZHANG, C.G., LI, Y.G., ZENG, Z., Transport, dissociation and rotation of small self-interstitial atom clusters in tungsten, J. Nucl. Mater. **453** (2014) 202.

STUDY ON DEUTERIUM RETENTION AND PERMEATION IN HEAVY-ION IRRADIATED TUNGSTEN AT ASIPP

G.-N. LUO, F. LIU, M. ZHAO, H. ZHOU

Institute of Plasma Physics, Chinese Academy of Sciences, Hefei 230031, China

Abstract

The work performed at Institute of Plasma Physics, Chinese Academy of Sciences (ASIPP) in connection with the IAEA coordinated research project “Plasma-Wall Interaction for Irradiated Tungsten and Tungsten Alloys in Fusion Devices” is summarized.

1. DEUTERIUM RETENTION IN QUASI-HOMOGENEOUSLY DAMAGED TUNGSTEN [1,2]

Fusion neutrons (n) have long mean free paths on the order of centimeters in solids, and tungsten (W) plasma-facing material with a thickness of 1-2 cm could be volumetrically damaged [3]. Therefore, tritium (T) bulk retention in n-irradiated W becomes a significant safety concern. Recently heavy ions are widely used as surrogates for neutrons to investigate the influence of n-produced defects on T retention in W [4-7]. But drawbacks with heavy ions are their limited incident ranges and the strongly peaked damage profiles. In this experiment we employed an ultra-high energy Ne-ion beam line together with an energy degrader for tailoring the depth distribution of implanting ions, a quasi-homogeneous distribution of defects within a depth of 50 μm was produced in W. Then deuterium (D, a surrogate of T) retention behavior in the damaged W was investigated.

Tungsten foils (99.95% purity, rolled product) with dimensions of Ø20×0.11 mm and Ø20×0.05 mm were used in this study. The foils were annealed at 1373 K for 2 h before irradiation to outgas the gas impurities and to reduce the densities of intrinsic defects. The high-energy heavy-ion irradiation was performed in a terminal chamber of the Heavy ion Research Facility in Lanzhou. High-energy Ne ions of 122 MeV from accelerators first penetrated through an energy degrader then implanted into the W specimens. The energy degrader was a wheel made of 30 pieces of Al-foils with various thicknesses and was slowly turning at 12 rounds per minute. High-energy Ne ions penetrating through different Al-foils possessed different energies then the corresponding implanting ranges of them in W kept varying. Figure 1 shows the depth distribution of atomic displacement damage (dpa) and Ne concentration at one side of W irradiated to a fluence of 3×10^{20} ions/m^2, calculated with SRIM in a suggested ‘‘quick’’ option [8]. We can see that a quasi-homogeneous distribution of radiation damage to 0.16 dpa and Ne concentration to 250 appm was produced within a depth of 22 μm. Thus after sample double-side irradiation, the W specimen with a thickness of 50 μm could be considered to be quasi-homogeneously damaged. During irradiation, the sample temperature was 713±15 K.

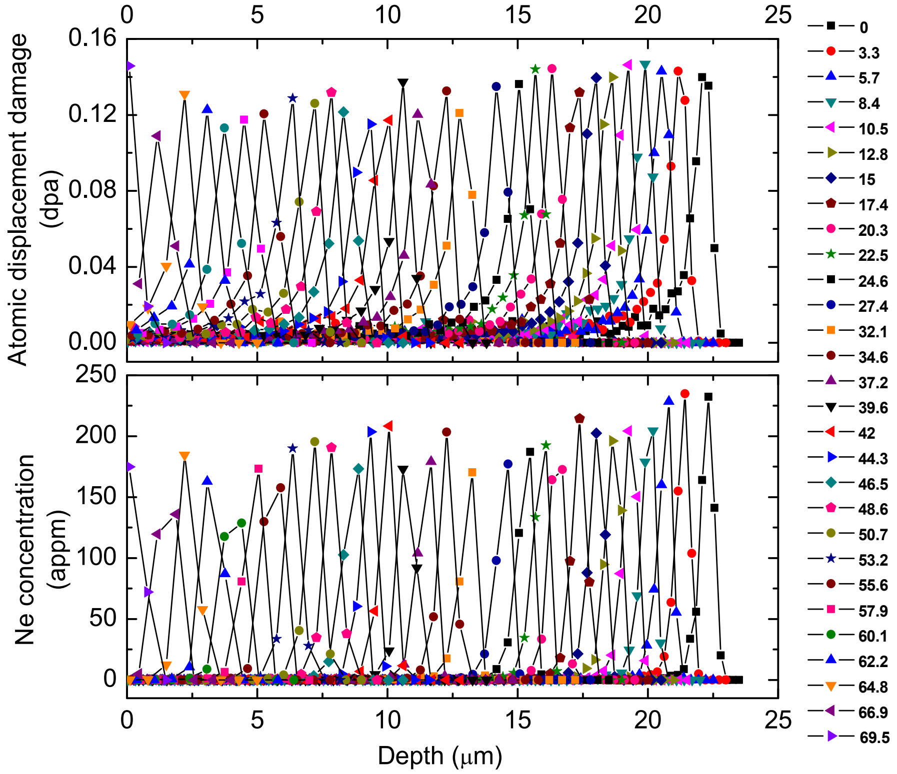

FIG.1. *Depth distribution of atomic displacement damage and Ne concentration at one side of W calculated with SRIM-2008 (E_d =90 eV). This corresponds to a total fluence of 3×10^{20} ions/m^2 under irradiation with 122 MeV $^{20}Ne^{7+}$ ions penetrating through an energy degrader. The right column shows the thickness (in micrometer) of Al foils used in the energy degrader.*

Following irradiation, the radiation defects in irradiated W was characterized with positron annihilation lifetime spectroscopy (PALS). With a ^{22}Na radioactive source, the incident depth of positrons in the PALS study was calculated to be within ~47 μm in W [1], which covers almost the whole Ne-ion damaged region. After that the irradiated samples were exposed to D_2 gas at 773 K for 2 h. Gas loading was performed instead of plasma exposure (i) to avoid further modification of near surface structure by plasma irradiation (ii) and to introduce an uniform distribution of D in the damaged W. The D bulk retention behavior then was studied with thermal desorption spectroscopy (TDS, a ramp rate of 1 K/s to 1273 K). Due to the limited number of available quasi-homogeneously damaged W samples and to further clarify the relationship between the radiation defects and D desorption behavior, the irradiated W after TDS experiments was further characterized with PALS and transmission electron microscopy (TEM) techniques [2].

TABLE 1. POSITRON ANNIHILATION LIFETIMES AND THEIR RELATIVE INTENSITIES FOR TUNGSTEN IN THREE STATES.

Specimens	τ_1 (ps)	I_1 (%)	τ_2 (ps)	I_2 (%)	τ_{av} (ps)
Un-irradiated W	139.6	100	---	---	139.6
As-irradiated W	118.6	59.5	406.8	40.5	235.3
Annealed W*	221.8	46.2	512.8	53.8	378.4

*Annealing conditions: 773 K/2h (D_2 atmosphere) + 1 K/s from RT to 1273 K (in vacuum).

The positron annihilation lifetime components and their relative intensities for the un-irradiated, as-irradiated and annealed W (referred to the irradiated W after D retention study) are listed in Tab.1. A brief summary is given here:

- Only one lifetime component τ_1=139 ps was given for the un-irradiated W, which corresponds to the annihilation of non-localized positrons and positrons trapped mainly at dislocations.
- Two distinct components were detected in the as-irradiated W. The longer lifetime component τ_2=406.8 ps had an intensity of 40.5%, strongly suggesting the generation of high densities of intermediate-size vacancy clusters (12 vacancies in average) in the as-irradiated W.
- Two lifetime components are also deduced for the annealed W, with both components shift to higher values. The longer lifetime component τ_2 has increased to 512.8 ps, which features positrons annihilate in quite large vacancy clusters containing more than 40 vacancies in W [9].

Figure 2 shows the TDS spectra of D from the un-irradiated and irradiated W samples. The amounts of D retained in the irradiated W samples were significantly higher than that in the un-irradiated ones. This increased D retention is mainly related to the higher D desorption with a release peak at ~1010 K in the irradiated W samples. Similar high temperature desorption peaks at ~1050 K were also observed by Hatano et al. [7,10] for the n-irradiated W after D plasma exposure at 773 K. Hatano et al. attributed this high temperature desorption peak to detrapping ($E_{det}\approx1.8$ eV) of hydrogen atoms from the inner walls of small voids or vacancy clusters [10].

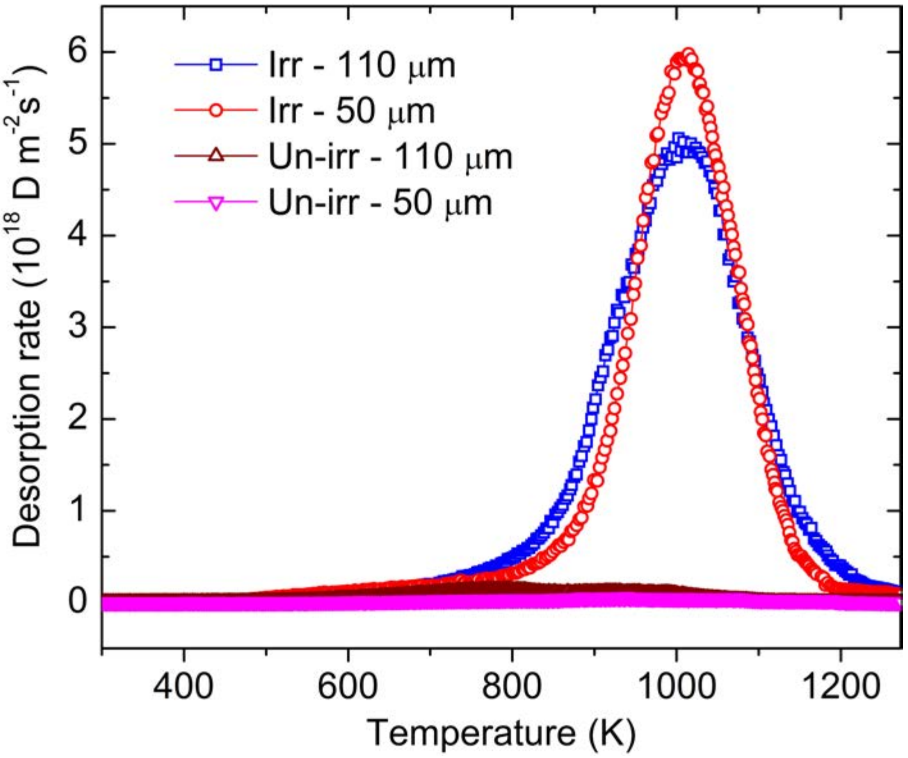

FIG.2. *TDS spectra of D for un-irradiated and Ne-ion irradiated tungsten after D_2 gas exposure at 773 K for 2 h. The D_2 gas pressure was 1.2*$\times 10^5$ *10^5 Pa. The rate of temperature ramp was 1 K/s during TDS experiments. Reproduced courtesy of Elsevier [4454510819301].*

From PALS results, we know these vacancy clusters may contain more than 40 vacancies. With the help of TEM, the morphology of these clusters was revealed. Figure 3 gives the TEM images (under and over-focus pairs) of the large vacancy clusters, i.e. voids, in it. It can be seen that plenty voids with an average diameter of ~1 nm are evenly distributed in the large observed area. Thus we conclude that the D trapping in nano-voids could lead to the ~1010 K D desorption peak in TDS measurements.

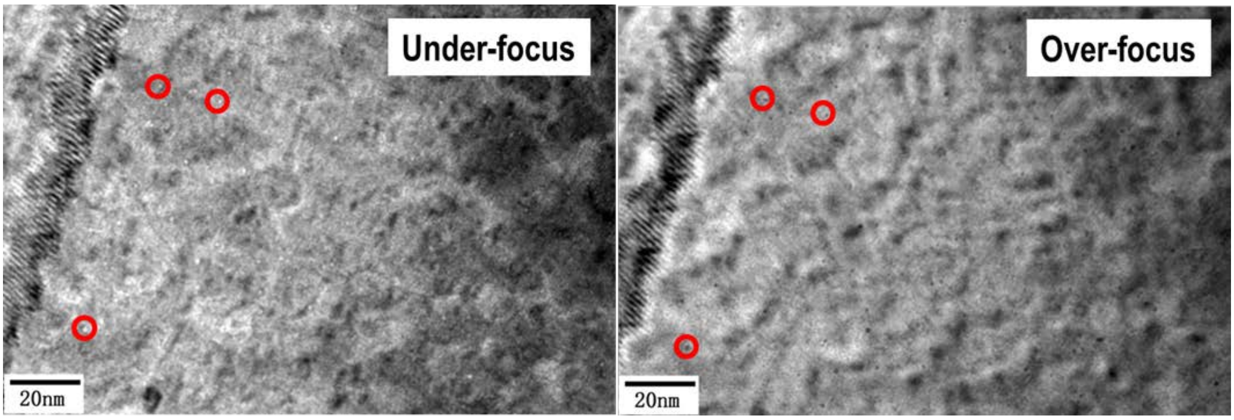

FIG.3. *Bright-field TEM micrographs of voids in the irradiated W after annealing (773 K/2h + 1 K/s from RT to 1273 K). The void-like character is manifested by the bright-to dark contrast change on going from under-focus to over-focus.*

Also from Fig.2, broad D desorption spectra from 730 K to 1173 K are observed for the irradiated W, similar to the broad desorption spectra for the n-irradiated W specimens [7,10]. As a comparison, TDS for W specimens irradiated with single-energy ions has only a narrow desorption peak [13]. All these results suggest that high-energy Ne-ion irradiation together with an energy degrader for tailoring the damage distribution may be an effective way to simulate volumetric defects production in W under neutron irradiation.

2. DEUTERIUM RETENTION IN W IRRADIATED WITH HE-IONS AND EAST DEUTERIUM PLASMA [11]

During the operation of Tokamak plasma, helium ions produced by D-T fusion reactions will impinge on wall materials. The microstructure of W will be dramatically changed under helium ion irradiation, thus it is necessary to understand the effect of helium ion irradiation on the microstructure and T retention behavior of W.

Materials used were high purity W foils (99.95% W by weight) annealed at the temperature of 1673 K for 2 h. W wafers with diameters of 20 mm and 3 mm were cut from the W foils. The 3 mm discs were prepared for TEM observation and they were polished using a two-jet electro-polisher with a 1wt.% NaOH aqueous solutions. Samples with a diameter of 20 mm were used for the TDS analysis. Both sides of the 20 mm W samples were mechanical polished to a mirror surface.

TEM and TDS specimens were irradiated simultaneously by 80 keV He^+ at room temperature on the 320 kV ECR platform at Institute of Modern Physics, Chinese Academy of Sciences. In order to get the fluence dependence of microstructure and desorption behavior change, three different fluences of 3×10^{15} ions/cm^2, 3×10^{16} ions/cm^2 and 3×10^{17} ions/cm^2 were used in the present study. The calculated depth distributions of dpa value and helium concentration under the fluence of 3×10^{15} ions/cm^2 were shown in Fig. 4. The results showed that the peak damage of 0.054 dpa was occurred at a depth of 140 nm. Note that the same irradiation energy leaded to similar dpa and helium concentration depth distribution in SRIM calculation. Hence, the dpa value and helium concentration for the fluence of 3×10^{16} ions/cm^2 and 3×10^{17} ions/cm^2 at the same depth were tenfold and hundredfold larger than that of 3×10^{15} ions/cm^2.

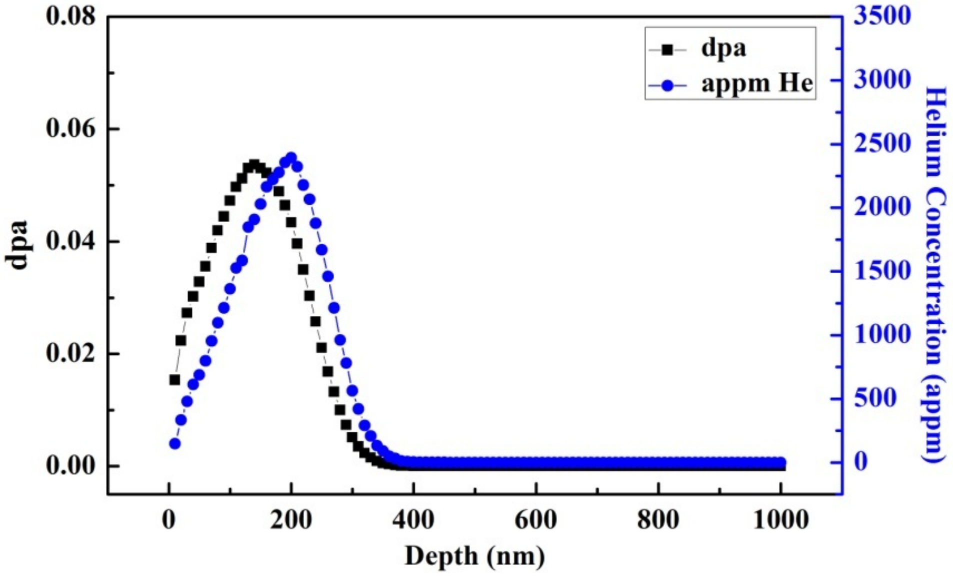

FIG.4. *The depth distribution of dpa and helium concentration under fluence of* 3×10^{15} *He*$^+$*/cm*^{2} *as calculated by SRIM-2008. Reproduced courtesy of Elsevier [4454511341136].*

After irradiation, TDS samples were exposed to EAST D plasma on the platform of the Material and Plasma Evaluation System (MAPES). The location of samples was 140 mm above the mid plane of EAST and 5 mm behind the limiter as shown in fig. 5. The samples were irradiated by 367 shots with a total plasma exposure time of ~2000 s. During EAST plasma discharge, the local electron temperature (T_e) and electron density (n_e) were measured to be T_e=5-10 eV and n_e=~1×10^{18} m^{-3} by a Langmuir probe. The temperature of samples varied from 323 to 623 K due to the heat from plasma which was measured by a K-type thermocouple.

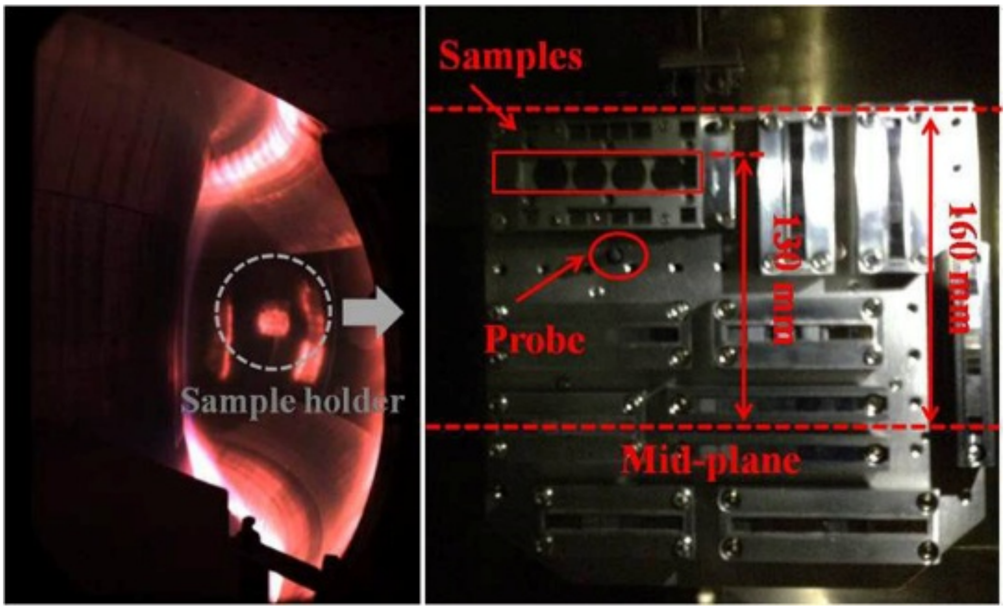

FIG. 5. *The position of W samples during EAST plasma exposure experiment.*

After EAST plasma exposure experiment, D retention in different samples was measured with TDS. During the TDS experiment, the sample was heated by infrared furnace up to the temperature of 1100 K with a heating rate of 1 K/s. The actual temperature of sample was measured by a K-type thermocouple which was contacted with the sample in vacuum. A quadruple mass spectrometer was used to measure the desorption signal of mass 4 which was calibrated by a standard leak for D.

The bright field micrographs of the He^+ irradiated W obtained with g= [110] under two beam condition were given in Fig. 6. Large number of irradiation induced dislocation loops (dark spots in Fig. 6) could be observed in W after helium ion irradiation. The dislocation loops in 3×10^{15} ions/cm^2 He^+ irradiated sample were isolated with each other as shown in Fig. 3(a). For the fluence of 3×10^{17} ions/cm^2, the tangling of dislocation loops was observed in Fig. 3(c). To identify the fluence dependence of the helium ion irradiation induced defects, the statistically analysis on the number density and size of dislocation loops were conducted as shown in Fig. 7. The size of dislocation loops under the fluence of 3×10^{15} ions/cm^2 spanned from 5 nm to 33 nm with the mean size of 11.75 nm. For the fluence of 3×10^{16} ions/cm^2, the size of dislocation loops was 10-53 nm with an average size of 26.89 nm. And the size of dislocation loops varied from 24 nm to 82 nm with an average size of 44.9 nm in the case of 3×10^{17} ions/cm^2. The difference in size distribution of dislocation loops was supposed to be the matter of the irradiation condition. Large number of interstitial atom and vacancy would be induced in W under 80 keV helium ion irradiation which was beyond the displacement threshold energy of W. The migration of interstitial atom could occur at room temperature due to its low migration energy (0.08 eV for W) [12]. Hence, the interstitial atoms could be formed and migrate thermally to form dislocation loops under the present experiment condition. With the irradiation fluence increase, the more interstitial atom and vacancy would be induced in W leading to the greater size of dislocation loops. There was no obvious change in the number density of dislocation loops which was consistent with others' results. According to the study of H. Iwakiri et al. the number density of dislocation loops in W would be saturated at a dose level of around 1.3×10^{15} ions/cm^2 under helium ion irradiation [13]. And the saturation of dislocation loop density in W was also occurred under hydrogen ion irradiation [14]. In the present study, no visible bubble was observed by TEM up to the fluence of 3×10^{17} ions/cm^2, which may resulted from that vacancies were immobile under RT [15].

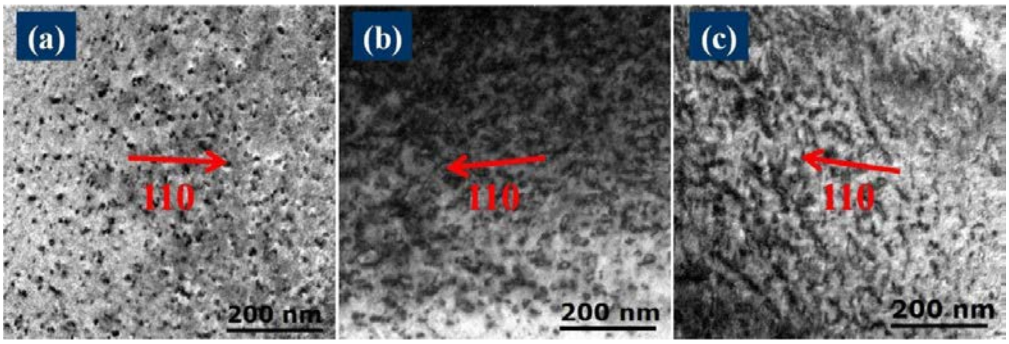

FIG. 6. *The bright field micrographs of W irradiated with 80 keV* He^+ *to fluences (a)* 3×10^{15}*ions/cm*^{2}*, (b)* 3×10^{16} *ions/cm*^{2} *and (c)* 3×10^{17} *ions/cm*^{2}*. All images were taken under a two-beam condition with g = (110) excited. Reproduced courtesy of Elsevier [4454511341136].*

The D desorption behaviors in un-irradiated and irradiated samples were given in Fig. 8(a). A release peak at 380 K was observed in all the samples. The desorption rate at 380 K was enhanced due to the presentation of irradiation defects. For the irradiated samples, another release peak occurred at 440 K. And

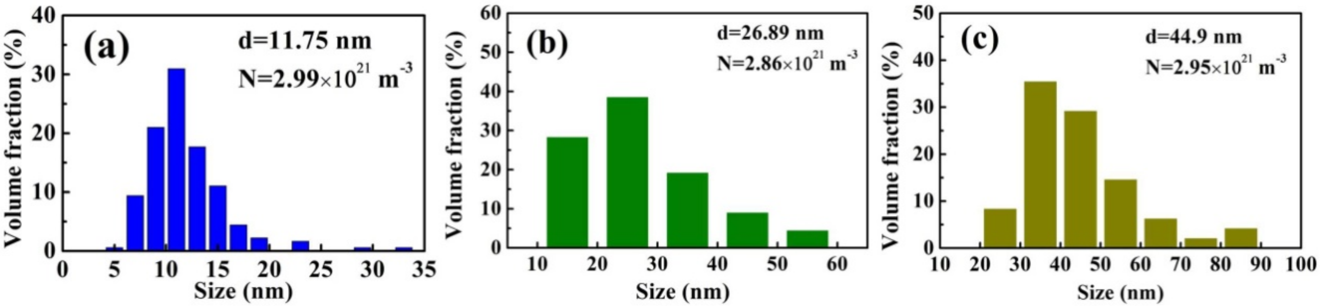

FIG. 7. *The size distribution and number density of dislocation loops under various irradiation fluence, (a) 3×10^{15} ions/cm^2, (b) 3×10^{16} ions/cm^2 and (c) 3×10^{17} ions/cm^2. Reproduced courtesy of Elsevier [4454511341136].*

the desorption rate at 440 K increased with the irradiation fluence. According to the previous study, the desorption peak at 380 k and 440 K corresponding to the D trapped by dislocation and vacancies respectively [9]. As discussed above, large amount of dislocation and vacancies were induced in W by helium irradiation. Hence, the present of helium irradiation defects was responsible for the change in desorption peak. The evolution of total D retention with irradiation fluence was shown in Fig. 8 (b). Within 1 dpa, the total D retention increase linearly with irradiation fluence. For the highest fluence (5.4 dpa), the increase of total D retention became slower compared with lower irradiation fluencies. The size of dislocation loops also increased dramatically at the initial fluence and then the increase became slower with the increase of fluence. Therefore, the degree of D retention in W was associated with the irradiation defects.

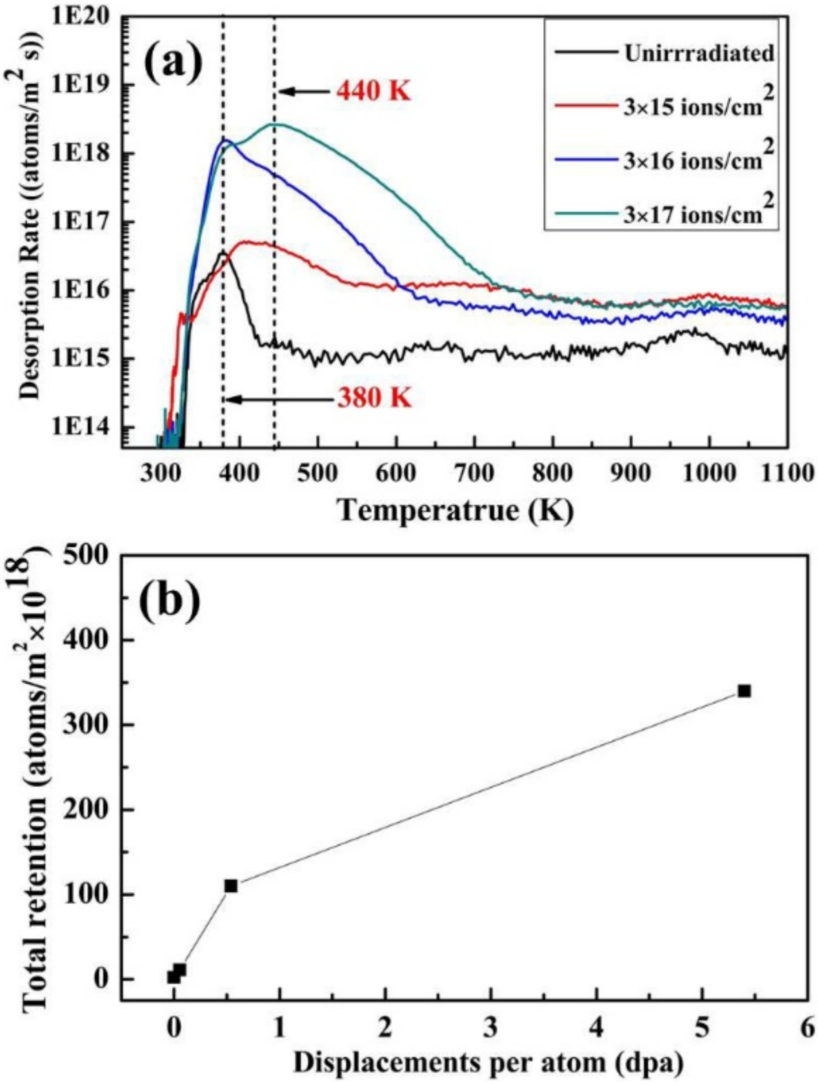

FIG. 8. *The D retention behavior in tungsten, (a) TDS spectra of D for un-irradiated and He$^+$ irradiated samples, (b) the total D retention.*

3. DEUTERIUM GAS-DRIVEN PERMEATION THROUGH TUNGSTEN WITH INTRINSIC OR RADIATION-INDUCED DEFECTS [16-18]

Numerical codes calculating hydrogen permeation behavior through first wall need the input of basic hydrogen transport parameters (such as diffusivity, permeability) in materials. At present, these basic data in W measured by several researchers are largely scattered [19-24]. Besides, the hydrogen permeation behaviors through W with defects, either intrinsic or radiation-induced, are seldom reported. Thus we built a hydrogen gas-driven permeation (GDP) facility at ASIPP (Fig. 9) to perform relevant experiments.

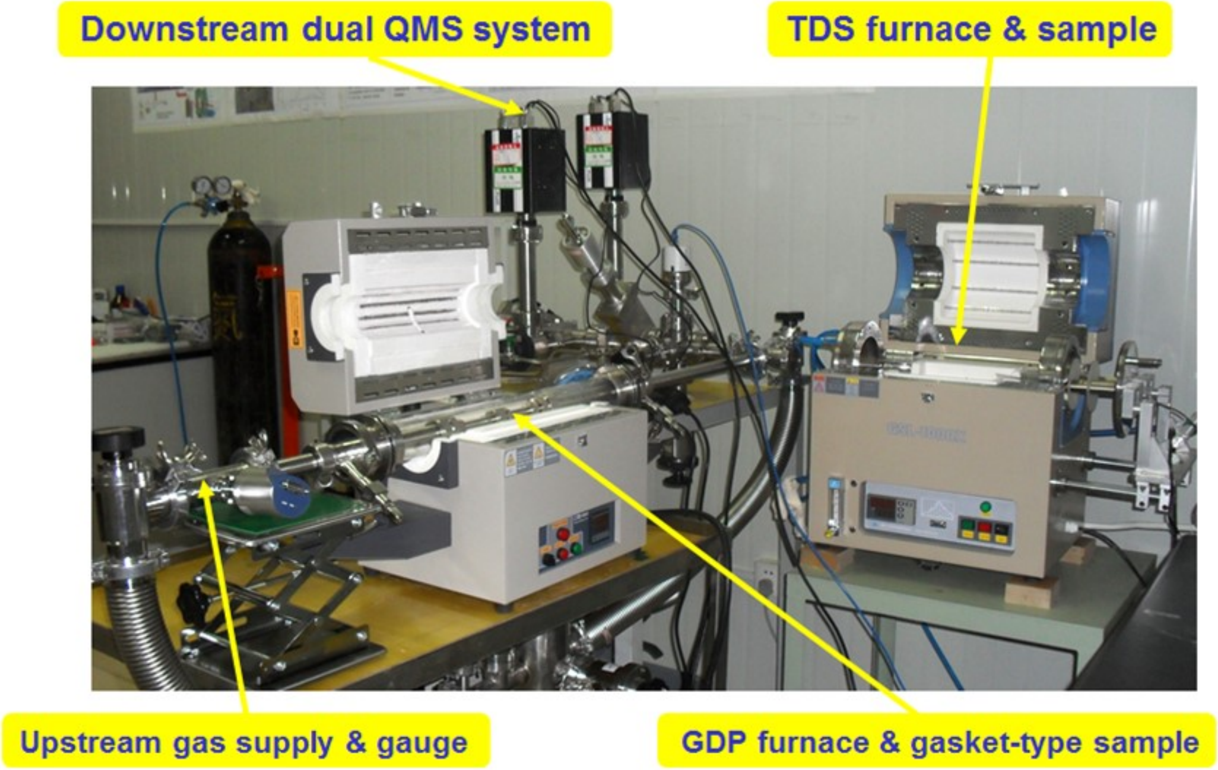

FIG. 9. *The gas-driven permeation setup (& TDS) at ASIPP.*

This GDP apparatus consists of an upstream for D_2 gas supply, a downstream for permeation signals monitoring and a middle part for W membrane sealing and heating. W samples of a diameter of 20 mm and various thicknesses were used for GDP measurement. Because W material is inherently brittle and W membranes were fragile after high temperature annealing, most W membranes in the study were sealed by two metal O-rings made of hollow steel pipes except the rolled W sealed by VCR couplings. Temperatures in the membrane were controlled between 700 K and 1000 K by an electric resistance heating furnace, while the temperature of samples was measured by a K-type thermal-couple squeezed into the leak-checking hole of the sealing settings. The upstream chamber was operated as a static state system during permeation, with the driving D_2 gas pressure at 10^4 Pa to 10^5 Pa. The downstream chamber was constantly pumped, providing a vacuum pressure at $\sim 10^{-5}$ Pa for the operation of a quadruple mass spectrometer (QMS). Both mass 4 (D_2) and mass 3 (HD) were monitored by QMS.

The effects of intrinsic defects (mainly dislocations) on D permeation were studied using W foils thermal-treated to three different states, namely rolled, annealed, and recrystallized W. Typical bright field transmission electron microscope images of dislocations in the three kinds of W foils are showed in Fig. 10. The rolled W possesses a dense network of dislocations; in the annealed one, dislocations have fragmented into short individual lines or even completely disappeared; in the recrystallized W, large areas free of dislocations could be observed.

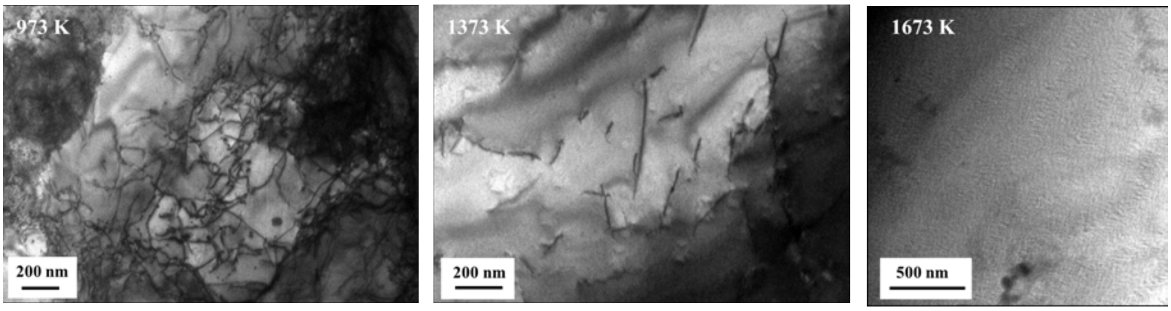

FIG. 10. *Typical bright field TEM micrographs of the rolled, annealed, recrystallized W. Samples are prepared by mechanically polishing followed by twin jet electro-polishing with a 1 wt.% NaOH solution at a voltage of 20 V.*

Figure 11 shows the effective diffusivities of D in the rolled, annealed and recrystallized W as a function of temperature. It can be seen that the effective diffusivities for W in three thermal states are significantly different. The rolled W foils have the lowest values of effective diffusivity. While for annealed ones, the values are about one order of magnitude higher. The recrystallized W possesses the highest values of effective diffusivity, which are approaching the data for W recrystallized at 2273 K measured by Zakharov [22]. Despite of the remarkable increased diffusivities for recrystallized W, our measured data are still two orders of magnitude lower than the extrapolating values of Frauenfelder' data obtained at higher temperatures [19].

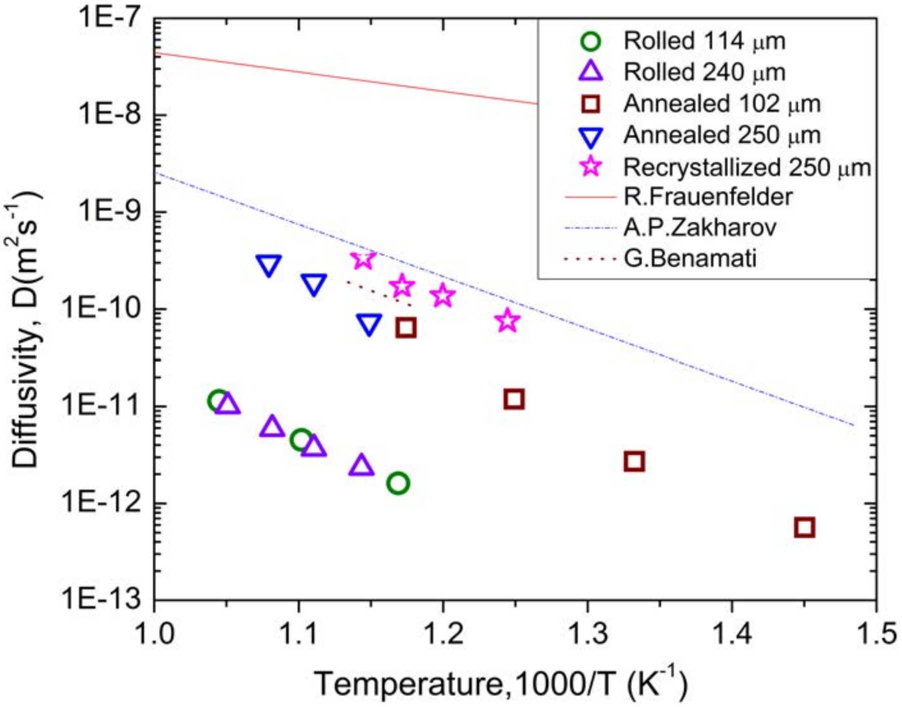

FIG. 11. *Temperature dependence of effective diffusivity of deuterium at ~10^5 Pa in rolled, annealed and recrystallized W foils. Data from literatures are showed for comparison. Reproduced courtesy of Elsevier [4454520118318].*

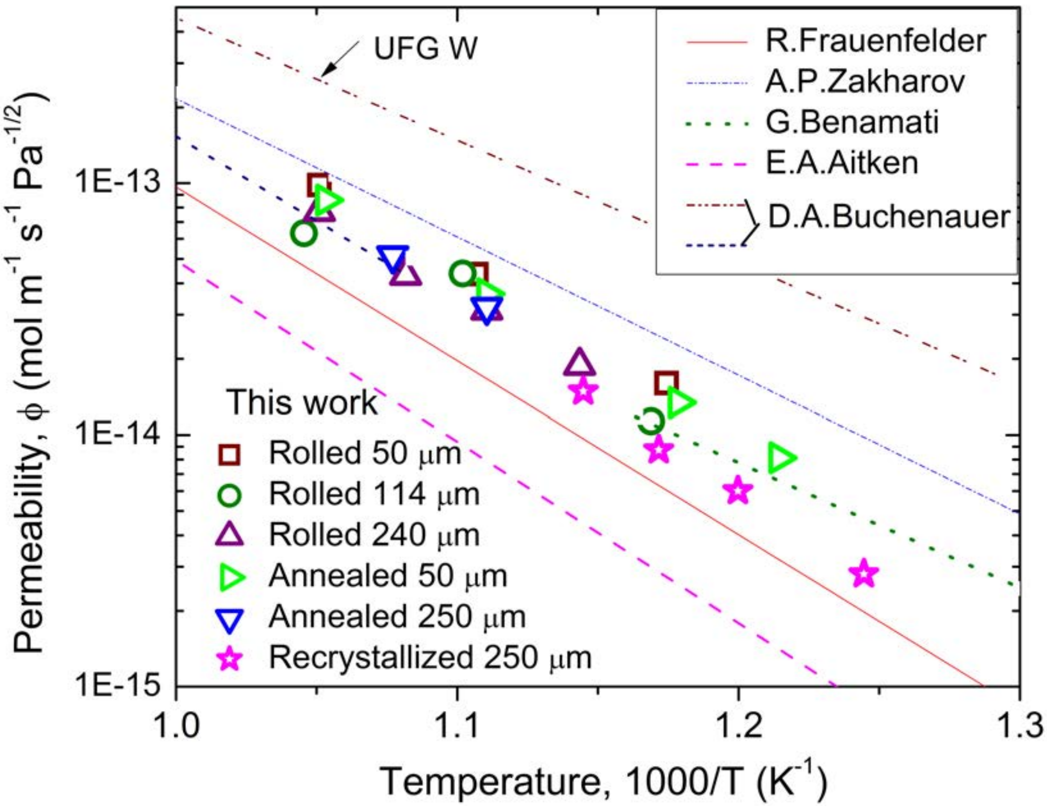

FIG. 12. *The effective permeability of deuterium through rolled, annealed and recrystallized W compared with data from literatures. Reproduced courtesy of Elsevier [4454520118318].*

The temperature dependence of effective permeability of D through the rolled, annealed and recrystallized W is showed in Fig. 12. The measured values did not show much difference for all samples measured. It is also interesting that, the values of permeability, measured independently by different researchers [20-24], are almost scattered within an order of magnitude in 800-1000 K (except those for the ultra-fine grain W).

To investigate the effects of radiation damage formation in W material on D permeation behavior, two annealed W samples were irradiated with 6 MeV Au^{3+} ions at the 2x1.7 MV tandem accelerator in Peking University. The ion fluences were 2×10^{14}, 6×10^{15} ions/cm^2, which correspond to peak damage doses of 1, 30 dpa at an incident range of ~300 nm respectively, according to the quick calculation of SRIM. The sample temperatures monitored were room temperature. To promote void formation in the irradiated W, the samples after irradiation were thermal treated at 1073 K for 2 h.

Doppler broadening spectrum of slow positron annihilation (DBS-SPA) measurements were used to investigate the radiation damage at near surface of irradiated W. The depth dependence of *S*- parameters (Fig. 13) was recorded by varying the incident positron energy in a range of 0.18 keV–25 keV. It is clear that *S*-value keeps at a low level for the un-damaged W, while it increases significantly for two irradiated samples. This demonstrates the formation of vacancy-type clusters in irradiated W. Two irradiated W showed comparable *S*-values, which may result from the saturation of radiation-induced traps at irradiation dose high than 1 dpa.

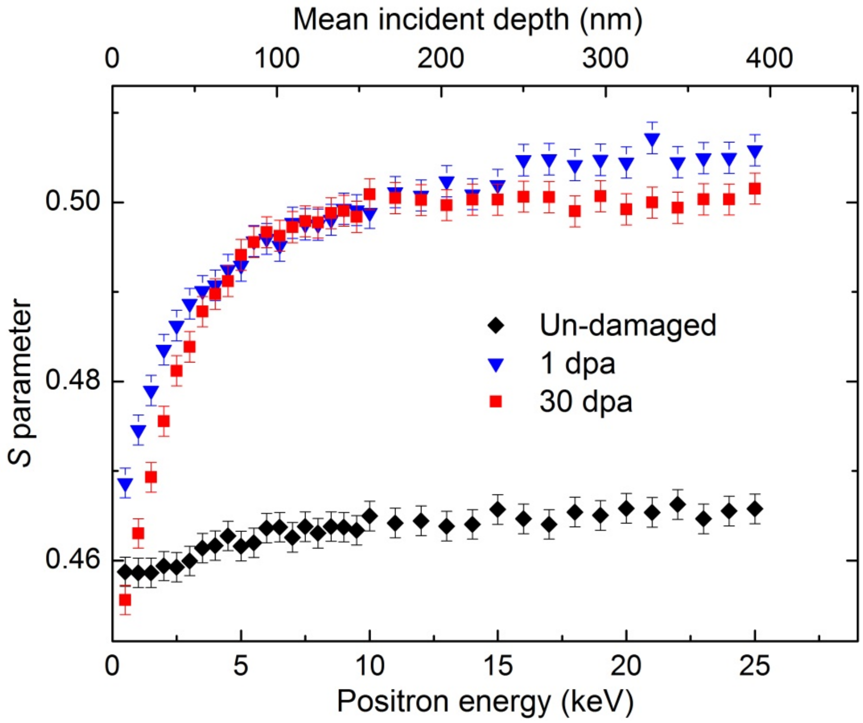

FIG.13. *The S- parameter versus depth in the W samples. The depth (nm) in the upper X-axis is calculated from the positron energy, E (keV), by the equation* $R=(40/19.35)*E^{1.6}$.

Figure 14 shows the downstream D permeation flux *vs.* time for three samples gone through the first permeation run. The un-damaged W reached to a steady state permeation state quickly, while two irradiated W increase to steady state permeation in a much slower way. With a time-lag method for effective diffusivity calculation, we get that the higher the irradiation dose (the density of irradiation-induced defects), the lower the effective diffusivity was measured.

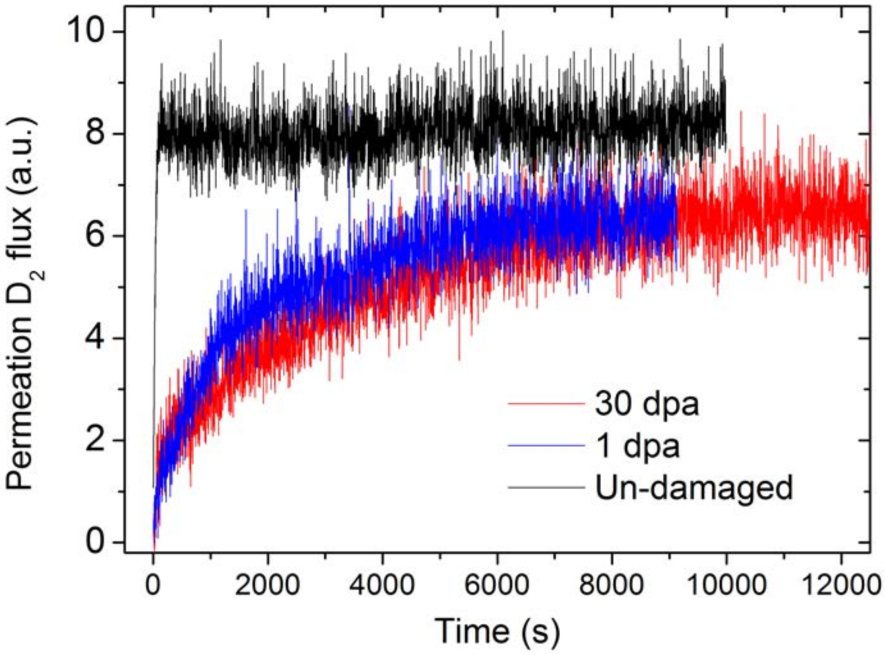

FIG.14. *The downstream D permeation flux vs. time for three samples gone through the first permeation run. All were performed with a driving* D_2 *gas pressure of* 10^5 *Pa.*

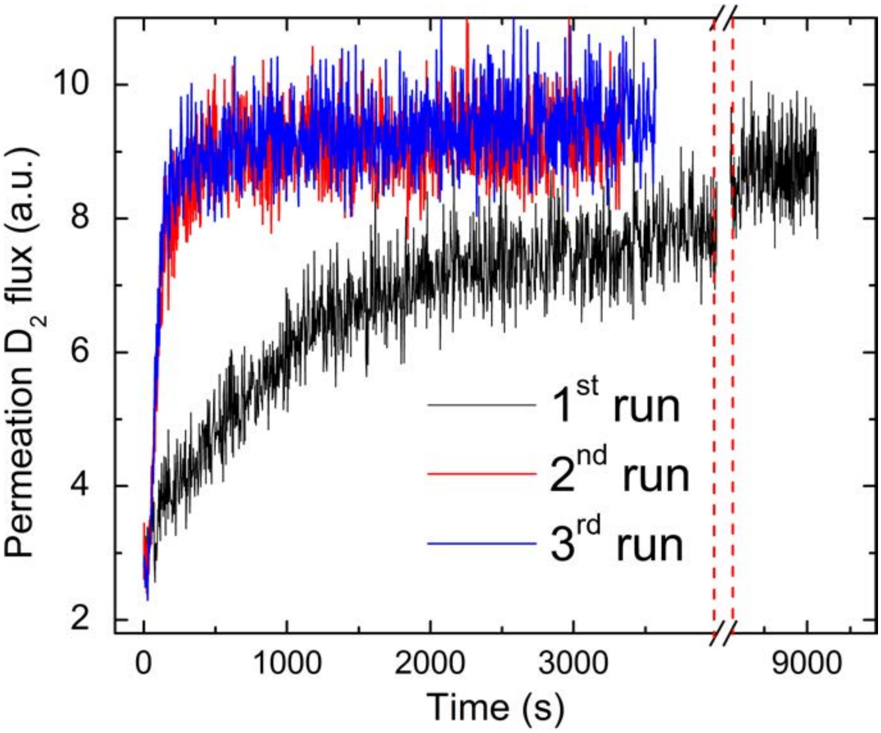

FIG.15. *The downstream D permeation flux vs. time for the W sample irradiated to 1 dpa gone through the first three permeation runs at 847 K, with a driving D_2 gas pressure of 10^5 Pa.*

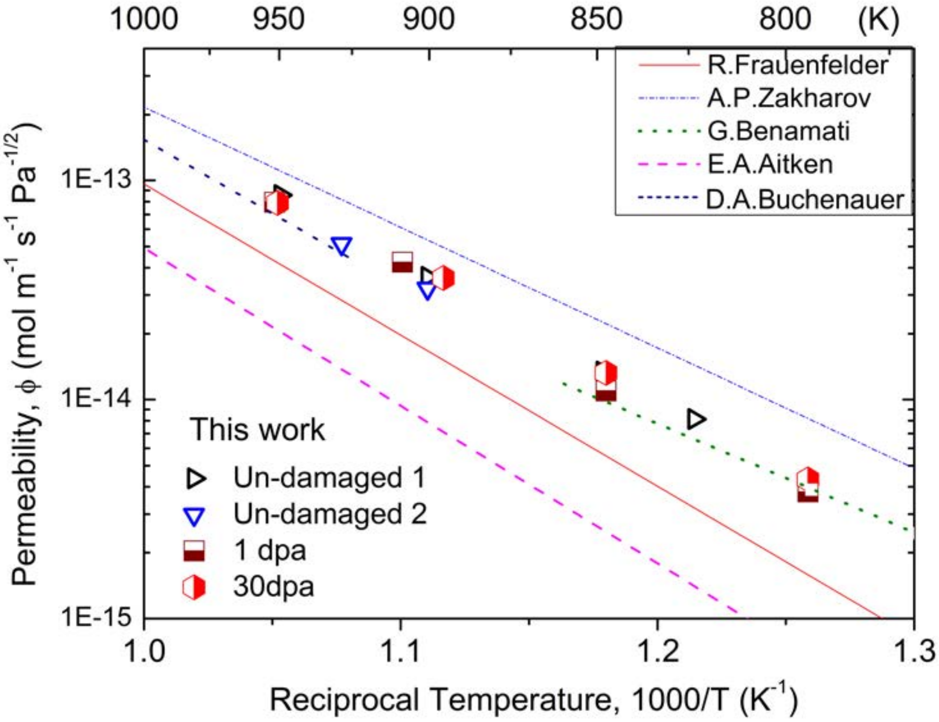

FIG.16. *The effective permeability of deuterium through un-damaged and damaged W compared with data from literatures.*

However, after the first permeation run, the second/third runs in the irradiated W samples were built up quickly (Fig. 15), almost the same as in the un-damaged W.

Figure 16 displays the measured permeability of D in un-irradiated and irradiated W. The permeability values are almost the same for all samples. This indicates that irradiation-induced vacancy-cluster formation in W did not significantly affect the effective permeability of hydrogen.

Here after, a brief discussion on the effects of intrinsic or radiation-induced defects on D permeation through W is given:

(1) Hydrogen atom diffusion in W lattice can be trapped by microstructural imperfections such as dislocations, vacancies, voids and grain-boundaries, either intrinsic or radiation-induced. The enthalpy difference between the hydrogen in a solid solution state and a trapped state can be described by the trap binding energy E_t [25]. Then on condition there is thermodynamic equilibrium between hydrogen in traps and hydrogen in solution, Oriani deduced that the effective diffusivity D_{eff} is related to the lattice diffusivity D_L through equation [26]:

$$D_{eff} = \frac{D_L}{1 + \frac{n_T}{n_L}\exp(\frac{E_t}{kT})} \tag{1}$$

where n_T, n_L is the density of trap sites and solution sites respectively, k is Boltzmann's constant. Clearly, the higher the density of trap sites is, the lower the diffusivity will be measured. In our study, the density of traps (mainly dislocations) in rolled, annealed and recrystallized W decreased one by one, thus the effective diffusivity increased one by one. Also from eq (1), one can see that the effective diffusivity is always smaller than the lattice diffusivity and the effective diffusivity approaches lattice diffusivity only when the trapping effect can be neglected (i.e., the temperature is high enough). This could be the main reason why our measured data is significantly lower than those extrapolated from Frauenfelder's data measured at higher temperatures [19].

Accompany the radiation-induced traps (mainly vacancy-clusters) formation in W, the effective diffusivity also decreased in the first permeation run. However, their effects on the second/third runs could not be observed. From literatures [27], we know that there are two kinds of traps in W: irreversible or reversible traps. Irreversible trap (e.g.: vacancy-clusters, voids) has a large E_t for hydrogen, which normally release no hydrogen once hydrogen is trapped; reversible trap (e.g.: edge dislocations, grain-boundaries) has an upper limit E_t of ~60 kJ/mol for hydrogen, it de-trap/re-trap hydrogen depending on the thermal state. Due to the vacancy-clusters produced in the irradiated W, which are irreversible traps for hydrogen, they will not affect the D permeation behavior once they are filled by D in the first run. Thus the D effective diffusivities for the second/third runs approach those in the un-damaged W.

(2) As to the permeability, irrespective of the large difference in the density of traps, either intrinsic or radiation-induced [18], all W samples showed identical permeability values. Also our permeability data are comparable to the literature data measured for various W [20-24]. Actually, McNabb and Foster [28] have explained that once the transport of hydrogen between traps is by lattice diffusivity (i.e., in accordance with Fick' first law), the permeation flux of hydrogen through a slab of material in the steady state regime will not be affected by the traps, since all time dependent terms in the Fick's equation disappear. Thus, the effective permeability, measured under the steady state permeation, will not be influenced by traps. Our results confirm their theory and others' experimental results on W.

From the above, one can say that microstructure defects in the bulk of W, either intrinsic or radiation-induced, may delay the transient for the hydrogen isotopes to reach the steady state permeation; yet they will not affect the steady state permeation flux.

ACKNOWLEDGMENTS

This work is supported by National Magnetic Confinement Fusion Science Program of China (No. 2015GB109001), National Natural Science Foundation of China (Nos. 11405201, 11505232).

Parts of this article are reprinted with permission from *Nucl. Instr. Meth. Phys.Res. B* **351**, 23 (2015); *Nucl. Instr. Meth. Phys. Res. B* **414**, 121 (2018); and *Fusion Eng. Des.* **113**, 216 (2016).

REFERENCES

[1] LIU, F., XU, Y., ZHOU, H., LI, X., SONG, Y., ZHANG, C., LI, Q., HE, C., LUO, G., Defect production and deuterium retention in quasi-homogeneously damaged tungsten, Nuclear Instruments and Methods in Physics Research Section B: Beam Interactions with Materials and Atoms **351** (2015) 23.

[2] LIU, F., ZHANG, C. H., LUO, G.-N. ET AL., submitted manuscript.

[3] WHYTE, D., On the consequences of neutron induced damage for volumetric fuel retention in plasma facing materials, Journal of Nuclear Materials **390-391** (2009) 911.

[4] ALIMOV, V., HATANO, Y., SUGIYAMA, K., ROTH, J., TYBURSKA-PÜSCHEL, B., DORNER, J., SHI, J., MATSUYAMA, M., ISOBE, K., YAMANISHI, T., The effect of displacement damage on deuterium retention in tungsten exposed to D neutrals and D_2 gas, Journal of Nuclear Materials **438** (2013) S959.

[5] OGORODNIKOVA, O., TYBURSKA, B., ALIMOV, V., ERTL, K., The influence of radiation damage on the plasma-induced deuterium retention in self-implanted tungsten, Journal of Nuclear Materials **415** (2011) S661.

[6] OYA, Y., HATANO, Y., SHIMADA, M., BUCHENAUER, D., KOLASINSKI, R., MERRILL, B., KONDO, S., HINOKI, T., ALIMOV, V. Kh., Recent progress of hydrogen isotope behavior studies for neutron or heavy ion damaged W, Fusion Engineering and Design **113** (2016) 211.

[7] HATANO, Y., SHIMADA, M., ALIMOV, V., SHI, J., HARA, M., NOZAKI, T., OYA, Y., KOBAYASHI, M., OKUNO, K., ODA, T., CAO, G., YOSHIDA, N., FUTAGAMI, N., SUGIYAMA, K., ROTH, J., TYBURSKA-PÜSCHEL, B., DORNER, J., TAKAGI, I., HATAKEYAMA, M., KURISHITA, H., SOKOLOV, M., Trapping of hydrogen isotopes in radiation defects formed in tungsten by neutron and ion irradiations, Journal of Nuclear Materials **438** (2013) S114.

[8] STOLLER, R., TOLOCZKO, M., WAS, G., CERTAIN, A., DWARAKNATH, S., GARNER, F., On the use of SRIM for computing radiation damage exposure, Nuclear Instruments and Methods in Physics Research Section B: Beam Interactions with Materials and Atoms **310** (2013) 75.

[9] ELEVELD, H., VAN VEEN, A., Void growth and thermal desorption of deuterium from voids in tungsten, Journal of Nuclear Materials **212-215** (1994) 1421.

[10] HATANO, Y., SHIMADA, M., OTSUKA, T., OYA, Y., ALIMOV, V., HARA, M., SHI, J., KOBAYASHI, M., ODA, T., CAO, G., OKUNO, K., TANAKA, T., SUGIYAMA, K., ROTH, J., TYBURSKA-PÜSCHEL, B., DORNER, J., YOSHIDA, N., FUTAGAMI, N., WATANABE, H., HATAKEYAMA, M., KURISHITA, H., SOKOLOV, M., KATOH, Y., Deuterium trapping at defects created with neutron and ion irradiations in tungsten, Nuclear Fusion **53** (2013) 073006.

[11] ZHAO, M., LIU, F., YANG, Z., XU, Q., DING, F., LI, X., ZHOU, H., LUO, G., Fluence dependence of helium ion irradiation effects on the microstructure and mechanical properties of tungsten, Nuclear Instruments and Methods in Physics Research Section B: Beam Interactions with Materials and Atoms **414** (2018) 121.

[12] YOSHIDA, N., IWAKIRI, H., TOKUNAGA, K., BABA, T., Impact of low energy helium irradiation on plasma facing metals, Journal of Nuclear Materials **337-339** (2005) 946.

[13] IWAKIRI, H., YASUNAGA, K., MORISHITA, K., YOSHIDA, N., Microstructure evolution in tungsten during low-energy helium ion irradiation, Journal of Nuclear Materials **283-287** (2000) 1134.

[14] SAKAMOTO, R., MUROGA, T., YOSHIDA, N., Microstructural evolution induced by low energy hydrogen ion irradiation in tungsten, Journal of Nuclear Materials **220-222** (1995) 819.

[15] EL-ATWANI, O., HATTAR, K., HINKS, J., GREAVES, G., HARILAL, S., HASSANEIN, A., Helium bubble formation in ultrafine and nanocrystalline tungsten under different extreme conditions, Journal of Nuclear Materials **458** (2015) 216.

[16] LIU, F., ZHOU, H., LI, X., XU, Y., AN, Z., MAO, H., XING, W., HOU, Q., LUO, G., Deuterium gas-driven permeation and subsequent retention in rolled tungsten foils, Journal of Nuclear Materials **455** (2014) 248.

[17] LIU, F., ZHOU, H., XU, Y., LI, X., ZHAO, M., ZHANG, T., XIE, Z., YAN, Q., ZHANG, X., DING, F., LIU, S., LUO, G., Gas-driven permeation of deuterium through tungsten with different microstructures, Fusion Engineering and Design **113** (2016) 216.

[18] LIU, F., ZHOU, H.-S., LUO, G.-N. ET AL., submitted manuscript.

[19] FRAUENFELDER, R., Solution and Diffusion of Hydrogen in Tungsten, Journal of Vacuum Science and Technology **6** (1969) 388.

[20] FRAUENFELDER, R., Permeation of Hydrogen through Tungsten and Molybdenum, The Journal of Chemical Physics **48** (1968) 3955.

[21] AITKEN, E. A., BRASSFIE, H. C., CONN, P. K., Trans. Metall. Soc. AIME **239** (1967) 1565-1574.

[22] ZAKHAROV, A. P., SHARAPOV, V. M., EVKO, E. I., Fiz. Khim. Mekh. Mater. **9** (1973) 29-33.

[23] BENAMATI, G., SERRA, E., WU, C., Hydrogen and deuterium transport and inventory parameters through W and W-alloys for fusion reactor applications, Journal of Nuclear Materials **283-287** (2000) 1033.

[24] BUCHENAUER, D. A., KARNESKY, R. A., ZAK FANG, Z., REN, C., OYA, Y., OTSUKA, T., YAMAUCHI, Y., WHALEY, J. A., Gas-driven permeation of deuterium through tungsten and tungsten alloys, Fusion Engineering and Design **109-111** (2016) 104.

[25] CAUSEY, R. A., KARNESKY, R. A., SAN MARCHI, C., Tritium Barriers and Tritium Diffusion in Fusion Reactors, Comprehensive Nuclear Materials **4** (2012), 511-549.

[26] ORIANI, R., The diffusion and trapping of hydrogen in steel, Acta Metallurgica **18** (1970) 147.

[27] TAL-GUTELMACHER, E., ELIEZER, D., ABRAMOV, E., Thermal desorption spectroscopy (TDS)—Application in quantitative study of hydrogen evolution and trapping in crystalline and non-crystalline materials, Materials Science and Engineering: A **445-446** (2007) 625.

[28] MCNABB, A., FOSTER, P. K., Trans. Metall. Soc. AIME **227** (1963) 618-627

DEUTERIUM RETENTION IN SELF-DAMAGED AND HE-IRRADIATED TUNGSTEN - *IN SITU* BENCHMARK EXPERIMENTS

S. MARKELJ[1], A. ZALOŽNIK[1], M. PEČOVNIK[1], P. VAVPETIČ[1], M. KELEMEN[1], P. PELICON[1], I. ČADEŽ[1], T. SCHWARZ-SELINGER[2], K. SCHMID[2], E. HODILLE[3], Ch. GRISOLIA[3]

[1]Jožef Stefan Institute,
Ljubljana, 1000, Slovenia

[2]Max-Planck-Institut für Plasmaphysik,
Garching, Germany

[3]CEA, IRFM,
Cadarache, France

Abstract

We present recent *in situ* studies on the dynamics of hydrogen isotope (HI) retention and transport, isotope exchange and D outgassing in tungsten irradiated by high energy W ions, so-called self-damaged W. Damaged samples were exposed to low energy (0.3 eV) HI atoms with typical fluxes of $5x10^{18}$ - $3x10^{19}$ at.$m^{-2}s^{-1}$, that populate the traps induced by 20 MeV W ion irradiation. By the help of rate equation models the experiments enabled us to pin down the nature of traps and detrapping energies, parameters for the surface processes and energy barrier for inward diffusion. In order to further study the influence of the energy barrier for D atom inward diffusion an additional benchmark experiment was performed where D retention was studied as a function of loading temperature. Namely, recrystallized self-damaged W samples were loaded at different temperatures from 450 K to 600 K by D atom beam. It was shown that exposure tempearature has a large effect on deuterium uptake and explains why neutral atoms can be neglected at plasma exposures at temperatures below 450 K. A major step forward in *in situ* studies was done by performing simultaneous W ion irradiation and D atom loading which was performed for the first time and the effect of the presence of D on evolution of lattice defects was studied. Simultaneous exposures were compared with sequential ones such as W irradiation and post defect annealing and W irradiation at elevated temperature. As a result synergistic effects were identified. The effect of He as an analysing beam and its influence on HI retention and transport was also presented where an accumulation of deuterium around helium was observed. Such studies help us explain the differences between low energy atom loading versus low energy (few ten eV) ion/plasma exposure and set the basis to predict the influence of neutrals on HI retention at fluxes higher by orders of magnitude as well as HI retention in remote areas in future fusion devices.

1. INTRODUCTION

Tungsten or advanced tungsten alloys are considered to be the most suitable material for plasma-facing components in future fusion reactors such as DEMO. In these nuclear devices tritium retention in neutron-damaged tungsten will become a significant issue. Namely, the predicted neutron damage for DEMO produced by neutrons from the fusion D-T reaction is more than one order of magnitude higher than in ITER, 2–6 dpa/fpy [1].

Before trying to understand the recycling and hydrogen isotope (HI) retention in plasma facing materials at particle fluxes up to 10^{24} $s^{-1}m^{-2}$ we need to understand the basic processes such as transport in a material with lattice defects, the effect of interstitial impurity atoms on defect evolution and the role of surface on HI uptake and release. Lattice defects, produced due to 14 MeV neutron irradiation and ions from the plasma, act as trapping sites for HIs with high de-trapping energy as compared to the energy of diffusion between solute interstitial sites. For this purpose benchmark experiments are needed where D atoms are only a tool to detect and pin down the nature of defects: their de-trapping energy for HI and evolution with sample temperature with and without presence of

HI. In order to study the influence of material displacement damage on fuel retention, high energy ions are used [2] where fuel retention both in neutron-damaged [3] and in W-ion-damaged tungsten (so-called self-damaged W) is strongly increased as compared to undamaged tungsten (e.g. [4]).

For this purpose we used the well-suited installation of JSI laboratory where samples are exposed to low energy (0.3 eV) HI atoms with typical fluxes of $5x10^{18}$ - $3x10^{19}$ at.$m^{-2}s^{-1}$, that populate the traps induced by 20 MeV W ion irradiation. In contrast to ion or plasma exposures with high flux density this does not create any additional damage or lattice stress. Moreover, the ability of performing studies *in-situ* by ion beam methods, i.e. measuring D depth profile during a specific exposure, minimizes the ambiguities that might occur with sample change or transfer through air.

2. EXPERIMENT

In most of the studies that will be mentioned a polycrystalline 99.997 wt. % hot-rolled tungsten samples (PW) manufactured by Plansee, 12 ×15 mm^2 in size and 0.8 mm thick was used. Its grains are oriented parallel to the surface. Samples were chemo-mechanically polished to a mirror-like finish at Max- Planck-Institut für Plasmaphysik (IPP), Garching [5]. After polishing, samples were heated for 2 min in vacuum at 2000 K for recrystallization. This procedure enlarges the grain size to 10–50 μm [6].

The samples were mounted in the INSIBA chamber at the 2 MV Tandem accelerator at Jožef Stefan Institute. The set up shown in Fig. 1 enables in situ Nuclear Reaction Analysis (NRA) measurements before, during or after the D-atom loading (see details in [7]), and irradiation of the samples by a high energy ion beam such as W^{6+} ion beam with energy up to 10.8 MeV. An electro-static quadrupole lens is positioned in the beam line (not shown in Fig. 1), 4.5 m before the sample, in order to gather and focus the ion beam on the sample. The ion beam is shaped by two apertures that can be changed for each irradiation/analysis. They are positioned before the ion beam mesh charge collector [8], mounted at the entrance to the experimental vacuum chamber. The ion beam mesh charge collector was specially specifically redesigned for the experiment involving simultanoues W ion damaging and D-atom loading, enabling us to retract it out of the ion beam or placing it in the beam for current measurement.

The sample is mounted by two Ta clamps on a holder with a temperature-controlled heater, capable of heating the samples up to 1200 K. A hydrogen atom beam source (HABS) for sample exposure to D atoms is mounted on the vacuum chamber at an angle of 51° with respect to the sample surface normal. It enables us to expose samples to a beam of neutral D atoms with a flux density of 5.4×10^{18} $Dm^{-2}s^{-1}$ at the NRA ion beam position. The flux density was determined by eroding an a-C:H film and measuring the crater by ellipsometry [9,10]. The atom beam is created by thermal dissociation of D_2 gas on a hot tungsten capillary that is heated to 2170 K ± 20 K for all cases. By assuming that the kinetic energy of the atoms is determined by the capillary temperature the mean energy of neutral atoms ($E = 3/2\ kT$) in the beam is 0.28 eV. The deuterium gas pressure in the gas supply side was controlled by an all-metal leak valve and measured by an absolute capacitance manometer, Baratron by MKS. The average driving pressure during the atom exposures of tungsten samples was 26 ±1 Pa for D_2 .

In most cases except for the experiment with simultaneous W-ion irradiation and D-atom loading the samples were damaged at IPP, Garching. They were self-implanted in the tandem laboratory setup TOF beam-line at IPP, Garching, [11] at room temperature with a 20 MeV W^{6+} ions with a fluence 7.8 10^{17} m^{-2} (ion flux of 2.8×10^{14} Wm^{-2} s^{-1}), corresponding to a peak damage level of 0.5 dpa (SRIM calculation 90 eV displacement energy, 3 eV lattice binding energy, full cascade mode). However, according to [4] and recommendations by Stroller et al. [12] the proper damaging level corresponding to fluence of 7.8×10^{17} m^{-2} is 0.25 dpa. The W beam was scanned over an area of 25×25 mm^2. In front of the sample a water cooled aperture was used having four faraday cups in its corners to determine the W ion flux. A central hole in the aperture cuts the beam down to 12 mm in diameter before it finally hits the W sample. Such damaged tungsten samples are labelled d-PW in the following in order to distinguish them from undamaged material, PW.

In the case of the experiment studying simultaneous W-ion irradiation and D-atom loading and damaging at elevated temperatures samples were irradiated by W^{6+} ions with an energy of 10.8 MeV. The beam size was defined by two 4 mm circular apertures. Before starting the irradiation the beam was checked for homogeneity by observing the glow (by ionoluminescence) on a quartz glass inserted into the irradiating beam. The quartz can be placed instead of the first collimating aperture and a blue glow is observed from the side by a mirror when it is irradiated by the beam. The ion current was first set to the proper value by measuring it on the ion mesh charge collector with 77.4% geometrical transmission. The ion mesh charge collector was then retracted in order not to have a mesh-print on the sample. The stability of the current was checked every 20–30 min. The ion current was stable within 5–10% yielding an uncertainty for the total ion fluence of about 5% for all irradiated samples. The corresponding W-ion irradiation current on the sample was 1.2 nA and irradiation time was 4 h yielding a W-ion fluence of $(1.4\pm0.1)\times10^{18}$ W/m^2 on the irradiated 4 mm diameter spot. With a fluence of 1.4×10^{18} W/m^2 we create a damage dose of 0.47 $\mathrm{dpa_{KP}}$ (Kinchin–Pease calculation, 90 eV displacement damage energy, evaluating the “vacancy.txt”output) at the peak maximum yielding a displacement rate of 3.3×10^{-5} dpa/s.

For simultaneous damaging with the W-ion beam a sputter ion source is used and in the case of NRA analysis with the ^{3}He beam a duoplasmatron source is used. The deuterium depth profile in the sample is obtained by analysing the energy distribution of protons produced by the D(^{3}He,p)^{4}He nuclear reaction [13]. For this purpose a 1500 µm thick partially depleted Passivated Planar Silicon (PIPS) detector is used. The NRA detector is mounted at 135° with respect to the incoming beam with a solid angle of 26.7 msr. A 24 µm Al absorber was placed in front of it, to stop the backscattered ^{3}He ions. The second PIPS detector with 300 µm thick depletion region is placed at 165° with respect to the incoming beam for detecting the backscattered projectile particles (RBS detector). The ^{3}He beam was collimated by a circular aperture with diameter of 2 mm. The diameter of the analyzing beam for NRA is smaller than the diameter of the W irradiated area (diameter 4 mm), to be assured that we analyse the damaged area only. In order to determine the D depth profile [14] down to a depth of 7 µm, six different ^{3}He ion beam energies were used: 776, 1555, 2580, 3399 and 4322 keV. We used the same collected charge for all six energies, corresponding to 14.9 µC ion dose He$^+$ (9.3×10^{13} He ions) for the four lower energies and 7.45 µC He^{2+} (4.65×10^{13} He ions) for the two highest energies. The ion beam data were evaluated by the NRADC program, which deconvolutes the measured proton spectra obtained at different ^{3}He energies and gives the most probable depth profile [15].

Most of the samples were also analysed by thermal desorption spectroscopy (TDS) after the NRA analysis. By measuring the total amount of D retained in the samples gives us the information about the binding energies of deuterium in the traps. Samples were installed in the glass tube of the TESS device at IPP, Garching with a background pressure of 10^{-7}–10^{-8} mbar during the heating ramp. A movable oven with a maximal temperature of 1323 K and heating rate of 15 K min^{-1} was used for sample heating. Desorbed gas species were monitored by a quadrupole mass spectrometer. Details about the setup and the calibration procedure can be found in [16] and references therein.

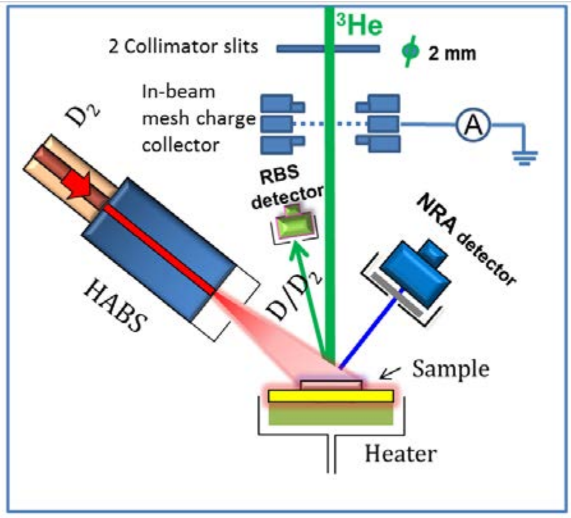

FIG. 1. Schematic figure of the INSIBA experimental set-up for in situ measurement of the deuterium depth profile during the exposure to D atoms from a Hydrogem Atom Atom Beam (HABS) together with the detector for Nuclear Reaction Analysis (NRA detector) and Rutherford Backscattering Spectroscopy (RBS detector).

3. RESULTS AND DISCUSSION

In this section we will summarize the results of *in-situ* studies of the dynamics of HI retention and transport, isotope exchange and D outgassing in self-damaged W [7] and the results obtained for sequential damaging and D-atom loading experiments [17,18] coupled with simulations to explain the experimental results [19]. Fisrt successful experiment with simultaneous W ion irradiation and D-atom exposure was performed and compared to the sequential studies on irradatited W [20]. The influence of He implanted into self-damaged W on D retention and transport was also studied [21].

3.1 Isothermal D atom loading and outgassing and isotope exchange

In situ studies of isotope exchange processes on the surface and in the bulk of self-ion damaged tungsten were performed. Here we will only describe the bulk isotope exchange while for the details concerning the surface isotope exchange, the reader is encouraged to see [7]. The processes in the bulk take place on timescales ranging from hours to days, whereas on the surface the processes are much faster, their time-scales being seconds to minutes for the used flux of 10^{19} at.m^{-2}s^{-1}. The average D and H flux densities at the probing ion beam position were $(5.8 \pm 0.3) \times 10^{18}$ Dm^{-2}s^{-1} and $(6.9 \pm 0.1) \times 10^{18}$ Hm^{-2}s^{-1}, respectively.

The re-crystallized and free of hydrogen d-PW tungsten sample was first exposed to an deuterium atom beam for 48 h at 600 K. The deuterium depth profiles were measured by NRA and are shown in Fig. 2(a). The deuterium concentration first increases near the surface and then steadily increases also deeper in the layers until it is almost homogeneous over the entire damaged layer. The sample was exposed for 48 h, fluence 1.0×10^{24} D/m^2, and immediately after termination of the exposure the sample was cooled down to room temperature. The last depth profile shown in Fig. 2(a) was obtained on cooled sample just before thermal outgassing was started. Beyond the damaged area, the deuterium concentration is two orders of magnitude lower. This is in agreement with the damaged profile, calculated by SRIM, also shown in Fig 2(a), which allows separating the two distinct areas: damaged area down to 2.5 mm and undamaged area beyond that.

Since the exposures are performed at 600 K one would expect, following the thermal desorption study of ITER grade tungsten damaged sample [22], a presence of deuterium thermal desorption at this relatively high temperature. In order to evaluate the release dynamics at a constant temperature, the sample was heated again to 600 K and kept at this temperature for a time similar to the time of the loading itself. After 20 h and at the end of the hold (43 h), a D depth profile was measured and shown in Fig. 2(b). In addition the initial D depth profile before the outgassing at 600 K is shown for comparison. It can be clearly seen from the depth profiles (DP) that most of the deuterium decreased already after 20 h.

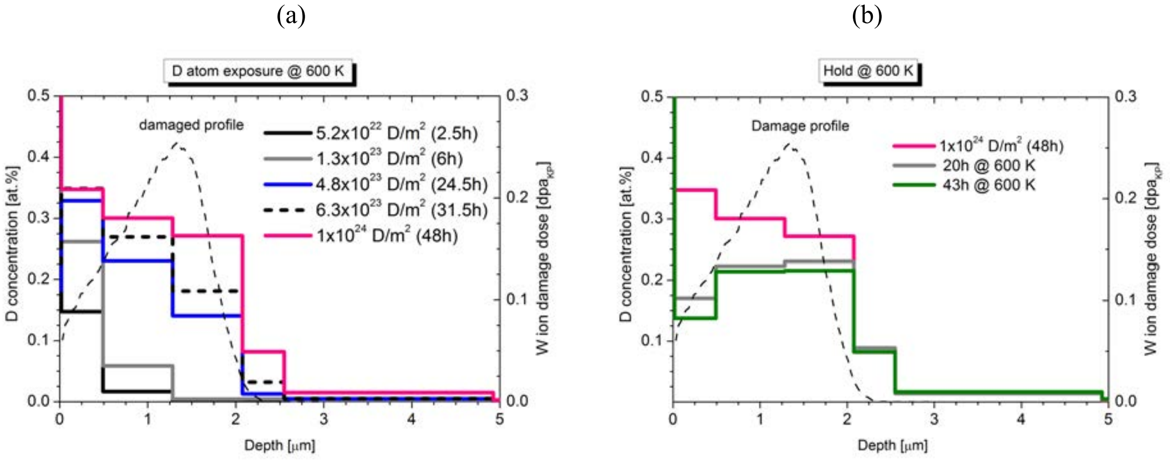

FIG. 2. (a) Deuterium concentration depth profiles measured during D atom exposure of self-ion damaged W at 600 K. Total D atom exposure time was 48 h corresponding to fluence of 1×10^{24} Dm^{-2}. The damage depth profile is shown as a thin dashed line, with a maximum of 0.5 dpa at 1.2 mm.

(b) Deuterium concentration depth profiles measured during self-damaged W sample hold at 600 K at different waiting times.

In order to study the isotope exchange mechanism, the same sample (deuterium loaded self-damaged W) was exposed to protium atom beam at 600 K directly after the second D exposure. Since protium concentration cannot be measured directly we can only record the decrease of the deuterium signal from NRA. The decrease of the NRA proton signal is different as compared to the isothermal outgassing. The signal is exponentially decaying with a single decay time and after 20 h the signal has dropped by 48% and after 43 h it has decreased by 68%. Therefore there is a clear indication that deuterium is being additionally released in some other way, not by thermal desorption. The whole D depth profiles measured during the protium exposure after 4 h, 22 h, 29 h, 45 h and finally after 96 h when the H atom exposure was terminated are shown in Fig. 3. The total accumulated protium fluence was 2.4×10^{24} Hm^{-2}. In contrast to isothermal outgassing, the deuterium concentration first decreases almost to zero at the surface and then the removal slowly proceeds also deeper.

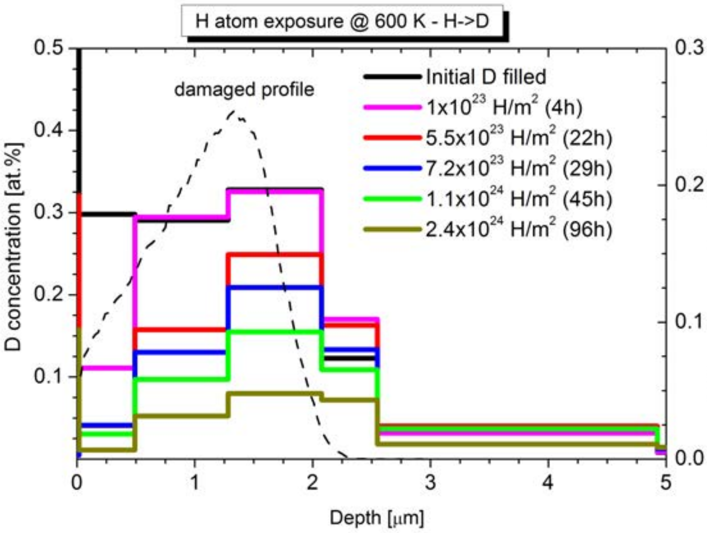

FIG. 3. Deuterium depth profiles measured during isotope exchange, H→D, at 600 K measured on the sample d-PW: exchange measured after the isothermal desorption and additional D loading.

In Fig. 4 comparisons of the total deuterium amounts summed over the damaged layer are shown versus time for the indicated exposures and isotope exchange measurements. There we show also the isotope exchange measured when the sample was first exposed to H atoms and after that to D atoms, thereby exchanging H by D. When comparing the total deuterium amount increase as a function of time in Fig. 4, for the case of the D loading only and isotope exchange with D atoms, the growth trend is the same if one would subtract the initial offset amount for the first three points and the data merge at 23 h of D exposure. The isotope exchange was modelled by a simple rate equation model described in detail in [7] and from this we obtained effective bulk exchange cross sections which are: $\sigma_{excB}(eff;H\rightarrow D;\#1)=(5.2\pm0.5)\times10^{-25}$ m^2, $\sigma_{excB}(eff;H\rightarrow D;\#2)=(6.5\pm0.3)\times10^{-25}$ m^2 and $\sigma_{excB}(eff;D\rightarrow H)=(1.1\pm0.5)\times10^{-24}$ m^2. The surface and bulk exchange cross sections are in good agreement with the cross sections obtained in Ref. [23] for the isotope exchange near-surface layer and through the whole depth.

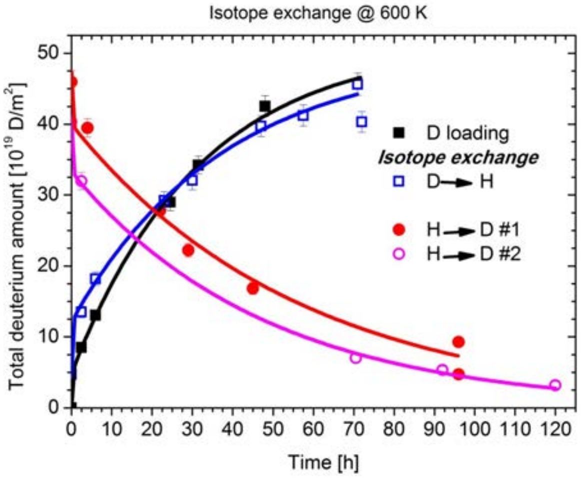

FIG. 4. Total deuterium amount as a function of exposure time, together with modelled total amounts shown as full and dotted lines for different variations of exposure and isotope exchange on self-damaged W.

We have shown that the isotope exchange with atomic hydrogen species is efficient in the bulk at 600 K and also on the surface at 380 K and 480 K [7]. Much longer times were needed to saturate and exchange the trap sites in the damaged layer by D atoms as compared to the surface dynamics. From this study we have seen that in both cases, on the surface and in the bulk of tungsten, a two times larger fluence was needed to exchange D by H as compared to H by D exchange. Consequently, there is about a factor of two when comparing the exchange cross sections for D on H compared to H on D, which closely corresponds to the mass ratio. Since the isotope exchange is considered to be one of the possible cleaning procedures in future fusion devices for tritium removal the observed isotope effect is not in favour for tritium exchange by protium, where the mass ratio is even larger. Therefore, when considering tritium exchange by deuterium it is expected to be much more effective due to the smaller mass ratio between deuterium and tritium. The study of isothermal desorption at 600 K showed that for the given loading conditions about 30% of deuterium is released from the damaged area within 43 h after stopping the exposure with a slow exponential decay, while in the same time during the isotope exchange the deuterium concentration decreased by 68%, having different decay trend. From the present study we have obtained a rather thorough set of parameters for deuterium loading only, isothermal thermal desorption and bulk isotope exchange.

3.2 Infleunce of annealing temperature on deuterium retention

The influence of the annealing temperature on deuterium retention was studied for self-ion damaged tungsten in the range from 600–1200 K [17]. The effect of damage annealing has been addressed by the analysis of D concentration depth profile using nuclear reaction analysis (NRA) technique, by thermal desorption (TDS) of deuterium and by scanning transmission electron microscopy (STEM).

Samples were damaged by 20 MeV W ions at room temperature to the peak damage level of 0.5 dpa. Samples were then annealed at the desired temperature for 1 h and exposed to deuterium atom beam at 500 K with the flux of 2.6×10^{19} D m^{-2}s^{-1} for 144 h to populate the remaining defects. An unannealed sample was also used as a reference. After the annealing and D atom exposure, samples were transported to the ion beam analysis vacuum chamber for D depth profile measurement. NRA was used for deuterium depth profile analysis. Corresponding depth profiles obtained for different annealing temperatures are shown in Fig 5(a). Deuterium concentration for all samples was found to be noticeable to the depth of approximately 2.5 μm what coincides with the calculated damage profile and dropped significantly under 0.01 atomic % for larger depths. Deuterium concentration was decreasing monotonously with increasing annealing temperature and took place homogeneously throughout the damaged layer.

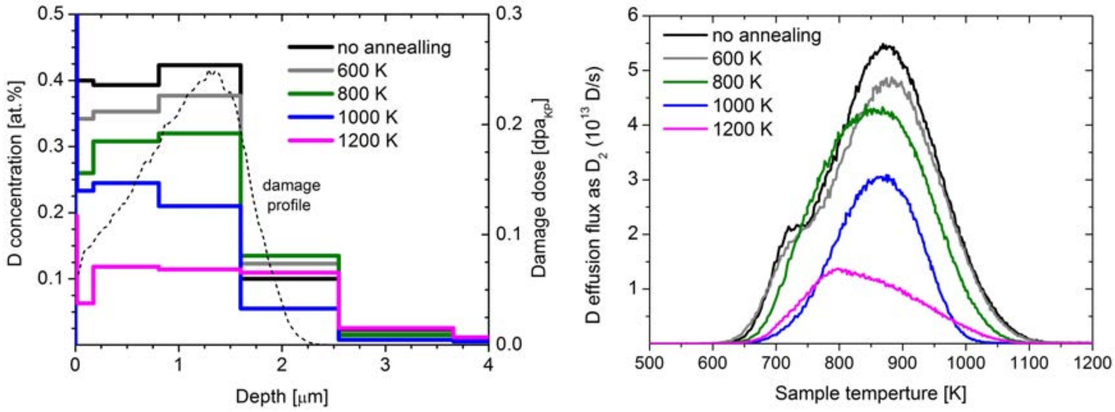
(a) (b)

FIG. 5. (a) D concentration depth profiles for samples, annealed at different temperatures. The initial damage profile, calculated by SRIM, is also shown. (b) D_2 thermal desorption spectra for damaged samples, annealed at different temperatures. Heating rate was 15 K min^{-1}.

To asses the total amount of D retained in the samples, thermal desorption analysis was performed. Samples were heated to around 1270 K with a heating rate of 15 K min^{-1}. The shape of TDS spectra for mass 4 (D_2^+) varied depending on the annealing temperature, as shown in Fig. 5(b). Deuterium desorption in the form of HD was 7% for all samples except for the one annealed at 1200 K where it was twice as much. Here, only D_2 desorption is shown for simplicity. For unannealed sample and sample annealed at 600 K, two peaks are visible in the spectrum at the sample temperatures of approximately 720 and 875 K. The high temperature peak is significantly more pronounced than the low temperature peak. Only one symmetrical peak at the temperature of approximately 855 K was observed in case of annealing temperatures of 800 and 1000 K, and one asymmetrical peak at 780 K is visible in case of annealing at 1200 K. These differences may be explained with different stages of damage annealing, occurring at different temperatures. According to [24, 25], at temperatures in the range between 400–720 K single vacancies become mobile and can form larger defects or annihilate at sinks such as grain boundaries (stage III). Between 720 and 920 K a recovery region of uncertain origin is observed and in the temperature range of 920–1220 K a large vacancy recovery is taking place (stage IV). Since the temperature regions are only approximate, the results of unannealed sample and the sample, annealed at 600 K, may be assigned to stage III recovery, annealing temperature of 800 and 1000 K to intermediate recovery region and the results for annealing at 1200 K to stage IV recovery.

By summing the deuterium concentration in the analyzed layer obtained by NRA we calculated the total amount of D retained in the first 7 μm of the sample, not shown. Annealing temperature was found to have strong influence on the retained D concentration in the damaged layer. The maximal concentration and the total retained D amount in the unannealed reference sample were 0.42 atomic % and 52×10^{19} Dm^{-2}, respectively. On the other hand, for the sample annealed at 1200 K, the maximal concentration was 0.12 atomic % and total D amount was 21×10^{19} Dm^{-2}, what is 71% and 60% lower than in the unannealed case, respectively. This reduction is in good agreement with the results, where damage population analysis was conducted by plasma exposure at 400 K with ion energy of 15 eV [4, 26], where also 70% decrease of D amount was observed for annealing temperature of 1150 K.

STEM analysis was also preformed and used to determine the dislocation densities in the samples. It was performed on five samples from the same manufacturing batch which have undergone the same polishing and recrystallization treatment as the samples used for D depth profiling and thermal desorption. Therefore the initial state of all samples was the same.

The only difference was the highest annealing temperature, namely, the sample used for STEM was annealed at 1130 K instead of 1200 K and the deuterium exposure was performed at 450 K instead of 500 K. STEM analysis confirmed the thickness of the damaged layer to be approximately 2.3 μm for all samples (Fig. 6(a)), which is in good agreement with the SRIM calculation. In figure 6(a) a STEM image of a un-annealed sample is shown and the damage layer is marked with an arrow. A close-up of the damaged region for unanealed sample is shown in figure 6(b), where the dislocation lines and dislocation loops can be observed. The dislocation densities with the estimated contributions of dislocation lines and loops for damaged regions were estimated from STEM figures on samples with different annealing tempeartures [17]. It should be taken into account that the calculated values also include the defects induced by the FIB processing. Dislocation density drops by 66% for the highest annealing temperature compared to the unannealed sample. This is in good agreement with the total D amount results obtained by NRA and TDS, where 60% and 75% decrease was observed, respectively.

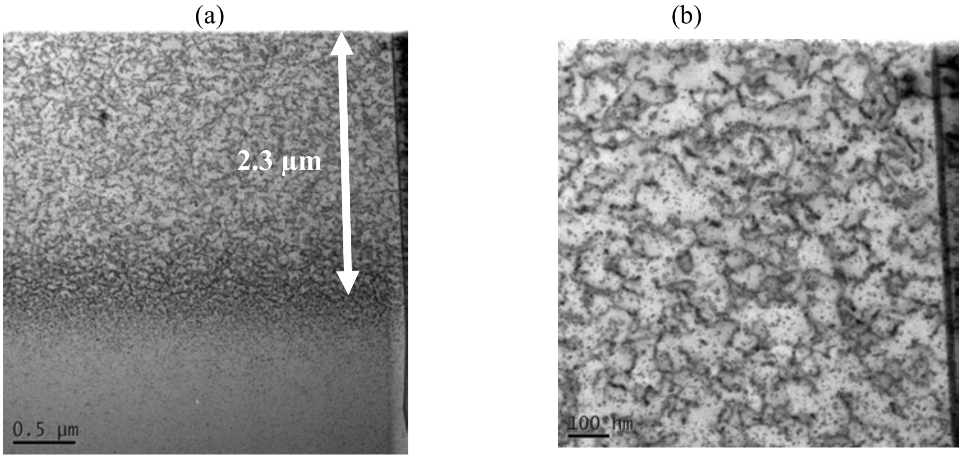

FIG. 6. (a) STEM cross section image of a un-annealed sample . The thickness of the damage layer is marked with an arrow. (b) STEM image of the damaged region of the un-nanealed sample.

The annealing temperature was found to have a strong influence on D retention as confirmed by both the depth profile analysis and the TDS. Different shapes of TDS spectra were observed for annealing at different temperatures, which was associated with different recovery stages at different temperatures. The annealing of the sample up to 1200 K decreased the total amount of retained D by 60%. Since the deuterium atoms are trapped mostly at the defects created by W ion damaging, one can conclude that such a high temperature is still not enough to completely anneal the damage. STEM analysis has also shown the decrease of dislocation densities with increasing annealing temperature, obtaining similar decrease trend as in the case of NRA and TDS analysis. A similar dislocation density decrease was observed earlier by Grzonka et al. [27] in a model experiment of annealingof a single W foil and was attributed to the intensive growth and recombination of dislocation loops. One could infer from this that the kinetics of dislocation defects healing process matches that of D traps annihilation /evacuation in self-damaged tungsten.

3.3 Modelling the D atom loading and the annealing experiment

Simulations of deuterium atom uptake and retention in self-damaged polycrystalline tungsten presented at 500 K and 600 K were performed using an evolution of the MHIMS (migration of hydrogen isotopes in materials) code in which a model to describe the interaction of D with the surface is implemented [19]. For this study the MHIMS (migration of hydrogen isotopes in metals) [28] code, which is based on a macroscopic rate equation (MRE) model that couples both diffusion and trapping of HIs, has been upgraded to simulate the experimental results presented in subsections 3.1 and 3.2 and in [7, 17]. Self-damaged polycrystalline W samples were exposed to a beam of deuterium (D) atoms with a low kinetic energy of ~0.3 eV. Due to such a low kinetic energy, D atoms may not directly reach the bulk and be implanted as they would be in the case of energetic D ions. Instead, they are first adsorbed on the W surface [29, 30]. In order to include this kind of events in simulations, a surface model was built and one of the goals of this study was to describe the implementation of such a model in the MHIMS code.

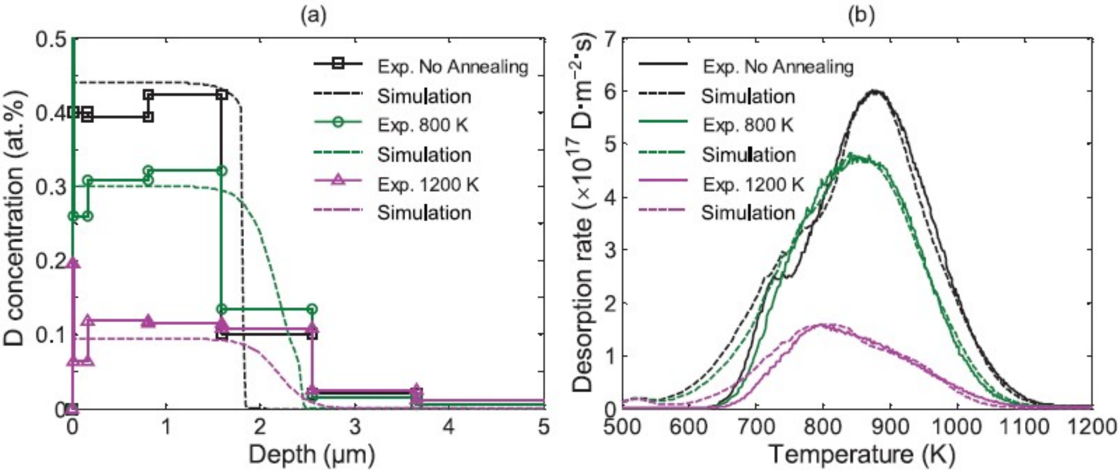

FIG. 7. (a) Comparison between simulation and experimental D depth profiles obtained after a 144 h D atom exposure on self-damaged W sample with a flux of 2.6×10^{19}D m^{-2} s^{-1} at 500 K. (b) Comparison between simulated and experimental TDS spectra obtained after the same D atom exposure. The heating ramp is 0.25 K s^{-1}. For the sake of clarity, only the results for un-annealed, 800 K-annealed and 1200 K-annealed case are shown. [19]

The surface model was decribed and particle fluxes to and from the surface as well as the flux of atoms from the bulk to the surface and vice-versa were included in the MHIMS code. The surface-energy barriers and chemisorption energies for both temperatures were determined analytically with a steady-state analysis model, more details can be found in [19]. From this the surface adsorption energy which is also half of desorption energy was determined to be 0.69 ± 0.02 eV at 500 K and 0.87 ± 0.03 eV at 600 K. These values are in good agreement with *ab initio* calculations as well as experimental determination of desorption energies. The absorption energy (barrier from the surface to the bulk) was determined to be 1.33 ± 0.04 eV at 500 K, 1.55±0.02 eV at 600 K when assuming that the resurfacing energy (from the bulk to the surface) is 0.2 eV.

After including these surface parameters the first task was to model the annealing experiment. The experimental TDS spectra shown in figure 5(b) exhibit a predominant D desorption peak at 875 K, a desorption tail at high temperature up to 1100 K for all annealing cases and a smaller peak at 720 K for the non-annealed and 600 K-annealed case. This observation suggests the presence of at least three different detrapping energies. In order to reproduce the experimental TDS spectra from [17] (figure 5(*b*)), three new traps were introduced into the model. Experimental depth profiles in Fig 5(a) show a nearly uniform concentration of D up to about 1.5 μm for the non-annealed sample and up to about 2.5 μm (the entire thickness of the damage layer) for the 1200 K-annealed case. Thus, in order to reproduce the NRA depth profile , a uniform concentration for trap 1, trap 2 and trap 3 was considered in the damaged layer up to a depth of around 2.2 μm. This assumption is strengthened by the STEM images of the damage layer shown in Fig. 6(a) where a homogeneous distribution of the radiation defects through the entire damaged layer that decreases between 2.2 μm and 2.4 μm. Figure 7 shows the simulation results (depth profile (*a*) and TDS spectra (*b*)) for the samples in the non-annealed case, the 800 K-annealed case and the 1200 K-annealed case. The determined detrapping energies for the three traps were $E_{t,1}$ = 1.65±0.01 eV, $E_{t,2}$ = 1.85±0.03 eV and $E_{t,2}$ = 2.06±0.04 eV. The experimental TDS spectra are well reproduced, especially the main peak at 875 K (detrapping from trap 2) and the high-temperature shoulder (detrapping from trap 3). Due to the presence of trap 1, a low-temperature shoulder appears that is slightly more pronounced in our simulation than experimentally. The presence of trap 3, however, is necessary in our simulations because otherwise the low-temperature shoulder (observed experimentally) would not appear in the simulations.

The second part of this study was the simulation of the experiments presented in subsection 3.1 and in more detail in [7], where the experiment was composed of two phases: the atomic exposure at 600 K and the isothermal desorption at 600 K. The above presented surface parameters and the de-trapping energies determined in the annealing experiment were used also in this case. In order to simplify the simulation, the cooling and the re-heating phases were not simulated. Figure8 shows the comparison between the D depth profiles during the atom exposure (figure 8(*a*)) and during the isothermal desorption (figure 8(*b*)). The simulation is able to reproduce (with good agreement) the evolution of the retention with time during the atom exposure and during the isothermal desorption.

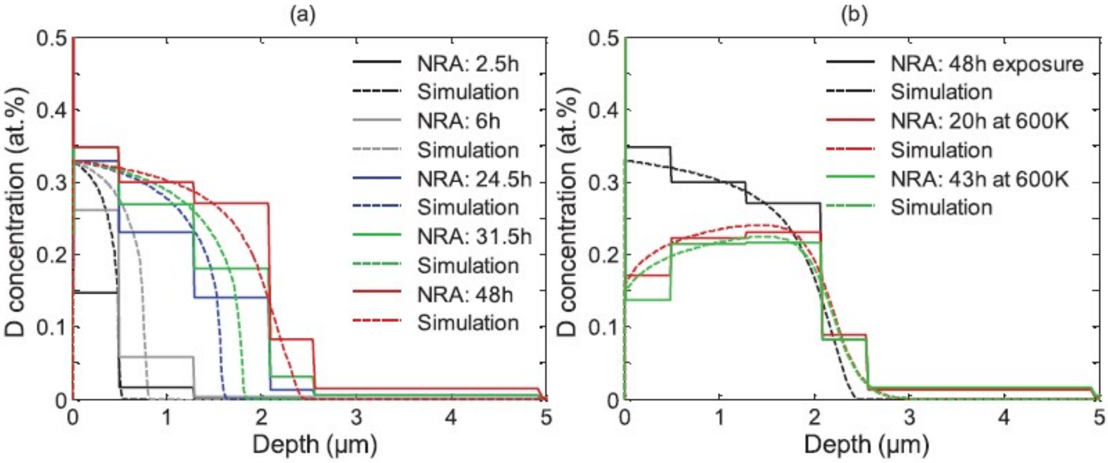

FIG. 8. (a) Comparison between experimental and simulated D depth profiles during atomic exposure at 600 K (maximum exposure time = 48 h). (b) Comparison between experimental and simulated D depth profiles during the isothermal desorption at 600 K. [19]

Thermal-desorption spectrometry data after D atom exposure at 500 K and isothermal desorption at 600 K after D atom exposure at 600 K can be reproduced quantitatively with three bulk-detrapping energies, namely 1.65 ± 0.01 eV (trap 1), 1.85 ± 0.03 eV (trap 2) and 2.06 ± 0.04 eV (trap 3), in addition to the intrinsic detrapping energies known for undamaged tungsten (0.85 eV and 1.00 eV). Previous simulations of retention/desorption from self-damaged W samples [22, 31, 32] and neutron-irradiated samples [33] exhibit similar trends. Notably, we rationalize the absence of lower detrapping energy traps in experiments [7,17], in contrast to other experimental works, by the mobility kinetics of mono-vacancies upon annealing. By comparing these detrapping energies with DFT values for various traps [34-37], we propose that trap 1 should be related to trapping in jogged dislocation lines filled with one to three HIs, while trap 2 should be related to dislocation loops filled with one to two HIs. These propositions are strengthened by analyses of the annealing defects presented in [7]. A decrease of the concentrations of jogged dislocation lines and dislocation loops is simulated with sample annealing, similarly to STEM measurements [7]. We consider that trap 3 could be attributed to cavities (vacancy clusters), since its detrapping energy and its density evolution with annealing temperature is consistent, respectively, with DFT calculations of HIs. It must also be noted that such high detrapping energies could be related to the desorption of D from D-carbon bounds that can appear in case of hydrocarbon contamination of the sample surface.

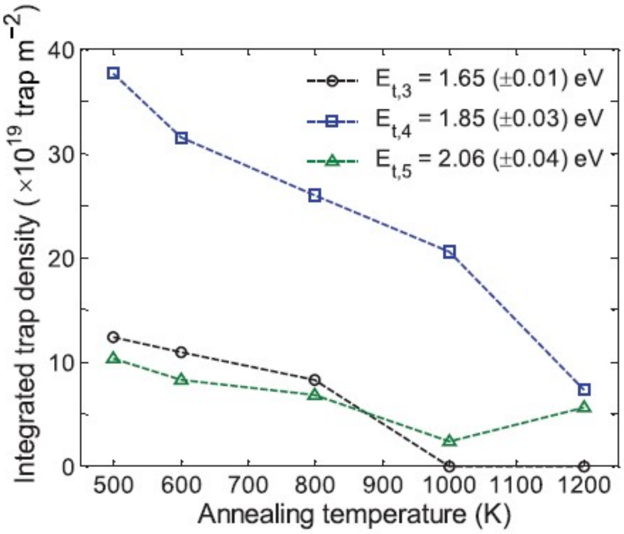

FIG. 9. Integrated trap amount between 0 and 2.4 μm as function of the annealing temperature for the simulation of D atom exposure at 500 K. The point at 500 K corresponds to the unannealed case. [20]

To test the assignment proposed above, we looked at the distribution and evolution of these dislocations-type traps for different annealing temperatures and compared this to the evolution of defects seen by STEM images [17]. In order to do this comparison, the trap distributions obtained for each trap in the damaged layer are integrated between 0 and 2.4 μm (figure 9). Figure 9 show that, in the simulations, the dominant trap is trap 2, which we attributed to dislocation loops. Experimental STEM images of the damaged layer show that the density of dislocation loops is higher than the density of dislocation lines, even though it is not in the same ratio as we determined in figure 9. Furthermore, upon annealing up to 1200 K, the total amount of dislocations (trap 2 and 3) decreases by 70% in the simulations, similarly to the experimental analysis of STEM images , which showed a decrease of 66% in the dislocation density. Given the quantitative agreement between DFT calculations and our simulations, determination of detrapping energy as well as the at-least qualitative reproduction of their kinetic behavior with experimental annealing observations, we believe that our assignment of trap 1 and 2 to jogged dislocation lines and dislocation loops, respectively, is well supported.

From this study we could from the obtained energy barrier for D atom inward diffusion being 1.33 ± 0.04 eV at 500 K, 1.55±0.02 eV at 600 K, also determine the solution energy E_S. It was found to be E_S=0.44 eV − 0.48 eV for both exposure temperatures. This value is much lower than the solution energy E_S = 1.04 eV determined experimentally by Frauenfelder [38]. Our simulated low solution energy has been attributed to differences in the preparation of W samples which may affect: (i) surface contamination, e.g. with oxygen or (ii) the density of grain boundaries, which may provide preferential paths through which to enter the bulk. The acceleration of the D atoms arriving on the surface thanks to the additional potential energy, compared to D_2 molecules, can also be proposed as an explanation of the low solution energy obtained in the simulations: this acceleration helps the D atoms to reach the energy barrier. However, the additional potential energy is not enough to allow incident D atoms to reach the bulk directly because a part of it is quickly dissipated, mainly through electron–hole pair excitation [39-41].

3.4 Infleunce of the exposure temperature on D atom retention and transport

In order to further elaborate the effect of surface parameters, especially the energy barrier for D atom inward diffusion and from this determined solution energy, the influence of exposure temperature on hydrogen isotope atom absorption into self-damaged tungsten was studied [18]. For this purpose a series of experiments was performed, exposing tungsten pre-damaged by tungsten ions to low energy deuterium atoms with the flux density of 4.2×10^{18} $Dm^{-2}s^{-1}$ for 121 h. Exposures were performed at four sample temperatures between 450 K and 600 K. Deuterium concentration was measured in situ and in real time during the exposure by NRA. After the exposure, TDS was performed on the samples.

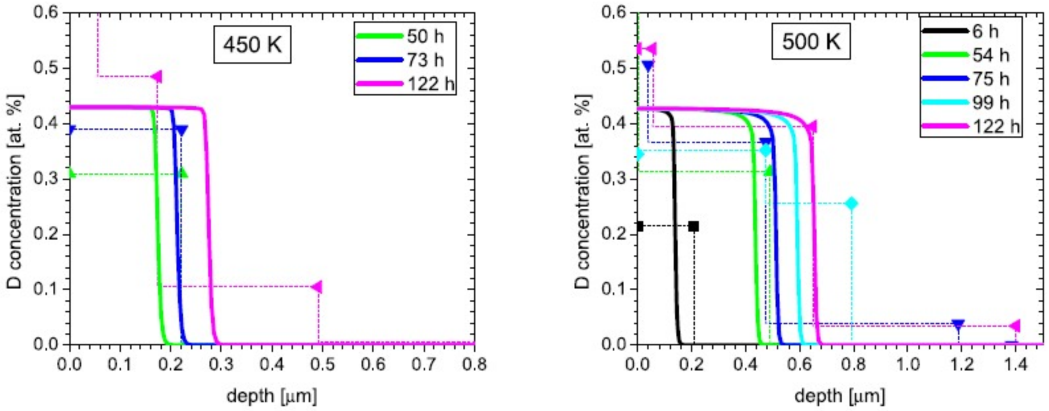

(a) 450 K (b) 500 K

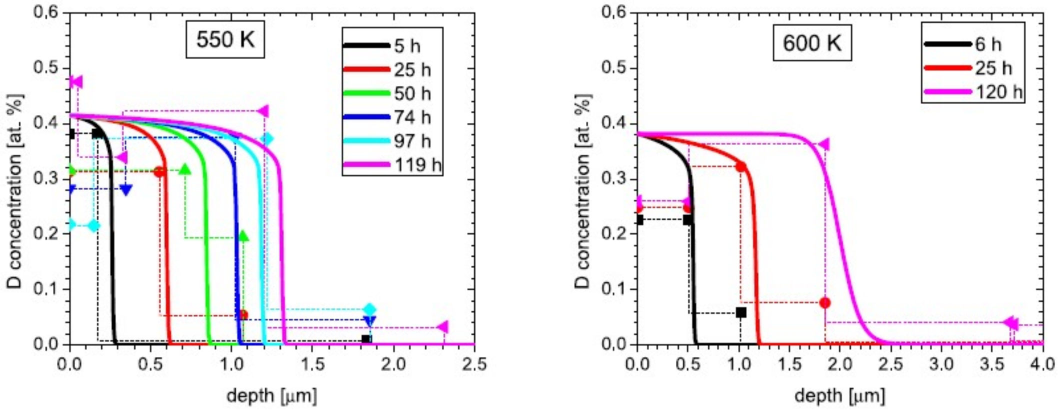

(c) 550 K (d) 600 K

FIG. 10. Deuterium concentration depth profiles at different times during D atom exposure at 450 K, 500 K, 550 K and 600 : Simulated (lines) and measured (dots).[1]

Deuterium depth profiles were measured at certain times during the exposure and are shown in Fig. 10 for each exposure temperature. A clear temperature dependence of the deuterium diffusion range after 121 h can be observed. For the sample temperature of 600 K the entire damaged layer is filled with deuterium, whereas for the temperature of 450 K only the first 0.5 mm are populated. Moreover, higher D concentration is found in depth of samples exposed at lower temperature, namely the maximum concentration in the sample exposed at 450 K was 0.5 at. % whereas for 600 K it was around 0.36 at. %.

Integrated deuterium amounts as a function of exposure time, obtained by summing D concentration over the NRA information depth, are shown in Fig. 11(a) for all exposure temperatures. The rate at which the damaged layer fills with deuterium depends strongly on the sample temperature. At 450 K the integrated D amount is approximately 20% of the amount found at 600 K after the same exposure time of 121 h. The thermodesorption spectra were recorded for the four self-damaged W samples after D atom loading. Deuterium effusion fluxes, shown in Fig. 11(b), were determined as a sum of mass 4 (D_2) and mass 3 (HD) contributions. The observed peaks are a result of a collective effect of D diffusion, trapping, detrapping, self-clustering, etc. Only one peak is visible for the sample loaded at 600 K and is positioned at approximately 850 K. This is indicating that only one trapping site type is filled at this temperature. For the sample temperature of 550 K two peaks are visible in the

---

[1] Reprinted from Journal of Nuclear Materials, vol. 496, A. Založnik et al. Deuterium atom loading of self-damaged tungsten at different sample temperatures, 1-8., Copyright (2018), with permission from Elsevier

spectrum, whereas for the lowest two temperatures three peaks are visible. One can also observe that the high temperature peak shifts to the right with decreasing exposure temperature. In the previous study presented above (subsection 3.2 and [17]) an identical sample was exposed at 500 K to a D atom beam fluence high enough to populate the entire damaged layer. There, only two peaks were observed, therefore we can assume that the additional middle peak in the current study is only due to the damaged layer being only partially filled with D atoms and not due to additional trapping site type. Namely, during the heating of a partially filled sample, atoms do not diffuse only towards the surface but also deeper into depth until a flat D concentration profile throughout the damaged layer is achieved. After that, a D flux towards the surface depletes the deuterium out of the sample. This results in a peak with an additional low temperature shoulder or two separated peaks in the TDS spectrum, depending on the initial range of D atoms.

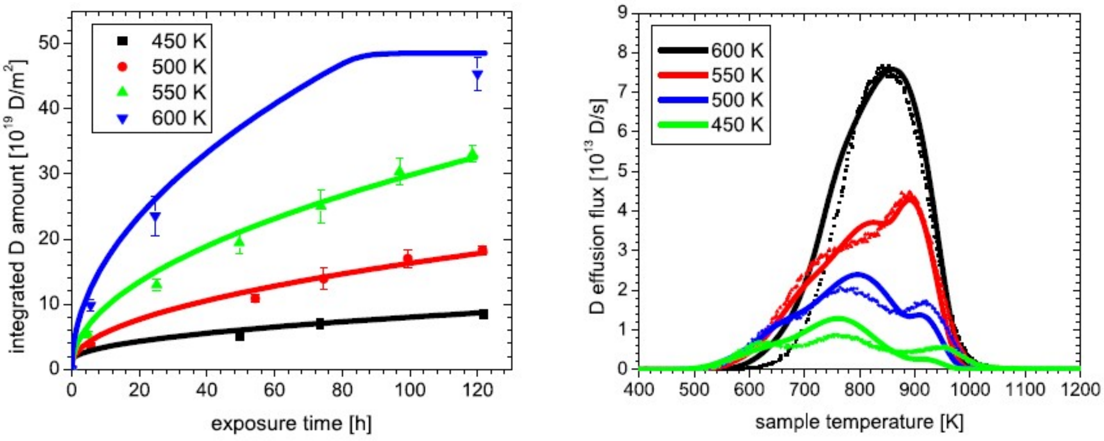
(a) (b)

FIG. 11(a) Time evolution of measured (dots) and modeled (lines) integrated deuterium amounts within the NRA information depth for exposure temperatures of 450 K, 500 K, 550 K and 600 K. (b) Simulated (solid lines) and measured (dotted lines) deuterium thermodesorption spectra for self-damaged tungsten samples, exposed to D atoms at different temperatures. Heating rate was 15 K/min.[1]

To simulate our experimental results we have used a 1-D rate equation code [29], called TESSIM. This code was developed for the simulation of deuteriumion implantation, diffusion and trapping in the bulk of tungsten [42]. In order to describe low energy hydrogen atom interaction with W, as argumented already above, equations describing processes on the surface had to be coupled with the TESSIM code. The same surface proceses as included in the MHIMS code were also included here. We have modeled the experimental data using a 1-D rate equation model and determined the detrapping energies and values of modeling parameters, which are describing deuterium atom adsorption on the surface of tungsten and migration of atoms from the surface to the bulk of the material.

The TESSIM code without surface processes was first used to simulate the TDS spectra. The experimental TDS spectra and simulation results are shown in Fig. 11(b) for all exposure temperatures. For the initial conditions we used D range and concentration, as determined from the D depth profiles measured by NRA. We have again assumed that each trap type is distributed homogeneously through the damaged layer down to a depth of 2 mm. The simulation confirmed that reducing the D range results in an additional low temperature shoulder or peak positioned between the low and high temperature peak, as observed in the TDS spectra of samples, exposed at lower temperatures. The TDS spectrum of the sample exposed at 600 K was used to determine the detrapping energy and trap density of the high energy trap type, being 1.87 eV with concentration 40.9×10^{19} traps/m^2, respectively. The position of the lowest temperature peak was used to determine the detrapping energy of low energy trap type, being 1.6 eV. The density of the low energy trap type

---

[1] Reprinted from Journal of Nuclear Materials, vol. 496, A. Založnik et al. Deuterium atom loading of self-damaged tungsten at different sample temperatures, 1-8., Copyright (2018), with permission from Elsevier

was determined as the difference between the integrated D amount and the D amount of the high energy trap type, which results in the trap density of 12.4×10^{19} traps/m^2. Such detrapping energies were in good agreement determined by the above presented simulation with the MHIMS code and interpreted to belong to jogged dislocation lines and dislocation loops for low and high energy trap type, respectively.

This set of parameters was used in the following simulations, where D uptake at different sample temperatures was simulated. Our next step was to determine the unknown surface parameters, i.e. adsorption energies, concentrations of adsorption sites and the height of the potential barrier for atom to jump from surface to bulk. These parameters were obtained by fitting the experimentally determined integrated D amounts shown in Fig. 11(a) using the TESSIM code with surface processes included. Results obtained at different exposure temperatures were all fitted simultaneously since the values of fitting parameters should be the same for all cases. For the different temperatures as well as for the different fluence steps the integrated D amounts could be reproduced with high accuracy, as shown in Fig. 11(a). We have also compared the simulated deuterium depth profiles to the experimentally obtained ones. We found a good agreement between the simulation and experimental depth profiles, as shown in Fig. 10. The calculated diffusion range coincides nicely with the diffusion range determined by the NRA technique. The obtained values of the fitting parameters were: two adsorption site types, the determined surface adsorption energies are 0.68±0.02 eV and 0.71±0.02 eV and the energy barier for migration from the surface to the bulk are 1.41±0.02 eV and 1.44±0.02 eV, respectively. This number is in good agreement with the value obtained from the modelling by MHIMS on different set of experimental data obtaining 1.33 ± 0.04 eV at 500 K, 1.55±0.02 eV at 600 K. From the height of the barrier for surface to bulk diffusion we calculated the heat of solution for tungsten and is found to be E_S=0.343 eV±0.003 eV, assuming that the resurfacing energy (from the bulk to the surface) is 0.39 eV (diffusion energy obtained by Fraunfelder [38]). The value is approximately three times lower compared to the value reported in the literature by Fraunfelder 1.04 eV. Additional modelling of D retention as a function of exposure temperature with the fixed literature value for the barrier height resulted in a huge discrepancy between experimental data and modelling results.

3.5 Infleunce of hydrogen presence on defect production and annihilation

Untill recently all hydrogen retention studies were performed by sequential high energy ion damaging and subsequent plasma/gas/atom loading of the material by hydrogen isotopes. However, in a real fusion reactor environment both implantation of energetic hydrogen ions and neutrals as well as damage creation by neutron irradiation will take place at the same time. The consequences of synergistic effects for hydrogen retention in tungsten are unknown but theory predicts defect stabilization in the presence of hydrogen atoms in tungsten [43,44].

To make one step further towards more realistic situation we have performed the first experimental study on simultaneous defect creation by 10.8 MeV self-ion implantation and D-atom-beam loading (E=0.28eV, j = 5.4×10^{18} Dm^{-2}s^{-1}) in tungsten between 450 K and 1000 K [20]. After the damaging and loading, D depth profiles were measured by NRA. In order to determine how many traps were actually created in the material, the samples were after simultaneous damaging & loading and NRA analysis, exposed to D atoms for additional 19 h at 600 K, fluence 3.7x10^{23} Dm^{-2}. The deuterium depth profiles obtained after populating the defects by D atoms were measured. It was shown that the highest concentration was obtained for the 450 K case, decreasing with damaging temperature. In order to sort out the observed effects comparison to a series of sequential damaging/annealing/exposure experiments is made. Namely, three sequential experimental series were performed in addition with different damaging/exposure procedures, that help to separate the processes: i) *W-ion damaging at elevated temperatures + D-atom exposure at 600 K* afterwards to determine the trap concentration; ii) *W-ion damaging at room temperature + samples post-damaging annealing at different temperatures* for one hour + *D-atom loading at 500 K* afterwards to determine the trap concentration; and iii) *W-ion damaging at room temperature + D-atom exposure at elevated temperatures* afterwards. Comparison of the maximum deuterium concentration obtained at the maximum of the peak displacement damage for simultaneous self-damaging and D-atom loading and processes under i) and ii) are shown in figure 12. Higher D concentrations were found in the case of simultaneous damaging and D-atom loading as compared to sequential damaging at elevated temperatures and populating the defects afterwards. However, the deuterium retention is still lower as compared to sequential damaging at room temperature and post-damaging annealing. The observations are explained by stabilization of the created defects by the presence of solute hydrogen in the simultaneous case in the bulk that would annihilate at high temperatures without the presence of hydrogen.

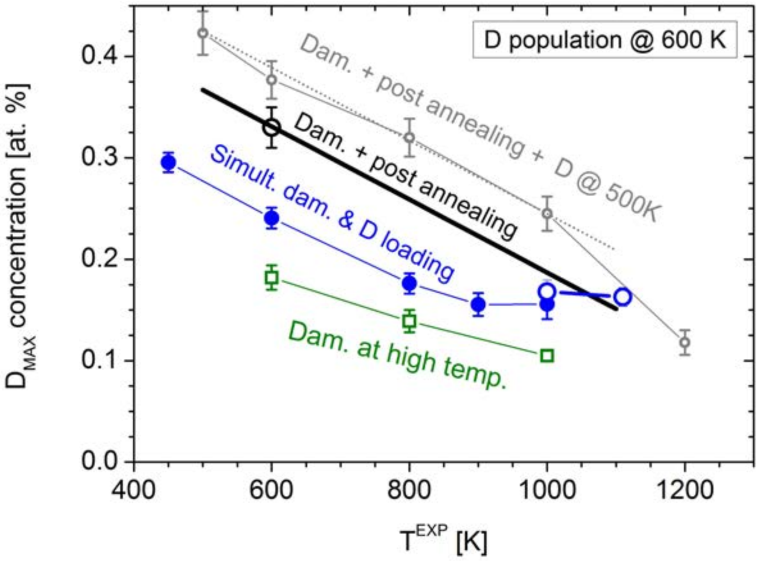

FIG. 12. Maximum D concentration obtained at the position of the maximum of the peak displacement damage profile versus damage temperatures obtained from D depth profiles for the damaging at high temperatures (process (i)) and simultaneous self-damaging and D loading. The data are compared to damaging at room temperature and afterward post-damaging annealing and defect population by D: damaging process (ii) (grey data) and extrapolation for population of defects at 600 K (black data).

3.6 Influence of He on D atom retention and transport

Recent experiments studying the interaction of hydrogen isotopes and helium with tungsten using He seeded deuterium plasmas showed that He addition leads to reduced D retention. While there are several attempts to explain the reduced D retention, the actual cause for these observations remains unclear. One possibility for the reduced retention is that implanted He might create a diffusion barrier for D transport. Likewise nano-sized bubbles might open-up additional pathways for D towards the surface thereby decreasing its transport into the bulk. Contrary to these experimental findings density functional theory (DFT) calculations show strong attraction between He and hydrogen, indicating preferential trapping of deuterium around He clusters. MD simulations show that a large amount of H can be accommodated around He bubbles. Increased retention was found experimentally also in ion beam experiments. However, the challenge of these studies is that the applied He and D implantation energies cause displacement damage which is known to increase retention in tungsten substantially. Hence one cannot distinguish with confidence the influence of the presence of He from the displacement damage that He causes.

In order to elucidate the possibility of He acting as a diffusion barrier or inducing preferential binding of hydrogen around He, we took an alternative experimental approach. We tried to avoid the surface effects of He on D retention by implanting He well below the surface. To minimize the influence of displacement damage created during He implantation on D retention, so-called self-damaged W was used. The W implantation dose was chosen such that D retention would not increase any further with increasing ion damaging dose. Existing defects were D decorated till saturation was reached by gentle low temperature plasma loading at room temperature before He implantation.

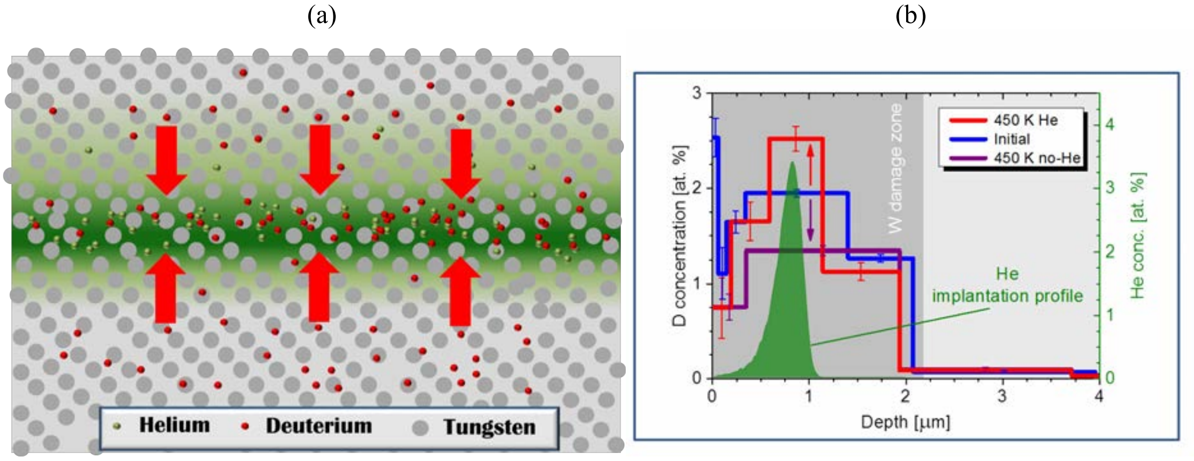

FIG. 13(a) Schematics showing D accumulation in the He-implantation zone during annealing. (b) Comparison of D concentration depth profiles (left scale) of the initial depth profile, before He implantation (blue line), of the He-irradiated sample and the non-He-implanted reference obtained after annealing at 450 K for two hours. The deuterium accumulated around helium implantation zone after sample annealing at 450 K. No such accumulation was observed on the reference sample. The green filled area shows the He concentration profile (right scale) as calculated by SRIM for 500 keV He ions. The grey area indicates the so-called self-damaged zone.

The possible effect of He acting as a diffusion barrier was studied by outgassing of deuterium through the He implantation zone by isochronal annealing in the temperature range between 300 K and 800 K as well as during isothermal D atom exposure at 600 K. Deuterium depth profiling was performed in situ during isochronal annealing and during D atom exposure. For the first time, we have unambiguously shown [21] that He does not act as a diffusion barrier, but attracts D and locally increases D trapping. Namely, after sample annealing at 450 K D retention in the He-enriched zone increased by a factor of two as compared to the non-He-implanted W reference as is shown in Fig. 13. There comparison of D concentration depth profiles of the He-irradiated sample and of the non-He-implanted reference obtained after annealing at 450 K for two hours are shown. The initial depth profile measured before He implantation and annealing is shown. The deuterium accumulated around helium implantation zone after sample annealing at 450 K. No such accumulation was observed on the reference sample. Rate equation modelling can explain the measured D depth profiles quantitatively when keeping the de-trapping parameters unchanged but only increasing the number of traps in the He zone. These results bolster confidence in theoretical calculations predicting that more hydrogen isotopes can be stored around a He-cluster zone.

4. CONCLUSIONS

We have presented recent advances on the field of *in-situ* studies on the dynamics of HI retention and transport, isotope exchange and D outgassing in self-damaged W [7]. By the help of rate equation models these experiments [7,17] enabled us to pin down the nature of traps and detrapping energies [19], parameters for the surface processes and energy barrier for inward diffusion [19]. In order to further study the influence of energy barrier for D atom inward diffusion additional benchmark experiments where performed as a function of loading temperature. Namely, recrystallized self-damaged W samples were loaded at different temperatures from 450 K to 600 K by D atom beam [18]. The studies showed that there are difference between loading by D atoms with thermal energy of 0.3 eV and plasma loading with ion energy of <5 eV. A major step forward in *in situ* studies was performed with simultaneous W ion irradiation and D-atom loading which was performed for the first time and the effect of the presence of D on the evolution of lattice defects was studied [20]. Simultaneous exposures were compared with sequential ones such as W irradiation and post defect annealing and W irradiation at elevated temperature. As a result synergistic effects have been identified [20]. The effect of He as an analysing beam and its influence on HI retention and transport was also presented where accumulation of deuterium around helium was observed [21].

Such data are necessary for modelling of JET and ITER recycling dynamics and retention dynamics, where especially in the divertor fluxes of neutral species are 10^{23} $m^{-2}s^{-1}$ which is much higher compared to the atom flux applied here ~ 10^{19} m^2s^{-1}. Even though the neutral species are often neglected in the case of plasma exposures we have shown that they can penetrate into the bulk of damaged tungsten. Due to the high energy barrier between surface and bulk their contribution at low temperatures <450 K to retention compared to energetic ions above 5 eV can probably be neglected, as is usually done. However, as was presented in Ref. [29] the ions with energy below 5 eV behave on the other hand as atoms with low energy, where they do not penetrate directly into the bulk but first neutralize and chemisorb on the surface and then penetrate in the bulk by hopping from chemisorbed state to subsurface. Their role is then first filling the surface binding states and keeping the surface saturated and if the temperature is high enough and they manage to hop into the bulk, they fill the empty traps induced by irradiation. Ions with higher energy on the other hand penetrate directly into the bulk and directly fill the traps produced by damaging. However, at higher temperatures above >450 K neutral species contribution for filling the trapping sites in the bulk of tungsten will have to be taken into account.

ACKNOWLEDGMENTS

This work has been carried out within the framework of the EUROfusion Consortium and has received funding from the Euratom research and training programme 2014–2018 under grant agreement No. 633053 . Work was performed under EUROfusion WP PFC. The views and opinions expressed herein do not neces- sarily reflect those of the European Commission.

Parts of this article are reproduced by permission from *Journal of Nuclear Materials* **469**, 133 (2016) [Elsevier: 4542400442646]; and *Nuclear Fusion* **57**, 056002 (2017).

REFERENCES

[1] YOU, J., A review on two previous divertor target concepts for DEMO: mutual impact between structural design requirements and materials performance, Nuclear Fusion **55** (2015) 113026.

[2] WAMPLER, W., DOERNER, R., The influence of displacement damage on deuterium retention in tungsten exposed to plasma, Nuclear Fusion **49** (2009) 115023.

[3] HATANO, Y., SHIMADA, M., OTSUKA, T., OYA, Y., ALIMOV, V., HARA, M., SHI, J., KOBAYASHI, M., ODA, T., CAO, G., OKUNO, K., TANAKA, T., SUGIYAMA, K., ROTH, J., TYBURSKA-PÜSCHEL, B., DORNER, J., YOSHIDA, N., FUTAGAMI, N., WATANABE, H., HATAKEYAMA, M., KURISHITA, H., SOKOLOV, M., KATOH, Y., Deuterium trapping at defects created with neutron and ion irradiations in tungsten, Nuclear Fusion **53** (2013) 073006.

[4] OGORODNIKOVA, O., GASPARYAN, Y., EFIMOV, V., CIUPIŃSKI, Ł., GRZONKA, J., Annealing of radiation-induced damage in tungsten under and after irradiation with 20MeV self-ions, Journal of Nuclear Materials **451** (2014) 379.

[5] MANHARD, A., MATERN, G., BALDEN, M., A Step-By-Step Analysis of the Polishing Process for Tungsten Specimens, Practical Metallography **50** (2013) 5.

[6] MANHARD, A., BALDEN, M., ELGETI, S., Quantitative Microstructure and Defect Density Analysis of Polycrystalline Tungsten Reference Samples after Different Heat Treatments, Practical Metallography **52** (2015) 437.

[7] MARKELJ, S., ZALOŽNIK, A., SCHWARZ-SELINGER, T., OGORODNIKOVA, O., VAVPETIČ, P., PELICON, P., ČADEŽ, I., In situ NRA study of hydrogen isotope exchange in self-ion damaged tungsten exposed to neutral atoms, Journal of Nuclear Materials **469** (2016) 133.

[8] EL BOUANANI, M., PELICON, P., RAZPET, A., ČADEŽ, I., BUDNAR, M., SIMČIČ, J., MARKELJ, S., Simple and accurate spectra normalization in ion beam analysis using a

transmission mesh-based charge integration, Nuclear Instruments and Methods in Physics Research Section B: Beam Interactions with Materials and Atoms **243** (2006) 392.

[9] SCHWARZ-SELINGER, T., VON KEUDELL, A., JACOB, W., Plasma chemical vapor deposition of hydrocarbon films: The influence of hydrocarbon source gas on the film properties, Journal of Applied Physics **86** (1999) 3988.

[10] MARKELJ, S., PELICON, P., ČADEŽ, I., SCHWARZ-SELINGER, T., JACOB, W., In situ study of erosion and deposition of amorphous hydrogenated carbon films by exposure to a hydrogen atom beam, Journal of Vacuum Science & Technology A: Vacuum, Surfaces, and Films **30** (2012) 041601.

[11] SCHWARZ-SELINGER, T., Deuterium retention in MeV self-implanted tungsten: Influence of damaging dose rate, Nuclear Materials and Energy **12** (2017) 683.

[12] OGORODNIKOVA, O., GASPARYAN, Y., EFIMOV, V., CIUPIŃSKI, Ł., GRZONKA, J., Annealing of radiation-induced damage in tungsten under and after irradiation with 20MeV self-ions, Journal of Nuclear Materials **451** (2014) 379.

[13] STOLLER, R., TOLOCZKO, M., WAS, G., CERTAIN, A., DWARAKNATH, S., GARNER, F., On the use of SRIM for computing radiation damage exposure, Nuclear Instruments and Methods in Physics Research Section B: Beam Interactions with Materials and Atoms **310** (2013) 75.

[14] ALIMOV, V., MAYER, M., ROTH, J., Differential cross-section of the D(3He,p)4He nuclear reaction and depth profiling of deuterium up to large depths, Nuclear Instruments and Methods in Physics Research Section B: Beam Interactions with Materials and Atoms **234** (2005) 169.

[15] MAYER, M., GAUTHIER, E., SUGIYAMA, K., VON TOUSSAINT, U., Quantitative depth profiling of deuterium up to very large depths, Nuclear Instruments and Methods in Physics Research Section B: Beam Interactions with Materials and Atoms **267** (2009) 506.

[16] SCHMID, K., VON TOUSSAINT, U., Statistically sound evaluation of trace element depth profiles by ion beam analysis, Nuclear Instruments and Methods in Physics Research Section B: Beam Interactions with Materials and Atoms **281** (2012) 64.

[17] WANG, P., JACOB, W., GAO, L., DÜRBECK, T., SCHWARZ-SELINGER, T., Comparing deuterium retention in tungsten films measured by temperature programmed desorption and nuclear reaction analysis, Nuclear Instruments and Methods in Physics Research Section B: Beam Interactions with Materials and Atoms **300** (2013) 54.

[18] ZALOŽNIK, A., MARKELJ, S., SCHWARZ-SELINGER, T., CIUPIŃSKI, Ł., GRZONKA, J., VAVPETIČ, P., PELICON, P., The influence of the annealing temperature on deuterium retention in self-damaged tungsten, Physica Scripta **T167** (2016) 014031.

[19] ZALOŽNIK, A., PELICON, P., RUPNIK, Z., ČADEŽ, I., MARKELJ, S., In situ hydrogen isotope detection by ion beam methods ERDA and NRA, Nuclear Instruments and Methods in Physics Research Section B: Beam Interactions with Materials and Atoms **371** (2016) 167.

[20] HODILLE, E., ZALOŽNIK, A., MARKELJ, S., SCHWARZ-SELINGER, T., BECQUART, C., BISSON, R., GRISOLIA, C., Simulations of atomic deuterium exposure in self-damaged tungsten, Nuclear Fusion **57** (2017) 056002.

[21] MARKELJ, S., SCHWARZ-SELINGER, T., ZALOŽNIK, A., KELEMEN, M., VAVPETIČ, P., PELICON, P., HODILLE, E., GRISOLIA, C., Deuterium retention in tungsten simultaneously damaged by high energy W ions and loaded by D atoms, Nuclear Materials and Energy **12** (2017) 169.

[22] MARKELJ, S., SCHWARZ-SELINGER, T., ZALOŽNIK, A., Hydrogen isotope accumulation in the helium implantation zone in tungsten, Nuclear Fusion **57** (2017) 064002.

[23] GASPARYAN, Y., OGORODNIKOVA, O., EFIMOV, V., MEDNIKOV, A., MARENKOV, E., PISAREV, A., MARKELJ, S., ČADEŽ, I., Thermal desorption from self-damaged tungsten exposed to deuterium atoms, Journal of Nuclear Materials **463** (2015) 1013.

[24] ROTH, J., SCHWARZ-SELINGER, T., ALIMOV, V., MARKINA, E., Hydrogen isotope exchange in tungsten: Discussion as removal method for tritium, Journal of Nuclear Materials **432** (2013) 341.

[25] KEYS, L., MOTEFF, J., Neutron irradiation and defect recovery of tungsten, Journal of Nuclear Materials **34** (1970) 260.

[26] SCHULTZ, H., Defect parameters of b.c.c. metals: group-specific trends, Materials Science and Engineering: A **141** (1991) 149.

[27] GRZONKA, J., CIUPIŃSKI, Ł., SMALC-KOZIOROWSKA, J., OGORODNIKOVA, O.V., MAYER, M., KURZYDŁOWSKI, K.J., Electron microscopy observations of radiation damage in irradiated and annealed tungsten. Nuclear Instruments and Methods in Physics Research Section B: Beam Interactions with Materials and Atoms, 20th International Workshop on Inelastic Ion-Surface Collisions (IISC-20) **340** (2014) 27.

[28] MARKINA, E., MAYER, M., MANHARD, A., SCHWARZ-SELINGER, T., Recovery temperatures of defects in tungsten created by self-implantation, Journal of Nuclear Materials **463** (2015) 329.

[29] GRZONKA, J., CIUPIŃSKI, Ł., SMALC-KOZIOROWSKA, J., OGORODNIKOVA, O., MAYER, M., KURZYDŁOWSKI, K., Electron microscopy observations of radiation damage in irradiated and annealed tungsten, Nuclear Instruments and Methods in Physics Research Section B: Beam Interactions with Materials and Atoms **340** (2014) 27.

[30] HODILLE, E., BONNIN, X., BISSON, R., ANGOT, T., BECQUART, C., LAYET, J., GRISOLIA, C., Macroscopic rate equation modeling of trapping/detrapping of hydrogen isotopes in tungsten materials, Journal of Nuclear Materials **467** (2015) 424.

[31] ’T HOEN, M. H. J., MAYER, M., KLEYN, A. W., ZEIJLMANS VAN EMMICHOVEN, P. A., Strongly Reduced Penetration of Atomic Deuterium in Radiation-Damaged Tungsten, Physical Review Letters **111** (2013) 225001.

[32] MAYA, P., Molecular dynamics studies of sticking and reflection of low-energy deuterium on single crystal tungsten, Journal of Nuclear Materials **480** (2016) 411.

[33] OGORODNIKOVA, O. V., MARKELJ, S., VON TOUSSAINT, U., Interaction of atomic and low-energy deuterium with tungsten pre-irradiated with self-ions, Journal of Applied Physics **119** (2016) 054901.

[34] 'T HOEN, M., MAYER, M., KLEYN, A., SCHUT, H., ZEIJLMANS VAN EMMICHOVEN, P., Reduced deuterium retention in self-damaged tungsten exposed to high-flux plasmas at high surface temperatures, Nuclear Fusion **53** (2013) 043003.

[35] SHIMADA, M., CAO, G., HATANO, Y., ODA, T., OYA, Y., HARA, M., CALDERONI, P., The deuterium depth profile in neutron-irradiated tungsten exposed to plasma, Physica Scripta **T145** (2011) 014051.

[36] FERNANDEZ, N., FERRO, Y., KATO, D., Hydrogen diffusion and vacancies formation in tungsten: Density Functional Theory calculations and statistical models, Acta Materialia **94** (2015) 307.

[37] XIAO, W., GENG, W., Role of grain boundary and dislocation loop in H blistering in W: A density functional theory assessment, Journal of Nuclear Materials **430** (2012) 132.

[38] TERENTYEV, D., DUBINKO, V., BAKAEV, A., ZAYACHUK, Y., VAN RENTERGHEM, W., GRIGOREV, P., Dislocations mediate hydrogen retention in tungsten, Nuclear Fusion **54** (2014) 042004.

[39] HEINOLA, K., AHLGREN, T., NORDLUND, K., KEINONEN, J., Hydrogen interaction with point defects in tungsten, Physical Review B **82** (2010) 094102.

[40] FRAUENFELDER, R., Solution and Diffusion of Hydrogen in Tungsten, Journal of Vacuum Science and Technology **6** (1969) 388.

[41] GALPARSORO, O., PÉTUYA, R., BUSNENGO, F., IÑAKI JUARISTI, J., CRESPOS, C., ALDUCIN, M., LARREGARAY, P., Hydrogen abstraction from metal surfaces: when electron–hole pair excitations strongly affect hot-atom recombination, Physical Chemistry Chemical Physics **18** (2016) 31378.

[42] BUNERMANN, O., JIANG, H., DORENKAMP, Y., KANDRATSENKA, A., JANKE, S. M., AUERBACH, D. J., WODTKE, A. M., Electron-hole pair excitation determines the mechanism of hydrogen atom adsorption, Science **350** (2015) 1346.

[43] GALPARSORO, O., PÉTUYA, R., JUARISTI, J. I., CRESPOS, C., ALDUCIN, M., LARRÉGARAY, P., Energy Dissipation to Tungsten Surfaces upon Eley–Rideal Recombination of N2 and H2, The Journal of Physical Chemistry C **119** (2015) 15434.

[44] SCHMID, K., RIEGER, V., MANHARD, A., Comparison of hydrogen retention in W and W/Ta alloys, Journal of Nuclear Materials **426** (2012) 247.

[45] KATO, D., IWAKIRI, H., WATANABE, Y., MORISHITA, K., MUROGA, T., Super-saturated hydrogen effects on radiation damages in tungsten under the high-flux divertor plasma irradiation, Nuclear Fusion **55** (2015) 083019.

[46] MIDDLEBURGH, S., VOSKOBOINIKOV, R., GUENETTE, M., RILEY, D., Hydrogen induced vacancy formation in tungsten, Journal of Nuclear Materials **448** (2014) 270.

EVALUATION OF TRITIUM INVENTORY IN IRRADIATED TUNGSTEN BY ATOMIC-SCALE MODELING

T. ODA, G.-H. KIM, H. J. SHIM, K.-B. ROH, Y. JIN, N.-K. KIM, M.-G. LEE, D. ZHU, M. J. BANISALMAN

Department of Energy Systems Engineering, Seoul National University
Seoul, 08826, Republic of Korea

Abstract

In this program, we have studied several key processes and properties that are important in the evaluation of tritium inventory and behaviour in irradiated tungsten. In this report, we present four outcomes. In Section 1, the desorption energy of trapped deuterium in the defects of tungsten is determined to be 1.50 eV for dislocation, 1.80 eV for vacancy, and 2.28 eV for defect cluster. In Section 2, the threshold displacement energy is determined to be 85 eV with an error of ±4.5%, which is comparable with the ASTM standard (90 eV). In Sections 3 and 4, models to describe the vacancy and grin boundary effects on hydrogen behaviours are presented. Based on the comparison results with available experimental data on hydrogen diffusivity and permeability, several quantities such as diffusion coefficient in the bulk, effective diffusion coefficient along GBs, and effective trapping energy by GBs are determined.

1. DESORPTION ENERGY OF TRAPPED DEUTERIUM IN THE DEFECTS OF TUNGSTEN

To establish a common reference for various TDS (Thermal Desorption Spectroscopy) devices, thin D+W film deposited tungsten sample was shared with other groups, which samples for TDS were provided by IPP. Here TDS system was constructed in the Plasma Application Laboratory of Seoul National University [1][2]. The heating rate (β) of TDS operation set as 0.33 K s^{-1} which satisfies the Redhead approximation [3] andadapted to analyze the desorption energy. The desorption energy approximated by using Redhead approximation is.

$$\mathrm{E_{des}} = RT\left[\ln\left(\frac{\nu_1 T}{\beta}\right) - 3.64\right], \tag{1}$$

where E_{des} is the activation energy of desorption, ν_1 is the Debye frequency as the pre-exponential factor of the first order desorption (~10^{13} s^{-1}), R is the gas constant and T is the peak temperature of the TDS spectrum. According to Eq. (1), the peak temperature of TDS represents the desorption energy of the deuterium from the trapping source and the defect type can be analysed. The approximation provides a low error rate of <1.5% on the temperature to desorption energy conversion.

Proper step for our TDS system contains 1 week of time interval after ion irradiation to reduce the effect of dynamic retention. We received the reference sample in about 3 months after deposition, and then we only take time for vacuum conditioning in chamber. FIG. 1 shows the TDS spectrum of HD and D2 with approximated peak deconvolution based on Gaussian fitting. Note that they give not an absolute value of amount but the temperature of each peak. Table 1 summarizes the desorption energy (E_{des}) of deuterium interacting with defect in tungsten. Binding energy (E_b) of each trapping site was calculated using diffusion energy (E_{diff}) of deuterium in tungsten lattice (E_{diff}=0.4 eV [4]) which is in relation of $E_{des}=E_{diff}+E_b$. As a intrinsic trapping site, TDS results show the dislocation-induced trapping peak at 522 K (corresponding to the binding energy E_d~1.1 eV) and the vacancy-induced trapping peak at 614 K (E_d~1.4 eV). Defect cluster-induced trapping peak was not measured at the reference sample. The desorption energy of defect cluster was measured in our previous works as found in [2]. And the defect cluster generated tungsten showed defect cluster-induced trapping peak at 799 K (E_d~2.28 eV).

TABLE 1. SUMMARY OF DESORPTION ENERGY OF DEUTERIUM INTERACTING WITH DEFECTS.

Defects	Hydroen Isotope	E_{des} (eV)	E_b (eV)	Methods/Conditions
Dislocation	Deuterium	1.50 (522 K)	1.10	TDS with β=0.3 K/s
Vacancy	Deuterium	1.80 (614 K)	1.40	TDS with β=0.3 K/s
Defect cluster	Deuterium	2.28 (799 K) [2]	1.88	TDS with β=1 K/s

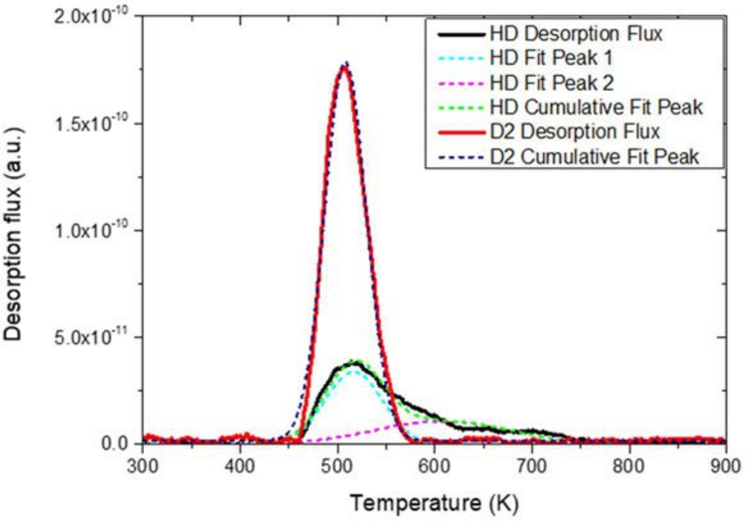

FIG. 1. TDS results for deuterium retained tungsten sample distributed from IPP (Sample ID: B3219-B).

2. THRESHOLD DISPLACEMENT ENERGY FOR TUNGSTEN [5]

2.1 Introduction

For the determination of the number of created radiation defects, the threshold displacement energy (TDE) is one of the most important quantities. The TDE is defined as the minimum recoil energy required to form a stable Frenkel pair. The TDE is used in theoretical models such as the Kinchin–Pease model [6] and the NRT model [7] to estimate the number of defects created by collision cascades. Although there are some flaws in these theoretical models, such as an underestimation by the NRT model for a high-energy collision cascade in which the linearity between the damage energy and the defect number is broken [8], the models are still widely used to quantify radiation damage in the unit of displacement-per-atom (dpa) and to then compare the radiation effects of materials irradiated under different conditions.

As for the TDE of tungsten (W), however, there is a discrepancy in previous studies: 45-61 eV [9] and 98 eV [8], determined by molecular dynamics (MD) calculations; 55.3 eV [10], obtained with a theoretical interpolation model [11] using a few available experimental values [12]; and 90 eV, recommended by the American Society for Testing and Materials (ASTM) [13]. The discrepancies in the TDE values cause inconsistencies in the evaluation of dpa and the number of created radiation defects. Indeed, different TDE values were sometimes employed for the damage evaluation in previous studies: for example, 55.3 eV in ref. [14], 90 eV in ref. [15] and some others, and values not specifically mentioned in many other studies.

Therefore, we determined the TDE of W using the MD method as accurately as possible through careful analysis of the effects of MD calculation settings. We also discussed the reason why the large discrepancies appeared among the previous studies. In the present study, we define the TDE as the average value of the threshold displacement energies for all recoil directions, which has often been used as the definition of the TDE in previous MD studies. Hereafter, this average value is denoted $E_{d,avg}$, which is equivalent to $E^{av}_{d.ave}$ in ref. [16].

2.2 Method

MD simulations were performed by using the LAMMPS code [17]. The interatomic interactions between W atoms were described with an embedded-atom method (EAM) [18] potential that was originally parameterized by Derlet et al. [19] and then modified by Björkas et al. [20] for recoil simulations.

Each recoil MD simulation was performed up to around 5 ps after the onset of the recoil event. The initial temperature of the system was set to be 30 K. For the last structure of each recoil simulation, whether a defect was formed in the system or not was judged by Wigner-Seitz defect analysis [21] using the LAMMPS Voro++ package [22]. Specifically, we first defined Wigner-Seitz cells with respect to the initial atomic configuration, which is a perfect bcc-W lattice at 30 K. Then, in recoil simulations for which there was a Wigner-Seitz cell that did not contain an atom, the cell was regarded as a vacancy, and we judged that a defect was formed.

To determine the minimum displacement energy for each recoil direction, we conducted the following two steps:

- ✓ (Step-1) The recoil energy was first set to 25 eV, and it was then increased by ΔE_{step} eV until a defect was first detected;
- ✓ (Step-2) After the first detection of a defect, the recoil energy was decreased by 1 eV to determine the minimum energy for defect formation.

The minimum energy for a specific recoil direction is denoted as $E_{d,i}$ hereafter, where the index i indicates the recoil direction. We also use a similar notation to represent the $E_{d,i}$ value for a specific recoil direction: for example, $E_{d,<100>}$ represents the $E_{d,i}$ of the <100> recoil direction.

The $E_{d,avg}$ value determined by MD calculation depends on (i) the system size (N_{atom}), (ii) the number of sampled recoil directions (N_{ICD}), (iii) the ΔE_{step} value used in searching the threshold, (iv) the number of sampled recoil timings (N_{timing}), (v) the potential model, and (vi) the temperature. In the present study, the effects of (i)-(iv) were investigated.

The effect of (v) the potential model was not examined because we consider the potential model used in the present study to be one of the best W potential models available for recoil simulations. As will be presented in Section (3), this potential model gives $E_{d,<100>}$ and $E_{d,<111>}$ values comparable with experiment: 43 eV and 41 eV in the MD simulation with the present potential model and 42±1 eV and 44±1 eV in the experiment [12], respectively.

The effect of (vi) temperature was not investigated in the present study because we consider $E_{d,avg}$ to be a reasonable estimate of the TDE for MD calculations conducted at low temperatures such as 30 K, based on the results of bcc-Fe [16]. It is expected that $E_{d,i}$ (and thus $E_{d,avg}$) is enlarged for simulations performed at higher temperatures because thermal defect recovery processes may more frequently occur within 5 ps of the recoil simulation.

More details are presented elsewhere [5].

2.3 Results and Discussion

2.3.1 Estimation of the $E_{d,avg}$ value and error

The errors induced by the four simulation settings (N_{atom}, ΔE_{step}, N_{ICD} and N_{timing}) are summarized as follows:

- ✓ The result for the effects of N_{atom} and ΔE_{step} indicates that $E_{d,avg}\left(N_{atom}\to\infty, \Delta N_{step}\to 0, N_{ICD}=210, N_{timing}=4\right)$ is 85 eV with an error of ±1.5%.
- ✓ The result for the effect of N_{ICD} indicates that the difference between the results with N_{ICD} = 210 and $N_{ICD} \to \infty$ is approximately 2%.
- ✓ The result for the recoi timing effect indicates that the error with N_{timing} = 4 is approximately 1%.

Consequently, the true $E_{d,avg}$ value, which is equal to $E_{d,avg}\left(N_{atom}\to\infty, \Delta N_{step}\to 0, N_{ICD}\to\infty, N_{timing}\to\infty\right)$, is estimated to be 85 eV with an error of ±4.5%. The obtained $E_{d,avg}$ = 85 eV is comparable with the TDE recommended by ASTM, which is 90 eV. Therefore, we recommend the use of 90 eV as the TDE for W. Details are presented elsewhere [5].

2.3.2 Comparison with previous studies

There are some apparent inconsistencies between the present study and previous studies. In this section, we discuss the reasons for this.

Fikar et al. reported the minimum threshold displacement energy over various recoil directions determined by MD [9]. It was found that the <100> recoil holds the minimum value, which ranges from 45 eV to 61 eV depending on potential models [9]. Since Fikar et al. evaluated the minimum value, not the average value over all directions, their result should correspond to $E_{d,<100>}$, which is 43 eV in the present study (or $E_{d,<111>}$ = 41 eV, the minimum value in the present study), not to $E_{d,avg}$. Thus, the result in ref. [9] is reasonably consistent with the present study.

Setyawan et al. reported $E_{d,avg}$ determined by MD in a study focusing on the cascade morphology transition in bcc metals [8]. An $E_{d,avg}$ value of 98.0 eV was obtained using the same EAM potential model as the present study, and a value of 122.6 eV was obtained using another EAM potential model [23]. The present EAM potential model shows good agreement with the experimental results of the <100> and <111> threshold displacement energies but not with results of the other EAM potential model [23]. Thus, we consider that 98.0 eV is more reliable than 122.6 eV. The difference between 98.0 eV in ref. [8] and 85 eV in the present study is mainly attributed to the ΔE_{step} effect. In ref. [8], ΔE_{step} = 5 eV was used, which induces up to an approximately 13 eV error according to Eqs. (3) and (4). Considering this effect, 85 eV should be more proper than 98.0 eV as the $E_{d,avg}$ of the present potential model.

Mason et al. reported $E_{d,avg}$ = 55.3 eV [10], which was obtained by using a theoretical equation proposed by Jan and Seeger [11]. In this equation, $E_{d,avg}$ is calculated only from three $E_{d,i}$ values, namely, $E_{d,<100>}$, $E_{d,<110>}$ and $E_{d,<111>}$. In Mason et al.'s study [10], the values $E_{d,<100>}$ = 42 eV, $E_{d,<110>}$ = 70 eV and $E_{d,<111>}$ = 44 eV were taken from ref. [12]. However, the theoretical equation of Jan and Seeger cannot appropriately predict $E_{d,avg}$, which was previously shown for bcc-Fe [24]. Indeed, the direction dependence of $E_{d,i}$ obtained with the theoretical equation, with $E_{d,<100>}$ = 43 eV, $E_{d,<110>}$ = 99 eV and $E_{d,<111>}$ = 41 eV, which are the values determined in the present MD simulations, is largely different from the MD simulation results. In the theoretical equation, it seems to be assumed that (i) $E_{d,i}$ smoothly changes around the <100>, <110> and <111> directions and (ii) the minimum and the maximum values of $E_{d,i}$ are achieved in two of the three directions. Although the patterns around <100> and <111> are relatively smooth and thus the agreement between the theoretical estimates and the MD results is reasonably good around these directions, disregarding the largest $E_{d,i}$ value around the <321> direction causes large underestimations of $E_{d,i}$ values for many directions in the theoretical estimates, which results in the underestimation of $E_{d,avg}$. Overestimations are only observed around the <100> direction up to 10 eV. Therefore, we attribute the discrepancy between ref. [10] and the present study to the inappropriateness of the theoretical equation used in ref. [10] for $E_{d,avg}$ estimation.

2.4 Conclusions

We have evaluated the TDE of tungsten using an MD simulation, where TDE is defined as the average value of the minimum displacement energies for creating a stable defect over all directions, namely, $E_{d,avg}$. To determine it as accurately as possible, the effects of calculation settings, such as the simulation cell size (N_{atom}), the number of displacement directions (N_{ICD}), the increment step of the recoil energy in searching the threshold value (ΔE_{step}), and the thermal vibration of atoms (N_{timing}), were analyzed. As a result, we have obtained 85 eV as the TDE of tungsten with a possible error of approximately 4.5%. This value is reasonably close to the one recommended by the American Society for Testing and Materials (ASTM), which is equal to 90 eV. Consequently, we conclude that 90 eV is a reasonable choice for the TDE of tungsten.

3. DIFFUSION COEFFICIENT OF HYDROGEN IN TUNGSTEN [25]

3.1 Introduction

The diffusion coefficient of hydrogen is one of the fundamental physical quantities that govern the tritium behavior in tungsten. It is directly relevant with tritium release and permeation from/through tungsten. In addition, it is a vital input in analyzing experimental results of thermal desorption spectroscopy (TDS; or temperature programed desorption, TPD), which has been widely conducted to acquire information on hydrogen-defect interactions. Among several reported hydrogen diffusivities, the equation given by Frauenfelder [26] has been most utilized:

$$D = 4.1 \times 10^{-7} \exp(-0.39\ eV/kT), \tag{2}$$

where D (m^2 s^{-1}) is the diffusion coefficient of hydrogen at temperature T (K), and k (=8.62×10^{-5} eV K^{-1}) is the Boltzmann constant. This formula was determined by degassing experiment of pre-loaded H_2 gas in 1100-2400 K [26].

First-principles calculation based on density functional theory (DFT) has also been applied to hydrogen in tungsten. For achieving a diffusion coefficient, DFT calculation is often coupled with transition state theory (TST). For example in bcc-Fe, DFT+TST approach produced diffusion coefficients comparable with experimental results [27,28]. Since bcc-Fe has similar characteristics to bcc-W in respect to hydrogen behavior, such as a positive solution energy and a low energy barrier for hydrogen diffusion, it is reasonable to expect a good result in tungsten as well. However, previous DFT calculations showed large disagreement with experiment in the case of tungsten: 0.20 eV as the migration barrier in DFT calculation [29] and 0.39 eV as the activation energy for diffusion in Frauenfelder's experiment [26] (Eq. (2)). Note that the migration barrier reported by Johnson and Carter [30], 0.42 eV and 0.39 eV with zero-point energy correction, was calculated along a higher-barrier path via octahedral site (O-site), not along the minimum-barrier path via trigonal site (Tri-site). Therefore, it is inappropriate to compare this calculation value with the experimental value.

Heinola and Ahlgren [31] examined the disagreement between DFT calculation and Frauenfelder's experiment by using DFT+TST approach. They showed that the diffusion coefficients obtained with DFT+TST approach are comparable with those of Frauenfelder's experiment, if experimental data at low temperatures (<1500 K) are excluded. The exclusion decreases the activation energy for hydrogen diffusion in Frauenfelder's experiment from 0.39 eV to 0.25 eV, as given in the following Arrhenius equation [31]:

$$D = 1.58 \times 10^{-7} \exp(-0.25\ eV/kT). \tag{3}$$

This finding indicates significant influence of lattice defects which act as hydrogen traps up to high temperatures like 1500 K. Indeed, the influence of defects has been considered to be a main cause of scattering of hydrogen diffusion coefficients [32]. However, the influence is yet to be clearly quantified.

In this project, we quantified the influence of traps in hydrogen diffusivity in bcc-W in order to verify the Heinola's suggestion and Eq. (3). For this aim, we performed Kinetic Monte Carlo (KMC) simulation utilizing diffusion coefficients given by Eq. (3). Among several lattice defects which can act as hydrogen traps including grain boundary [33] and dislocation [34], we focused on vacancy as a typical trap. Vacancy-hydrogen (V-H) interactions were modeled based on DFT calculation results reported by Ohsawa et al. [35]. Diffusion coefficients determined by KMC simulations in systems with and without vacancies were compared with those of Frauenfelder's experiment.

3.2 Method

3.2.1 KMC model

For this aim, we performed KMC simulation considering the following 3 processes: (i) the bulk diffusion, (ii) the trap by a monovacancy, and (iii) the detrap from a monovacancy. The diffusion procsss was modeled with Eq. (3). The trap and detrap processes were modeled using available DFT calculation results [30][35][36][37][38].

More details are reported in elsewhere [25].

3.2.2 KMC simulation conditions: hydrogen and trap concentrations

Since the main purpose of this study is to verify the Heinola's suggestion on hydrogen diffusivity in tungsten in comparison with Frauenfelder's experiment, KMC simulations need to be done in conditions close to Frauenfelder's experiment. In Frauenfelder's experiment [26], as far as we can read from the paper, a series of degassing experiments were performed after loading hydrogen into a tungsten specimen at the same temperatures with the degassing experiments. The hydrogen loading was made to equilibrate with 600 Torr of H_2 gas. Thus, in the present KMC simulations, the hydrogen concentration is set based on the hydrogen solubility reported in the same Frauenfelder's paper [26]. Specifically, hydrogen concentrations at eight temperatures tested in the present study are as follows in H-atom/W-atom unit: 1.1×10^{-7} (0.11 ppm) at 1023 K, 2.5×10^{-7} (0.25 ppm) at 1103 K, 5.9×10^{-7} (0.59 ppm) at 1197 K, 1.4×10^{-6} (1.4 ppm) at 1307 K, 3.2×10^{-6} (3.2 ppm) at 1441 K, 7.6×10^{-6} (7.6 ppm) at 1605 K, 1.8×10^{-5} (18 ppm) at 1811 K, and 4.2×10^{-5} (42 ppm) at 2078 K.

The concentration of vacancy is determined by referring to an experimental result of Anderl et al. [39], where the trap concentration was estimated to be 2.6×10^{-5} atomic fraction (trap/W-atom) for a sample annealed at 1273 K for 1 hour and 1.3×10^{-5} for a sample annealed at 1673 K for 1 hour, respectively. The trap energy was estimated to be 1.34-1.42 eV, which is similar to that assumed in the present KMC model. Therefore, we consider that the trap found in Anderl's experiment is a vacancy-type trap or a trap which affects hydrogen diffusivity in a similar manner to a vacancy. In Frauenfelder's experiment, heat treatment was done at 2400 K for more than 10 hours (in 600 Torr H_2 gas and in a vacuum) [26]. Thus, the trap concentration should be lower than Anderl's experiment: probably around 1×10^{-5} (10 ppm) or less.

The present KMC model assumes that a vacancy can trap up to twelve H atoms based on the DFT calculation result [35], while Anderl assumed that a trap can capture only one H atom. Considering this difference in the trap capacity, it is reasonable to reduce the vacancy concentration in the present KMC model by a factor of up to 10 from the trap concentration in Anderl's experiment. Consequently, the expected vacancy concentration in Frauenfelder's experiment becomes 1 ppm in the present KMC model. Indeed, the equilibrium concentration of vacancy at the pre-treatment temperature of Frauenfelder's experiment (2400 K) is calculated to be 0.2 ppm using the vacancy formation entropy and enthalpy reported by Rasch et al. [40], which is smaller than but reasonably comparable with the estimate of 1 ppm. Based on the consideration here, we perform KMC simulations with four vacancy concentrations for comparison: 0 ppm (no vacancy), 0.1 ppm, 1 ppm and 10 ppm.

For each simulation condition, to achieve the equilibrium state of the system, more than a few million steps of equilibration run were performed. Then, a diffusion constant was evaluated by using the mean square displacement of H atom based on Einstein's relation. Expected errors in determined diffusion coefficients are less than 10%.

3.3 Results

FIG. 2 compares KMC simulation results with Frauenfelder's experimental data [26] and the formula given by Heinola and Ahlgren [31], namely Eq. (3), which was fitted only to high-temperature data (> 1500 K) of Frauenfelder's experiment. The KMC results clearly show that the effective hydrogen diffusivity is largely decreased at low temperatures as the vacancy concentration increases. The influence of vacancy is evident below 1600 K when the vacancy concentration is 10 ppm, and below 1300 K when 1 ppm. When the vacancy concentration is 0.1 ppm, the influence is mild even at around 1000 K.

The KMC result of 1 ppm vacancy concentration nicely agrees with all the Frauenfelder's experimental data. 1 ppm is a reasonable value as the expected trap concentration of Frauenfelder's experiment. This agreement underpins the Heinola's interpretation on the gap between theoretical simulation and experimental data [41]: low-temperature data (< 1500 K) are largely affected by defects, and then the true coefficients are derived as Eq. (3) by excluding these data. Thus, we recommend $D = 1.58 \times 10^{-7} \exp(-0.25\, eV/kT)$ m^2 s^{-1} [41] as the equation for hydrogen diffusion coefficient in bcc-W, rather than the most cited equation $D = 4.1 \times 10^{-7} \exp(-0.39\, eV/kT)$ m^2 s^{-1} [26], which is considered to be affected by traps.

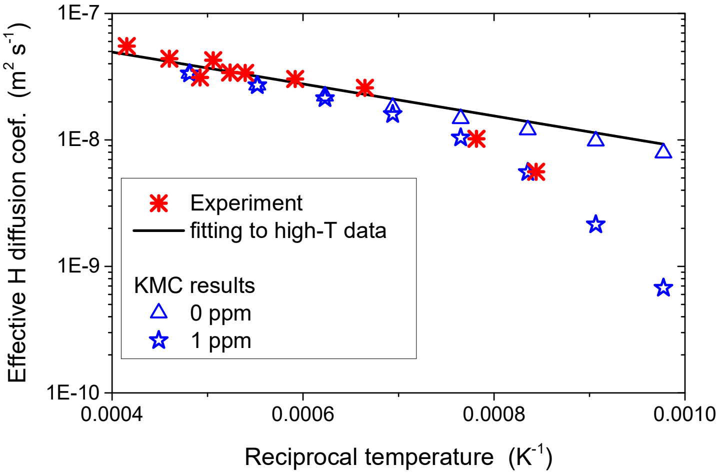

FIG. 2. KMC simulation results on effective hydrogen diffusivities in systems of different vacancy concentrations. The experimental data were taken from ref. [26]. The fitting line was taken from ref. [31] as given by Eq. (3) in the present study. This figure is reproduced using the data of Fig. 6 in [25].

3.4 Comparison with other experimental results

We further analyzed trap effects on the effective hydrogen diffusivity in order to explain why diffusivities reported in previous experiments largely disagree with each other and with Frauenfelder's result.

For this purpose, first we considered the correspondence between the fraction of solute hydrogen atoms and the effective hydrogen diffusivity. When vacancies exist in the lattice, hydrogen diffusion is mostly caused by H atoms solute in the lattice, not H atoms trapped by vacancies. Therefore, the fraction of solute H atoms should be proportional to the effective diffusion coefficient of hydrogen [42].

FIG. 3 shows a correlation between hydrogen concentration and the normalized effective diffusion coefficient in KMC simulation results. There are three characteristic regions in FIG. 3: (i) low H/V ratio region (H/V < 1), where effective diffusion coefficients are almost constant; (ii) intermediate H/V ratio region (1 < H/V < 100), where the effective diffusion coefficient increases as the H/V ratio increases; (iii) high H/V ratio region (H/V > 100), where effective diffusion coefficients are comparable with the true diffusion coefficient, which is given by Eq. (3).

Obviously, the upper limit of the effective diffusion coefficient appears in the region (iii) and is equal to the true hydrogen diffusivity. The lower limit can be obtained when the majority of H atoms in a solid is trapped in the most stable state, which are V_1H_1 and V_1H_2 complexes having largest detrapping energy for trapped H atom. This condition is satisfied when the H/V ratio is sufficiently low, because a vacancy hardly traps more than two H atoms in such a system.

In order to evaluate the lower limit, we consider a system in which one H atom and one vacancy are contained. In this system, interaction between H atoms is totally eliminated and possible V-H interaction is only of V_1H_1 complex, which is consistent with the condition at which the lower limit is achieved. In a steady state of this system, the fraction of trapped H atoms (and the fraction of solute H atoms) are required to be constant. This condition can be formulated by equating the trap rate and the detrap rate, and the following equation is obtained for the fractions of solute H atoms (f_{solute}) as

$$f_{solute} = \Gamma_{detrap}/\left(\Gamma_{detrap} + 4c_{vacancy}\Gamma_{trap}\right) = 1/\left(1 + 4c_{vacancy} \times \exp(E_{binding}/kT)\right), \quad (4)$$

where Γ_{trap} (s^{-1}) and Γ_{detrap} (s^{-1}) are the rates of trap and detrap events per H atom, respectively, $c_{vacancy}$ is the vacancy concentration and $E_{binding}$ is the binding energy for H atom to a vacancy. Note that this resultant equation is almost identical to the classic McNabb and Forster formula [43] for the effective diffusion coefficient in the field of defects [44], except for the factor 4.

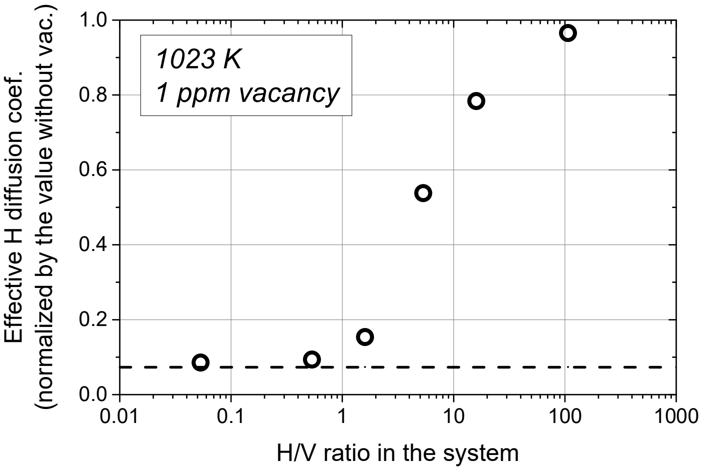

FIG. 3. KMC simulation results on effective hydrogen diffusivities as a function of H/V ratio. The temperatures and the vacancy concentrations are fixed at 1023 K and 1 ppm. This figure is reproduced using the data of Fig. 9 in [25].

FIG. 4 compares (i) the upper limit of the effective hydrogen diffusivity, which is given by Eq. (3) as the true hydrogen diffusivity in the bulk, (ii) the lower limit of the effective hydrogen diffusivity in systems where vacancies act as trap, which is given by Eq. (4), and (iii) available experimental results [44–51] other than the Frauenfelder's result [26]. Almost all the experimental data are encompassed by the upper and lower limits, although the spanned range is quite broad due to the large detrap energy for H atom in V_1H_1 complex (1.568 eV). Strictly speaking, the data given by Gasparyan et al. is smaller than the lower limit. However, this deviation is acceptably small considering possible errors and uncertainties in the present model: (i) Eq. (3) should contain some errors from the true hydrogen diffusivity, because it was derived from experimental data of a sole study [31]; (ii) V-H binding energies given by DFT should contain some errors; (iii) only vacancy is taken into account as a hydrogen trap in the present KMC simulation and simple trap/detrap models are utilized; (iv) the experimental data of Gasparyan is also not free of errors.

In experiments, the effective diffusivity of hydrogen is usually defined as a function of temperature, although it also depends on hydrogen concentration, trap concentration and trap type. The dependencies on hydrogen concentration and trap concentration basically become negligible at high temperatures. However, for a deep trap like vacancies, these dependencies cannot be neglected up to around 1500 K in bcc-W, as demonstrated in the present study. Therefore, it is reasonable to assume that H/V ratios in most previous experiments are of the intermediate H/V ratio region or of the low H/V ratio region given in FIG. 3. In the intermediate H/V ratio region, effective hydrogen diffusivities are very sensitive to experimental conditions, which would cause inconsistent results on effective hydrogen diffusivities in previous experiments.

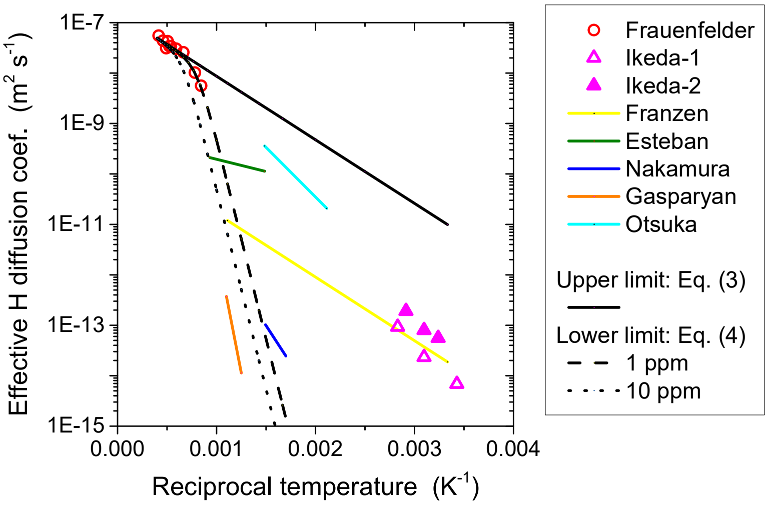

FIG. 4. Comparison between available experimental data and theoretical lower and higher limits of hydrogen diffusivity. The experimental data are taken from ref. [26] (Frauenfelder), ref. [46] (Ikeda-1), ref. [47] (Ikeda-2), ref. [48] (Franzen), ref. [49] (Esteban), ref. [50] (Nakamura), ref. [44] (Gasparyan), and ref. [51] (Otsuka). This figure is reproduced using the data of Fig. 10 in [25].

3.5 Conclusions

KMC simulations were performed to quantify the influence of trap in hydrogen diffusivity in bcc-W. As a typical trap, mono-vacancy is considered. In the KMC simulations, Frauenfelder's experimental results [26] were nicely reproduced when hydrogen and trap concentrations expected in the experiment were assumed in the simulation.

Those KMC results are consistent with the Heinola's interpretation [31] on the data of Frauenfelder's experiment: low-temperature data (< 1500 K) are largely affected by defects, and then the true coefficients are better derived if these data are excluded. Therefore, we recommend $D = 1.58 \times 10^{-7} \exp(-0.25\, eV/kT)$ m^2 s^{-1} as the equation for hydrogen diffusion coefficient in tungsten, which was derived by Heinola by fitting to high-temperature data of Frauenfelder's experiment [31], rather than the most cited equation $D = 4.1 \times 10^{-7} \exp(-0.39\, eV/kT)$ m^2 s^{-1}, which was derived by Frauenfelder by fitting to all the experimental data [26]. Since some influences of traps should be mixed up with in the original Frauenfelder's equation, its usage may cause a mis-estimation of trap influence. It should be noted that the recommended Heinola's equation also agrees well with DFT+TST calculation results [31], while the original Frauenfelder's equation does not.

4. EFFECTS OF GRAIN BOUNDARIES ON HYDROGEN SOLUBILITY / DIFFUSIVITY / PERMEABILITY IN TUNGSTEN [52]

4.1 Introduction

Among the lattice defects, grain boundary (GB) has been attracting increasing attention due to the importance of GBs in fine-grain W materials [53,54], which are expected to bring improved mechanical properties. Several computational studies were performed to uncover GB effects on the hydrogen behaviors in atomic scale [33,55–58]. Specifically, two methods of atomistic simulations have been applied to study the GB effects. One is first-principles calculation based on density functional theory (DFT), and the other is classical molecular dynamics (MD) method with two bond-order potential (BOP) models parameterized by Juslin et al. [59] and Li et al. [60]. DFT calculation was used to evaluate the stability and the mobility at/around specific GBs, including Σ5 tilt GB [33], Σ3 tilt GB [55] and W(110)/W(112) interface [56], while MD simulation was employed to find general trends of hydrogen stability and mobility in systems containing various types of GBs [57,58].

Despite the accumulation of detailed information on the GB effects thanks to atomistic simulations, the information has not been effectively utilized to interpret and analyze experimental results. One of the reasons of this is that quantities that can be determined by atomistic simulation such as the binding energy of H atom to GB are not simply reflected in quantities that can be obtained by experiment such as effective hydrogen solubility. This is because apparent effects of GBs depend on several parameters including grain size, hydrogen concentration, temperature, etc. In the present study, therefore, in order to systematically relate these two types of quantities, a thermodynamic model is constructed. This model enables us to calculate the effective solubility, diffusivity and permeability of hydrogen in poly-crystalline bcc-W equilibrated with surrounding H_2 gas, as a function of grain size, temperature and partial pressure of H_2 in the gas phase.

In Section (2), the framework of the thermodynamic model is introduced. The modeling procedure and the definition of model parameters are described. In Section (3), calculation results with the thermodynamic model on the effective solubility, diffusivity and permeability of hydrogen are presented with varying grain sizes. The calculation results are compared with available experimental data. In addition, since some model parameters involve non-negligible uncertainties at present, results of sensitivity analyses on such parameters are also provided. In Section (4), after discussing uncertainties in the model and model parameters, experimental studies that are expected to contribute to refining the model are suggested and implications to fusion engineering R&D are mentioned. Finally, the paper is closed with concluding remarks in Section (5).

4.2 Methods

4.2.1 Modeling of GB effects

In the present study, among several typical traps (vacancy, GB, surface, dislocation), only GB effects are focused on. Consequently, H atoms at the lattice sites and at GBs are only possible states of hydrogen in W in the present model, and the effective diffusivity (D_{eff}) can be expressed as

$$D_{eff} = f_{H-lat} D_{H-lat} + f_{H-GB} D_{H-GB}, \tag{5}$$

$$f_{H-lat} + f_{H-GB} = 1, \tag{6}$$

where, f_{H-lat} and D_{H-lat} are respectively the fraction of H atoms located in the lattice, which are tetrahedral interstitial sites in bcc-W, and the diffusivity of the H atoms in the lattice, and f_{H-GB} and D_{H-GB} are respectively the fraction of H atoms trapped by GBs and the diffusivity of the H atoms along GBs.

A schematic drawing of the potential energy curve for H atom assumed in the present study is shown in FIG. 5. $E_{sol-lat}$ corresponds to the solution energy of hydrogen at lattice site of bcc-W, $E_{dif-lat}$ is the diffusion barrier of hydrogen at lattice sites, $E_{bind-GB}$ is the binding energy of hydrogen at GB, and E_{dif-GB} is the diffusion barrier of hydrogen along GB.

To determine f_{H-lat}, the free energy of the system is expressed as a function of f_{H-lat}, and the free energy is minimized with respet to f_{H-lat}. This thermodynamic modeling gives the following expression for the effective solubility (S_{eff}, mol m^{-3} Pa$^{-0.5}$), effective diffuvitty (D_{eff}, m^2 s^{-1}) and effective permeability (P_{eff}, mol m^{-1} s^{-1} Pa$^{-0.5}$) of H atoms in polycrystalline W samples:

$$S_{eff} = \frac{1}{1 - f_{H-GB}} \times S_{H-lat} = \left\{ 1 + \frac{3\beta l_{lat}}{\alpha l_{grain} \exp\left(-E_{bind-GB} / RT\right)} \right\} \times S_{H-lat}, \tag{7}$$

$$D_{eff} = \left\{ 1 + \frac{3\beta l_{lat}\left(\left(D_{H-GB} / D_{H-lat}\right) - 1\right)}{3\beta l_{lat} + \alpha l_{grain} \exp\left(-E_{bind-GB} / RT\right)} \right\} \times D_{H-lat}, \tag{8}$$

$$P_{eff} = \left\{ 1 + \frac{3\beta l_{lat}\left(D_{H-GB} / D_{H-lat}\right)}{\alpha l_{grain} \exp\left(-E_{bind-GB} / RT\right)} \right\} \times P_{H-lat}, \tag{9}$$

where α is the number of tetrahedral interstitial sites in each conventional unit cell of bcc lattice, β is the number of GB sites on each {100} plane of the unit cell, l_{grain} [μm] is the size of the cubic grain, l_{lat} [μm] is the lattice constant of bcc-W (0.316×10^{-3} μm), $E_{bind-GB}$ is the effective binding energy of H atoms at GBs, S_{H-lat} is the solubility of hydrogen in the lattice, and P_{H-lat} is the permeability of H atoms in defect-free W. Based on the consideration of bcc-W structure, we determined α and β to be 12 and 2, respectively, and compared with available experimental data with changing the other uncertain paramters in the following range: 0.01~100 μm (10 μm) for l_{grain}, 0.5~1.4 eV (1.0 eV) for $E_{bind-GB}$, 0.2~1.0 eV (0.4 eV) for E_{dif-GB}, where the value in the parenthesis is the default value. More details are reported in elsewhere [52].

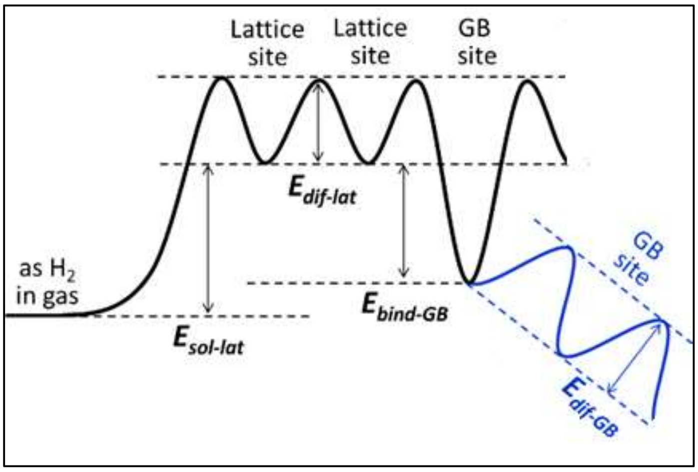

FIG. 5. Potential energy curve for H atom assumed in the present study. This figure is reproduced using the data of Fig. 1 in [52].

4.2.2 Experimental data for comparison

D_{eff} and P_{eff} calculated by the constructed thermodynamic model are compared with available experimental data in Section (3). Since the available data on S_{eff} is limited, such comparison is not made for it. The experimental data used in the comparisons are labelled with the author's name and the year of publication as follows:

- ✓ Diffusivity: Frauenfelder-1969 [26]; Zakharov-1975 [61]; Esteban-2001 [49]; Nakamura-2003 [50]; Otsuka-2009 [51]; Gasparyan-2009 [44]; Heinola-2010 [31]; Ikeda-PDP-2011 [47]; Ikeda-GDP-2011 [46].
- ✓ Permeability: Aitken-1967 [62]; Frauenfelder-1968 [63]; Frauenfelder-1969 [26]; Zakharov-1975 [61]; Benamati-2000 [64]; Esteban-2001 [49].

4.3 Results

4.3.1 GB effects in hydrogen solubility

FIG. 6 compares effective hydrogen solubility (S_{eff}) calculated with various grain sizes (l_{grain}). $E_{bind-GB}$ and E_{dif-GB} were fixed to be the reference values, 1.0 eV and 0.4 eV, respectively. Since the area of GBs increases as the grain size decreases, larger influence of GBs is observed in a smaller grain. The solubility in GB-free system,is presented by dash line and labelled with “GB-free”.

The slope of the temperature dependence of the solubility in the GB-free system corresponds to 1.18 eV, which is equal to the solution energy of H atoms at the lattice site ($E_{sol\text{-}lat}$). The slopes in poly-crystalline systems also converge to 1.18 eV at high temperatures. This is because the entropy effect causes a higher fraction of H atoms to stay in the lattice sites at a higher temperature, and then H atoms in the lattice sites becomes the dominant state at sufficiently high temperatures. On the other hand, at low temperatures, the slopes converge to $E_{sol\text{-}lat} - E_{bind\text{-}GB}$, which is the energy difference between H atom trapped by GB and H atom composing H_2 molecule in the gas phase. For example, the slope in l_{grain} = 10 μm case is around 0.18 eV below 600 K, as $E_{sol\text{-}lat} - E_{bind\text{-}GB}$ = 1.18 eV – 1.0 eV = 0.18 eV. This low temperature behavior indicates that the dominant hydrogen state at low temperatures is H atoms trapped by GBs in poly-crystalline W.

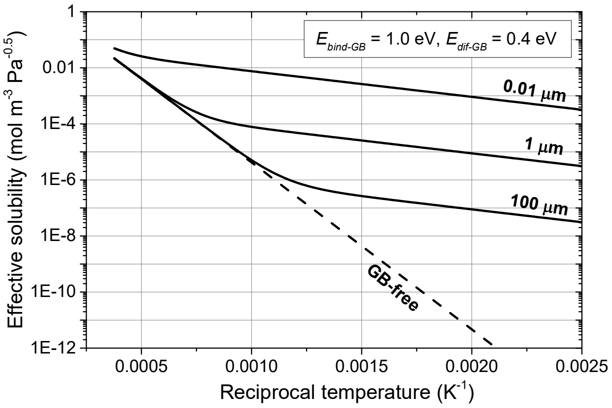

FIG. 6. Comparison of effective hydrogen solubility (S_{eff}) calculated with various grain sizes (l_{grain}). This figure is reproduced using the data of Fig. 3 in [52].

4.3.2 GB effects in hydrogen diffusivity

FIG. 7 compares effective hydrogen diffusivity (D_{eff}) calculated with various grain sizes (l_{grain}). $E_{bind\text{-}GB}$ and $E_{dif\text{-}GB}$ were fixed to be the reference values. The data of the GB-free system is given with dash line and labelled “GB-free”, which corresponds to the diffusivity in singe-crystal W of the infinite size. As a general trend in FIG. 7, effects of GBs are more pronounced for smaller grain sizes because more GB sites are involved in the system.

In comparison with trap effects by vacancy, the reduction of effective diffusivity caused by GBs is much smaller than that by vacancy [25]. This is because H trapped at GBs can still diffuse in the system along GBs. In a general trend, D_{eff} converges to $D_{H\text{-}lat}$ at high temperatures unless the grain size is very small like 0.01~0.1 μm, while it converges to $D_{H\text{-}GB}$ at low temperatures. This trend is due to the entropy effect.

The model with $E_{dif\text{-}GB}$ = 0.4 eV nicely reproduces the effective diffusivity of some experiments, specifically Otsuka-2009, Ikeda-PDP-2011 and Ikeda-GDP-2011. In these experiments, the diffusivity was determined at low temperatures (around 300~700 K) [46,47,51], where the dominant diffusion mechanism is the diffusion along GBs as shown in FIG. 7. Therefore, it is more appropriate to assign the diffusivity of Otsuka-2009, Ikeda-PDP-2011 and Ikeda-GDP-2011 to the diffusivity along GBs ($D_{H\text{-}GB}$), not to that in the lattice ($D_{H\text{-}lat}$).

Even with 1 mm or 1 cm grain, D_{eff} is largely affected by GBs below 600 K and becomes almost equal to $D_{H\text{-}GB}$ below 500 K. The grain size of 1~10 mm is comparable with that of commercially available single-crystals. DFT calculation on a W surface indicated that the migration barrier for hydrogen diffusion on (100) surface is 0.43 eV [65], which is comparable with the reference value of $E_{dif\text{-}GB}$ (0.4 eV), and the binding energy to the same surface is 1.86 eV [65], which is larger than the reference value of $E_{bind\text{-}GB}$ (1.0 eV). Therefore, even if a single-crystal is used in experiments, hydrogen diffusion on the surface would largely contribute to D_{eff} unless hydrogen diffusion through the surfaces of side planes is avoided. It seems that determining $D_{H\text{-}lat}$ in experiments is technically difficult at low temperatures like below 600 K, which is basically due to the large positive solution energy for hydrogen in W lattice.

Regarding the diffusivity of Zakharov-1975, Nakamura-2003 and Gasparyan-2009, it is more appropriate to relate these results with other deeper traps like vacancy than with GBs. Indeed, the authors of Nakamura-2003 and Gasparyan-2009 pointed out possible influence of traps in their results [44,50]. In addition, effects of vacancy-type trap can nicely explain the deviation of these data from Eq. (3), especially for Zakharov-1975 [38] and Gasparyan-2009 [25]. On the other hand, Esteban-2001 cannot be explained with the present model nor with the vacancy model [25]. In order to explain Estenban-2001, we may need to construct a more sophisticated model, for example, like a model to consider both GB effects and vacancy-type trap effects simultaneously, which is a subject for future study.

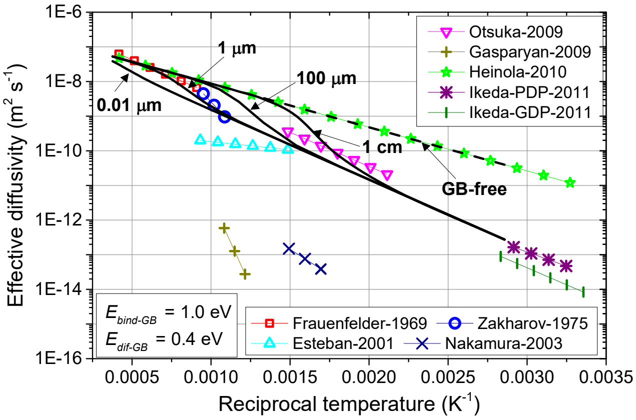

FIG. 7. Comparison between effective hydrogen diffusivity (D_{eff}) calculated with various grain sizes (l_{grain}) and experimental results. Marks on lines of experimental results are used for visualization purpose and are not measured data points of experiments. This figure is reproduced using the data of Fig. 6 in [52].

4.3.3 Detailed comparison with Frauenfelder-1969

The diffusivity of Frauenfelder-1969 [26] has been most widely utilized in previous studies as hydrogen diffusivity in the lattice of bcc-W, namely $D_{H\text{-}lat}$. It is expressed by Eq. (2)

Our previous study using KMC simulation, which is described in Section 2, confirmed that two low-temperature data points in Frauenfelder's experiment [26] could be affected by vacancy-type traps [25], as suggested by Heinola et al. [31]. One may think that the deviation of the low-temperature data points in the Frauenfelder's experiment may be also explained by GB effect. FIG. 8 shows detailed comparison between the measured data points of Fraunfelder-1969 and the calculation results obtained with l_{grain} = 0.1 μm, 1 μm or 10 μm. $E_{bind\text{-}GB}$ and $E_{dif\text{-}GB}$ are fixed to be the reference values. The result of l_{grain} = 1 μm reasonably reproduces the deviation of the two low-temperature data points.

In the Fraunfelder's paper [26], a photo of crystal grains is presented with no scale, and the grain size in the experiment is not specifically described in the main body. Therefore, it is difficult to deepen the discussion more. Nevertheless, the present result reconfirms that the two low-temperature data in the Frauenfelder's study [26] are significantly affected by lattice defects, such as vacancy or/and GBs or/and else. And it is also confirmed that experimental data obtained at high temperatures like $T > 1500$ K are hardly affected by GB and by vacancy [25] unless the grain size is very small and unless the vacancy concentration is very high, respectively. Therefore, as proposed by Heinola et al. [31], excluding the two low-temperature data is appropriate to obtain the diffusivity of hydrogen in the lattice of W ($D_{H\text{-}lat}$). Accordingly, Eq. (3) should be a more appropriate equation for $D_{H\text{-}lat}$ than Eq. (2) derived in the Frauenfelder's paper [26].

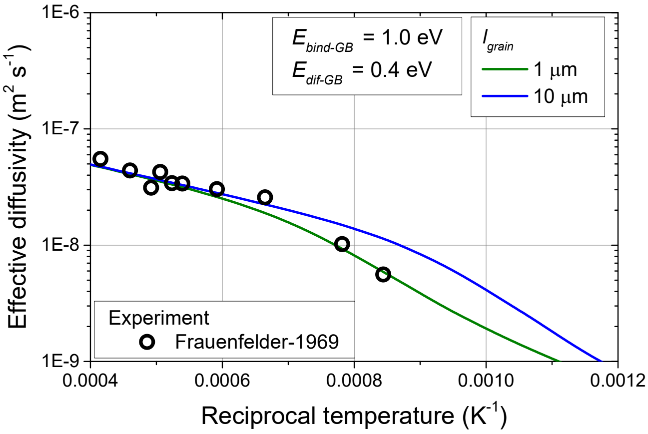

FIG. 8. Detailed comparison on effective hydrogen diffusivity between model calculation results and experimental data points of Frauenfelder-1969. This figure is reproduced using the data of Fig. 9 in [52].

4.3.4 GB effects in hydrogen permeability

FIG. 9 compares effective hydrogen permeability (P_{eff}) calculated with various grain sizes (l_{grain}). $E_{bind\text{-}GB}$ and $E_{dif\text{-}GB}$ were fixed to be the reference values. The data of the GB-free system is given with dash line and labelled "GB-free", which corresponds to the result in singe-crystal W of the infinite size. Roughly speaking, the GB effect is visible below around 1000 K for 10 μm grain and below around 1200 K for 1 μm grain. This result agrees with a trend in experimental data: experimental results at temperatures below around 1000-1200 K show some disagreement with each other, while those at higher temperatures show good agreement.

If a fine-grain material is used as a specimen, e.g. l_{grain} = 0.1 μm, the temperature where the GB effect becomes visible shifts to the higher temperature side and becomes unclear. In such a case, the activation energy for effective permeability may be evaluated to be smaller than 1.4 eV even at high temperatures.

The effective permeability is defined as the product of the effective solubility and the effective diffusivity. Therefore, if both effective solubility and effective diffusivity obey Arrhenius equations, the activation energy of the effective permeability is expressed as $E_{eff\text{-}P} = E_{eff\text{-}S} + E_{eff\text{-}D}$, where $E_{eff\text{-}S}$, $E_{eff\text{-}D}$ and $E_{eff\text{-}P}$ are respectively the activation energies in the effective solubility, diffusivity and permeability. Thus, in a temperature range where H atoms trapped at GBs dominantly contribute to the effective solubility and the effective diffusivity, the activation energy for the effective permeability is expected to converge to $E_{eff\text{-}P} = (E_{sol\text{-}lat} - E_{bind\text{-}GB}) + E_{dif\text{-}GB}$.

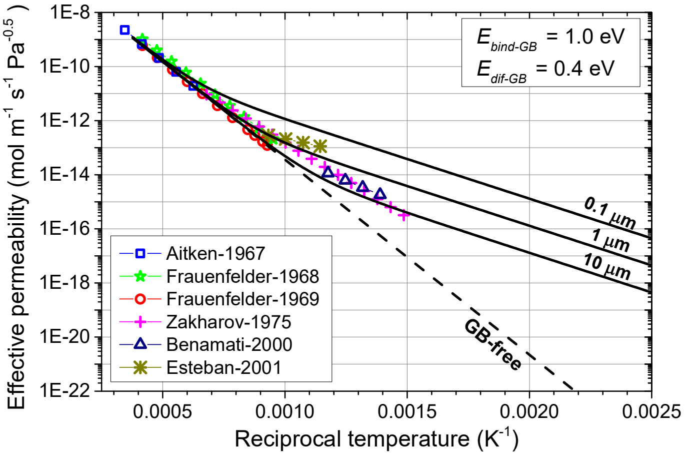

FIG. 9. Comparison between effective hydrogen permeability (P_{eff}) calculated with various grain sizes (l_{grain}) and experimental results. Marks on lines of experimental results are used for visualization purpose and are not measured data points of experiments. This figure is reproduced using the data of Fig. 10 in [52].

4.4 Discussion: Uncertainties in $E_{sol\text{-}lat}$, $E_{bind\text{-}GB}$, $E_{dif\text{-}lat}$ and $E_{dif\text{-}GB}$

By varing $E_{sol\text{-}lat}$, $E_{bind\text{-}GB}$, $E_{dif\text{-}lat}$ and $E_{dif\text{-}GB}$ and comparing the calculation results with the experimental data, we suggest the most likely values and estimated uncertainties for $E_{sol\text{-}lat}$, $E_{bind\text{-}GB}$, $E_{dif\text{-}lat}$ and $E_{dif\text{-}GB}$ as in TABLE 2, assuming that the four quantities ($E_{sol\text{-}lat}$, $E_{bind\text{-}GB}$, $E_{dif\text{-}lat}$ and $E_{dif\text{-}GB}$) are constant and independent of experimental conditions such as temperature, hydrogen concentration, etc. If this is not the case, the uncertainties in these quantities would be larger than what was estimated in TABLE 2.

More details are presented in [52].

TABLE 2. MOST LIKELY VALUES AND UNCERTAINTIES FOR $E_{sol\text{-}lat}$, $E_{bind\text{-}GB}$, $E_{dif\text{-}lat}$ and $E_{dif\text{-}GB}$. THIS TABLE IS REPRODUCED USING THE DATA OF TABLE 4 IN [52].

	Most likely	Lower limit	Upper limit
$E_{sol\text{-}lat}$	1.17 eV	0.98 eV	1.27 eV
$E_{bind\text{-}GB}$	1.0 eV	0.8 eV	1.2 eV
$E_{dif\text{-}lat}$	0.25 eV	0.20 eV	0.39 eV
$E_{dif\text{-}GB}$	0.4 eV	0.3 eV	0.5 eV

4.5 Conclusions

In the present study, a thermodynamic model to evaluate effects of grain boundary (GB) on hydrogen behaviors in poly-crystalline W was established based on the equilibrium theory. With this model, the effective solubility, diffusivity and permeability of hydrogen in W equilibrated with surrounding H_2 gas are calculated as a function of grain size, temperature and H_2 partial pressure.

By setting 1.0 eV to the binding energy of hydrogen to GBs ($E_{bind\text{-}GB}$) and 0.4 eV to the diffusion barrier of hydrogen along GBs ($E_{dif\text{-}GB}$), the model reasonably reproduces experimental data on the effective diffusivity and permeability. These values ($E_{bind\text{-}GB}$ = 1.0 eV and $E_{dif\text{-}GB}$ = 0.4 eV) fairly agree with results obtained by atomistic simulations in previous studies. The uncertainties in the values were estimated to be around ±0.2 eV for $E_{bind\text{-}GB}$ and ±0.1 eV for $E_{dif\text{-}GB}$, respectively, in comparison with available experimental results.

Throughout the present study, it was confirmed that GBs significantly affect the hydrogen behaviors up to around 1000 K or higher in practical materials. Hence, the effects of GBs should be considered in analysis of experimental results and in prediction of tritium inventory and leakage in fusion reactors. Particularly for fine-grain materials, close attention needs to be paid to possible increases in the effective solubility and permeability.

The thermodynamic model constructed in the present study are expected to help analyze experimental data and then uncover GB effects.

ACKNOWLEDGMENTS

This research was supported by National R&D Program through the National Research Foundation of Korea (NRF) funded by the Ministry of Science, ICT & Future Planning (No. 2014M1A7A1A03045186) and by NRF under Nuclear Fusion Basic Research program. This work also was partially supported by the Ministry of Science, ICT and Future Planning of the republic of Korea under the Korean ITER project contract, and partially supported by the Brain Korea 21 PLUS Project (No. 21A20130012821).

Parts of this article are reprinted by permission from *J. Nucl. Mater.* **495**, 277 (2017) [Elsevier: 4450190756987*]; J. Nucl. Mater.* **467**, 439 (2015) [Elsevier: 4450191252068, 4450191083989]; and *Fusion Eng. Des.* **112**, 102 (2016) [4450191504343, 4450191410487].

REFERENCES

[1] JIN, Y., SONG, J.-M., ROH, K.-B., KIM, N.-K., ROH, H.-J., JANG, Y., ET AL., Observation of oversaturation-induced defect formation in tungsten irradiated by low energy deuterium ion, J. Korean Phys. Soc. **69** (2016) 518.

[2] JIN, Y., ROH, K.-B., SHEEN, M.-H., KIM, N.-K., SONG, J., KIM, Y.-W., ET AL., Enhancement of deuterium retention in damaged tungsten by plasma-induced defect clustering, Nucl. Fusion. **57** (2017) 126042.

[3] REDHEAD, P. A., Thermal desorption of gases, Vacuum. **12** (1962) 203.

[4] POON, M., HAASZ, A. A., DAVIS, J. W., Modelling deuterium release during thermal desorption of D+-irradiated tungsten, J. Nucl. Mater. **374** (2008) 390.

[5] BANISALMAN, M. J., PARK, S., ODA, T., Evaluation of the threshold displacement energy in tungsten by molecular dynamics calculations, J. Nucl. Mater. **495** (2017) 277.

[6] KINCHIN, G. H., PEASE, R. S., The Displacement of Atoms in Solids by Radiation, Reports Prog. Phys. **18** (1955) 301.

[7] NORGETT, M. J., ROBINSON, M. T., TORRENS, I. M., A proposed method of calculating displacement dose rates, Nucl. Eng. Des. **33** (1975) 50.

[8] SETYAWAN, W., SELBY, A. P., JUSLIN, N., STOLLER, R. E., WIRTH, B. D., KURTZ, R. J., Cascade morphology transition in bcc metals, J. Phys. Condens. Matter. **27** (2015) 225402.

[9] FIKAR, J., SCHÄUBLIN, R., Molecular dynamics simulation of radiation damage in bcc tungsten, J. Nucl. Mater. **386–388** (2009) 97.

[10] MASON, D. R., YI, X., KIRK, M. A., DUDAREV, S. L., Elastic trapping of dislocation loops in cascades in ion-irradiated tungsten foils, J. Phys. Condens. Matter. **26** (2014) 375701.

[11] JAN, R. V., SEEGER, A., Zur Deutung der Tieftemperatur-Elektronenbestrahlung von Metallen, Phys. status solidi. **3** (1963) 465.

[12] MAURY, F., BIGET, M., VAJDA, P., LUCASSON, A., LUCASSON, P., Frenkel pair creation and stage I recovery in W crystals irradiated near threshold, Radiat. Eff. **38** (1978) 53.

[13] WECHSLER, M. S., LIN, C., SOMMER, W. F., DAEMEN, L. U. L., FEGUSON, P. D., Standard Practice for Neutron Radiation Damage Simulation by Charged-Particle Irradiation, E 521-96, Annu. B. ASTM Stand. **12.02** (1996) 1.

[14] FERRONI, F., YI, X., ARAKAWA, K., FITZGERALD, S. P., EDMONDSON, P. D., ROBERTS, S. G., High temperature annealing of ion irradiated tungsten, Acta Mater. **90** (2015) 380.

[15] HATANO, Y., SHIMADA, M., ALIMOV, V. K., SHI, J., HARA, M., NOZAKI, T., ET AL.,

Trapping of hydrogen isotopes in radiation defects formed in tungsten by neutron and ion irradiations, J. Nucl. Mater. **438** (2013) S114.

[16] NORDLUND, K., WALLENIUS, J., MALERBA, L., Molecular dynamics simulations of threshold displacement energies in Fe, Nucl. Instruments Methods Phys. Res. Sect. B Beam Interact. with Mater. Atoms. **246** (2006) 322.

[17] PLIMPTON, S., Fast Parallel Algorithms for Short-Range Molecular Dynamics, J. Comput. Phys. **117** (1995) 1.

[18] DAW, M. S., BASKES, M. I., Embedded-atom method: Derivation and application to impurities, surfaces, and other defects in metals, Phys. Rev. B. **29** (1984) 6443.

[19] DERLET, P. M., NGUYEN-MANH, D., DUDAREV, S. L., Multiscale modeling of crowdion and vacancy defects in body-centered-cubic transition metals, Phys. Rev. B - Condens. Matter Mater. Phys. **76** (2007) 54107.

[20] BJÖRKAS, C., NORDLUND, K., DUDAREV, S., Modelling radiation effects using the ab-initio based tungsten and vanadium potentials, Nucl. Instruments Methods Phys. Res. Sect. B Beam Interact. with Mater. Atoms. **267** (2009) 3204.

[21] NORDLUND, K., GHALY, M., AVERBACK, R. S., CATURLA, M., DIAZ DE LA RUBIA, T., TARUS, J., Defect production in collision cascades in elemental semiconductors and fcc metals, Phys. Rev. B. **57** (1998) 7556.

[22] RYCROFT, C. H., <scp>VORO++</scp> : A three-dimensional Voronoi cell library in C++, Chaos An Interdiscip. J. Nonlinear Sci. **19** (2009) 041111.

[23] JUSLIN, N., WIRTH, B. D., Interatomic potentials for simulation of He bubble formation in W, J. Nucl. Mater. **432** (2013) 61.

[24] OLSSON, P., BECQUART, C. S., DOMAIN, C., Ab initio threshold displacement energies in iron, Mater. Res. Lett. **4** (2016) 219.

[25] ODA, T., ZHU, D., WATANABE, Y., Kinetic Monte Carlo simulation on influence of vacancy on hydrogen diffusivity in tungsten, J. Nucl. Mater. **467** (2015) 439.

[26] FRAUENFELDER, R., Solution and Diffusion of Hydrogen in Tungsten, J. Vac. Sci. Technol. **6** (1969) 388.

[27] JIANG, D. E., CARTER, E. A., Diffusion of interstitial hydrogen into and through bcc Fe from first principles, Phys. Rev. B. **70** (2004) 064102.

[28] SORESCU, D. C., First principles calculations of the adsorption and diffusion of hydrogen on Fe(100) surface and in the bulk, Catal. Today. **105** (2005) 44.

[29] LIU, Y. L., ZHANG, Y., LUO, G. N., LU, G. H., Structure, stability and diffusion of hydrogen in tungsten: A first-principles study, J. Nucl. Mater. **390–391** (2009) 1032.

[30] JOHNSON, D. F., CARTER, E. A., Hydrogen in tungsten: Absorption, diffusion, vacancy trapping, and decohesion, J. Mater. Res. **25** (2010) 315.

[31] HEINOLA, K., AHLGREN, T., Diffusion of hydrogen in bcc tungsten studied with first principle calculations, J. Appl. Phys. **107** (2010).

[32] SERRA, E., BENAMATI, G., OGORODNIKOVA, O. V, Hydrogen isotopes transport parameters in fusion reactor materials, J. Nucl. Mater. **255** (1998) 105.

[33] ZHOU, H.-B., LIU, Y.-L., JIN, S., ZHANG, Y., LUO, G.-N., LU, G.-H., Investigating behaviours of hydrogen in a tungsten grain boundary by first principles: from dissolution and diffusion to a trapping mechanism, Nucl. Fusion. **50** (2010) 025016.

[34] TERENTYEV, D., DUBINKO, V., BAKAEV, A., ZAYACHUK, Y., VAN RENTERGHEM, W., GRIGOREV, P., Dislocations mediate hydrogen retention in tungsten, Nucl. Fusion Lett. **54** (2014) 042004.

[35] OHSAWA, K., GOTO, J., YAMAKAMI, M., YAMAGUCHI, M., YAGI, M., Trapping of multiple hydrogen atoms in a tungsten monovacancy from first principles, Phys. Rev. B. **82** (2010) 184117.

[36] HEINOLA, K., AHLGREN, T., NORDLUND, K., KEINONEN, J., Hydrogen interaction with point defects in tungsten, Phys. Rev. B. **82** (2010) 94102.

[37] YOU, Y.-W. W., KONG, X.-S. S., WU, X.-B. B., XU, Y.-C. C., FANG, Q. F., CHEN, J. L., ET AL., Dissolving, trapping and detrapping mechanisms of hydrogen in bcc and fcc transition metals, AIP Adv. **3** (2013) 12118.

[38] FERNANDEZ, N., FERRO, Y., KATO, D., Hydrogen diffusion and vacancies formation in tungsten: Density Functional Theory calculations and statistical models, Acta Mater. **94** (2015)

307.
[39] ANDERL, R. A., HOLLAND, D. F., LONGHURST, G. R., PAWELKO, R. J., TRYBUS, C. L., SELLERS, C. H., Deuterium transport and trapping in polycrystalline tungsten, Fusion Technol. **21** (1992) 745.
[40] RASCH, K.-D., SIEGEL, R. W., SCHULTZ, H., Quenching and recovery investigations of vacancies in tungsten, Philos. Mag. A. **41** (1980) 91.
[41] AHLGREN, T., HEINOLA, K., JUSLIN, N., KURONEN, A., Bond-order potential for point and extended defect simulations in tungsten, J. Appl. Phys. **107** (2010).
[42] ZHU, D., ODA, T., Trap effect of vacancy on hydrogen diffusivity in bcc-Fe, J. Nucl. Mater. **469** (2016) 237.
[43] MCNABB, A., FOSTER, P. K., A New Analysis of the Diffusion of Hydrogen in Iron and Ferritic Steels, Trans. Metall. Soc. AIME. **227** (1963) 618.
[44] GASPARYAN, Y. M., GOLUBEVA, A. V, MAYER, M., PISAREV, A. A., ROTH, J., Ion-driven deuterium permeation through tungsten at high temperatures, J. Nucl. Mater. **390–391** (2009) 606.
[45] MATSUYAMA, M., MURAI, T., YOSHIDA, K., WATANABE, K., IWAKIRI, H., YOSHIDA, N., Studies on retention of tritium implanted into tungsten by ??-ray-induced X-ray spectrometry, J. Nucl. Mater. **307–311** (2002) 729.
[46] IKEDA, T., OTSUKA, T., TANABE, T., Determination of hydrogen diffusivity and permeability in W near room temperature applying a tritium tracer technique, J. Nucl. Mater. **415** (2011) S684.
[47] IKEDA, T., OTSUKA, T., TANABE, T., Application of tritium tracer technique to determination of hydrogen diffusion coefficients and permeation rate near room temperature for tungsten, Fusion Sci. Technol. **60** (2011) 1463.
[48] FRANZEN, P., GARCIA-ROSALES, C., PLANK, H., ALIMOV, V. K., Hydrogen trapping in and release from tungsten: Modeling and comparison with graphite with regard to its use as fusion reactor material [Internet], Journal of Nuclear Materials 1997 Feb Hydrogen trapping in and release from tungsten: Modeling and comparison with graphite with regard to its use as fusion reactor material [Internet];
[49] ESTEBAN, G. A., PERUJO, A., SEDANO, L. A., DOUGLAS, K., Hydrogen isotope diffusive transport parameters in pure polycrystalline tungsten, J. Nucl. Mater. **295** (2001) 49.
[50] NAKAMURA, H., SHU, W., HAYASHI, T., NISHI, M., Tritium permeation study through tungsten and nickel using pure tritium ion beam, J. Nucl. Mater. **313–316** (2003) 679.
[51] OTSUKA, T., HOSHIHIRA, T., TANABE, T., Visualization of hydrogen depth profile by means of tritium imaging plate technique: determination of hydrogen diffusion coefficient in pure tungsten, Phys. Scr. **T138** (2009) 014052.
[52] ODA, T., Thermodynamic model for grain boundary effects on hydrogen solubility, diffusivity and permeability in poly-crystalline tungsten, Fusion Eng. Des. **112** (2016) 102.
[53] KURISHITA, H., AMANO, Y., KOBAYASHI, S., NAKAI, K., ARAKAWA, H., HIRAOKA, Y., ET AL., Development of ultra-fine grained W–TiC and their mechanical properties for fusion applications, J. Nucl. Mater. **367–370** (2007) 1453.
[54] KURISHITA, H., ARAKAWA, H., MATSUO, S., SAKAMOTO, T., KOBAYASHI, S., NAKAI, K., ET AL., Development of Nanostructured Tungsten Based Materials Resistant to Recrystallization and/or Radiation Induced Embrittlement, Mater. Trans. **54** (2013) 456.
[55] XIAO, W., GENG, W. T., Role of grain boundary and dislocation loop in H blistering in W: A density functional theory assessment, J. Nucl. Mater. **430** (2012) 132.
[56] GONZÁLEZ, C., PANIZO-LAIZ, M., GORDILLO, N., GUERRERO, C. L., TEJADO, E., MUNNIK, F., ET AL., H trapping and mobility in nanostructured tungsten grain boundaries: a combined experimental and theoretical approach, Nucl. Fusion. **55** (2015) 113009.
[57] VON TOUSSAINT, U., GORI, S., MANHARD, A., HÖSCHEN, T., HÖSCHEN, C., Molecular dynamics study of grain boundary diffusion of hydrogen in tungsten, Phys. Scr. **T145** (2011) 014036.
[58] PIAGGI, P. M., BRINGA, E. M., PASIANOT, R. C., GORDILLO, N., PANIZO-LAIZ, M., DEL RÍO, J., ET AL., Hydrogen diffusion and trapping in nanocrystalline tungsten, J. Nucl. Mater. **458** (2015) 233.
[59] JUSLIN, N., ERHART, P., TRÄSKELIN, P., NORD, J., HENRIKSSON, K. O. E.,

NORDLUND, K., ET AL., Analytical interatomic potential for modeling nonequilibrium processes in the W–C–H system, J. Appl. Phys. **98** (2005) 123520.

[60] LI, X.-C., SHU, X., LIU, Y.-N., GAO, F., LU, G.-H., Modified analytical interatomic potential for a W–H system with defects, J. Nucl. Mater. **408** (2011) 12.

[61] ZAKHAROV, A. P., SHARAPOV, V. M., EVKO, E. I., Hydrogen permeability of polycrystalline and monocrystalline molybdenum and tungsten, Sov. Mater. Sci. **9** (1975) 149.

[62] AITKEN, E. A., BRASSFIELD, H. C., CONN, P. K., DUDERSTADT, E. C., FRYXELL, R. E., H mermeability in tungsten, Aitken, Trans. Met. Soc. AIME. **239** (1967) 1565.

[63] FRAUENFELDER, R., Permeation of Hydrogen through Tungsten and Molybdenum, J. Chem. Phys. **48** (1968) 3955.

[64] BENAMATI, G., SERRA, E., WU, C. H., Hydrogen and deuterium transport and inventory parameters through W and W-alloys for fusion reactor applications, J. Nucl. Mater. **283–287** (2000) 1033.

[65] HEINOLA, K., AHLGREN, T., First-principles study of H on the reconstructed W(100) surface, Phys. Rev. B - Condens. Matter Mater. Phys. **81** (2010) 1.

HYDROGEN ISOTOPE RETENTION IN TUNGSTEN IRRADIATED BY HEAVY ION IRRADIATION

M. SAKAMOTO[1], H. TANAKA[1], H. WATANABE[2], S. INO[1], M. TOKITANI[3]

[1]Plasma Research Center, University of Tsukuba,
Tsukuba, Ibaraki, Japan

[2]Research Institute for Applied Mechanics, Kyushu University,
Kasuga, Fukuoka, Japan

[3]National Institute for Fusion Science,
Toki, Gifu, Japan

Abstract

In this study, deuterium (D) retention in tungsten (W) irradiated with 2.4 MeV Cu^{2+} ions as surrogate of neutron irradiation has been investigated focusing on the effect of damage dose, dose rate and temperature during the damage production. A new desorption peak appeared at ~830 K in thermal desorption spectra due to the heavy ion irradiation, which is attributed to nano-voids and vacancy clusters. The D retention in W irradiated with 2.4 MeV Cu^{2+} ions increased with the damage dose up to 0.4 dpa and then saturated in the case of high dose rate. On the other hand, the D retention increased with the damage dose up to 2 dpa in the case of low dose rate. The D retention in the irradiated W significantly reduced by simultaneous annealing with irradiation.

1. INTRODUCTION

Tungsten (W) is a candidate material for plasma facing components of DEMO as well as divertor plates of ITER [1], because it has favorable properties such as a very low solubility for hydrogen (H) isotopes. However, surface condition of the plasma facing material is certainly changed by plasma-wall interaction (PWI) such as erosion, re-deposition and bubble formation. In addition to the surface modification, neutron irradiation produces trapping sites throughout the W bulk, leading to significant enhancement of tritium (T) retention in W. The increase in the T retention is a key concern for safety hazards and T economy in a future fusion reactor. The effect of defects that are induced by fission neutrons on H isotope retention have recently been investigated through the TITAN and PHENIX projects [2-5]. On the other hand, systematic parameter studies of the effect of defects produced by high energy ions on the H isotope retention have been done as surrogate of neutron irradiation [6-18]. The both studies are complementary and important to understand impact of fusion neutrons on T retention.

In this CRP report, H isotope retention in W irradiated with 2.4 MeV Cu^{2+} ions as surrogate of neutron irradiation are described focusing on the effect of damage dose, dose rate and temperature during the damage production.

2. EXPERIMENTAL

2.1. Sample

Recrystallized W with a purity is 99.99 wt.%. manufactured by A.L.M.T. Corp. (Japan) was used in this study. It was annealed at 2273 K for 1 h. The sample size was 10 x 10 mm^2 and 1 mm in thickness. The grain size is in the range of 10 μm to ~100 μm as shown in Fig. 1. Samples were mechanically polished to mirror-like finish before the annealing. The recrystallized W was used to reduce the intrinsic defects, since we focus on the damage creation and its effect on the hydrogen isotope retention.

The sample was irradiated with 2.4 MeV Cu^{2+} ions using a tandetron accelerator at the Research Institute for Applied Mechanics of Kyushu University. The irradiated area is about 8 mm in a diameter. The ion beam was expanded to cover the irradiated area. The damage dose was up to 4 dpa. Figure 2 shows damage profiles in W irradiated with 2.4 MeV Cu^{2+} ions at different doses, which is calculated using the SRIM code with displacement energy of 55 eV. The damage peak is around 0.4 μm. The depth of damaged zone increases with increase in the dose.

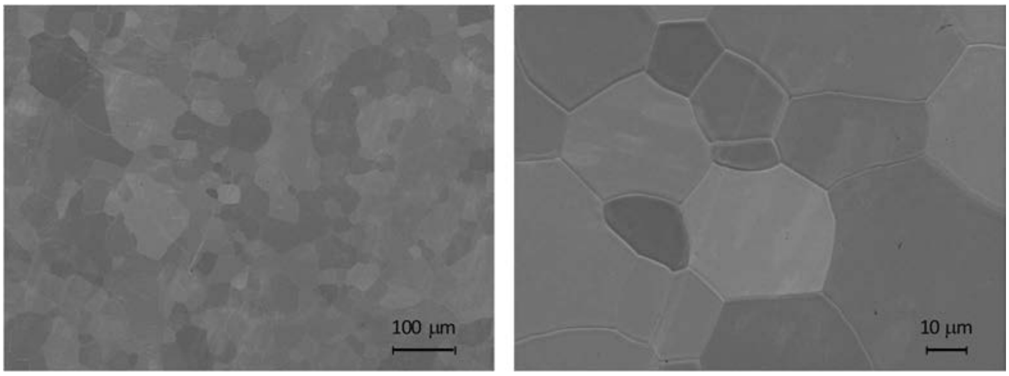

FIG. 1. SEM images of the surface of the recrystallized W which was annealed at 2273 K for 1 h. The grain size is in the range of 10 μm to ~100 μm. Reproduced with permission of the IAEA.

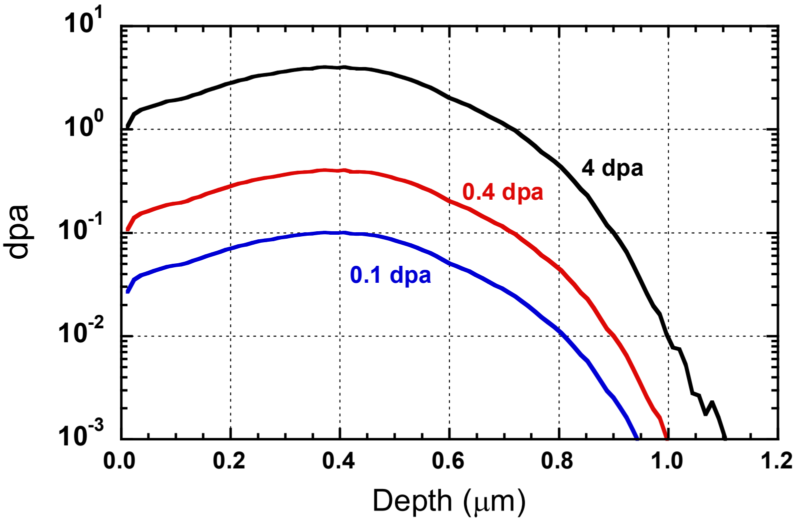

FIG. 2. SRIM calculation of the damaged profile in W irradiated with 2.4 MeV Cu^{2+} ions with different damage doses. Reproduced with permission of the IAEA.

2.2. Plasma exposure and thermal desorption spectrometry

Plasma exposure was carried out using a linear plasma device APSEDAS [19] in University of Tsukuba. Cylindrical plasma with the diameter of ~50 mm is produced by radio frequency wave of 13.56 MHz, which is supplied from an RF oscillator through a matching box to a helical antenna. A vacuum vessel and the antenna are also water-cooled. A target sample is fixed on a water-cooled sample holder by a 0.5 mm thick W disc with a hole of which diameter is 8 mm (i.e. exposed area). The sample holder is grounded.

The plasma parameters (i.e. electron density n_e, electron temperature T_e, plasma potential V_p) are measured using a Langmuir probe at 10 cm above the sample. Ion flux Γ_i to the sample was estimated by using n_e and T_e (i.e. $\Gamma_i = 0.61 n_e (kT_e/m_i)^{1/2}$), where k is Boltzmann constant and m_i is ion mass). Energy E_i of an incident ion to the sample is considered to be the same as V_p, since the sample was grounded. The typical plasma parameters in this study are $n_e \sim 3 \times 10^{17}$ m^{-3}, $T_e \sim 10$ eV and $E_i \sim 30$ eV. It is noted that the incident D^+ energy is too low to create additional trapping site in W.

After D plasma exposure, the sample is transferred to a small sample holder in an IR image furnace and then it is heated up in vacuum. A thermocouple is attached on the sample holder. The sample temperature during the heating is estimated from the thermocouple data and a calibration function which was evaluated from a result of a simultaneous measurement of the sample temperature and the sample holder one. D retention is measured using thermal desorption spectroscopy (TDS) with a quadrupole mass spectrometer (QMS). During TDS, the sample was heated at 1 K s^{-1} to 1127 K. The TDS system was calibrated by using a D_2 standard leak and/or a He standard leak just before heating the sample.

3. EXPERIMENTAL RESULTS AND DISCUSSION

Recrystallized W irradiated at a room temperature with 2.4 MeV Cu^{2+} ions of which flux was 5 x 10^{15} Cu^{2+} m^{-2} s^{-1} at a different damage dose (i.e. 0.1, 0.4, 4 dpa) and non-irradiated W (0 dpa) were exposed to low energy and high flux D plasma up to ~2 x 10^{25} D m^{-2} and then D retention in the sample was evaluated by TDS. The flux of D plasma exposure was ~3.7 x 10^{21} D m^{-2} s^{-1} and the surface temperature during the plasma exposure was ~480 K. Figure 3 shows thermal desorption spectra of D from the W samples. Two desorption peaks exist at ~520 K and ~690 K for the non-irradiated W. As for the irradiated W, on the other hand, three desorption peaks exist at ~510 K, ~700 K and ~830 K. The peak at ~830 K appeared newly by the heavy ion irradiation. Such three stages of desorption from damaged W were observed in other devices [e.g. 10, 12, 15, 18]. TEM observation of another W sample irradiated with 2.4 MeV Cu^{2+} ions revealed that interstitial dislocation loops, nano-voids and fine vacancy clusters existed beneath the surface [12]. It is considered that the new peak at the highest temperature (~ 860 K) is attributed to nano-voids and vacancy clusters.

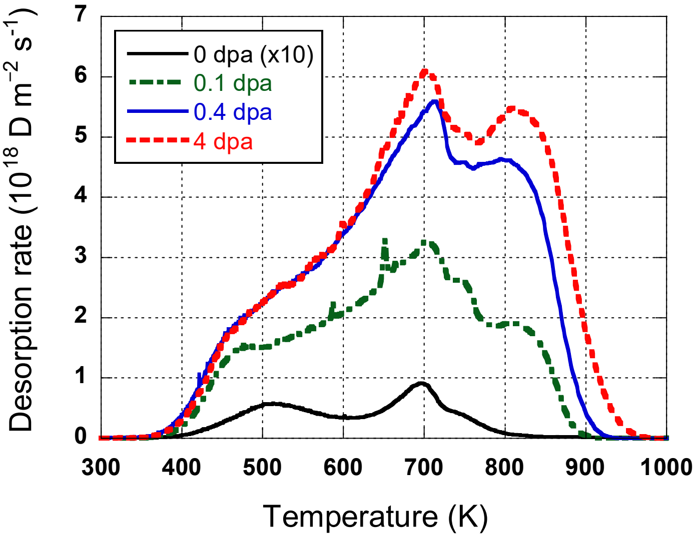

FIG. 3. Comparison of thermal desorption spectra of D from W samples damaged with three damage doses and without damage. Reproduced with permission of the IAEA.

Figure 4 shows thermal desorption spectra of D from W samples that were irradiated with 2.4 MeV Cu^{2+} ions at low and high dose rates of which ion fluxes were 1 x 10^{15} Cu^{2+} m^{-2} s^{-1} and 5 x 10^{15} Cu^{2+} m^{-2} s^{-1}, respectively. The damage dose of the both samples is 0.4 dpa. The data of high flux irradiation is the same as that of Fig. 3(a). The desorption spectrum of the low flux irradiation also consists of three stages of desorption of which peak temperatures are ~460 K, ~630K and ~780 K, respectively. Each peak temperature becomes lower than that for the high flux irradiation. Besides, D retention becomes 3.5 times lower than that for the high flux irradiation.

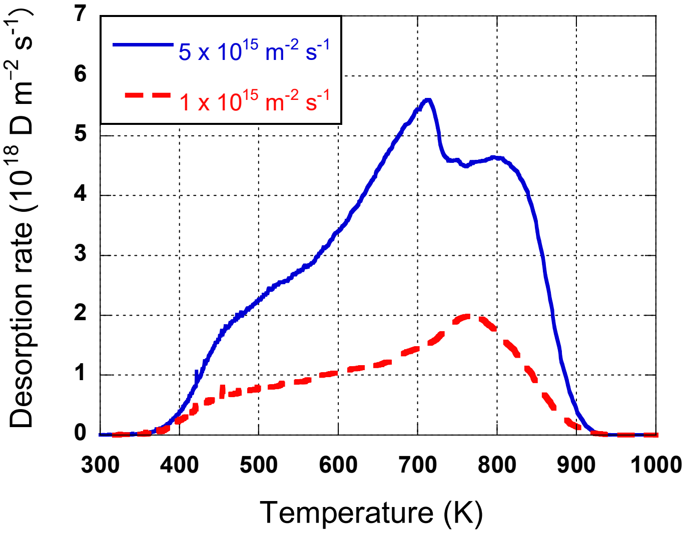

FIG. 4. Comparison of thermal desorption spectra of D from W samples damaged with the Cu^{2+} flux of 1 x *10^{15} ions m^{-2} s^{-1} and 5* x *10^{15} ions m^{-2} s^{-1}. The damage dose of the both samples is 0.4 dpa. Reproduced with permission of the IAEA.*

As shown in Fig. 5, D retention in the irradiated W increases with the damage dose but it saturates around 0.4 dpa in the case of the high dose rate (5 x 10^{15} Cu^{2+} m^{-2} s^{-1}). The saturation of D retention was observed in other experiments [15, 18]. The dpa dependence of the D retention for the high dose rate is consistent with their observations. It is suggested that newly introduced defects may be cancelled by already existing vacancies and voids with high density. In the case of low dose rate (1 x 10^{15} Cu^{2+} m^{-2} s^{-1}), on the other hand, D retention increases with the damage dose up to 2 dpa.

These results suggest that defect formation due to heavy ion irradiation depends on not only a damage dose but also a damage dose rate. However, the dependence of D retention on the dose rate in this study differs from the result of another study [7], where D retention was not influenced by changing the average dose rate by three orders of magnitude. The mechanism of defect formation which depends on the damage dose rate in this study is a future work.

Figure 6(a) shows thermal desorption spectra of samples with the damage dose of 4 dpa, which were irradiated at a room temperature, 500 K and 873 K, respectively. The desorption rate decreased as a whole with the sample temperature during the irradiation and there is little change in each peak temperature of the thermal desorption spectra. The D retention for the sample temperature of 500K and 873 K decreased by 60 % and 80 %, respectively, indicating a significant effect of simultaneous annealing with irradiation on D retention. As reported in [12], no remarkable changes in the microstructure of W annealed after irradiation were observed up to 873 K from TEM observation of interstitial-type dislocation loops and cascade-induced nano-voids formed by 2.4 MeV Cu^{2+} ion irradiation. It is suggested that the simultaneous annealing with irradiation is effective for suppressing production of defects leading to reduce the D retention.

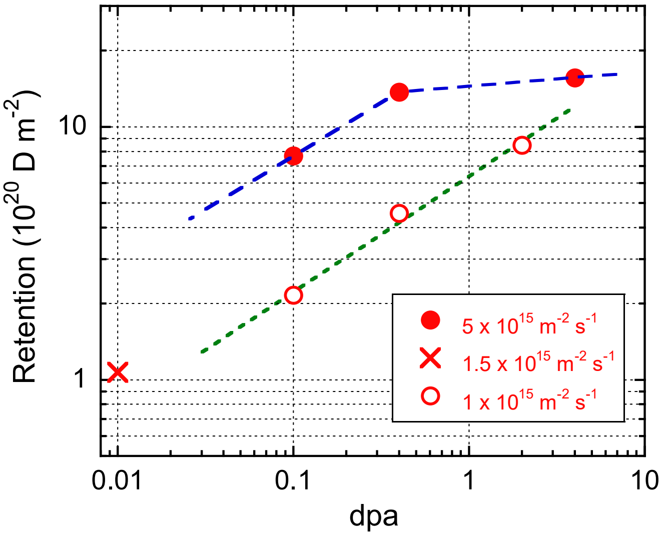

FIG. 5. Dependence of retention in the W samples on the damaged level for high and low Cu^{2+} irradiation. The broken lines are plotted to guide the eye.

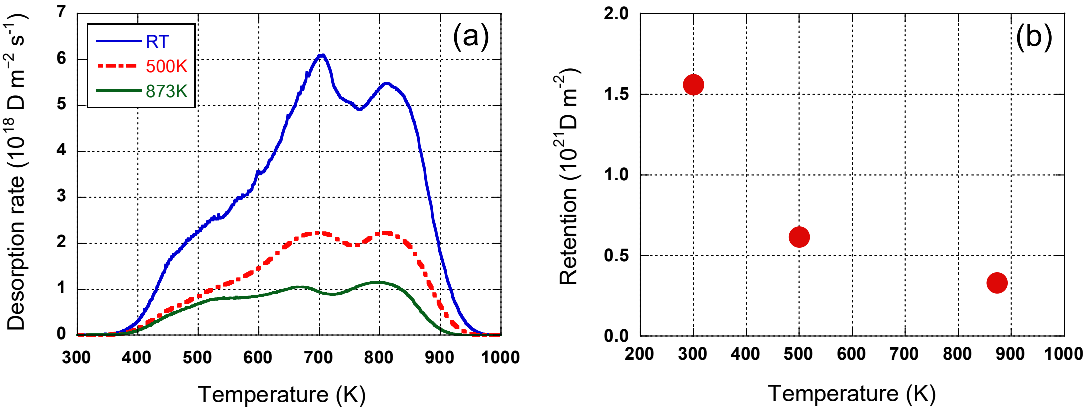

FIG. 6. (a) Comparison of thermal desorption spectra of D from W samples which were irradiated by Cu^{2+} at room temperature, 500 K and 873 K, respectively. (b) D retention as a function of a temperature during Cu^{2+} irradiation.

4. SUMMARY

Deuterium retention in W samples irradiated by 2.4 MeV Cu^{2+} ions has been investigated to study effects of the damage on hydrogen isotope retention in W. The damaged samples were exposed to low energy and high flux D plasma with a linear plasma device APSEDAS and then D retention was evaluated with TDS.

A new D desorption peak appeared at ~830 K in thermal desorption spectra, which is considered to be attributed to nano-voids and vacancy clusters from TEM observation. The D retention in the irradiated W increased with the damage dose but it saturates around 0.4 dpa in the case of high dose rate (5 x 10^{15} Cu^{2+} m^{-2} s^{-1}). On the other hand, the D retention increased with the damage level up to 2 dpa and no saturation was observed. It is suggested that defect formation due to heavy ion irradiation depends on not only a damage level but also flux of the high energy ions. Simultaneous annealing with irradiation seems to be effective to reduce D retention in W.

ACKNOWLEDGEMENTS

This work was performed with the support and under the auspices of the NIFS Collaboration Research program (NIFS14KUTR106, NIFS14KUGM098) and was also supported by JSPS KAKENHI Grant Number JP26289352.

REFERENCES

[1] PITTS, R.A., CARPENTIER, S., ESCOURBIAC, F., HIRAI, T., KOMAROV, V., LISGO, S., KUKUSHKIN, A.S., LOARTE, A., MEROLA, M., SASHALA NAIK, A., MITTEAU, R., SUGIHARA, M., BAZYLEV, B., STANGEBY, P.C., A full tungsten divertor for ITER: Physics issues and design status, J. Nucl. Mater. **438** (2013) S108.

[2] OYA, Y., SHIMADA, M., KOBAYASHI, M., ODA, T., HARA, M., WATANABE, H., HATANO, Y., CALDERONI, P., OKUNO, K., Comparison of deuterium retention for ion-irradiated and neutron-irradiated tungsten, Phys. Scr. **T145** (2011) 014050.

[3] HATANO, Y., SHIMADA, M., OTSUKA, T., OYA, Y., ALIMOV, V. Kh., HARA, M., SHI, J., KOBAYASHI, M., ODA, T., CAO, G., OKUNO, K., TANAKA, T., SUGIYAMA, K., ROTH, J., TYBURSKA-PÜSCHEL, B., DORNER, J., YOSHIDA, N., FUTAGAMI, N., WATANABE, H., HATAKEYAMA, M., KURISHITA, H., SOKOLOV, M. A., KATOH, Y., Deuterium trapping at defects created with neutron and ion irradiations in tungsten, Nucl. Fusion **53** (2013) 073006.

[4] SHIMADA, M., CAO, G., OTSUKA, T., HARA, M., KOBAYASHI, M., OYA, Y., HATANO, Y., Irradiation effect on deuterium behaviour in low-dose HFIR neutron-irradiated tungsten, Nucl. Fusion **55** (2014) 013008.

[5] SHIMADA, M., OYA, Y., BUCHENAUER, D. A., HATANO, Y., Hydrogen isotope retention and permeation in neutron-irradiated tungsten and tungsten alloys under PHENIX Collaboration, Fusion Sci. Technol. **72** (2017) 652.

[6] FUJITA, H., UEMURA, Y., SAKURADA, S., AZUMA, K., ZHOU, O., TOYAMA, T., YOSHIDA, N., HATANO, Y., CHIKADA, T., OYA, Y., The damage depth profile effect on hydrogen isotope retentionbehavior in heavy ion irradiated tungsten, Fusion Eng. Des. **125** (2017) 468.

[7] SCHWARZ-SELINGER, T., Deuterium retention in MeV self-implanted tungsten: Influence of damaging dose rate, Nucl. Mater. Energy **12** (2017) 683.

[8] OGORODNIKOVA, O. V., MARKELJ, S. and VON TOUSSAINT, U., Interaction of atomic and low-energy deuterium with tungsten pre-irradiated with self-ions, J. Appl. Phys. **119** (2016) 054901.

[9] GASPARYAN, YU.M., OGORODNIKOVA, O.V., EFIMOV, V.S., MEDNIKOV, A., MARENKOV, E.D., PISAREV, A.A., Markelj, S., CˇADEZ, I., Thermal desorption from self-damaged tungsten exposed to deuterium atoms, J. Nucl. Mater. **463** (2015) 1013.

[10] OYA, Y., LI, X., SATO, M., YUYAMA, K., ZHANG, L., KONDO, S., HINOKI, T., HATANO, Y., WATANABE, H., YOSHIDA, N., CHIKADA, T., Thermal desorption behavior of deuterium for 6 MeV Fe ion irradiated W with various damage concentrations, J. Nucl. Mater. 461 (2015) 336.

[11] OGORODNIKOVA, O.V., GANN, V., Simulation of neutron-induced damage in tungsten by irradiation with energetic self-ions, J. Nucl. Mater. **460** (2015) 60.

[12] WATANABE, H., FUTAGAMI, N., NAITOU, S., YOSHIDA, N., Microstructure and thermal desorption of deuterium in heavy-ion-irradiated pure tungsten, J. Nucl. Mater. 455 (2014) 51.

[13] OGORODNIKOVA, O.V., GASPARYAN, Y., EFIMOV, V., CIUPIN´ SKI, Ł., GRZONKA, J., Annealing of radiation-induced damage in tungsten under and after irradiation with 20 MeV self-ions, J. Nucl. Mater. **451** (2014) 379.

[14] ALIMOV, V.KH. HATANO, Y., TYBURSKA-PÜSCHEL, B., SUGIYAMA, K., TAKAGI, I., FURUTA, Y., DORNER, J., FUßEDER, M., ISOBE, K., YAMANISHI, T., MATSUYAMA, M., Deuterium retention in tungsten damaged with W ions to various damage levels, J. Nucl. Mater. **441** (2013) 280.

[15] TAKAGI, I., YAMAMICHI, K., FURUTA, Y., AKIYOSHA, M., SASAKI, T., TSUCHIDA, H., HATANO, Y., In situ observation of deuterium trapping in self-ion irradiated tungsten, J. Nucl. Mater. **442** (2013) S246.

[16] 'T HOEN, M.H.J., TYBURSKA-PÜSCHEL, B., ERTL, K., MAYER, M., RAPP, J., KLEYN, A.W. and ZEIJLMANS VAN EMMICHOVEN, P.A., Saturation of deuterium retention in self-damaged tungsten exposed to high-flux plasmas, Nucl. Fusion **52** (2012) 023008.

[17] WRIGHT, G.M., MAYER, M., ERTL, K., DE SAINT-AUBIN, G. and RAPP, J., Hydrogenic retention in irradiated tungsten exposed to high-flux plasma, Nucl. Fusion **50** (2010) 075006.

[18] TYBURSKA, B., ALIMOV, V.KH., OGORODNIKOVA, O.V., SCHMID, K., ERTL, K., Deuterium retention in self-damaged tungsten, J. Nucl. Mater. **395** (2009) 150.

[19] Sakamoto, M., Miyazaki, T., Higashizono, Y., Ogawa, K., Ozaki, K., Ashikawa, N., Tokitani, M., Shoji, T., Masuzaki, S., Tokunaga, K., Ohya, K., Sagara, A., Yoshida, N. and K N Sato, K.N., Surface modification of tungsten mirrors due to low-energy helium plasma irradiation in the compact PWI simulator APSEDAS, Phys. Scr. **T138** (2009) 014043.

CLUSTERING BEHAVIORS OF HELIUM, RHENIUM AND OSMIUM IN TUNGSTEN: A FIRST-PRINCIPLES INVESTIGATION

H.-B. ZHOU, G.-H. LU

Department of Physics, Beihang University, Beijing 100191, China
Beijing Key Laboratory of Advanced Nuclear Materials and Physics, Beihang University, Beijing 100191, China

Abstract

Tungsten (W) has been considered as the primary choice for plasma-facing materials (PFMs). Nevertheless, W will be exposed to low energy helium (He) plasma and high energy neutrons in a nuclear fusion environment, leading to the formation of He bubbles and Rhenium (Re)/Osmium (Os)-rich precipitation in W, which have serious negative effect on the properties of W. We have investigated the thermodynamic and kinetics behaviors of He/Re/Os in W employing a first-principles method, and revealed their clustering mechanism in W under fusion irradiated condition. Here, we review these studies.

1. INTRODUCTION

The successful achievement of fusion energy is strongly related to the availability of applicable materials [1-3]. Tungsten (W) has been considered as the primary choice for plasma-facing materials (PFMs), mainly owing to the high melting point, low sputtering erosion, and low hydrogen (H) isotopes and helium (He) retention [4-6]. However, in future fusion environment, W-PFM will be irradiated by the high heat flux, the deuterium-tritium (D-T) fusion neutrons as well as the low energy and high fluxes D/T/He plasma. Such excessive irradiated environment will remarkably influence the microstructures and properties of materials, resulting in the performance degradation. Therefore, the performance of W-PFM under irradiation and its effects on the properties of materials are the great concerns and have been investigated intensively [4-10].

Previous experiments observed the significant retention and prominent surface modification of W induced by low energy (< 100 eV) He plasma irradiation at different temperature, such as the formation of nano-bubbles and the fuzz nanostructures [9-12]. These surface morphology and He retention have detrimental effect on the long-term application of materials [9-12]. Interestingly, besides the He plasma irradiation, the irradiation of fusion neutrons can also apparently influence the behaviors of W. It is found that not only the cascade damage but also the transmutation reaction will be induced by high energy neutrons irradiation. So far, due to the unfeasible of the experimental identification for W-PFM in a fully realistic condition of fusion neutrons irradiation, the content of the transmutation elements (TEs) in W-PFM are primarily estimated by burn-up simulations [13-16]. Based on the recent computational results [15], rhenium (Re) and osmium (Os) are identified as the main production of transmutation in pure W, and their concentration reach 3.80 atomic% (at.%) and 1.38 at.%, respectively. Although the content of TEs is low, its effects on the properties of W should not be neglected. For example, the alloying of TEs will improve the ductility of W in irradiation-free condition and reduce the H isotopes retention under D plasma exposure [17-19]. More importantly, the Re/Os atoms will aggregate in W under high energy particles irradiation, forming the Re/Os-rich clusters and precipitates [20-23]. These clusters/precipitates exacerbate the irradiation hardening and embrittlement of W-PFM, severely decreasing the lifetime of materials.

Owing to the rapidly developing of algorithms and programing techniques, modeling and simulations become the effective tools to explore the performance and properties of materials under extreme conditions [24, 25]. Recently, employing the first-principles methods, our group have been systematically examined the behaviors of He and TEs in W. Here, we review these studies.

2. BEHAVIORS OF HE IN W

2.1. Influence of hydrostatic strain on the behaviors of He

Previous studies demonstrated that there is a very high pressure (up to several GPa) for He bubbles in W [26, 27], resulting in the serious distortion (strained) for W lattice nearby. Obviously, the presence of strained region in W will inevitably influence the behaviors of He, which may play a key role on the formation and growth of He bubbles. Therefore, employing the first-principles method, the dissolution and diffusion of He in strained W (hydrostatic strain) have been determined [28].

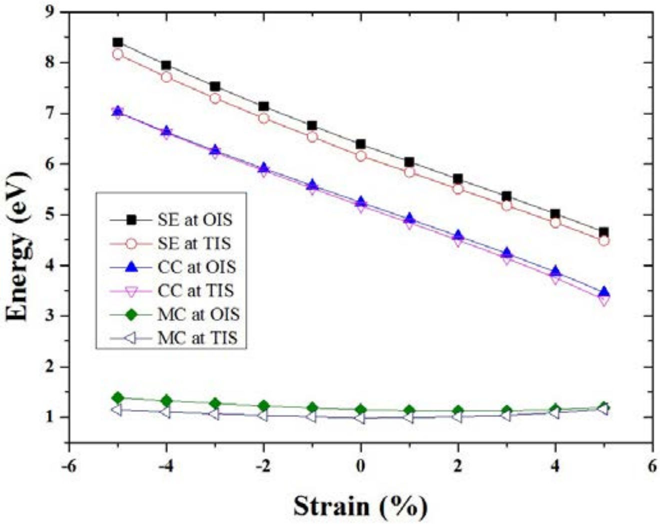

FIG. 1. Influence of hydrostatic strain on the solution energy of interstitial He in W. The corresponding mechanical contribution (MC) and electronical contribution (EC) are also given [28].

In order to determine the influence of hydrostatic strain on the behaviors of He, the solution energy of interstitial He in strained W have been examined [28]. The applied strain ranges from -5% (compressive strain) to 5% (tensile strain). As displayed in Fig.1, the solution energies of interstitial He show an evident linear correlation with the applied hydrostatic strain, in which it increases as the decreasing (increasing) of tension (compression). Namely, the He atom prefers to reside in the position in the tension region rather than that in the compression region. Besides, it should be noted that the He solution energies at the tetrahedral interstitial site (TIS) is lower compared to that at the octahedral interstitial site (OIS) in W, implying that the TIS is the preferable H-occupied position in comparison with OIS in strained W.

To illustrate the dissolution of interstitial He, the solution energy has been decomposed into the *mechanical contribution* (MC) and the *electronical contribution* (EC) [28]. The MC corresponds to the lattice distortion generated by the inserted He, while the EC is the electronical interaction of He with neighboring W atoms. Here, to calculate the MC for the He solution energy, one He atom is set at the interstitial site (TIS or OIS) and minimize the energy with fully relaxed condition. Then, the He atom is deleted, and the atomic positions are fixed to estimate the distortion energy induced by He (corresponding to the energy difference between the deformed system and the perfect system). As for EC, it can be obtained by the difference between the He solution energy and the MC. Similar with He solution energy, the EC almost linearly decreases (increases) as the tension (compression) increase, while the MC is almost invariable, suggesting that the influence of strain on the stability of He is largely dependent on the EC rather than the MC. This is due to the closed-shell structure for the electrons in He, resulting in the repulsive interaction of He with neighboring W atoms. Thus, the tensile strain will increase the atomic distance between He and W, weakening the repulsion of He-W and reducing the He solution energy.

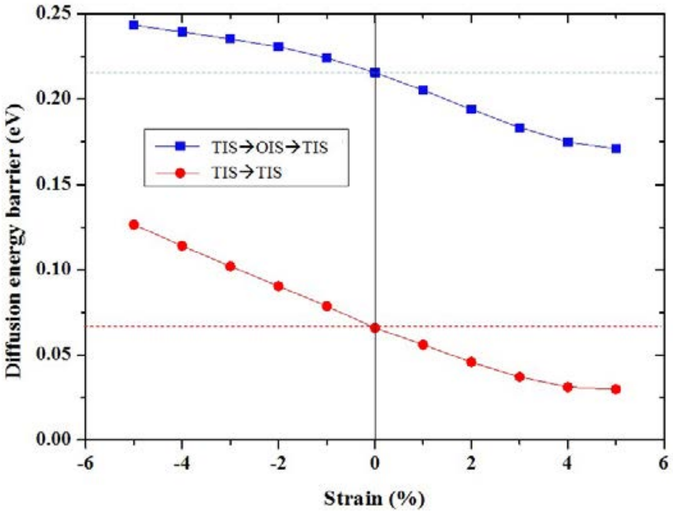

FIG. 2. Influence of hydrostatic strain on the diffusion energy barrier for interstitial He in W [28].

Next, the energy barriers for the diffusion of interstitial He in strained W have been investigated [28]. Here, two potential paths are considered. The first one is jumping from a TIS to a first nearest neighboring (1NN) TIS site directly (TIS→TIS), while the second path is the migration from a TIS to a 2NN TIS via the metastable OIS (TIS→OIS→TIS). As shown in Fig.2, the energy barriers for He diffusion through both TIS→TIS and TIS→OIS→TIS paths monotonically increase as the decreasing (increasing) of tensile (compressive) strain, suggesting that the tensile strain can enhance the migration of He. This is also due to the tensile strain can weaken the repulsion of He-W, reducing the migration energy barrier. Moreover, compared with the TIS→OIS→TIS, the TIS→TIS is the preferable migration path for He in strained W.

2.2. Effects of carbon on He behaviors

As one of the typical impurities in metals, carbon (C) always plays an important role on the microstructure evolution and performance of materials [29, 30]. Thus, it is expected that the presence of C can change the behaviors of He in W. Addressing this issue, we have further determined the interaction between C and He in W by calculating the clustering energy of them [31]. It has been found that the TIS and OIS is the preferred occupation for He and C in W, respectively. Therefore, the C atom resides in one OIS and the He atom is set at the different TIS. It can be found that the clustering energy of C-He pair is positive, indicating the attraction of C-He in W, and the strongest attraction corresponds to the interatomic distance of 2.32 Å with largest clustering energy ~ 0.41 eV. This suggests that C is the trapping center for isolated He atoms, which is due to the volume variation induced by C. It is found that the presence of C at OIS will result in the volume expansion of neighboring TISs, reducing the electron density of He-occupied position and decreasing the He solution energy.

Furthermore, the interactions of He with C in the vicinity of vacancy have also been investigated [31]. It is found that there is attraction between C and vacancy in W, indicating the formation of C-vacancy complex. Interestingly, the C-vacancy complex can substantially reduce the He solution energy nearby, implying the C-V cluster is the trapping center for He atoms. However, the trapping energy of C-free vacancy for He is much lower compared to that in C-vacancy complex. Besides, a C-vacancy complex only hold 5 He atoms in W, far below the maximum number of He atoms in C-free vacancy. Therefore, the presence of C weakens the capability of vacancy trapping for He.

2.3. Influence of Nb on the behaviors of He

Alloying is an effective method to enhance the performance of metals. As the typical alloying element in W, niobium (Nb) not only improve the mechanical properties but also influence the behaviors of He. Thus, the interactions of He with Nb in W have also been investigated [32]. Because of the Nb-induced variation of electron density induced, the interaction between interstitial He and substitutional Nb in W is attractive. The largest clustering energy of Nb-He in W can reach up to 0.37 eV, which occurs at the 1NN Nb-He distance. This suggest that the substitutional Nb is the trapping center for He atoms. Moreover, the energy barrier for the diffusion of interstitial He decreases as the interstitial He move close towards the substitutional Nb, indicating that the He atom can be easily trapped by Nb. Therefore, we propose that the alloying of Nb in W may contribute to the aggregation of He.

2.4. He at surfaces

According to previous studies, the damage region in W induced by low energy He ion/plasma irradiation is the near-surface zone (< 2 μm) [33, 34], which indicates that the effects of surface on the behaviors of He are very important. Thus, taking (110) surface (the most stable one with lowest surface energy within many surfaces) as an example, the dissolution and aggregation of He atoms in W surface have been examined [35]. Due to the repulsive interaction of He with W, both the surface and the subsurface (within the depth of 2.8 Å) in W cannot provide the stable occupations for He. After that, the H atom can be dissolved in W stably with the He solution energy of 6.10±0.05 eV, which is comparable with that in pure W. Besides, the interaction between He atoms in W surface is always attractive, and the clustering energy can reach up to ~1.0 eV at certain He-He distance (~ 1.5 Å), suggesting the aggregation of He atoms near the surface. It should be noted that the vacancy formation energy in W surface (~1.85 eV) is about 40% less than that in bulk(~ 3.07 eV), and thus the vacancy can be easily created due to the formation of He clusters, indicating the presence of He-vacancy complexes at the surface.

2.5. Mechanism of He self-trapping: Electrophobic interaction

As reported in previous studies [36, 37], the He atoms will aggregate in W spontaneously, leading to the formation of He clusters and creating the point defects, which is mainly responsible for the radiation damage and performance degradation of W-PFM under low energy He ion irradiation. The spontaneous clustering is a well-known phenomenon for noble gas elements (including He, Ne, Ar, etc.) in metals, and called self-trapping, while the physical mechanism for this interesting observation remains to be elucidated. Therefore, in analogy with the hydrophobic interaction in water, the electrophobic interaction in metals (or electron gas) has been proposed [38], providing a reasonable explanation for self-trapping of noble gas elements and also promoting the understanding of solutes/impurities dissolution in metals.

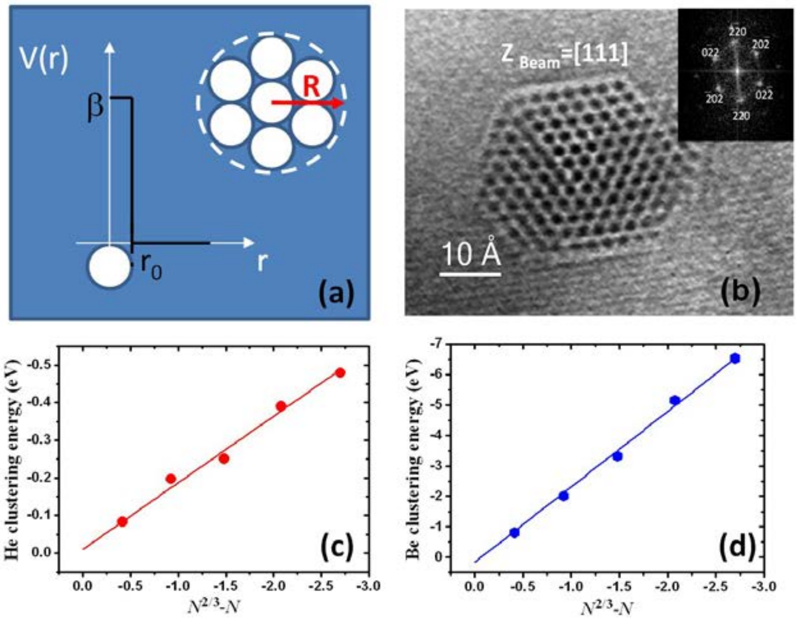

FIG. 3. (a) Schematics of the hard-sphere potential for the electrophobic solute in the homogeneous electron gas. The solute clusters shows the close-packed spherical structure (inset). (b) Experimental observation for the aggregation of Xe in Al. The clustering energy of (c) He and (d) Be in the homogeneous electron gas with the density of 0.08 e/Å^3 [38].

As mentioned above, the most distinctive character for noble gas elements is the closed-shell electronic structure, resulting in the repulsive interaction of noble gas elements with host atoms and leading to the high solution energy. To mimic this behavior, the dissolution and clustering of X (X denotes the noble gas elements) in a homogeneous electron gas have been considered firstly [38]. Here, as shown in Fig. 3a, the repulsion of X (with atomic radio of r_0) with electron media is approximated to the hard-sphere potential, namely $V(r)=\begin{cases}\beta, r=r_0\\ 0, r\geq r_0\end{cases}$, in which β is the repulsive factor of X. Based on the above models, the solution energy of X (E_X^{sol}) can be quantified by the factor β and the surface area of interactive region, $E_X^{sol}=(4\pi r_0^2)\beta$. Thus, for the dispersed distribution of X in the homogeneous electron gas, the total solution energy can be defined by $E_{NX}^{sol}=NE_X^{sol}=N(4\pi r_0^2)\beta$, where N is the number of X atoms. As for the state of X aggregated distribution, the corresponding solution energy ($E_{X_N}^{sol}$) can be simply obtained by $E_{X_N}^{sol}=(4\pi R^2)\beta$, where R is the effective radius of X clusters. From the observation of previous experimental study, the clustering of X shows the close-packed structure (see Fig. 3b), and the effective radio is approximately calculated by $R=\sqrt[3]{Nr_0^3}$. Therefore, the clustering energy of X ($E_{X_N}^c$) in electron gas is strongly related to the cluster size, being expressed as $E_{X_N}^c=E_{X_N}^{sol}-E_{NX}^{sol}\propto(N^{2/3}-N)$.

Fig. 3c shows the He clustering energy in the homogeneous electron gas (~ 0.08 e/Å^3) from the first-principles calculation. It is clearly found that the clustering energy of He can be well fitted by the analytical function derived above. Similar results can also be obtained for the clustering of Be in electron gas, as displayed in Fig. 3d, verifying the correctness of the hard-sphere model to describe the dissolution of noble gas elements in the electron gas. This suggests that the aggregation of noble gas atoms in the homogeneous electron gas is originated from the repulsive interaction of noble gas elements with electrons, i.e., the electrophobic interaction. This is also confirmed by the clustering energy of He_2 in vacuum and electron gas.

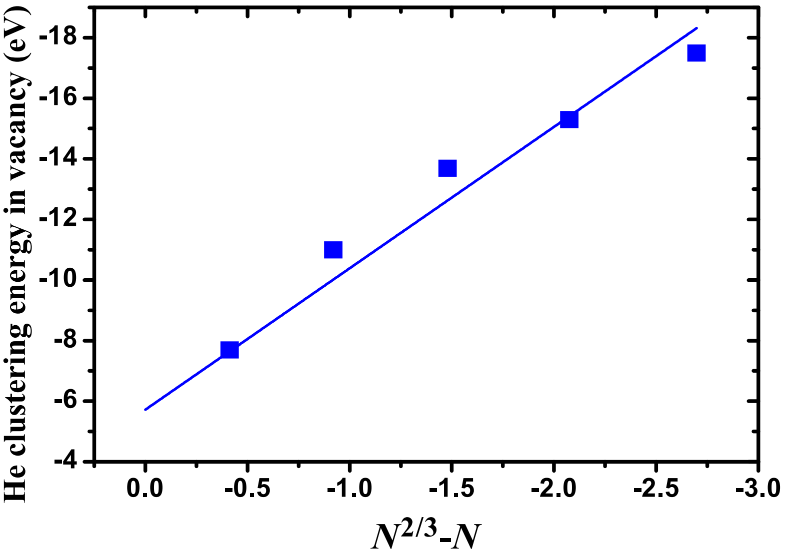

FIG. 4. The He clustering energy at a mono-vacancy in W [38].

Moreover, due to the low electron density nearby, the vacancy-type defects in metals are the strong trapping center for He. Thus, we further investigated the aggregation of He atoms surrounding a mono-vacancy in W. According to our calculation, the He clustering energies in a mono-vacancy are higher compared to that in defect-free system, because of the attraction of He with vacancy. More importantly, the He clustering energies in a mono-vacancy also follow the function derived above, namely $E^c \propto (N^{2/3} - N)$, as shown in Fig. 4. This unexpected result indicates that the electrophobic/electrophilic interaction is a general phenomenon, which provides a new insight into the dissolution of solutes in metals. Consequently, our calculations give the fundamental mechanism for the self-trapping of noble gas elements in metals and contribute to the materials design for W-PFM.

3. THE CLUSTERING BEHAVIOR OF RE AND OS IN W

3.1. Dissolution and aggregation of TEs in W

As discussed in *Section 1*, Re and Os are the main production of transmutation in W. Thus, the stabilities of Re/Os in pure W have been determined firstly by calculating the solution energies of them [39, 40]. It should be clarified that we only consider the substitutional occupation, due to the comparable atomic radius of W with Re/Os. Based on our calculation, the solution energy for a single substitutional Re in pure W is 0.19 eV, while that of a Os atom is 0.76 eV, suggesting that the dissolution of Re/Os is endothermic.

Then, to explore the atomic interactions of Re/Os atoms, we calculated the clustering energies of them [40]. Both the Re and Os atoms are located at the substitutional sites. As demonstrated in Fig. 5, the clustering energies for Re-Re/Os pairs are negative, implying the repulsion. On the contrary, the clustering energy of Os-Os is positive, indicating the attraction. Specifically, at the 1NN distance, the clustering energies for Re-Re, Re-Os and Os-Os pairs are -0.065 eV, -0.065 eV and 0.04 eV, respectively. After that, as the increasing of interatomic distance (except for Os-Os at ~ 4.5 Å), the interaction of Re/Os-Re/Os pairs will be gradually weakened, and the clustering energies converge to zero at ~ 5.5 Å.

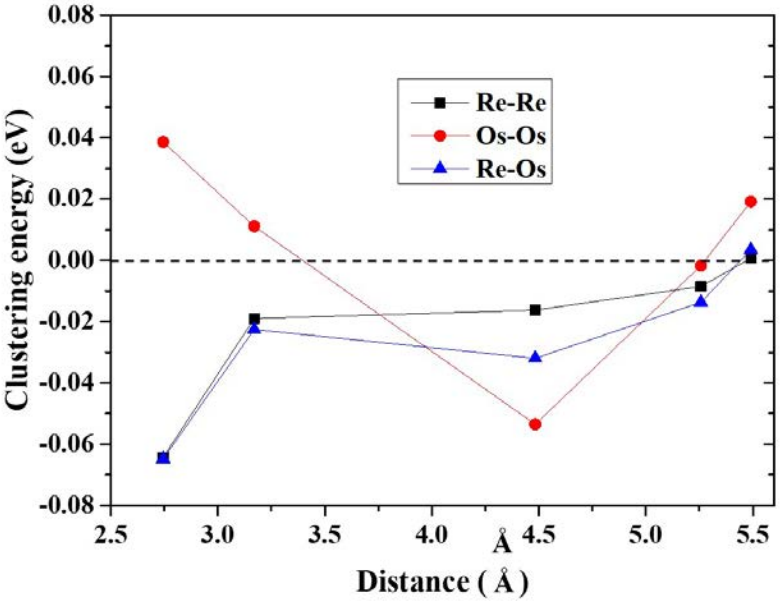

FIG. 5. The clustering energy of Re/Os-Re/Os pairs with different interatomic distance. Positive value represents the attractive interaction, while the negative ones denote repulsion [40].

Furthermore, to examine the interaction of multi TEs atoms, the clustering energies for TEs clusters (up to 7 atoms) in W have been calculated [40]. As displayed in Fig. 6, the clustering energies for Re (Os) clusters are negative (positive) and decrease (increase) with the cluster size increase, indicating that the Re atoms energetically prefer to dispersed separately, but Os is favorable to be aggregated in W. Besides, the variation of clustering energies become quicker with the cluster size increase. For instance, the clustering energy for Os-Os pair is ~ 0.04 eV, but that of Os_4 becomes ~ 0.30 eV.

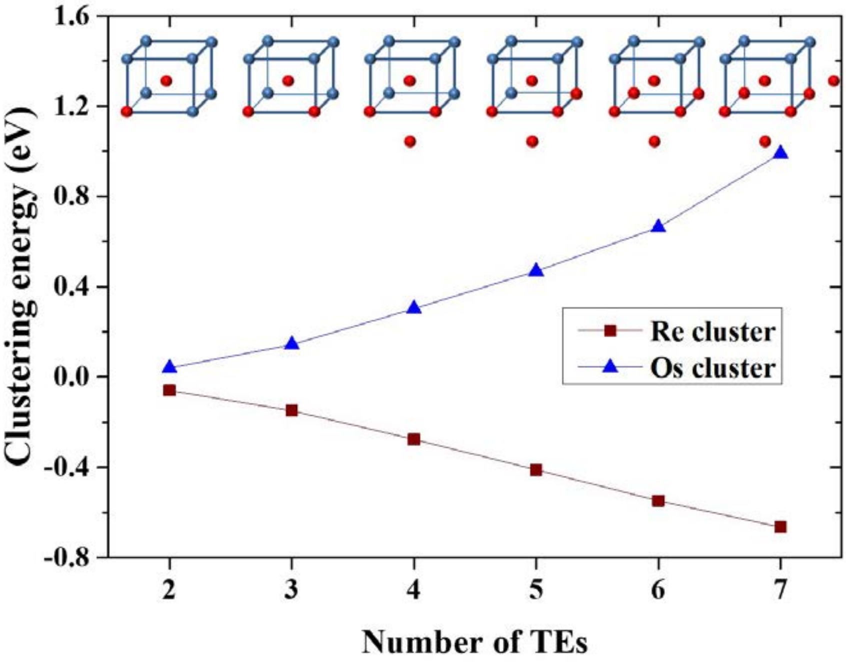

FIG. 6. The clustering energy of Re and Os clusters (up to 7 atoms) in W. The red and blue spheres indicate the TEs and W atoms, respectively [40].

3.2. Interaction of TE with point defects in W

Next, the interactions of Re/Os with point defects in W have been determined [41]. Table 1 displays the clustering energies and the interaction ranges of Re/Os-defect pairs, and the energy barriers for the segregation of point defects towards the Re/Os atom are also given. On the one hand, the clustering energy of Re-vacancy (Os-vacancy) pair is 0.24 eV (0.54 eV), far below that of Re-SIA (Os-SIA) with the clustering energy of 0.80 eV (1.82 eV). Moreover, as shown in Fig. 5, the Re-vacancy and Os-vacancy interactions are largely restricted within 2NN distance, containing the interaction range of 14 lattice points (8 for 1NN and 6 for 2NN). This is much smaller compared to the Re/Os-SIA pair, in which the total interaction range can reach up to 31/37 lattice points, respectively. On the other hand, the energy barrier for vacancy-mediated diffusion is larger compared to that of interstitial diffusion. As for the diffusion of SIA and Re/Os via interstitial-mediated method, the energy barrier is only 0.05 eV and 0.23/0.09 eV, respectively. Consequently, from above results, the Re/Os atoms are the trapping centers for the point defects in W, and more importantly, SIAs are favorably captured in comparison with vacancy both thermodynamically and kinetically.

TABLE 1. THE CLUSTERING ENERGIES AND THE INTERACTION RANGES OF RE/OS-DEFECTS (VACANCY OR SIA) PAIRS, AND THE ENERGY BARRIERS FOR THE POINT DEFECTS SEGREGATE TOWARDS RE/OS IN W. THE DIFFUSION ENERGY BARRIERS OF POINT DEFECTS IN PURE W ARE ALSO GIVEN. LPS DENOTES THE LATTICE POINTS [41].

		SIA	*Vacancy*
Re	Clustering energy (eV)	0.80	0.24
	Interaction range (LPs)	31	14
	Energy barrier for segregation (eV)	≤ 0.23	≥ 1.49
Os	Clustering energy (eV)	1.82	0.54
	Interaction range (LPs)	37	14
	Energy barrier for segregation (eV)	≤ 0.09	≥ 1.28
Diffusion energy barrier in bulk W (eV)		≤ 0.05	1.65

3.3. Interstitial-mediated aggregation of Re/Os in W

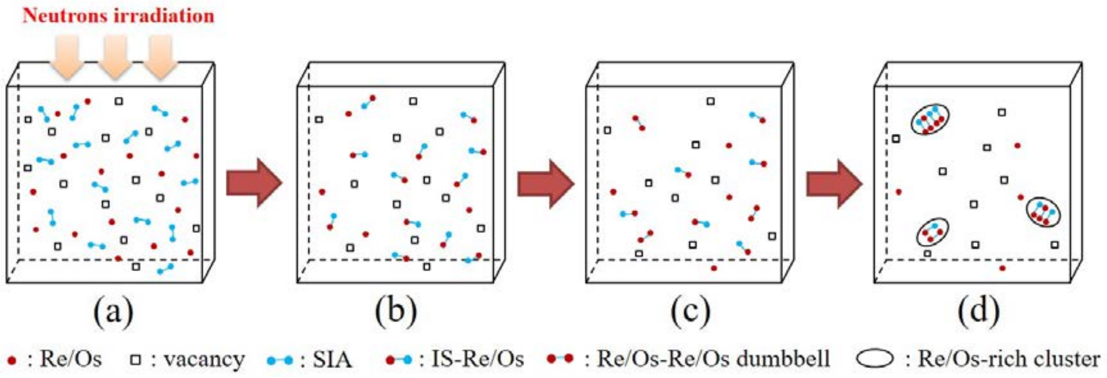

FIG. 7. Schematics of the interstitial-mediated mechanism reponsible for radiation-induced solute clustering in W-TEs alloys [41].

According to above calculations, we proposed a possible interstitial-mediated mechanism, which may be dominate the aggregation and precipitation of TEs in irradiated W [41], as displayed in Fig. 7. In the thermal equilibrium condition (without irradiation), the TEs have dispersed distribution in W-TEs alloys (see Fig. 7a). Once the materials are irradiated by high energy neutrons, a massive number of point defects (both vacancies and SIAs) are formed (see Fig. 7a). Due to the attraction with TEs and the low energy barrier, SIA is preferentially captured by substitutional TEs atom, leading to the formation of TEs-SIA (or IS-TEs) (see Fig. 7b). Owing to the low energy barrier, the motion of IS-TEs in W is very easy. Then, the substitutional TEs are the strong trapping centers for IS-TEs, producing the TEs-TEs dumbbell along <110> direction (see Fig. 7c). More importantly, IS-TEs will move towards the TEs-TEs dumbbell continuously, resulting in the further aggregation of TEs (see Fig. 7d). These processes provide a microscopic origin for the aggregation of TEs in irradiated W.

Although the proposed model is very simple, this mechanism will offer a plausible explanation to the experimental observations in recent studies. Based on the atom probe tomography method, the aggregation of TEs in irradiated W shows three distinctive characteristics clearly: (1) The clustering of Re in W is much faster compared to the aggregation of Os in same irradiated condition; (2) The presence of Os inhibit the formation of large Re clusters; (3) There are some mixed clusters (containing both Re and Os) in W-Re-Os ternary alloys under irradiation. Surprisingly, the above apparent characteristics will be rationally interpreted via the interstitial-mediated model. For example, due to the difference of diffusion energy barrier for IS-TEs (see table 1), the aggregation of Os in W should be slower than that of Re under same irradiated condition. Besides, compared with Re-SIA pair, the attraction of Os-SIA pair is much stronger, and thus the IS-Os can be preferentially formed, leading to the reduction of IS-Re and constraining the aggregation of Re. As for the third feature, it is ascribed to the attraction of Re/Os with defects, which suggests that Re and Os atoms will segregate towards defects, forming the mixed clusters.

4. CONCLUSION

In general, based on the first-principles calculation, the dissolution, diffusion and accumulation of He/Re/Os in W as well as the influence of defects and impurities are examined systematically. These results provide an important reference to understand the behaviors of W-PFM under fusion irradiated condition. However, due to the limitation by computational method, there are some restrictions in our current studies, especially for the temperature. Therefore, in future investigations, we will employ the different computational methods to explore the temperature-dependent microstructure evolution of W-PFM, such as the He bubbles formation and Re/Os precipitations, in different space-time scale, advancing the development of materials design.

ACKNOWLEDGEMENTS

This research is supported by the National Natural Science Foundation of China with Grant No. 11675011.

REFERENCES

[1] ZINKLE, S.J., WAS, G.S., Materials challenges in nuclear energy, Acta Mater. **61** (2013) 735-758.

[2] ZINKLE, S.J., BUSBY, J.T., Structural materials for fission & fusion energy, Mater. Today **12** (2009) 12-19.

[3] BARABASH, V., PEACOCK, A., FABRITSIEV, S., KALININ, G., ZINKLE, S., ROWCLIFFE, A., RENSMAN, J.-W., TAVASSOLI, A., MARMY, P., KARDITSAS, P., Materials challenges for ITER–Current status and future activities, J. Nucl. Mater. **367** (2007) 21-32.

[4] BOLT, H., BARABASH, V., KRAUSS, W., LINKE, J., NEU, R., SUZUKI, S., YOSHIDA, N., TEAM, A.U., Materials for the plasma-facing components of fusion reactors, J. Nucl. Mater. **329** (2004) 66-73.

[5] KNASTER, J., MOESLANG, A., MUROGA, T., Materials research for fusion, Nature Phys. **12** (2016) 424-434.

[6] SHU, W., WAKAI, E., YAMANISHI, T., Blister bursting and deuterium bursting release from tungsten exposed to high fluences of high flux and low energy deuterium plasma, Nucl. Fusion **47** (2007) 201.

[7] SEFTA, F., JUSLIN, N., WIRTH, B.D., Helium bubble bursting in tungsten, J. Appl. Phys. **114** (2013) 243518.

[8] HASEGAWA, A., TANNO, T., NOGAMI, S., SATOU, M., Property change mechanism in tungsten under neutron irradiation in various reactors, J. Nucl. Mater. **417** (2011) 491-494.

[9] SANDOVAL, L., PEREZ, D., UBERUAGA, B.P., VOTER, A.F., Competing kinetics and he bubble morphology in W, Phys. Rev. Lett. **114** (2015) 105502.

[10] SAKAMOTO, R., BERNARD, E., KRETER, A., YOSHIDA, N., Surface morphology of tungsten exposed to helium plasma at temperatures below fuzz formation threshold 1073 K, Nucl. Fusion **57** (2017) 016040.

[11] SHARAFAT, S., TAKAHASHI, A., HU, Q., A description of bubble growth and gas release of helium implanted tungsten, J. Nucl. Mater. **386** (2009) 900.

[12] KAJITA, S., SAKAGUCHI, W., OHNO, N., YASHIDA, N., SAEKI, T., Formation process of tungsten nanostructure by the exposure to helium plasma under fusion relevant plasma conditions, Nucl. Fusion **49** (2009) 095005.

[13] FORTY, C.B.A., BUTTERWORTH, G.J., SUBLET, J.C., Burnup of some refractory metals in a fusion neutron spectrum, J. Nucl. Mater. **212** (1994) 640.

[14] COTTRELL, G.A., Sigma phase formation in irradiated tungsten, tantalum and molybdenum in a fusion power plant, J. Nucl. Mater. **334** (2004) 166.

[15] GILBERT, M.R., SUBLET, J.C., Neutron-induced transmutation effects in W and W-alloys in a fusion environment, Nucl. Fusion **51** (2011) 043005.

[16] MAISONNIER, D., COOK, I., PIERRE, S., LORENZO, B., EDGAR, B., KARIN, B., LUIGI, D.P., ROBIN, F., LUCIANO, G., STEPHAN, H., CLAUDIO, N., PRACHAI, N., ALDO, P., NEILL, T., DAVID, W., The European power plant conceptual study, Fusion Eng. Des. **75** (2005) 1173.

[17] GARFINKLE, M., WITZKE, W.R., KLOPP, W.D., Superplasticity in tungsten-rhenium alloys, NASA TN. **D-4728** (1968) 1

[18] TYBURSKA-PÜSCHEL, B., ALIMOV, V.K., On the reduction of deuterium retention in damaged Re-doped W, Nucl. Fusion **53** (2013) 123021.

[19] HATANO, Y., AMI, K., ALIMOV, V.K., KONDO, S., HINOKI, T., TOYAMA, T., FUKUDA, M., HASEGAWA, A., SUGIYAMA, K., OYA, Y., OYAIDZU, M., HAYASHI, T., Deuterium retention in W and W-Re alloy irradiated with high energy Fe and W ions: Effects of irradiation temperature, Nucl. Mater. Energy **9** (2016) 93-97.

[20] ARMSTRONG, D.E.J., YI, X., MARQUIS, E.A., ROBERTS, S.G., Hardening of self ion implanted tungsten and tungsten 5-wt% rhenium, J. Nucl. Mater. **432** (2013) 428-436.

[21] XU, A., ARMSTRONG, D.E.J., BECK, C., MOODY, M.P., SMITH, G.D.W., BAGOT, P.A.J., ROBERTS, S.G., Ion-irradiation induced clustering in W-Re-Ta, W-Re and W-Ta alloys: An atom probe tomography and nanoindentation study, Acta Mater. **124** (2017) 71-78.

[22] XU, A., BECK, C., ARMSTRONG, D.E.J., RAJAN, K., SMITH, G.D.W., BAGOT, P.A.J., ROBERTS, S.G., Ion-irradiation-induced clustering in W–Re and W–Re–Os alloys: A comparative study using atom probe tomography and nanoindentation measurements, Acta Mater. **87** (2015) 121-127.

[23] HASEGAWA, A., FUKUDA, M., YABUUCHI, K., NOGAMI, S., Neutron irradiation effects on the microstructural development of tungsten and tungsten alloys, J. Nucl. Mater. **471** (2016) 175-183.

[24] LU, G.-H., ZHOU, H.-B., BECQUART, C.S., A review of modelling and simulation of hydrogen behaviour in tungsten at different scales, Nucl. Fusion **54** (2014) 086001.

[25] MARIAN, J., BECQUART, C.S., DOMAIN, C., DUDAREV, S.L., GILBERT, M.R., KURTZ, R.J., MASON, D.R., NORDLUND, K., SAND, A.E., SNEAD, L.L., SUZUDO, T., WIRTH, B.D., Recent advances in modeling and simulation of the exposure and response of tungsten to fusion energy conditions, Nucl. Fusion **57** (2017) 092008.

[26] GILLIAM, S.B., GIDCUMB, S.M., PARIKH, N.R., FORSYTHE, D.G., PATNAIK, B.K., HUMN, J.D., SNEAD, L.L., LAMAZE, G.P., Retention and surface blistering of helium irradiated tungsten as a first wall material, J. Nucl. Mater. **347** (2005) 289.

[27] TOKUNAGA, K., TAMURA, S., YOSHIDA, N., EZATO, K., TANIGUCHI, M., SATO, K. SUZUKI, S., AKIBA, M., Synergistic effects of high heat loading and helium irradiation of tungsten, J. Nucl. Mater. **329** (2004) 757.

[28] LI, Y.H., ZHOU, H.B., JIN, S., ZHANG, Y., LU, G.H., Strain-induced variation of electronic structure of helium in tungsten and its effects on dissolution and diffusion, Comp. Mater. Sci. **95** (2014) 536.

[29] POON, M., HAASZ, A.A., DAVIS, J.W., Modelling deuterium release during thermal desorption of D+-irradiated tungsten, J. Nucl. Mater. **374** (2008) 390.

[30] LUO, G.N., SHU, W.M., NISHI, M., Incident energy dependence of blistering at tungsten irradiated by low energy high flux deuterium plasma beams, J. Nucl. Mater. **347** (2005) 111.

[31] ZHOU, H.B., OU, X., ZHANG, Y., SHU, X., LIU, Y.L., LU, G.H., Effect of carbon on helium trapping in tungsten: A first-principles investigation, J. Nucl. Mater. **440** (2013) 338.

[32] WANG, X.X., ZHANG, Y., ZHOU, H.B., WANG, J.L., Effects of niobium on helium behaviors in tungsten: a first-principles investigation, Acta Phy. Sin. **63** (2014) 046103.

[33] NISHIJIMA, D., YE, M.Y., OHNO, N., TAKAMURA, S., Incident ion energy dependence of bubble formation on tungsten surface with low energy and high flux helium plasma irradiation, J. Nucl. Mater. **313** (2003) 97.

[34] DEBELLE, A., BARTHE, M.F., SAUVAGE, T., BELAMHAWAL, R., CHELGOUM, A., DESGARDIN, P., LABRIM, H., Helium behaviour and vacancy defect distribution in helium implanted tungsten, J. Nucl. Mater. **362** (2007) 181.

[35] WANG, J.L., ZHANG, Y., ZHOU, H.B., JIN, S., LU, G.H., First-principles investigation of helium dissolution and clustering at a tungsten (110) surface, J. Nucl. Mater. **461** (2015) 230.

[36] BECQUART, C.S., DOMAIN C., Ab initio calculations about intrinsic point defects and He in W, Nucl. Instrum. Methods Phys. Res. Sect. B **255** (2007) 23-26.

[37] BECQUART, C.S., DOMAIN C., Migration energy of He in W revised by Ab initio calculations, Phys. Rev. Lett. **97** (2006) 196402.

[38] ZHOU, H.B., WANG, J.L., JIANG W., ET AL. Electrophobic interaction induced impurity clustering in metals, Acta Mater., **119** (2016) 1.

[39] YAN, W.L., ZHOU, H.B., JIN, S., ZHANG, Y., LU, G.H., Dissolution energetics and its strain dependence of transition metal alloying elements in tungsten, J. Nucl. Mater. **456** (2015) 260.

[40] LI, Y.H., ZHOU, H.B., JIN, S., ZHANG, Y., DENG, H., LU, G.H., Behaviors of transmutation elements Re and Os and their effects on energetics and clustering of vacancy and self-interstitial atoms in W, Nucl. Fusion **57** (2017) 046006.

[41] LI, Y.H., ZHOU, H.B., DENG, H., LU, G., LU, G.H., Towards understanding the mechanism of rhenium and osmium precipitation in tungsten and its implication for tungsten-based alloys, J. Nucl. Mater. **505** (2018) 30-43.

IAEA
International Atomic Energy Agency

No. 26

ORDERING LOCALLY

IAEA priced publications may be purchased from the sources listed below or from major local booksellers.

Orders for unpriced publications should be made directly to the IAEA. The contact details are given at the end of this list.

NORTH AMERICA

Bernan / Rowman & Littlefield
15250 NBN Way, Blue Ridge Summit, PA 17214, USA
Telephone: +1 800 462 6420 • Fax: +1 800 338 4550
Email: orders@rowman.com • Web site: www.rowman.com/bernan

Renouf Publishing Co. Ltd
22-1010 Polytek Street, Ottawa, ON K1J 9J1, CANADA
Telephone: +1 613 745 2665 • Fax: +1 613 745 7660
Email: orders@renoufbooks.com • Web site: www.renoufbooks.com

REST OF WORLD

Please contact your preferred local supplier, or our lead distributor:

Eurospan Group
Gray’s Inn House
127 Clerkenwell Road
London EC1R 5DB
United Kingdom

Trade orders and enquiries:
Telephone: +44 (0)176 760 4972 • Fax: +44 (0)176 760 1640
Email: eurospan@turpin-distribution.com

Individual orders:
www.eurospanbookstore.com/iaea

For further information:
Telephone: +44 (0)207 240 0856 • Fax: +44 (0)207 379 0609
Email: info@eurospangroup.com • Web site: www.eurospangroup.com

Orders for both priced and unpriced publications may be addressed directly to:

Marketing and Sales Unit
International Atomic Energy Agency
Vienna International Centre, PO Box 100, 1400 Vienna, Austria
Telephone: +43 1 2600 22529 or 22530 • Fax: +43 1 26007 22529
Email: sales.publications@iaea.org • Web site: www.iaea.org/books

ISBN 978–92–0–109119-2
ISSN 1018–5577